# Fusion Machine Scale Wall Material Erosion and Re-deposition Modeled with GITR as a Part of an Integrated Simulation to Evaluate Tungsten Plasma Facing Component Lifetimes and Feedback on Fusion Plasmas

A Dissertation Presented for the

Doctor of Philosophy

Degree

The University of Tennessee, Knoxville

Timothy Reed Younkin

December 2019

# Abstract

Creating a neutron source via fusion in a confined core plasma and extracting the necessary energy creates an adverse environment at the plasma-material interface (PMI). In order for the fusion reaction to be sustainable, the response of the coupled plasma-surface interaction must radiate in the edge plasma while an atomic fraction of $10^{-5}$ of W in the core will make fusion unachievable. Because of this limitation, the underlying physics in the plasma-material interaction must be understood in order to make fusion feasible and economical.

This dissertation extends simulation capabilities of the plasma-surface interaction to higher fidelity with the inclusion of multi-scale physics modeling and code integration. Of relevance to the performance of both the divertor and fusion plasma is the migration, interaction kinetics, and re-deposition of the eroded wall material. Considerations of impurity transport can affect surface composition, surface evolution, material response to energetic ions, and radiative properties of the edge and core plasma. Therefore, the development of a high performance, 3D kinetic impurity transport code capable of simulating whole device geometries, and designed to accept high fidelity input for background plasma, plasma sheath, and material response models is necessary. The development of the global impurity transport code (GITR) addresses the necessary physics and computer science challenges associated with the impurity transport problem.

A high performance, platform portable, accelerator enabled implementation of the trace impurity model (GITR) has been developed to simulate impurity migration on the scale of a whole device fusion machine. GITR has been benchmarked with simple fluid theory to demonstrate accuracy of the physics model. Comparison to linear plasma device experiments has demonstrated accurate results for net erosion, volumetric impurity density profiles, and migration behavior characteristics. Bayesian statistics have been used to perform formal uncertainty quantification based on background plasma profile measurements in this linear device geometry. Tokamak scenarios for ITER He operation and D-T operation have also been simulated to demonstrate the impurity erosion and migration characteristics for this future device.

# Table of Contents


**1 Introduction and Background** **1**
1.1 Overview of Plasma-Material Interactions . . . . . 1
1.1.1 Synopsis . . . . . 1
1.1.2 Thermonuclear Fusion . . . . . 2
1.1.3 Radiative Losses In Fusion Plasmas . . . . . 4
1.1.4 Diffusional / Collisional Losses and the Scrape Off Layer . . . 6
1.1.5 The Plasma Sheath . . . . . 8
1.1.6 Candidate PFC Materials and Their Properties . . . . . 8
1.1.7 Implanted Gas Species Behavior . . . . . 10
1.1.8 Sources of Impurities in the Plasma . . . . . 11
1.2 The Role of Modeling the Plasma-Material Interaction . . . . . 12

**2 Assessment of Relevant Research** **14**
2.1 Approaches to Modeling Impurities For Fusion Applications . . . . . 14
2.2 Fluid Modeling of Impurities in 2D . . . . . 14
2.2.1 Fluid Simulation of Heavy Impurities . . . . . 14
2.2.2 Comparison of Fluid Model to Kinetic Model . . . . . 15
2.3 Kinetic Impurity Monte Carlo Codes . . . . . 17
2.4 Code-Experiment Comparisons . . . . . 18
2.4.1 ERO Modeling of PSI-2 Ar Exposed Tungsten . . . . . 18
2.4.2 ERO simulations of DIMES probe in DIII-D . . . . . 21
2.4.3 DIVIMP Modeling of JET ITER-Like Wall . . . . . 23
2.5 Impurity Transport Simulation Workflows . . . . . 23
2.5.1 WallDYN . . . . . 24
2.5.2 Rough Surface Simulation with SURO/ERO/SDPIC . . . . . 25
2.6 Summary . . . . . 28

**3 Modeling Tool Motivation and Development** **30**
3.1 High Performance Impurity Model to Extend To Larger Domains . . 30
3.2 GITR Code Development Effort . . . . . 31
3.2.1 Physics Requirements . . . . . 31
3.2.2 Computer Science Requirements and Challenges . . . . . 31
3.3 GITR Code Details . . . . . 32
3.3.1 Physics Model . . . . . 32
3.3.2 Computational Model . . . . . 35
3.3.3 Geometry Algorithms . . . . . 37
3.3.4 Benchmark Problems . . . . . 40
3.3.5 Performance . . . . . 48

3.3.6 Discussion and Future Work . . . 49
3.4 PSI Integrated Simulation . . . 51
3.4.1 Wrappers and data passing for the integrated simulation . . . 53
3.5 Summary . . . 55

**4 Integrated Benchmarks of GITR 56**
4.1 GITR Benchmarks with Simple Models and Code Comparison to DIVIMP . . . 56
4.1.1 Region A - the plateau region . . . 57
4.1.2 Region B - the impurity density decay region . . . 58
4.1.3 Region C - the impurity build-up region . . . 61
4.2 Additional GITR Benchmarks . . . 62
4.2.1 Cross-Field Diffusion With Curved field lines . . . 63
4.2.2 Lorentz Force Integration in Curved field lines . . . 67
4.3 Summary . . . 69

**5 Benchmarking GITR to Linear Plasma Device with UQ 72**
5.1 PISCES-A Experiments . . . 72
5.2 Method . . . 72
5.2.1 Experimental set-up . . . 72
5.2.2 Modeling method . . . 75
5.3 The integrated model of PISCES experiments . . . 78
5.4 Results . . . 79
5.4.1 Impurity transport . . . 79
5.5 Detailed Results of the Titania Tower Experiments Using F-TRIDYN He Sputtering of W . . . 87
5.5.1 Simulation Details . . . 89
5.5.2 GITR Simulation Result . . . 92
5.6 Uncertainty Quantification of W Transport . . . 95
5.6.1 UQ Methods . . . 95
5.6.2 Uncertainty Quantification Results . . . 96
5.6.3 Conclusions . . . 103
5.7 Summary . . . 105

**6 Simulation of ITER PSI 106**
6.1 ITER Integrated Model Simulation . . . 106
6.2 He plasma discharge . . . 106
6.2.1 Integrated Model for PSI . . . 106
6.2.2 GITR 2D Impurity Transport Study . . . 118
6.3 ITER Fusion Power Operation . . . 124
6.3.1 Integrated Modeling Results . . . 125
6.4 Summary . . . 133

**7 Summary and Direction for Future Research 134**
7.1 Motivation for Modeling PSI . . . 134
7.2 Prior Research . . . 134
7.3 Tool Development and Original Contribution . . . 135
7.4 Code Verification and Benchmarking . . . 135
7.5 PISCES-A simulations of He exposed W . . . 136

7.6 ITER Research . . . . . 136
7.7 Code adoption . . . . . 137
7.8 Direction for future research . . . . . 137

**Bibliography** **138**

**Vita** **143**

# List of Figures


1.1 Nuclear binding energy per nucleon vs. mass number. This curve demonstrates that the fusion of light elements results in a mass defect and the resulting release of energy. This difference is particularly significant moving from H to He which results in substantial energy yield from fusion [1]. . . . . 2

1.2 Maxwellian averaged reaction rate densities (as labeled) for D-D and D-T fusion as a function of plasma temperature, as reproduced from Ref. [1]. . . . . 3

1.3 Fusion reactants and by-products (showing energy carried by the neutron), as reproduced from Ref. [1]. Energy yield and threshold energy for the fusion reaction are also shown in K and keV. . . . . 4

1.4 Triple product values for ideal ignition and breakeven for a D-T plasma as a function of temperature, as reproduced from Ref. [2]. . . 5

1.5 Radiation loss or power function (left). Mean charge as a function of electron temperature (right), as reproduced from Ref. [1]. . . . . 5

1.6 Fraction of impurity density which produces a radiation power equal to half the fusion alpha heating power produced, as reproduced from [1]. . . . . 6

1.7 Schematic illustration of the different areas of a tokamak showing the distinct magnetic configuration and various plasma retions [6]. . . . . 7

1.8 The electrostatic potential,$\phi$, the ion speed, $v_i$, and the ion and electron densities and their spatial variation across the sheath. Wall is on the left and the pre-sheath on the right, as reproduced from Ref. [1]. . . . . 9

1.9 Diagram showing the range in time and spatial scale which fusion-relevant processes in the plasma, materials, and their interactions occur and how they are connected [12]. . . . . 13

1.10 Flow chart of a proposed integrated simulation made of high fidelity physics modules. Coupling of the edge plasma, including sheath and impurity transport effects to the materials response, including implantation and surface evolution. Feedback from recycled and sputtered atoms must also be fed back on the SOL plasma to investigate effects on core plasma performance. . . . . 13

2.1 Comparison of the net W erosion or deposition rate computed for various bundling schemes. The various wall regions are noted as: HFS: high field side, Top: upper X-point region, LFS: low field side, OD: outer divertor, PFR: private flux region, ID: inner divertor, as reproduced from Ref. [16]. . . . . 16

2.2 2D density profiles of tungsten impurity in poloidal cross-section. The densities for all the charge states are summed up and the results are plotted: (a) by B2.5 fluid code (case A) and (b) by IMPGYRO kinetic code (case B), as reproduced from Ref. [18]. . . . . 17
2.3 Experimental setup schematic for Ar exposed W in PSI-2, as reproduced from Ref. [23]. . . . . 19
2.4 Radial mass loss measurements and ERO simulated values, as reproduced from Ref. [23]. . . . . 20
2.5 Tungsten neutral 400.9nm emission spectroscopy for high power discharges of varying bias voltages, as reproduced from Ref. [23]. . . . . 20
2.6 Mass gain away from the target at the QMB sensor for varying discharge power, as reproduced from Ref. [23]. . . . . 21
2.7 Variation in redeposition ration for W and Mo as a function of fraction of sheath potential used (Brooks model for sheath used for each) [24]. 22
2.8 Adjusted experimental and simulated redeposition fractions for the large dot using the ERO value for redeposition on the small dot [24]. 22
2.9 Erosion profiles at the inner and outer target strikepoints, as reproduced from Ref. [26]. . . . . 24
2.10 Concentrations of W in the core, main SOL, divertor SOL, and private flux region for the varying input densities, as reproduced from Ref. [26]. . . . . 25
2.11 An example Be transfer matrix produced by DIVIMP and used as input to WallDYN, as reproduced from Ref. [27]. . . . . 26
2.12 Net deposition as predicted by WallDYN, as reproduced from Ref. [28]. . . . . 26
2.13 Illustration of the surface topography of the simulated rough surface and the experimental setup for the methane injection experiments done in TEXTOR, as reproduced from Ref. [29]. . . . . 27
2.14 Top view of the deposited (a), eroded (b), net deposited (c) 13C areal densities after the exposure of 500 s and surface topography at the exposure time of 0s (d) 300s (e) 500s (f) with a 13C flux ratio of 3.5% (a = b = c = 0.5$\mu$m), as reproduced from Ref. [29]. . . . . 28

3.1 GITR 3D boundary element particle intersection schematic and algorithm. With an initial position $P_0$ and a current position $P$ the plane equation is used to determine distance to the surface for each position. Then a set of cross-products is used to determine if the intersection is within the triangle. . . . . 38
3.2 GITR particle distance to 3D surface element calculation for force adjustment. The particle position is projected perpendicularly onto the plane. Cross products are used to determine if the projected point is within the triangle. . . . . 40
3.3 Charge state distribution fraction for W ions in a 20eV plasma from the analytic values (blue) and GITR prediction (red). . . . . 42
3.4 Characteristic times (inverses of the frequencies previously described in equation 3.2) for W1+ ion evolution due to Coulomb collisions with a Deuterium and electron background plasma as a function of particle kinetic energy. . . . . 43

3.5 Average W ion x-direction velocity over time. W impurity population gets dragged with the background D plasma on the order of milliseconds. . . . . 43
3.6 Average GITR simulated temperature evolution for 10eV W1+ launched into a flowing (2,000 m/s) D plasma background. Mean time for velocity equilibration $\tau_E$ is shown as a vertical black line. . . . . 44
3.7 Average GITR simulated perpendicular velocity evolution for W1+ in a D background compared to approximate velocity diffusion from Equation 3.15 and 3.16. . . . . 45
3.8 GITR example case simulated geometry with side cut away. Deposited particle rate (colored surfaces) and example particle tracks (different colored lines) are shown. . . . . 46
3.9 GITR example case ion-surface impact energy-angle distribution summed over all surfaces. . . . . 47
3.10 GITR example case W density profile (summed over all charge states) integrated over y-domain. . . . . 48
3.11 GITR run time with increasing particle number shows flat scalings for both OpenMP and CUDA until parallel threads are filled with work at which the run time becomes approximately linearly proportional to number of particles simulated (possibly super-linear or following a power law). . . . . 49
3.12 GITR full code execution time as a function of increasing number of time steps shows a flat region before reaching a linear relationship with number of time steps. Once the main loop execution time overcomes that of initialization, MPI reductions, and file writing the execution time is proportional to the time spent in the main loop. . . 50
3.13 GITR main loop run time with number of geometry elements shows vastly different behavior when using the hash. Without the hash, run time is linearly proportional to number of geometry boundary elements. Performance with CUDA is especially bad because of the scattered memory accessing without using a hash. Hashing flattens scaling and results in greater performance with CUDA. . . . . 50
3.14 GITR hash creation time as a function of number of boundary elements. Despite poor scaling with number of boundary elements (and fidelity required for the hash) compute times for hundreds of thousands of geometry elements are at most thousands of seconds. . . . . 51

4.1 Peak impurity density near the target as a function of flow velocity (towards the target). GITR and SFT solution are shown. . . . . 58
4.2 Peak impurity density near the target as a function of target ion temperature (and flow varying with $c_s$). GITR and SFT solution are shown. . . . . 59
4.3 Decay of impurity density in the SOL with competition of electric field and parallel velocity diffusion for several cases. . . . . 60
4.4 Decay of impurity density in the SOL with competition of drag force and parallel velocity diffusion. . . . . 60

4.5 Divertor leakage fraction as computed by GITR agrees with the SFT solution for the case B collisional case. Higher temperatures are shown to lead to greater divertor leakage with a $T^{-2}$ dependence. . . 62
4.6 SFT divertor leakge in a collisionless case is shown to be over-predicted compared to the results of GITR. . . . . 63
4.7 Deep injection divertor leakage with and without temperature variation (temperature gradient exists in both cases), which shows good agreement between GITR and SFT. . . . . 64
4.8 Parallel (z-directed) C4+ impurity velocity distribution compared to the analytic solution for T=50 eV. . . . . 64
4.9 Density profile using the solenoidal field and an injected impurity source at r=1.25 m, with D=10 $m^2/s$, and allowed to diffuse for 0.01 s 65
4.10 Conical frustum, as obtained from mathworld.wolfram.com, showing R1 as the beginning radius and s as the diffusion step length. . . . . 65
4.11 W10+ particles injected at r=1.5 m (shown by black dashed line) and diffusing perpendicular to the solenoidal field. . . . . 66
4.12 Comparison of the GITR radial position drift for the poloidal curvature (green) compared to the analytic drift approximation (blue). . . 67
4.13 Comparison of the GITR radial position drift (green) for the toroidal curvature compared to the analytic drift approximation (blue). . . . . 68
4.14 Impurity density using the updated diffusion algorithm and running an identical case to Figure 4.9 . . . . . 68
4.15 Density profile for the corrected and uncorrected diffusion. The corrected algorithm shows a flat density profile across the core decreasing towards the absorbing boundaries. . . . . 69
4.16 Particle tracks simulated by the Boris and RK4 integrators using the solenoidal magnetic field. . . . . 70
4.17 Paticle tracks for various integrators and time steps at the outer midplane. . . . . 70
4.18 Minor radius as a function of time for the various integration schemes and time steps. Boris shows no outward or velocity drift compared to that of the RK4. . . . . 71
4.19 Particle velocity over time is conserved by the Boris integration scheme. For large time step of the RK4, velocity is badly distorted. . . . . 71

5.1 PISCES Ti-Tower target and collector tower setup for experiments 20170313 and 20170314. . . . . 74
5.2 Langmuir probe measurements for ion flux, electron temperature, and electron density for 20170313. . . . . 75
5.3 Langmuir probe measurements for ion flux, electron temperature, and electron density for 20170314. . . . . 76
5.4 Flow chart demonstrating the connection of various physics processes (and models) for a proposed tokamak integrated model (left) and the present PISCES integrated model (right). . . . . 77
5.5 Sputtering yield (left) and reflection coefficient (right) for W as projectile and target. . . . . 80
5.6 Sputtered W atom (via 244 eV W) energy and angle distributions for various impact angles. . . . . 81

5.7 Schematic demonstration of the uncertainty/sensitivity scan performed with GITR. For both the lower (20170313) and higher flux (20170314) cases the original fit profiles as well as the ±20% values on $T_e$ and $n_e$ were simulated. Four varying sputtered particle angular distributions were used. . . . . 82
5.8 Titania tower bead mass gain during exposure 20170313 measured experimentally (black), and simulated by GITR (green band). . . . . 82
5.9 W I emission diagnostic during exposure 20170313 measured experimentally (black), and simulated by GITR (green band). . . . . 83
5.10 Titania tower bead mass gain during exposure 20170314 measured experimentally (black), and simulated by GITR (green band). . . . . 84
5.11 W I emission diagnostic during exposure 20170314 measured experimentally (black), and simulated by GITR (green band). . . . . 84
5.12 W impurity flux impinging on the 1 inch W disc in experiment 20180205. 86
5.13 Energy distribution of W ions impacting the W target. . . . . 86
5.14 Angle distribution of W ions impacting the W target. . . . . 87
5.15 W impurity flux impinging on the 1 inch W disc in experiment 20180213. 88
5.16 Energy distribution of W ions impacting the W target. . . . . 88
5.17 Angle distribution of W ions impacting the W target. . . . . 89
5.18 GITR simulated geometry showing only the W target plate and titania tower. . . . . 90
5.19 High flux (20170314) experimentally measured ion flux profile and data fit used in GITR simulation. . . . . 91
5.20 High flux (20170314) experimentally measured electron temperature profile and data fit used in GITR simulation. . . . . 91
5.21 High flux (20170314) experimentally measured electron density profile and data fit used in GITR simulation. . . . . 91
5.22 Neutral W (WI) emission spectroscopy 429.4 nm experimentally measured and simulated by GITR for the low flux case (20170313). . . . . 93
5.23 Low flux (20170313) results for titania bead mass gain by bead (1 is closest to the target plate, 13 is furthest). . . . . 93
5.24 Neutral W (WI) emission spectroscopy 429.4 nm experimentally measured and simulated by GITR for the high flux case (20170314). . . . 94
5.25 High flux (20170314) results for titania bead mass gain by bead (1 is closest to the target plate, 13 is furthest) . . . . . 94
5.26 Posterior predictive fits as well as posterior samples of the profiles $n(r)$ and $T(r)$. . . . . 98
5.27 Posterior predictive of GITR outputs together with experimental data. The left plot shows quantiles, while the right plot shows the variance contributions. . . . . 98
5.28 One-dimensional marginal output PDFs for all 14 outputs. . . . . 99
5.29 Total sensitivities, i.e. variance contributions with respect to the four components, for all 14 outputs of interest. . . . . 99
5.30 Posterior predictive of GITR outputs together with experimental data. The left plot shows quantiles, while the right plot shows the variance contributions. . . . . 100
5.31 Total sensitivities, i.e. variance contributions with respect to the four components, for all 9 outputs of interest. . . . . 101

5.32 Posterior predictive fits as well as posterior samples of the profiles $n(r)$ and $T(r)$. . . . . 101
5.33 Posterior predictive of GITR outputs together with experimental data. The left plot shows quantiles, while the right plot shows the variance contributions. . . . . 102
5.34 One-dimensional marginal output PDFs for all 14 outputs. . . . . 102
5.35 Total sensitivities, i.e. variance contributions with respect to the four components, for all 14 outputs of interest. . . . . 103
5.36 Posterior predictive of GITR outputs together with experimental data. The left plot shows quantiles, while the right plot shows the variance contributions. . . . . 104
5.37 Total sensitivities, i.e. variance contributions with respect to the four components, for all 11 outputs of interest. . . . . 104

6.1 SOLPS-ITER grid for B2.5 simulation of fluid quantities in the ITER geometry. . . . . 107
6.2 SOLPS-ITER outer midplane profiles for electron temperature (top) and density (bottom) for a 40 MW He plasma discharge. . . . . 108
6.3 Plasma flux and temperature profiles at the outer divertor target, as a function of distance $R$–$R_{sep}$ in meters, including red circles to denote the location of coupled F- TRIDYN and Xolotl simulations. . . . . 109
6.4 Ion temperature gradient parallel to the magnetic field line (a), as processed output and electron density profile interpolated (b) for He operation. . . . . 110
6.5 Magnetic field at the outer divertor target as shown along $R - R_{sep}$ in meters. Magnetic field vector is largely in the toroidal direction with some components in r and z. . . . . 110
6.6 Helium 2+ ion energy angle distribution along the divertor target. . 112
6.7 Ion energy angle distributions from hPIC summed over the angular component to predict the $He^{1+}$ energy distributions along the divertor target. . . . . 112
6.8 Ion energy angle distributions from hPIC summed over the angular component to predict the $He^{2+}$ energy distributions along the divertor target. . . . . 113
6.9 2D histogram of sputtering yields for He impacting W at various energies and angles. The scale is log10 and shows a sputtering threshold energy between 100 and 200 eV. . . . . 114
6.10 Helium sputtering yield and eroded W flux of helium as a function of the charge state of the helium ions responsible for the sputtering, as a function of distance along the outboard divertor target. . . . . 115
6.11 3D surface geometry modeled in GITR, comprised of 1/54th toroidal symmetry (e.g., 1 divertor cassette). The divertor tiles and refined GITR mesh along the tile faces of the target are also shown. . . . . 116
6.12 W erosion flux by the background plasma as displayed on the 3D GITR geometry. This is the vertical part of the outer divertor with the erosion source above the strikepoint. . . . . 117
6.13 Gross erosion and deposition, and net erosion W at the outer divertor target. Also the break-down of gross erosion of W is shown by species. 117

6.14 Mean times for atomic physics operations ionization (6.14a) and recombination (6.14b) in the ITER He plasma. . . . . 119
6.15 Velocity change in one time-step due to Coulomb collision forces. . . . 120
6.16 Total (all W charge state) impurity density on a log 10 scale for ITER He operation. . . . . 120
6.17 Contributions to radiation by W impurities in the divertor during He operation. Figure 6.17a shows a smaller contribution coming from recombination and Bremsstrahlung than excitation in Figure 6.17b. . 121
6.18 Characterization of the energy and angle of eroded W returning to the outer divertor target. Figure 6.18a shows the full W ion energy-angle distribution, while 6.18b shows the mean impacting energy of W ions. . . . . 122
6.19 Gross erosion (He and total), gross deposition, and net deposition as simulated for the ITER He operation. . . . . 123
6.20 Schematic of an eroded impurity being ionized and gyrating near the surface. The curved line is the impurity path, the solid straight line is the surface, and the dashed line is an imaginary surface which would result in prompt re-deposition. . . . . 124
6.21 Gross deposition flux along the ITER wall. The x-coordinate of this plot is distance along the first wall with zero being at the outer strike point, and working counter-clockwise around the machine. . . . . 125
6.22 Ion and electron temperatures at the outer divertor target in coordinates of $R - R_{sep}$ in meters. Fluxes for D, $He^{2+}$ and $Ne^{3+}$ are also plotted (log 10 scale). . . . . 126
6.23 A single ion temperature is used in SOLPS plasma simulation to represent all plasma ion species. This temperature [eV] is shown in the divertor for fusion power operation. . . . . 127
6.24 Neon energy distribution function and sputtering yield resulting from the energy-angle distribtution. . . . . 128
6.25 Neon sputtering yield on W as a function of energy and angle as produced by F-TRIDYN . . . . . 129
6.26 Sputtering yield for species included in the fusion power operation for ITER. The unlabeled (dashed) lines are the 10 charge states of neon. 129
6.27 Effectve erosion yield and flux by background ion species along the outer divertor target for fusion power operation. . . . . 130
6.28 Gross deposition and erosion, and net deposition of tungsten at the outer divertor for fusion power operation. . . . . 131
6.29 W impurity density at the outer divertor target. . . . . 132

# Chapter 1

# Introduction and Background

## 1.1 Overview of Plasma-Material Interactions

### 1.1.1 Synopsis

Creating a thermonuclear fusion reactor that is sustainable for commercial energy production faces many obstacles in becoming experimentally operational and then economically viable. Simultaneous goals of producing a burning fusion plasma and harnessing the energy output work against one another at the plasma-material interface (PMI). A high-temperature, high-density core plasma requires high plasma species purity to maintain a fusion reaction at a sufficient density. The fusion reaction produces energetic by-products which bombard and damage the surrounding materials and structures. This damage to the plasma-facing components along with the nominally high heat and particle fluxes from the power exhaust can alter the material ability to remove heat and resist erosion. A degraded ability to remove heat and particles, along with wall material lost to the plasma, has the potential to contaminate the core, making the fusion reaction more difficult to achieve. A fundamental scientific understanding of these physical processes must be understood for design changes and technological advances to be made and continue moving fusion science and energy forward.

Hydrogenic fuel species are heated and confined to increase the likelihood of overcoming Coulomb repulsion and fusing to produce energy. The helium ash by-product will give up its kinetic energy within the vacuum vessel, heating the plasma via Coulombic interactions and elastic collisions with atomic nuclei. The produced neutron will stream freely out of the fusion core and into the surrounding vessel and structural components or blanket structure. Maintenance of a hot core plasma acting as a neutron source along with an extractable energy source (kinetic energy/heat from the neutron) allows the fusion plasma to continue its reaction while producing electrical energy for the grid. Electron-ion and ion-ion Coulomb collisions that do not result in the fusion of two light nuclei can result in electronic excitations and radiation due to acceleration of the charged particles involved. Portions of this radiation streams out of the plasma and are not recoverable and results in a power loss term for a fusion plasma. In addition to radiation, collisions cause diffusive motion and are a cause for loss of confinement of plasma. This diffusive motion results in a source of particles and heat exiting the confined plasma, which drifting outward will come into contact with the limiting surfaces of the vessel containing

the plasma. At this point, there is no avoiding the plasma-material interaction, so the plasma-facing materials and components are designed to absorb and handle heat and particle loads in combination with the pumping of the chamber. The plasma will bombard the surface material with plasma ions, leading to the implantation of gas, and eroding of the wall material. The surface will serve as a plasma sink - recombining plasma ions to neutrals and adsorbing gas species into the bulk, and there are a variety of processes which thereby complicate the PMI and feedback on the response of the plasma to the materials and materials to the plasma. Processes that occur on picosecond time scales and atomistic length scales must be integrated out to years of operation on a fusion device scale to evaluate the performance and sustainability of the PFCs.

### 1.1.2 Thermonuclear Fusion

The world's current energy sources of fossil fuels and nuclear fission may last for hundreds or thousands of years, but the extent to which they can be used is indeed finite. For this reason, an energy source that uses hydrogen, the most abundant element in the universe with abundances available on earth as well, provides great promise for an energy solution. Einstein's famous $E = mc^2$ and the curve of nuclear binding energy per nucleon (Figure 1.1) is at the heart of nuclear power and thermonuclear fusion.

In order to access a reaction changing binding energy per nucleon by fusion, two nuclei must reach close enough proximity for the nuclear force to overcome the repulsive forces. Quantum mechanics and experimental measurements show that the fusion reaction is more easily achieved with the isotopes of hydrogen, deuterium (${}^2_1H$

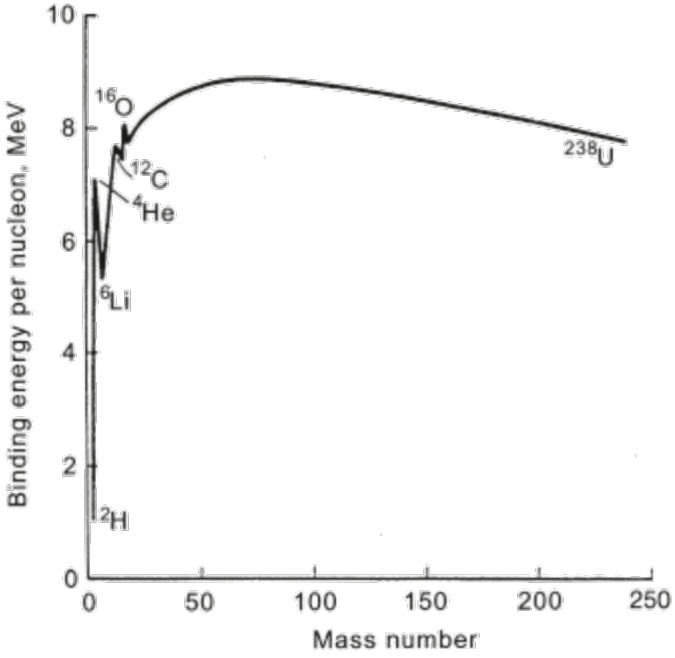


Figure 1.1: Nuclear binding energy per nucleon vs. mass number. This curve demonstrates that the fusion of light elements results in a mass defect and the resulting release of energy. This difference is particularly significant moving from H to He which results in substantial energy yield from fusion [1].

or D) and tritium ($^3_1H$ or T). Figure 1.2 shows cross-sections for for D-D and D-T fusion, in addition to that of $D - He^3$. This shows that the probability for fusion of D and T is larger than D-D fusion or D-He for the temperatures (1 keV to 100 keV). Figure 1.3 shows the reaction, energy release, and threshold energy needed for each of the fusion reactions. D-T fusion is the most easily achievable with respect to plasma parameters (temperature and density), and it also has a high energy yield (17.6 MeV).

Achieving conditions where more energy is released from the fusion reaction than it takes to maintain the plasma temperature, density, and confinement is called break-even. A power balance setting the energy loss rate equal to the heating from alpha particles gives

$$P_E = P_\alpha \tag{1.1}$$

$$\frac{3nT}{\tau_E} = \frac{1}{4}n^2 < \sigma v > E_\alpha \tag{1.2}$$

Where $n$ and $T$ are plasma density and temperature respectively, $\tau_E$ is energy confinement time, $< \sigma v >$ is reaction rate and $E_\alpha$ is kinetic energy of an alpha produced by fusion. Rearranging this equation to get the triple product of density, temperature and confinement time and using the most favorable conditions [2] (T≈15keV for D-T) it can be shown that

$$n\tau_E T \geq 3 \times 10^{21} m^{-3} keV s \tag{1.3}$$

$$n\tau_E \geq 2 \times 10^{20} m^{-3} s \tag{1.4}$$

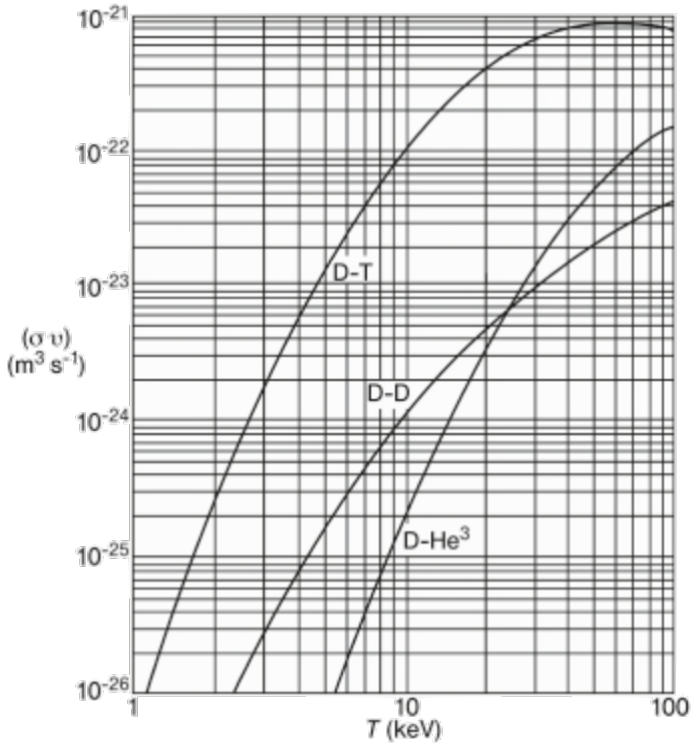


Figure 1.2: Maxwellian averaged reaction rate densities (as labeled) for D-D and D-T fusion as a function of plasma temperature, as reproduced from Ref. [1].

| Reaction | Thermonuclear energy release MeV | Threshold energy K | keV |
|---|---|---|---|
| $D + T \rightarrow {}^4He + n$ (14.1 MeV) | 17.6 | $4.5 \times 10^7$ | 4 |
| $D + D \rightarrow \begin{cases} T + p \\ {}^3He + n$ (2.5 MeV) | 4.0<br>3.25 | $4.0 \times 10^8$ | 35 |
| $D + {}^3He \rightarrow {}^4He + p$ | 18.2 | $3.5 \times 10^8$ | 30 |

Figure 1.3: Fusion reactants and by-products (showing energy carried by the neutron), as reproduced from Ref. [1]. Energy yield and threshold energy for the fusion reaction are also shown in K and keV.

Equation 1.3 shows the minimum triple product (density, energy confinement, and temperature) necessary for breakeven for a D-T fusion plasma. Assuming temperature is sufficiently maintained, equation 1.3 can be cast into a product of density and energy confinement as shown in equation 1.4. This product is familiarly known as the Lawson criterion which specifies the combination of density and energy confinement needed for break-even. By plotting the triple product as a function of plasma temperature as in Figure 1.4, it can be seen that there exists a minimum between 10 keV and 20 keV. This is the optimal range for achieving fusion in currently planned fusion devices. Magnetically confined fusion devices which make use of toroidal confinement of the plasma, in particular, the Tokamak is the leading design leading towards controlled fusion. Tokamak is a Russian acronym for "toroidal chamber magnetic" [3] and confines the plasma by using a toroidal field in combination with a transformer which induces a toroidal plasma current (which results in a poloidal field) [4].

In the progression towards producing commercial tokamak reactors, these machines have become increasingly complex. In addition to the coils mentioned, vertical field coils and shaping coils exist, and superconducting magnets are being introduced to maximize field strength. Many sources of heating, including radiofrequency, and neutral beams are used to heat the plasma, so ports and antennas exist in order to provide access to the vacuum vessel. Technologies for breeding blankets to produce tritium, neutron shielding, and many others are also under development.

### 1.1.3 Radiative Losses In Fusion Plasmas

One avenue for energy loss from the plasma which reduces the energy confinement time, $\tau_E$, given in Equations (1.2) to (1.4) is electromagnetic radiation.

The presence of impurities in plasma results in radiative losses of several types which cause cooling of the plasma: Bremsstrahlung radiation due to Coulomb collisions, cyclotron radiation due to charged particle motion in a magnetic field, line emission due to excitation and de-excitation of orbital electrons, and radiative and dielectric recombination. Of these types, Bremsstrahlung and line emission lead to the largest losses for high Z impurities. Figure 1.5 shows total power radiated by a tungsten impurity as a function of background plasma temperature and is compared to several atoms of lower Z. The reason for the large impurity radiation from tungsten is two-fold. First, Bremsstrahlung radiation is proportional to $Z^2$ rising to charge numbers as high as 15-20 in the edge plasma and even higher in the core.

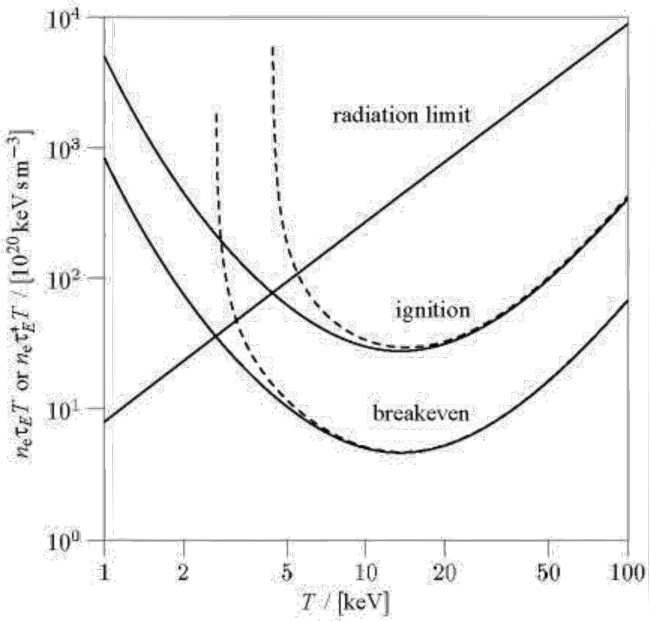


Figure 1.4: Triple product values for ideal ignition and breakeven for a D-T plasma as a function of temperature, as reproduced from Ref. [2].

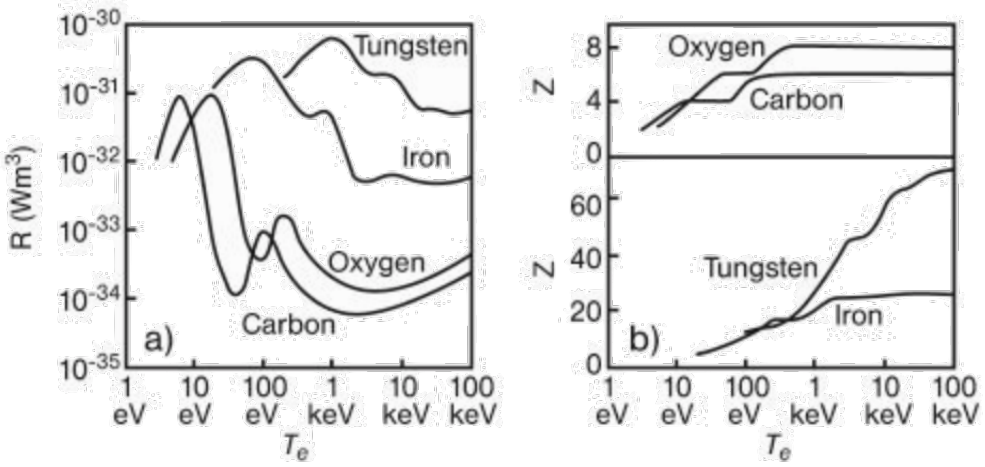


Figure 1.5: Radiation loss or power function (left). Mean charge as a function of electron temperature (right), as reproduced from Ref. [1].

Second, impurities with low atomic number, such as lithium or beryllium, can be completely stripped of electrons at temperatures of 1 keV and no longer produce line radiation. Whereas high atomic number elements, such as molybdenum or tungsten, still retain their lower orbital electrons even in regions of temperatures of 10 keV as supposed in the core of the ITER device. This effect is demonstrated in Figure 1.5 (right) showing the mean charge of several elements as a function of temperature.

Applying power balance arguments as done previously, fractional concentrations of impurities can be shown to have significant deleterious effects on a fusion plasma. The fractional concentration needed to radiate half of the power produced by alpha heating in a fusion plasma is shown in Figure 1.6. Taking into account other contributions to power loss in the plasma, the maximum tolerable He ash atomic fraction is approximately $1^{-1}$ whereas W atomic fractions of $1^{-5}$ are enough to cool the fusion plasma below an adequate temperature for fusion energy production [5].

### 1.1.4 Diffusional / Collisional Losses and the Scrape Off Layer

Because of the high plasma temperature and density required for an operational fusion reactor, an unmitigated particle (and heat) flux to the PFCs would quickly degrade these materials and produce an intolerable impurity content in the plasma. Therefore, a combination of closed and open magnetic field lines are an essential configuration for confining the plasma energy and protecting the first wall. Figure 1.7 shows a prototypical lower divertor tokamak magnetic field topology. Working from the core outward there are closed magnetic surfaces, the most outer of which is the last closed flux surface (LCFS, or separatrix), then are the open magnetic surfaces which connect to the divertor target plates. Between the divertor legs is the private plasma region, and the x-point which is a poloidal magnetic field null. Magnetic

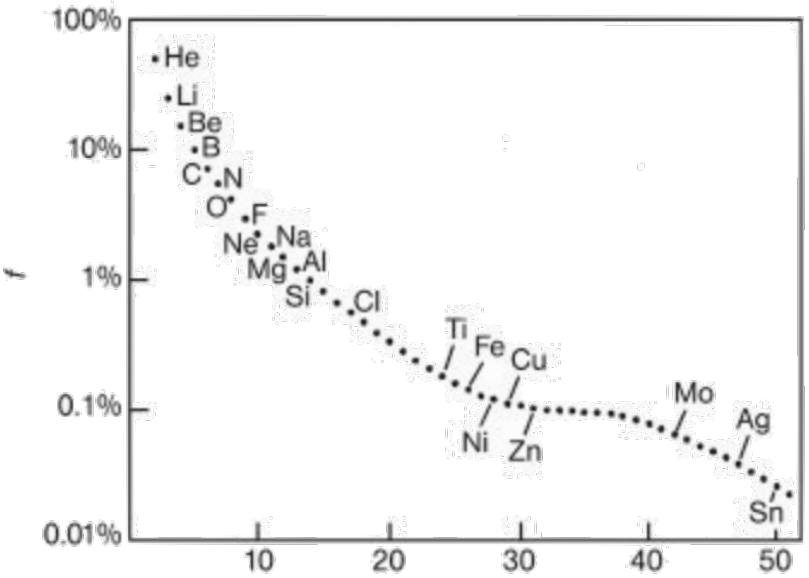


Figure 1.6: Fraction of impurity density which produces a radiation power equal to half the fusion alpha heating power produced, as reproduced from [1].

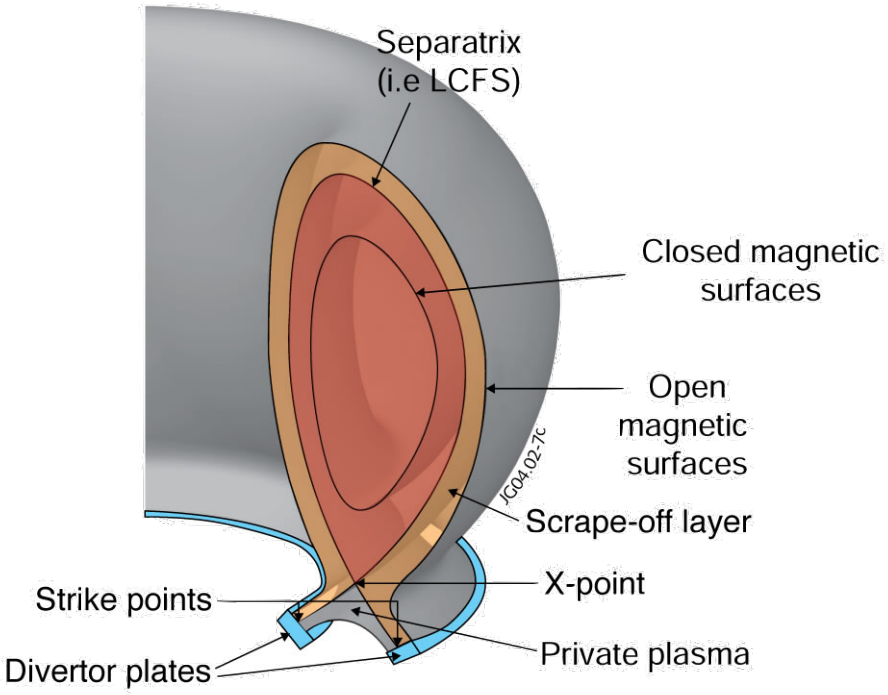


Figure 1.7: Schematic illustration of the different areas of a tokamak showing the distinct magnetic configuration and various plasma retions [6].

confinement of fusion plasma to the closed field lines is not perfect because of the inevitable processes in which plasma particles transport across field lines. The processes responsible for this cross-field motion include diffusion, collisions, finite radius orbit effects, turbulent transport, and edge localized modes (ELMs). In this magnetic configuration, particles which move across magnetic surfaces from closed field lines to open ones will be diverted to the desired target location designed to handle heat and particle flux and pump, thus reducing erosion of the first wall and contamination of the core. This region is called the divertor and it is outfitted with special materials to handle the high heat and particle flux. The divertor configuration is successful at reducing the plasma interaction with the first wall occurs because particles are transported along field lines much faster than across field lines. The region between the separatrix and the first wall where plasma flows towards the divertor targets is referred to as the scrape-off layer (SOL). The open field line design with field lines terminating on the divertor materials results in a plasma sink behavior in which the plasma flows strongly toward the divertor. This ion flux results in ion bombardment of divertor materials in which impinging ions implant within, reflect, and sputter surface material. These processes result in a source of neutral hydrogen, He ash, and impurities coming from the target which can enter the scrape-off layer. This source of atoms coming from the divertor help fuel the plasma and can buffer heat flux to the target via ionization and radiation. However, helium and other impurities can reach the core and dilute the plasma as well. For these reasons, strong flows and temperature and density gradients generally characterize the scrape-off layer region.

### 1.1.5 The Plasma Sheath

The plasma sheath describes a region of net positive charge that is established at the interface of a plasma and a material because of Debye shielding. Effectively, the faster-traveling electrons of the plasma rush ahead of the slower ions and establish a net negative charge and potential on the walls of the vessel containing the plasma. The collective behavior of the plasma acts to balance out the localized charge imbalance shielding the bulk plasma from the negative potential established on the walls. This negative wall potential results in a net positive charge region near the wall, which produces a strong electric field directed towards the wall. This electric field is often divided into a small (several Debye lengths) "Debye sheath" region and a "pre-sheath" region which extends further into the bulk plasma region. Since charge neutrality exists within the plasma, the outflow of electrons and ions is balanced, the electrons being slowed and repelled as they approach the surface and ions being accelerated into the wall. In most cases the electron temperature and density are the determining factors for the width and strength of the sheath electric field. However, in some cases, the magnetic field configuration and electrical surface biasing can have a significant impact on the size and form of the electric potential and field. This region and its structure have a significant effect on the plasma-material interaction as impurities are accelerated into the wall. Since the plasma sheath is an active area of research and configuration details are influential determining factors for the sheath form, details will be discussed and cited as needed throughout this document. A general form of the sheath potential and its effect on plasma ion flow velocity, and plasma density is shown in Figure 1.8. With the increasing negative sheath potential, an increase in ion flow speed occurs with the ion flow velocity reaching the ion acoustic speed, $c_{s0}$ at the sheath entrance. The increasing potential magnitude and ion flow speed results in a decreased ion density near the surface. The electron density is lower than the ion density as electrons are repelled from the negatively charged wall.

### 1.1.6 Candidate PFC Materials and Their Properties

Plasma facing components and materials are tasked with handling heat and particle fluxes and therefore must have favorable properties for thermal conductivity, gas retention, and mechanical structure. In addition to this, the PFC materials must maintain favorable properties and continue to perform well through and during significant ion and neutron irradiation. Ion irradiation and implantation of charged fuel species, helium ash, and impurities are responsible the plasma-material interaction, and neutron irradiation results from the 14.1 MeV (for D-T plasma) peaked neutron spectrum. In addition to the properties mentioned previously, PFC materials must have good qualities for radioactive activation, self-healing (displacements per atom, or DPA), and plasma compatibility. After consideration of such properties, beryllium (Be) and tungsten (W) have been selected for the plasma-facing materials and components for the ITER first wall and divertor, respectively. Tungsten and its application in ITER will be the focus of the present dissertation.

A demonstration fusion reactor the size of ITER is projected to produce 1 GW of energy which could result in approximately one $MWm^{-2}$ of neutron wall loading and ten $MWm^{-2}$ of heat flux to the divertor targets. ITER is expected to operate with core temperatures up to $10^8K$ and density of $10^{16}cm^{-3}$ with edge plasma

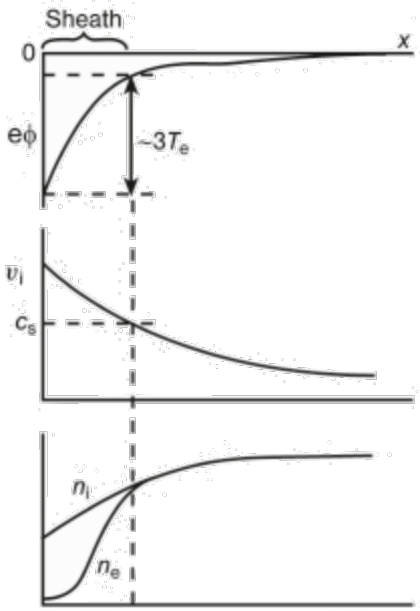


Figure 1.8: The electrostatic potential,$\phi$, the ion speed, $v_i$, and the ion and electron densities and their spatial variation across the sheath. Wall is on the left and the pre-sheath on the right, as reproduced from Ref. [1].

temperatures of $10^3 K$ and density of $10^{15} cm^{-3}$ [7]. The first wall of the reactor will experience a modest flux ($10^{19} - 10^{20} m^{-2} s^{-1}$) of high energy neutral particles (100s of eV) and low energy ions (10s of eV) and could reach temperatures as high as 550 K. The divertor target, in addition to the large heat loads, will experience more contact with the plasma ($10^{20} - 10^{22} m^{-2} s^{-1}$ flux) which results in accelerated ion velocities of plasma and impurity materials which can reach 100s of eV impinging on materials up to temperatures of 1500 K [8]. While the overall heat flux is not a topic that will be addressed here, the heat flux does affect the temperature at which the PFC materials are exposed to neutron irradiation and gas implantation. This material temperature will determine what recovery stage regime the materials experience and how much recovery or self-healing the materials will be capable of, as well as the mobility of vacancies, gas species, and interstitial atoms. The bulk plasma has a low impurity tolerance for Be ($10^{-2}$ atomic fraction), and an even lower tolerance for W ($10^{-5}$ atomic fraction). Thus, the constraints on materials and their performance are extensive, as they must satisfy the necessary criteria for heat loading, ion and neutron irradiation, erosion/sputtering, and gas recycling.

Tungsten will be used in baffle and divertor components of ITER where there will be a high concentration of neutral particles, and material erosion properties are important. W is useful because of its high melting temperature (3422 degrees C) and heat conductivity. Low sputtering yield and high sputtering threshold energy of W make contaminants to the plasma less likely [9]. However, the high Z of W leads to ionization and radiation losses in the plasma. By using W as a divertor material, the high level of T-retention experienced with C can be reduced, but disruptions become more dangerous to the machine. Tungsten has shown problems with blistering and helium bubble formation when exposed to D-He plasma [10]. Ion irradiation in the fusion environment also causes some displacement damage and can lead to H and

He trapping behavior in vacancy and interstitial positions in the material lattice.

While the D-T fusion reaction produces 14.1 MeV neutrons, there will also be fusion reactions (D-D) that produce a lower neutron energy. Neutrons at these energies will stream freely out of the plasma until coming into contact with a solid material. Two neutron interaction effects are essential to be considered in MCF device PFCs. Like those in fission reactors, fast neutrons above approximately 0.1 MeV are a source of displacement damage, and fast neutrons above 1 MeV are a source of He and H transmutation products via the (n,$\alpha$) and (n,p) transmutation reactions. Neutron displacement damage can lead to defect accumulation and void swelling in materials which can lead to degradation of PFC material qualities and eventually cause mechanical failure. Neutron irradiation leads to highly energetic displacement cascades which increases the point defect concentrations in materials. High defect concentration can lead to increased rates of diffusional processes (H trapping and permeation and He bubble formation) and displacement of material through the accumulation of vacancies within the material (void swelling). Tungsten is a leading candidate PFC because of its behavior under thermal loading and disruption (ELMs and MARFEs, which lead to increased heat and particle flux) conditions. Since tungsten will be used as a divertor material, the irradiation temperature of this material will usually be reduced from even the edge plasma temperatures. W will be irradiated between 150 and 500 °C, which will lead to embrittlement. W is a BCC metal where irradiation leads to increased ductile to brittle transition temperature (DBTT). It is estimated that W can become more brittle at neutron radiation fluences of 0.3 to 0.5 DPA (irradiated at less than 500 degrees C) [11]. Therefore it is strategically useful to use W in configurations that reduce the exposure to crack initiation (i.e., thermal stresses).

### 1.1.7 Implanted Gas Species Behavior

Incoming plasma fuel ions, neutral gas atoms, helium ash, and multiply charged impurity ions will interact with plasma-facing components, and there are a variety of interactions which can occur. Implantation, reflection and physical sputtering are the focal processes of this research; however, other processes do exist.

Implanted particles damage the surface layers of the material creating vacancies, interstitial atoms, and dislocation loops. Embedded particles can then diffuse, coalesce to form bubbles or blisters, and react chemically with other atoms in the surface. Reflected particles may return to the plasma as a source of neutral atoms.

There are several ways in which H can be introduced to a material surface. First, in MCF machines there is always a neutral H pressure ($H_2$) that is in contact with the PFCs and the absorption rate of $H_2$ by the metal is proportional to the $H_2$ pressure. Second, H ions are accelerated through the sheath potential ($\approx 3kTe \approx 60eV$) and can be implanted into the PFC material. Third, if the accelerated H ions are not implanted, they can reflect back into the plasma as neutrals where they can undergo charge exchange (CX) which will lead to a "hot neutral" impinging on the material surface. This cycle of adsorption, implantation, diffusion to the surface, desorption, ionization/CX returning to the material surface is referred to as recycling. Recycling is responsible for steadily fueling the plasma, but it is also crucial from a materials and irradiation damage perspective. Once H is introduced to the material, it will diffuse down concentration gradients or become trapped. H can become trapped at

defect clusters, H may also trap at He bubbles.

Helium, which is one of the by-products of the fusion reaction, is of particular interest to the fusion materials community because it is a product that must be dealt with and it presents a different set of problems because it is a noble gas. In addition to the ion acceleration and impact created from magnetic sheath effects, as mentioned previously, helium (alpha particles) are introduced to the materials via (n,$\alpha$) reaction. Noble gasses are insoluble in metals, meaning that He tends to cluster. Helium bubble nucleation can enhance cavity formation, cause embrittlement of grain boundaries, form bubbles that affect surface morphology and create trapping sites for H.

Exposure of W to He (D-He plasma) irradiation has been studied extensively and has shown to produce a variety of deleterious effects in the material. Below 1000 K blistering of the material has been observed, and above 1000 K formation of pits, holes, bubbles, and fuzz has been observed [10].

### 1.1.8 Sources of Impurities in the Plasma

Plasma impurities include any molecules, atoms, or ions besides the reacting fuel (hydrogen isotopes) and resulting helium ash present in a tokamak. There are a variety of ways that impurities can come about as part of the operation of the machine, but impurities are often intentionally introduced to the plasma for a desired effect as well. The plasma interaction with the plasma-facing components or wall of the vacuum vessel can result in desorption of atoms by thermal, particle, or photon interactions. Chemical reactions, physical and chemical sputtering evaporation of atoms from solid surfaces, and arcing and blistering can also be responsible for removing impurity atoms from the wall. All of these processes can result in both atoms of the material surface as well as atoms bound to their surfaces to be released. Increasing power input to the plasma results in more significant impurity generation. In some cases where large heat loads are expelled from the plasma, impurities can be released into the plasma via melting, evaporation, or ablation of the wall material. The effect and spread of these impurities can be small compared to some impurities intentionally introduced to the plasma such as nitrogen, argon and neon. These types of impurities can be introduced via cryogenic pellets or gas injection via nozzles in the vessel.

The most relevant source of impurities for ITER operation and the plasma and material performance is physical sputtering. Physical sputtering is the process in which a collision of an energetic ion with the wall will release an atom of the wall material. The incoming ion transfers sufficient energy to the surface material to overcome the surface binding energy (or threshold energy) and give the surface material atom (or atoms) kinetic energy [9]. This can occur at the edge of the free surface, or several atomic diameters into the material. This process is dependent on the incoming energy, the angle of incidence, and what the two colliding species are. In practice, experimental measurements, empirical fits to the data, and computational models are used to predict yield values. The most common interaction is for a plasma ion (Hydrogen isotope) to sputter a surface material (Be, W), however, when surface materials are sputtered and enter the plasma, they are often quickly ionized and then self-sputter. These self-sputter yields can be critical in the operation of a reactor.

## 1.2 The Role of Modeling the Plasma-Material Interaction

In the introduction, many aspects and processes of the plasma and materials have been discussed as isolated topics. A more accurate representation of these processes and how they are connected and coupled in a way that feeds back on one another is demonstrated in Figure 1.9. Processes on many spatial (angstroms to meters) and temporal scales (femtoseconds to days) are tightly coupled through a range of processes in the plasma and surface. The resulting web of interconnected physics makes it difficult to test and simulate any of these processes in isolation experimentally.

Modeling and simulation have become essential tools in nuclear and fusion sciences because of the long experimental lead-up times, difficulty in measurement, and the necessity for safety and design analysis. Increasing computational power and resources with the remaining demand for scientific discovery create an opportunity for simulation of physics processes to grow in scale and fidelity.

In order to simulate the plasma-surface interaction, self-consistent, experimentally validated models of materials performance and degradation in the fusion energy environment are needed. Bridging time-scales of the many physical processes in the materials and plasma requires an integrated simulation composed of many high-fidelity codes. Making use of simulation of the background fuel, ash, and impurity in the edge plasma, along with sheath modeling, and surface response and materials evolution models can enable a better understanding and a predictive capability for the performance of the plasma and PFCs moving towards future machines like ITER.

The present dissertation contributes to such an integrated simulation. In the proposed integrated simulation capability (depicted in Figure 1.10), high fidelity fluid simulation of the edge plasma is performed (SOLPS), sheath characteristics are modeled (hPIC), impurity migration patterns and kinetics are determined (GITR), surface interactions are simulated (Fractal-TRIDYN), and surface composition and morphology is modeled (Xolotl). These codes are enveloped within wrappers which interface with the Python framework for computational resource management, data passing, and execution through the Integrated Plasma Simulator (IPS). Development, benchmarking, and deployment of the impurity transport module (GITR) is demonstrated, and the results of the impurity simulation within GITR are presented. The research includes model validation of GITR with simple fluid theory and comparison with DIVIMP. Code-experiment benchmarking is performed by simulation of dedicated PISCES-A linear plasma device erosion experiments. For these PISCES-A simulations, a detailed uncertainty quantification effort is performed. Simulation of erosion and re-deposition of the ITER W divertor is also shown.

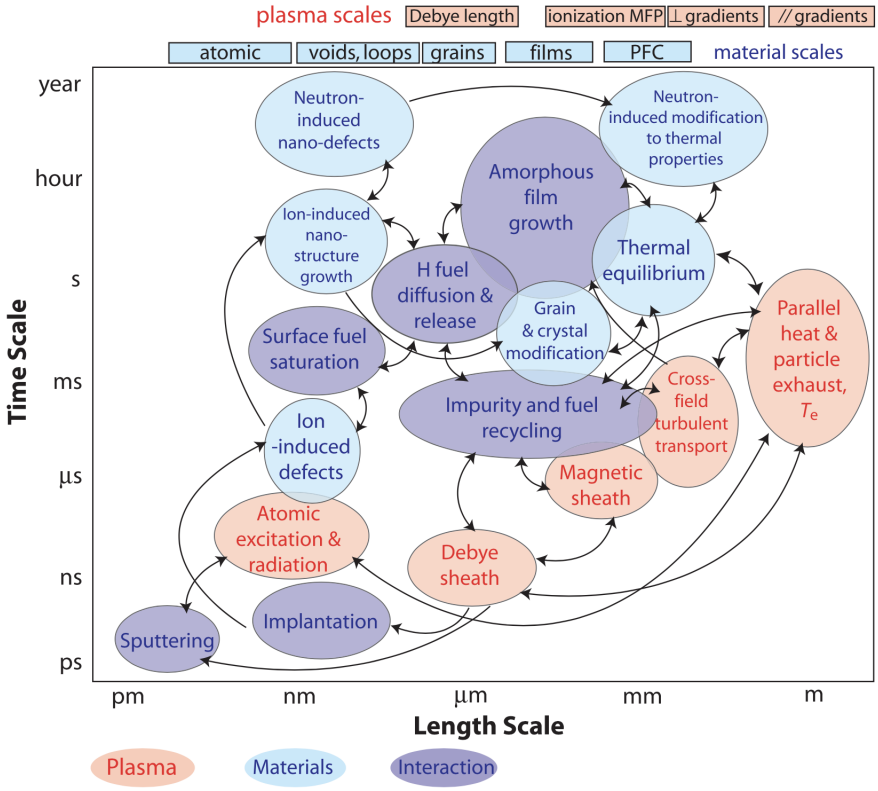


Figure 1.9: Diagram showing the range in time and spatial scale which fusion-relevant processes in the plasma, materials, and their interactions occur and how they are connected [12].

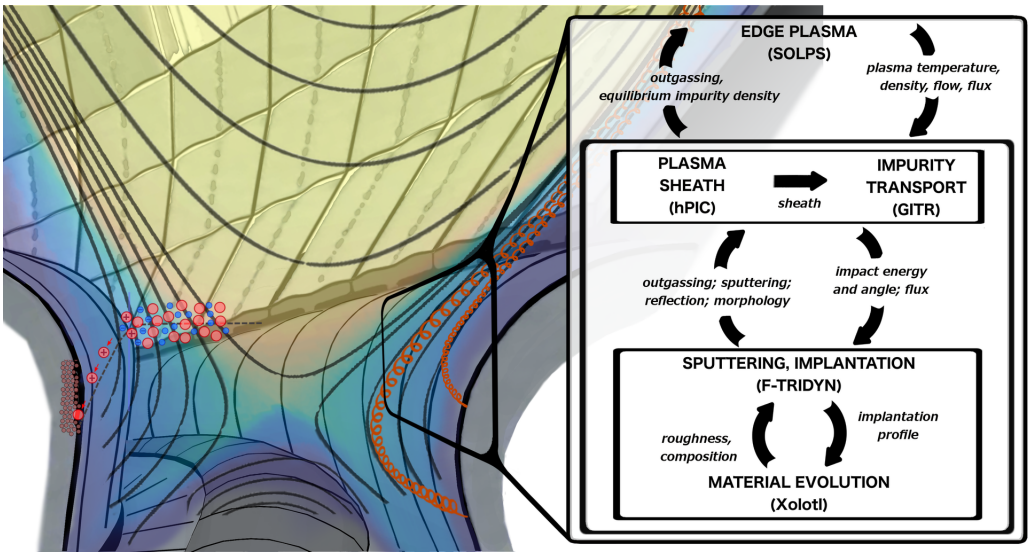


Figure 1.10: Flow chart of a proposed integrated simulation made of high fidelity physics modules. Coupling of the edge plasma, including sheath and impurity transport effects to the materials response, including implantation and surface evolution. Feedback from recycled and sputtered atoms must also be fed back on the SOL plasma to investigate effects on core plasma performance.

# Chapter 2

# Assessment of Relevant Research

## 2.1 Approaches to Modeling Impurities For Fusion Applications

Many approaches to modeling impurities have been taken, including fluid and kinetic simulations, 1 to 3 spatial dimensions, edge and core, single code and integrated models. It is essential to understand the design, assumptions, and limitations of existing tools in order to place the work performed and the results in context. It is also crucial to understand these approaches in order to build on and contribute to a scientific body of work which can guide our field to the realization of fusion power.

The classes of impurity simulation tools which will be summarized are fluid models of impurities in 2D and kinetic impurity Monte Carlo codes. These tools are used to model experimental scenarios, and an overview of some recent capabilities and works are provided. Finally, how these impurity simulation tools have been integrated into models for the plasma-surface interaction, and some results will be presented.

## 2.2 Fluid Modeling of Impurities in 2D

### 2.2.1 Fluid Simulation of Heavy Impurities

Numerical codes developed using a 2D fluid approximation such as SOLPS [13], UEDGE [14], and EDGE2D [15] are designed to simulate the SOL plasma. These codes operate under the fluid plasma assumption meaning that short collisional lengths are assumed (small compared to the domain), and distributions of plasma species are assumed to be Maxwellian. These types of codes have been successful in reproducing experimental values and performing sensitivity analyses of scrape-off layer plasmas. Many of the fluid codes are well established tools, spanning the era in which many magnetically confined fusion devices were predominately carbon devices. A steady transition of fusion devices moving towards metallic walls in devices such as Alcator C-Mod, ASDEX-Upgrade, JET, ITER, and DEMO has required additional development for the fluid codes. With experimental effects of edge radiation and impurities being investigated for the previously mentioned fusion devices, simulation efforts and capabilities to give modeling input on this front is also being developed.

The simulation, as performed in SOLPS, uses a two-dimensional multi-species fluid solution of background plasma parameters along with impurities (He, C, Be, W, etc.) performed by B2. A kinetic description of neutral atoms and molecules is performed with the EIRENE code. For each iteration step, EIRENE uses the fluid solution from B2 and calculates the source terms in the fluid equations resulting from the neutral-plasma interactions and gives this back to B2. Iterating in this fashion until the solution has converged results in self-consistent modeling of mutual effects between neutrals and the charged plasma species in the edge plasma. In B2 the surface refers to the edge of the B2 grid. This can be the divertor targets where the grid is aligned with the surface, or in the main chamber and private flux regions where the grid is not aligned with the surface, approximations are used to extend fluxes to the wall. From there a model for the sheath, the incident heat and particle flux, and a heat transport model are used as source terms for solving a zero-dimensional steady-state particle balance model at the target using sputtering yields, backscattering coefficients, and evaporation rates. The erosion rate for the plasma-facing surfaces is calculated according to this model.

The capabilities of SOLPS have been extended to include tungsten impurity species using both a full fluid treatment for all charge states as well as using a bundled charge state approach [16]. Simulating heavy ions such as tungsten (Z=74) with a fluid plasma edge code introduces 74 fluid species to solve for in addition to the background ion and electron species. In many cases, the ionization states may be truncated at a charge state above which there is very little population or contributed effect, and for tungsten, in the edge plasma, this truncation point lies between W+15 and W+20. Still, the large fluid species number places a demand on memory and execution time for such codes. Thus in order to balance considerations of accuracy, runtime, and completeness an approach for bundling several charge states into a single plasma species has been performed. In work by Bonnin [16] comparison of the different treatment of the impurity species is presented simulating the ASDEX-Upgrade experiment. Without giving much detail on the bundling schemes here (see [16]) net wall erosion/deposition rates are shown in Figure 2.1 as a comparison of schemes. Figure 2.1 shows net erosion or deposition as a function of accumulated wall area going around the machine starting in the lower corner of the inner wall, going up the high field side (HFS) to the top of the machine, down the outer wall (low field side LFS), the outer divertor (OD), private flux region (PFR) and inner divertor. The strike points of the plasma are shown as additional lines on each side of the PFR. It can be seen that the inner and outer walls are sources of net erosion, the outer divertor is a region of small relative net deposition, and the inner divertor is a location for strong deposition of impurities.

The difference in bundling schemes compared to no bundling shows accurate predictions on the inner wall, outer wall, and outer divertor. Significant differences exist in the inner divertor where the bundling schemes under-predict the net deposition of W by 5%-20% compared to the full simulation of all species.

### 2.2.2 Comparison of Fluid Model to Kinetic Model

A comparison of the SOLPS fluid model with the kinetic transport model of IMPGYRO [17] has been performed to compare the models [18]. For an ASDEX-Upgrade geometry and benchmark SOLPS case a deuterium plasma with tungsten impurities

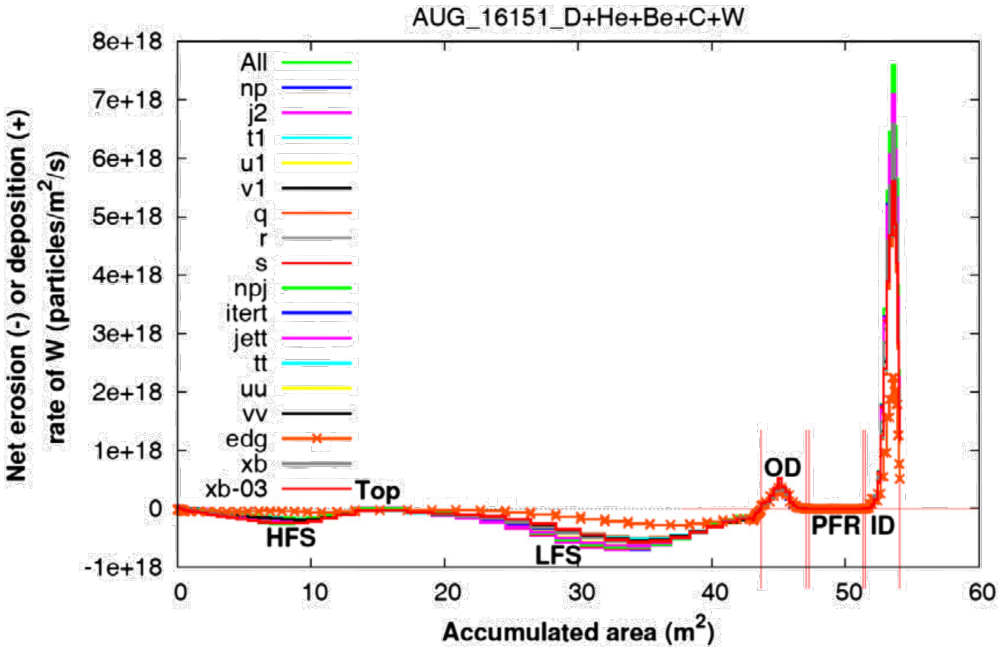


Figure 2.1: Comparison of the net W erosion or deposition rate computed for various bundling schemes. The various wall regions are noted as: HFS: high field side, Top: upper X-point region, LFS: low field side, OD: outer divertor, PFR: private flux region, ID: inner divertor, as reproduced from Ref. [16].

injected at a point source near the outer midplane the following cases was modeled:

- Case A: Deuterium and tungsten transport are calculated by multi-fluid modeling with B2.5 in SOLPS (EIRENE was not used for neutral transport). Charge state bundling was used for W+15 to W+74 for computational cost reduction.

- Case B: IMPGYRO (Monte Carlo kinetic simulation) is used for tungsten transport using a fixed deuterium background plasma (the same background as case A).

Two-dimensional poloidal cross-sections of tungsten density are generated in which all of the charge states are summed, as shown in Figure 2.2. Both cases show an increased impurity concentration at the upstream region of the SOL at the top of the plot compared to the impurity densities in the divertor region. Both simulations also show a peak poloidally at the outer mid-plane localized near the source of tungsten and near the stagnation point of the SOL plasma flow. A significant difference in the results is shown in the impurity density near the outer divertor region. While the SOLPS simulation shows similar impurity densities in the inner and outer divertor in a symmetric fashion, IMPGYRO shows a significant shift of the impurity density into the inner divertor. This difference in impurity density comes as a result of drift motion ($\vec{E} \times \vec{B}$ which rotates counter-clockwise in the poloidal direction and $\vec{B} \times \nabla \vec{B}$ which is directed towards the top of the device). Drift motion is turned off for these simulations in SOLPS but is naturally accounted for in the full gyro-orbit integration in IMPGYRO.

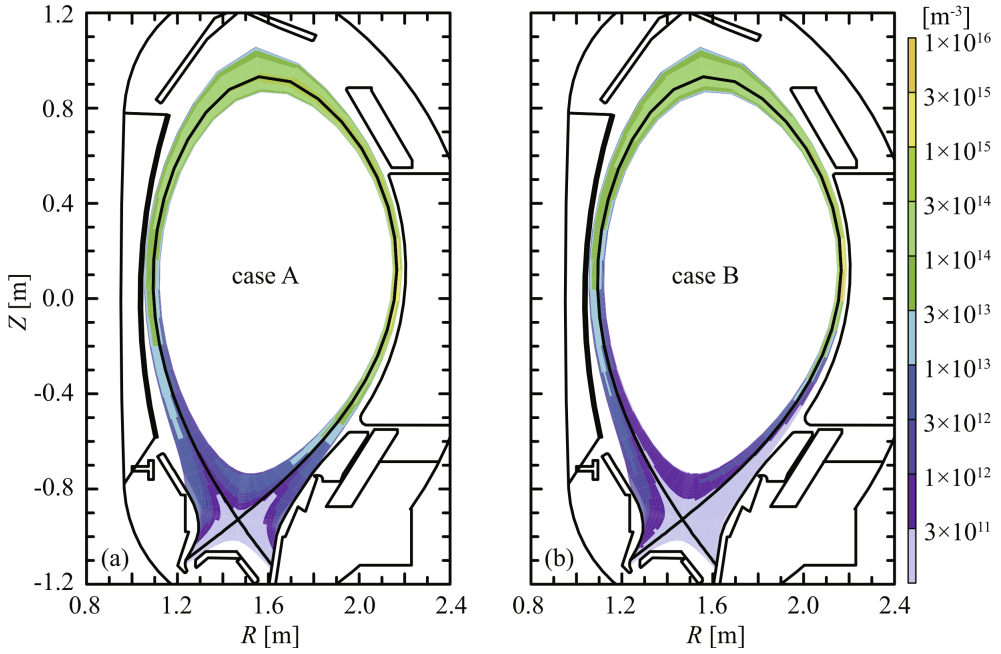


Figure 2.2: 2D density profiles of tungsten impurity in poloidal cross-section. The densities for all the charge states are summed up and the results are plotted: (a) by B2.5 fluid code (case A) and (b) by IMPGYRO kinetic code (case B), as reproduced from Ref. [18].

Drawing conclusions from the existing 2D fluid models, they perform well in many aspects of impurity transport; however, it can be seen that particular aspects of the kinetic impurity transport are missing from these models. SOLPS has shown success in treating the self-consistent calculation of flux-based erosion, impurity transport, and redeposition of impurities in applied cases for fusion devices with metallic walls. It is possible, although expensive, to track the relevant charge states of impurities, their densities, temperatures, and flows. Drawbacks include limitations in the simulation domain of the fluid codes such as the 2D grid which neglects toroidal asymmetries, and the gridded domain not matched or extended to the wall. Additionally, effects of finite ion gyro-orbits are not included in the fluid treatment of the impurities which would capture prompt redeposition, and kinetic effects of the eroded impurity interaction with the material boundary (resulting in variations in the surface model) are not included. Therefore kinetic treatment of impurities is needed and can be used as a supplement to the fluid description, as well as a standalone investigation of impurity migration and deposition.

## 2.3 Kinetic Impurity Monte Carlo Codes

A variety of 2D and 3D kinetic impurity tracking codes have been developed in order to simulate impurity migration. Codes for the 2D radial-azimuthal (r,$\theta$) coordinate system with guiding center averaging of particle motion include DIVIMP and DORIS. Full gyro-orbit resolving 3D codes include ERO, WBC [19], BBQ [20], and IMPGYRO [17]. While all of these codes use the trace impurity model (described in Appendix A), each code has its distinguishing characteristics, target domain for

simulation, or intended workflow.

Of most use and relevance to the present fusion community are the DIVIMP and ERO codes. The ERO code is a 3D Monte Carlo code to simulate impurity transport and the plasma/impurity interaction with the wall for fusion devices with magnetic confinement [21]. ERO was developed in the early 1990s but has continued to be modified and maintained for erosion simulations. ERO simulations have focused on localized wall components such as divertor target plates, limiter tiles, or samples exposed to linear machine plasmas. Typically ERO receives input for background plasma values at the last closed flux surface (electron T, n, ion Temp and magnetic field) and uses intrinsic models to calculate values for electric value, plasma flow, temperature, and density gradients. Since the code was designed and is somewhat limited to localized domains with enough particles to sample the domain, the geometry is simplified to planar or a parameterized surface. In the default version of the ERO code details of the density, temperature and electric field in the sheath are not resolved, and therefore the background plasma values at the sheath entrance is the same as the background plasma values at the material interface. This is not an important effect for many experimental cases; however, for promptly ionized tungsten in a strongly magnetized plasma, these effects become significant. The ERO code has been adapted for specific cases to include some of these effects. The surface model in ERO interfaces with various plasma-wall interaction databases. Sputtering and erosion yields come from SDTrimSP and molecular dynamics simulations which are applied in formulating an erosion source due to the background plasma as well as the self-sputter reactions.

Contrasting DIVIMP with ERO, DIVIMP uses a guiding center approach which by not simulating full gyro-orbits enables longer time stepping and allows enlarged domains to be simulated [22]. DIVIMP utilizes a set of parallel and cross-field force applications to simulate particles tracks, and volumetric densities provided a background plasma. Erosion and sputtering yields, as well as neutral ion energy and angle distributions, are similarly implemented in DIVIMP and ERO.

## 2.4 Code-Experiment Comparisons

### 2.4.1 ERO Modeling of PSI-2 Ar Exposed Tungsten

A series of experiments were performed in the PSI-2 linear plasma device to investigate tungsten erosion under exposure to an argon plasma [23]. The PSI-2 linear machine produces a 0.1 T magnetic field at the target with background electron temperatures of 2-4 eV and electron densities of $\approx 10^{12}\ cm^{-3}$. A rectangular tungsten target of 8 cm x 10 cm was under bias voltage between -50 and -150 Volts and contained 10, 0.5 cm x 0.5 cm polished tungsten samples embedded into the target (see Figure 2.3) to allow for mass loss measurements with spatial resolution. Additional diagnostics for this experiment included spectroscopy profiles in orthogonal directions in order to provide a 2D emission map, and a quartz micro-balance (QMB) deposition sensor serving as a moveable witness plate to measure the deposition of sputtered tungsten moved for measurements in the axial direction. Variations in discharge current were used in order to produce varying relative concentrations of Ar+2 to Ar+. This difference in plasma charge state distribution with variations in bias voltage of the target (50,70,100,130,150 Volts) results in different Ar and W

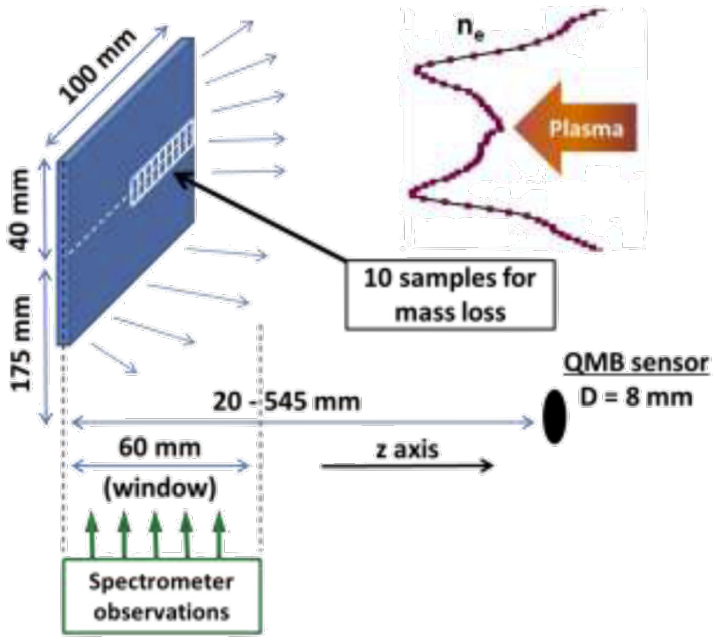


Figure 2.3: Experimental setup schematic for Ar exposed W in PSI-2, as reproduced from Ref. [23].

impact energies for sputtering.

Uncertainties are encountered when simulating this experiment including the energy and angular distributions of sputtered particles, cross-section values for ionization and recombination of impurity ions, experimental error bars on Langmuir probe measurements of $T_e$, $n_e$, and Ar ion flux. Also, variation in the plasma profiles from the location of the measurement to the target is not accounted for. In order to more accurately match simulations with experimental measurements, an adjustment of the sputtered W energy distribution was made, narrowing the peak of the Thompson distribution and moving it to lower energy. Angular distributions taken from experimental fits were used for different target bias voltages. In this case, the weight of the sputtered angle distribution far from normal incidence increases with decreasing impact energy. Ionization data from different sources show significant variance in values. This uncertainty in the ionization coefficient in combination with an uncertainty interval of 2-4 eV in the background electron temperature can result in differences in a factor of 10 in ionization rate. The simulated mass lost for the W array for a low discharge power case using 150 V bias of the target is shown in Figure 2.4. Qualitative and quantitative agreement is achieved for ERO vs. the experimentally measured mass loss. The most notable feature of the figure is the slight discrepancy of the predictions between the radius of 5 mm and 25 mm which still shows the qualitative trend and only differs from the experiment by approximately a factor of 2.

In addition to the previously mentioned uncertainties, there is minimal available data for the emission spectroscopy of WI and the functional dependence with electron temperature. The shape of the fall-off in WI emission intensity is accurately reproduced by the simulation in ERO as demonstrated in Figure 2.5.

Finally, results for mass gain away from the target as measured by QMB for low, medium, and high discharge power are shown in Figure 2.6. For this longer

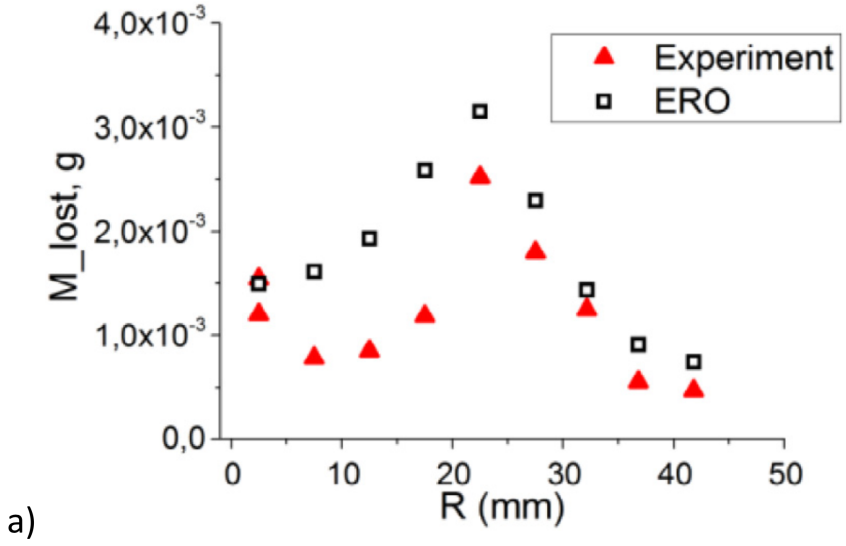


Figure 2.4: Radial mass loss measurements and ERO simulated values, as reproduced from Ref. [23].

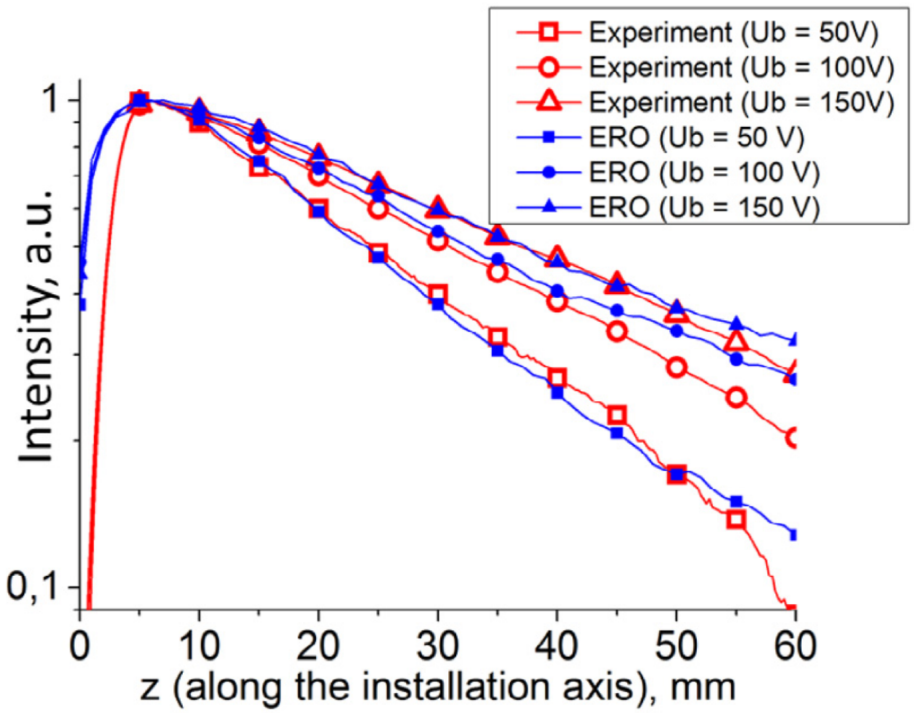


Figure 2.5: Tungsten neutral 400.9nm emission spectroscopy for high power discharges of varying bias voltages, as reproduced from Ref. [23].

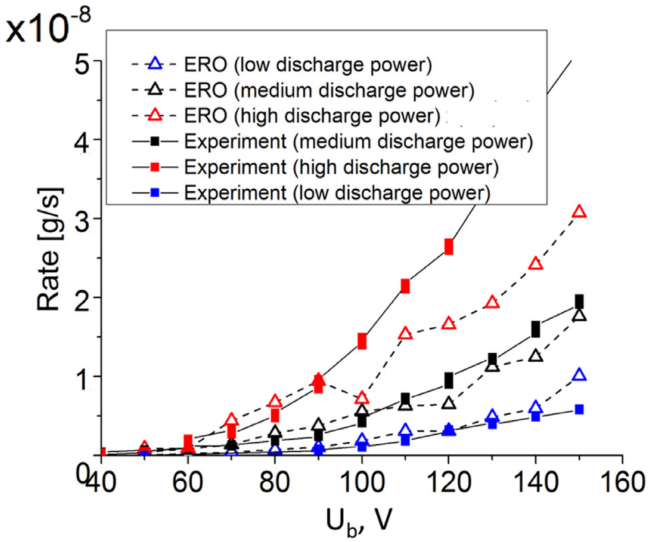


Figure 2.6: Mass gain away from the target at the QMB sensor for varying discharge power, as reproduced from Ref. [23].

range migration, ERO once again shows good agreement with experiment with slight variations.

### 2.4.2 ERO simulations of DIMES probe in DIII-D

Erosion experiments of high-Z materials molybdenum (Mo) and W have been performed using the divertor material evaluation system (DiMES) probe in the lower divertor of the DIII-D tokamak [24]. This probe uses a sample that has spots where a thin coating of Mo or W is placed on a silicon substrate. The sample is placed flush with the graphite divertor tiles near the outer strike point in the divertor. The small diameter spot (1 mm) is used to measure the gross erosion, as it is assumed that since the mean free path of ionization of the eroded material is on the order of 1 mm, very little eroded material will return to this spot. The larger spot (1 cm diameter) of high-Z material is used to measure the net erosion as much of the eroded material will be promptly redeposited. The coating thickness is measured by Rutherford back-scattering (RBS) before and after exposure in order to determine the net erosion. Local background plasma values are well diagnosed in this area by Langmuir probe for the L-mode shots in which the samples were exposed. Experimental analysis shows a net erosion rate for Mo of 0.42nm/s, and the ratio of net to gross erosion is 0.56. For W, the average net erosion rate is 0.18 nm/s, with a ratio of net to gross erosion of 0.37. ERO makes use of OEDGE to construct the background plasma profiles using Langmuir probe measurements and the onion skin model (OSM) to produce accurate plasma profiles at the DiMES exposure. Carbon fluxes are also obtained from OEDGE and used in ERO in a homogeneous surface mixing model. Initial simulation of the redeposited fraction of Mo resulted in a 58% redeposition rate for the large dot, and a 16% redeposition rate of the small dot, which is not the negligible fraction which was anticipated. Upon further investigation, this high redeposition rate was due to the sheath electric field. Therefore, varying sheath models were used to examine this effect - the Brooks model [19], the Stangeby model [25], and a model from a particle-in-cell code. The resulting simula-

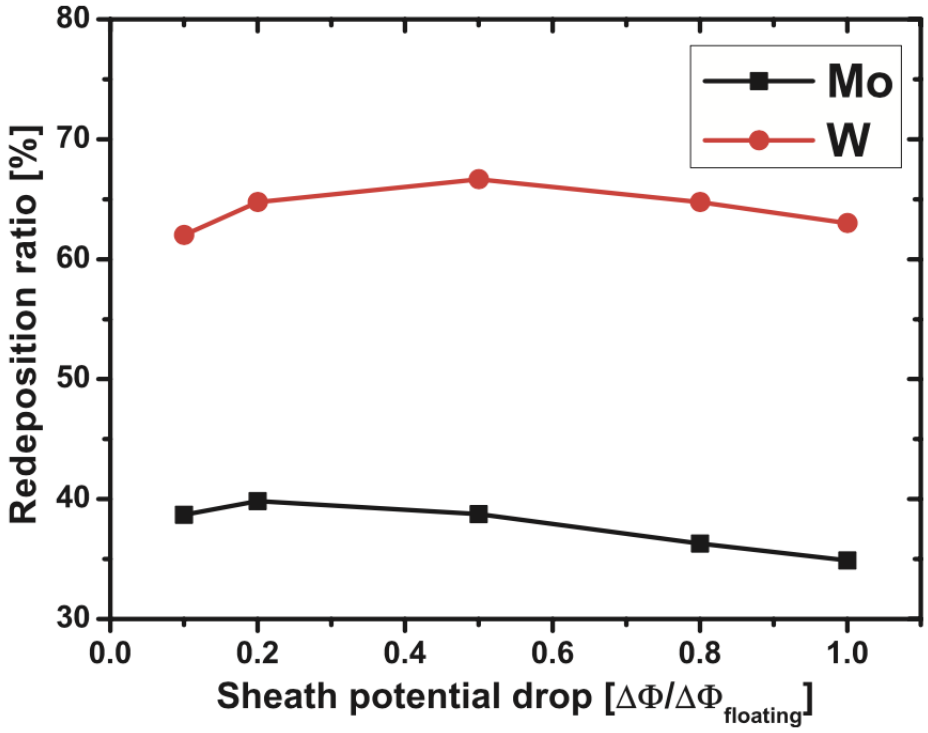


Figure 2.7: Variation in redeposition ration for W and Mo as a function of fraction of sheath potential used (Brooks model for sheath used for each) [24].

| | Mo | | W | |
|---|---|---|---|---|
| | 1 cm | 1 mm | 1 cm | 1 mm |
| Experiments | 44% (46%) | | 63% (67%) | |
| ERO (Brooks sheath) | 39% | 4% | 67% | 14% |
| ERO (Stangeby sheath) | 35% | 3% | 63% | 9% |
| ERO (PIC sheath) | 36% | 3% | 63% | 9% |

Figure 2.8: Adjusted experimental and simulated redeposition fractions for the large dot using the ERO value for redeposition on the small dot [24].

tions using the varying sheath models made very little difference in the redeposited ratio of Mo. Therefore, the sheath potential magnitude was varied (along with a sheath electron density model) to vary impact energy and sheath ionization rates, as shown in Figure 2.7. When the assumption of zero prompt redeposition on the small dot is relaxed, and the ERO-modeled redeposition rates for the small dot are used for the experimental measurement, agreement for the redeposition ratios for Mo and W is found as shown in Figure 2.8.

### 2.4.3 DIVIMP Modeling of JET ITER-Like Wall

In 2011 some of the carbon JET wall components were replaced with Be and W in order to address fuel retention issues and test such components for ITER. As a benchmark study for impurity transport in JET and in order to extrapolate for ITER, DIVIMP predicted estimates of tungsten divertor sputtering and transport based on different upstream densities for an H-mode discharge in JET [26]. EDGE2D/EIRENE simulations were performed for an inter-ELM H-mode plasma in which carbon was included in the background plasma solutions. Three different D inner puff experiments were performed and simulated in order to investigate different densities in the upstream SOL and their effect on sputtering in the tungsten divertor and the transport of impurities and resulting concentrations.

The modeling of the background edge plasma, which was tuned to agree with experimental measurements, shows a high-recycling or detached plasma for the inner target resulting in very little or none of the total eroded material in the simulations due to reduced plasma temperatures. For the low-density plasma, the outer target is predicted to be sheath-limited, giving temperatures near 100 eV for ions and electrons. The medium and high-density plasmas give temperatures of less than 10 eV significantly reducing the sputtering at the outer strike point. Note that the lower impact energies of carbon sputtering of W show much sharper energy dependence, and therefore a difference in small values of temperature in the divertor can make a significant difference in sputtering yield.

With these yields, EIRENE was used to transport the neutrals until ionized and passed as a source to DIVIMP. DIVIMP transports the ionized impurities in the divertor, along the SOL, and to the core and gives results for impurity densities and impurity fluxes to the wall. The results of the simulation show that with the low-density inter-ELM simulation, relative concentrations of W rise above $10^{-5}$, which are unacceptable levels for operation. Increasing the upstream density shows better retention of W in the divertor because of increased collisionality between the impurities and the background plasma. Increasing density further shows small decreases in divertor temperature, but because of the sharp characteristics in sputtering yield decreases impurity concentrations by several orders of magnitude.

## 2.5 Impurity Transport Simulation Workflows

Because of the disparity in spatial and temporal scales of physical processes that occur in the plasma-material interaction, integrated simulations of PMI must be separated into multiple components. This separation of physics modules results in the need for multi-physics integrated simulations and workflows. The combination of high fidelity models and passing of data allows simulations to grow and include

more widely varying physics spanning the spatial and time scales needed to model global effects of erosion and impurity migration. Examples of such workflows are presented next.

### 2.5.1 WallDYN

For the purposes of global impurity simulation, including erosion, redeposition, co-deposition, and materials mixing in a self-consistent manner, the WallDYN code was developed. WallDYN uses parameterized results from molecular dynamics or TRIM simulations which give the interaction of energetic plasma ions with the surface to determine erosion and reflection rates for a system of surfaces with different compositions [27]. With the background plasma given, DIVIMP is used to create a transfer matrix between wall elements. This transfer matrix gives the probability of a sputtered particle being transferred from a given wall element to another under steady-state conditions. With the information for erosion and redeposition, a system of ordinary differential equations is formulated for how each wall element evolves. Concentrations and net deposition or erosion are tracked in this series of ODEs, a system that is coupled by the impurity transfer fluxes. These equations can then be solved numerically to predict the evolution of the wall materials. This approach is successful because of the precise nature of the problem setup and the scheme which conserves fluxes and material properties. This approach limits the size of the set of coupled ODE because of computational demand. The demand in solving these equations results in a limit on the number of wall elements that can be simulated and, therefore, the fidelity of the simulated domain.

An example of the use of WallDYN in simulating JET and making extrapolations for ITER is given in a benchmark of the code predictions of the erosion/redeposition of the ITER-like wall in JET compared to the post-campaign wall tile analysis [28]. This work used characteristic ohmic and inter-ELM JET shots to simulate a background plasma in order to transport both Be and W impurities with DIVIMP. The

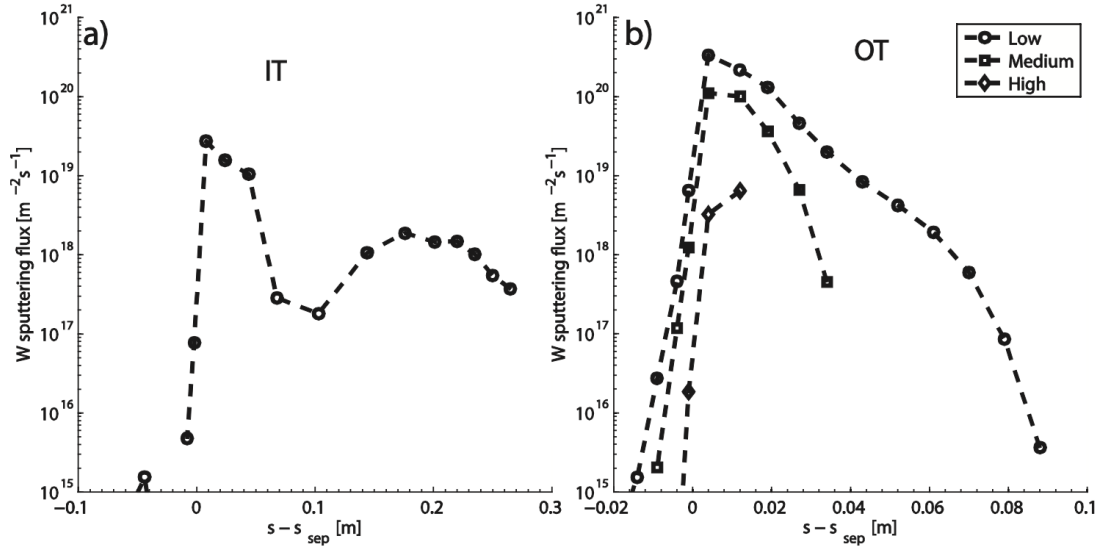


Figure 2.9: Erosion profiles at the inner and outer target strikepoints, as reproduced from Ref. [26].

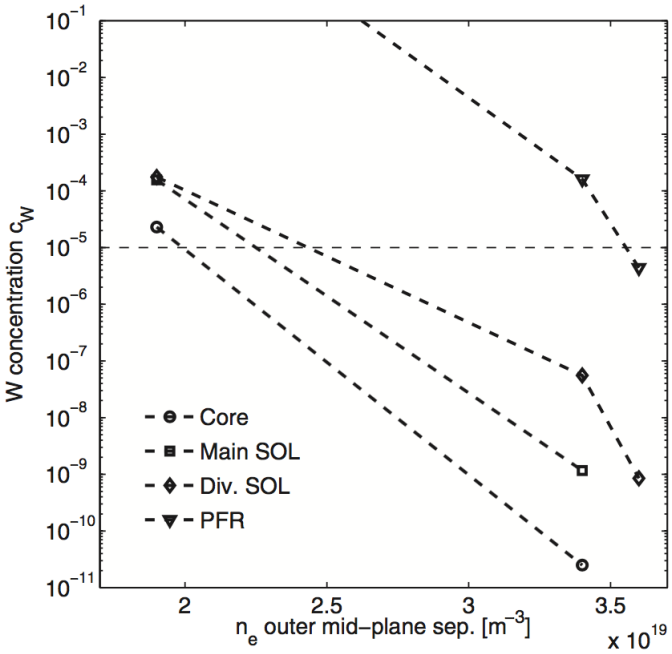


Figure 2.10: Concentrations of W in the core, main SOL, divertor SOL, and private flux region for the varying input densities, as reproduced from Ref. [26].

resulting erosion and redeposition, including fuel co-deposition, are used within the WallDYN model to show the poloidal variation of erosion and deposition of W, Be, and fuel species in the poloidal direction with 60 representative surfaces. The transfer matrix for eroded Be is shown in 2.11, which as produced by DIVIMP, gives the probability of an eroded Be atom migrating to another wall element. W erosion flux (left column) and net deposition (right column) is shown for H-mode (top row) and Ohmic discharges in Figure 2.12. During the ITER-ILW campaign, a total of approximately 13 hours of operation were accumulated. The qualitative trends in both the Be and the W agree well with the experiment. However, quantitatively, the predictions of the W net erosion and deposition are a factor of 20 lower than the experimental analysis shows. This discrepancy is large, but a small error accumulated over the entire experimental campaign is to be expected. Perhaps the difference can be rectified by including ELMs.

### 2.5.2 Rough Surface Simulation with SURO/ERO/SDPIC

It has been observed in experiment that rough surfaces can change the erosion/deposition characteristics of a surface. This change in erosion pattern can result in stronger erosion of protruding parts of the rough surface and deposition in the recessed areas, which can often result in a lower effective erosion yield than flat surfaces. In order to investigate this effect, a methane (13CH4) injection experiment was performed in TEXTOR, and a combination of codes was used to investigate the resulting physics. In these simulations, ERO and SDPIC (1D 3v particle in cell code) were used to simulate the incoming particle (background and impurity) flux, angle, and energy, and this data was then passed to SURO [29]. SURO is a 3D code that simulates rough surface topography and carries out the local reflection/erosion/deposition along with surface evolution (due to erosion), and surface concentrations are also

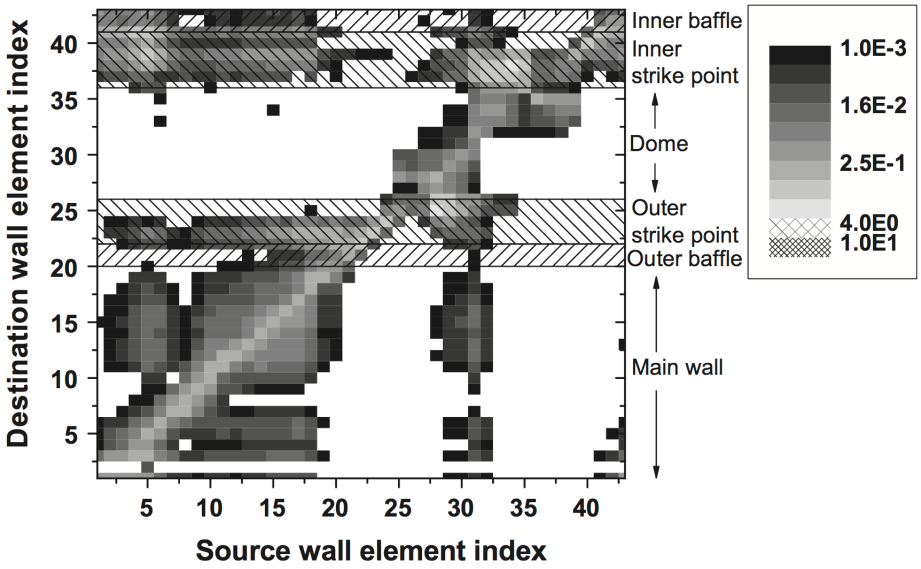


Figure 2.11: An example Be transfer matrix produced by DIVIMP and used as input to WallDYN, as reproduced from Ref. [27].

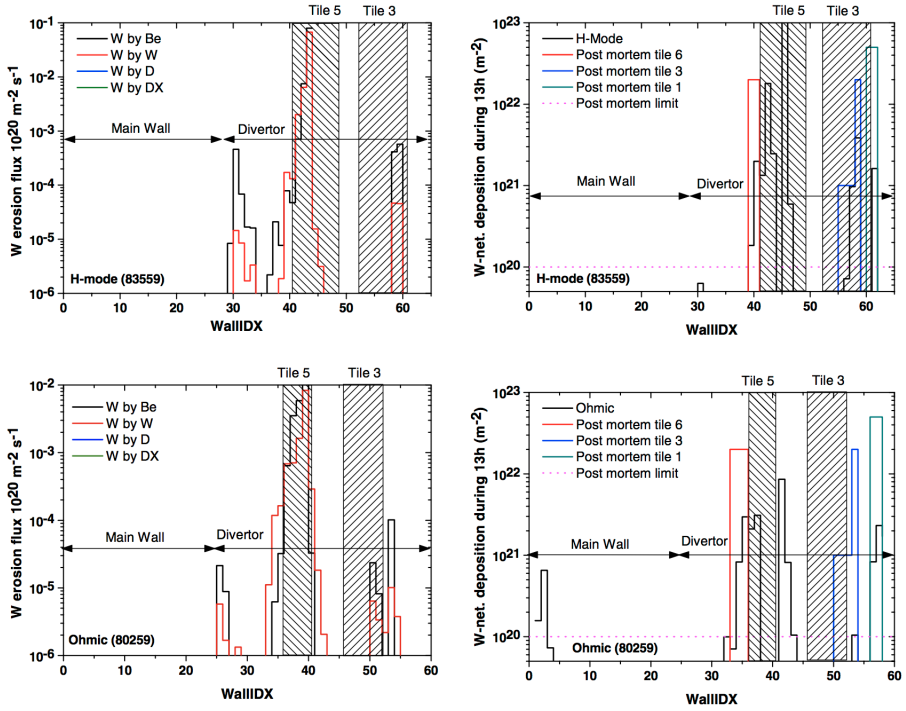


Figure 2.12: Net deposition as predicted by WallDYN, as reproduced from Ref. [28].

taken into account.

Using the measured temperatures and densities at the LCFS with the corresponding limiter geometry, and the given source strength of the methane, ERO simulates the background fields and the resulting local deposition of carbon on the surfaces. Similarly, SDPIC uses the boundary conditions of the TEXTOR ohmic discharge to simulate the local D and 12C fluxes. These codes assume a flat surface since the roughness of the surface ( 1 micron) is much less than the sheath width ( 40 microns), and these calculations give the flux, energy, and nominal angle to SURO which then accounts for the local surface features. The domain for the methane injection at the TEXTOR limiter used for ERO and SDPIC is shown in Figure 2.13 (right), as well as the rough surface topology used in SURO (left). The ERO simulation tracks methane ionization and dissociation and the resulting energy, angle, and flux to the surface. The angular distributions from ERO show a peak in impact angle around 20 degrees for charges species, and a uniform distribution for neutral carbon species. This information is passed to the SURO code. Results of the SDPIC code sheath electric field show very similar characteristics to the sheath model used in ERO, therefore SDPIC is used to simulate the energy-angle distribution of the deuterium background on the limiter. SDPIC gives a peak in angular distribution at 50 degrees from the surface normal for the background deuterium species. This information is also passed to SURO for evolution of the 3D surface topography. The results of the SURO code shown in Figure 2.14 enhanced deposition of 13C at recessed areas, which is enhanced because of the surface roughness (a). The gross erosion of 13C is also higher in the recessed areas because of the much greater deposited amount (b). The eroded 13C in the system is limited to what has been introduced to the system by deposition and is, therefore, lower than the deposited concentrations resulting in a net deposition of 13C in recessed areas (c). The bottom row of Figure 2.14 shows the time evolution of the surface topography. The starting surface (d) begins to show a shift in the peaks and troughs, but is still distinguishable in (e) after 300s. After 500s (f) the surface is largely changed with peaks nearly double their original height (1 micron) and nearly completely filled in troughs.

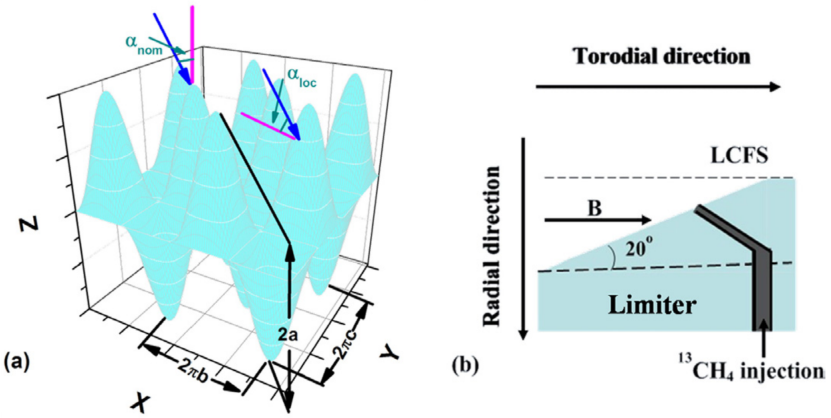


Figure 2.13: Illustration of the surface topography of the simulated rough surface and the experimental setup for the methane injection experiments done in TEXTOR, as reproduced from Ref. [29].

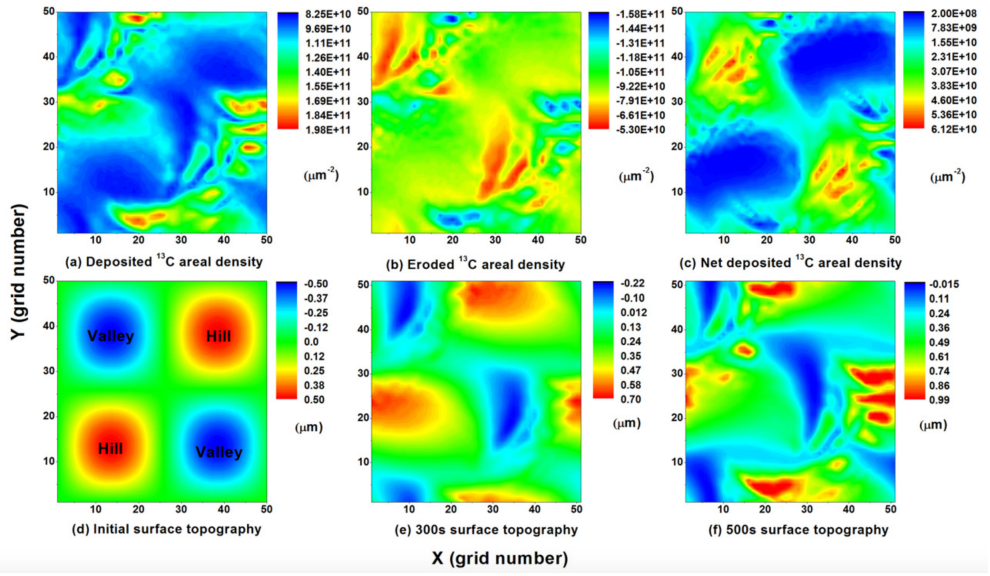


Figure 2.14: Top view of the deposited (a), eroded (b), net deposited (c) 13C areal densities after the exposure of 500 s and surface topography at the exposure time of 0s (d) 300s (e) 500s (f) with a 13C flux ratio of 3.5% (a = b = c = 0.5$\mu$m), as reproduced from Ref. [29].

## 2.6 Summary

In summary, 2D fluid simulations of impurities in the edge plasma, and 2D and 3D Monte Carlo impurity transport codes have been created and used to simulate erosion, impurity ionization, and migration. Effects of erosion and impurity migration on the SOL plasma as well as on the material lifetimes via net erosion have been investigated. Additionally, integrated models for erosion, impurity migration, and material deposition have been created.

Although it has been shown that grouping schemes of heavy impurities can be used to model impurity migration with fluid codes, this creates a large computational demand for fluid simulations. This difficulty along with added computational demands including particle drifts, and the lack of impurity kinetics and a wall-fitted grid leaves many physics questions to be addressed with this approach. It is not clear that implementation of such details is possible in the near future.

Kinetic, Monte Carlo codes for 2D and 3D impurity transport have shown accurate and reliable results in tokamak and linear device scenarios. While DIVIMP is capable of simulating a 2D global domain it neglects to simulate prompt redeposition, where for tungsten this is an important effect. Additionally 3D asymmetries cannot be captured. Additionally, ERO has been traditionally limited to simulation volumes which are not global along with simplified geometries as inputs.

In the context of an integrated model, DIVIMP is effectively coupled with OEDGE for acquiring plasma parameters and passes particle fluxes for evaluation of surface evolution in WallDYN. ERO contains built-in models for parallel temperature, density, and plasma flow profiles as well as perpendicular decay of plasma parameters. Being a self-contained model makes interfacing with additional physics modules difficult.

Based on the relative strengths and weaknesses of the current impurity transport

codes and integrated models for the plasma-surface interaction, an integrated model for PSI composed of modular high-fidelity physics codes is proposed. As a part of this new integrated simulation capability, a high performance impurity transport particle push capable of receiving background plasma profiles, sheath parameters, and surface models, and capable of simulating 3D particle gyro-motion in global scale high fidelity geometries is needed. The modularity of this impurity transport component is also important in passing impurity erosion/deposition fluxes to surface composition/morphology components as well as providing impurity densities to edge plasma simulations. This unique combination of impurity transport within an integrated model gives another PSI simulation capability to the field along with the work which has been presented in this chapter.

# Chapter 3

# Modeling Tool Motivation and Development

## 3.1 High Performance Impurity Model to Extend To Larger Domains

As mentioned in Chapter 2, other codes for impurity transport and integrated simulation of the plasma-surface interaction have been implemented. However, with the advances in computing power and the progressing emphasis on computational needs for scientific insight for fusion energy, larger-scale simulations have been made possible. This motivates an integrated model for PMI comprised of high fidelity physics models fitting into a framework for computational resource management and data transfer. These high fidelity models combined in an integrated simulation should meet a set of criteria to answer specific physics questions:

- Determine PFC lifetimes due to erosion. Background plasma fluxes to the surface provide information on sputtered source magnitude as well as ionization, migration, and deposition. Feedback and modification from modified surface composition and morphology should also be accounted for.

- Track T inventory through diffusive, sub-surface trapping processes, and co-deposition/erosion. Ion implantation profiles, diffusive and trapping processes within the surface, as well as changes to eroded and deposited impurity surface layers, can strongly affect gas inventories in materials.

- Account for the impact on core plasma through, e.g., recycling of H and contamination from eroded species. Reflected and released neutral and impurity fluxes from an evolving material surface are dynamic and can be accounted for in great detail as a feedback mechanism to the SOL and core plasma.

In addition to these points of performance for an integrated model, a framework for computational resource management, data passing, and execution should be used to manage high-performance physics modules. The integrated simulation capability should begin with analytic benchmarks for each component code. More advanced simulation of linear plasma device material exposures utilizing a coupling of code subset can follow. Moving to higher resolution, more code modules, and larger domains moving towards tokamak simulation is the goal.

As part of this development of an integrated model for PMI, a modular impurity transport particle push is needed. Established trace impurity codes have either made a guiding center approximation in order to simulate full fusion device domains, or performed full Lorentz orbit simulations and been restricted to a smaller physical domain (10s of cm). The GITR code development effort allows for the full gyro motion to be captured while performing well enough to simulate large domains (and enough particles to represent necessary statistics). Details of the physics and computer science requirements, as well as code details, are given in the following sections.

## 3.2 GITR Code Development Effort

The code development effort has been a large part of this dissertation. Parts of this code development effort have required a full understanding of the physics models, assumptions, and mathematical implementations. Approximations made in other codes had to be understood as well as possible in order to take the model to higher fidelity of computation. Also, significant computer science knowledge and algorithmic pragmas had to be utilized in order to efficiently structure implementation of the impurity transport model that would not be limited by the operations or computational hardware in order to achieve the desired result.

### 3.2.1 Physics Requirements

Presently many experimental efforts are focused on the global aspect of impurity transport, and effect on the macroscopic performance of the plasma and the PFCs. Examples of this include the DIII-D tungsten rings experiment and the ICRF heating problem. In such problems, both the local prompt ionization and redeposition, as well as the longer-range migration of impurities play a significant role. Insight to the patterns and mechanisms which affect the redistribution of wall material is required in order to mitigate adverse effects. This creates a requirement to resolve multiple length scales within the calculation, as particles must be transported long distances, but still accurately capture small scale features and fields near the boundary such as the sheath. Because of the scale of the additional component codes of the PSI workflow which pass data into the impurity transport model, GITR must operate at high fidelity in order to maintain the quality of computational results. With the input and component codes being high performance, this places the requirement on GITR that it too run at leadership compute scales and be designed in a platform portable way which makes use of accelerator technologies of the present and future.

### 3.2.2 Computer Science Requirements and Challenges

Generalizing the problem of interest into a computer science frame of reference, GITR is an ODE integrator with a sequence of Monte Carlo operations and boundary checking algorithms. This places the crux of the operations on interpolation from the background plasma for ODE integration and checks to determine if a particle has crossed a boundary. The requirement for resolving fine-scale fields creates a need for a mesh on which the background values are stored that could grow too

large to be stored on a singe node. Therefore irregular meshing technologies and other approaches need to be investigated.

## 3.3 GITR Code Details

GITR has been developed to simulate the removal of materials from PFCs via erosion, the impurity migration through electric and magnetic field and impurity-plasma forces, and resulting return and interaction with material surfaces. The goal for GITR is to capture global (machine size) impurity migration patterns without the loss of short spatial scale effects from background plasma and fields, or fine geometry details, while remaining platform portable and modular. That is, accepting input for background plasma parameters and surface physics.

Generalizing the problem of interest into a computer science frame of reference, GITR is an ordinary differential equation (ODE) integrator with a sequence of Monte Carlo operations and boundary checking algorithms. The crux of the mathematical operations are placed on interpolation from the background plasma for ODE integration and checks to determine if a particle has crossed a boundary.

The seven following sections describe the physics and computer science details of GITR. Section 3.3.1 contains details on the physics models contained within GITR. Section 3.3.2 introduces the computational model, data structures used in the code, and implementation. Section 3.3.3 describes the custom particle-geometry distance to surface and boundary crossing algorithms. Section 3.3.4 provides a set of benchmark problems simulated in which GITR has been compared to analytic results. Section 3.3.5 outlines the performance of GITR with different scalings (variation in problem size by changing the number of particles simulated or the number of boundary elements which make up the surface geometry) making use of different execution platforms. Section 3.3.6 discusses the present work and future research directions before acknowledgments are mentioned in section 3.3.7.

### 3.3.1 Physics Model

Contained within GITR are the necessary operations for two physics models; namely:

1. Impurity particle interaction with a plasma background. The impurity interaction with the background plasma includes the Lorentz force integration of particle tracks, Coulomb collisions with the background species, and atomic physics processes.

2. Impurity particle interaction with material plasma facing surfaces. The surface model includes reflection and sputtering yields as a function of incoming particle energy and angle, as well as the sampling of outcoming (sputtered and reflected impurities) energy and angle distributions.

Particles are tracked from their initial erosion event (caused by the background plasma) through ionization, 3-D particle gyromotion, and interaction with the background plasma until coming into contact with the material surfaces where they then can reflect or sputter more impurities from the surface. In the physical problem, this cycle can continue many times before deposition of the impurity particle.

**Impurity Transport Model**

The trace impurity transport model (also referred to as the "test particle" approach) has been used in GITR for both computational as well as physical reasons [30, 31, 32, 9]. The basis for this model is the assumption that the concentration of impurities in a background plasma is small enough to result in the impurity species self-collision frequency to be smaller than the impurity-ion collision frequency. Therefore, impurity-impurity collisions have a negligible effect on the transport of impurities along magnetic field lines. In the case where the impurity self-collision frequency grows to be larger than the impurity collision frequency with the background species this may result in canceling opposing forces as is further discussed in [9]. However, if impurity concentrations grow to a level which would alter the effective background charge of the plasma this could result in collisions not being properly accounted for. In this case impurities are not at a trace level and simulations with the test particle approach will be incorrect. Impurity (surface/wall) atom contamination of the plasma is often a result of PMI in MCF devices, as well as in laboratory experiments, and many applications such as plasma etching and processing. However, the concentration of the impurity species is often much smaller than the background plasma species making this a valid assumption. Small impurity fraction is a necessity for fusion reactors as high concentrations of impurities can lead to radiative losses and fuel dilution.

Additionally, the trace impurity model has simplifying assumptions for both the physics and computational needs of the present problem. In this model, the background plasma forces act on the simulated particles, but there is no feedback from the simulated particles to the background - allowing the use of static background profiles. It also leads to a reduction to zero of the pressure terms and species self-interactions for collisions in the equations of motion. Derivations for the test particle equations of motion as well as the characteristic frequencies for physical processes are found in references [30, 31, 32, 9]. Impurity particles respond to the following equations of motion;

$$\vec{F} = q(\vec{E} + \vec{v} \times \vec{B}) + \vec{F}_c \tag{3.1}$$

Where $\vec{F}$ is the force on the particle, $q$ is the impurity particle charge, $\vec{E}$ is the background electric field, $\vec{v}$ is the impurity particle in the lab frame, $\vec{B}$ is the background magnetic field, and $\vec{F}_c$ is the force on the impurity particle due to collisions with the background plasma. Equation 3.1 contains the Lorentz force, along with a set of collisional terms $\vec{F}_c$, which can be expanded as

$$\vec{F}_c = m\frac{\Delta v}{\Delta t} = -\nu_S m\vec{U} \pm m\sqrt{\frac{\nu_\perp}{2\Delta t}}\vec{U}_\perp \pm m\sqrt{\frac{\nu_\parallel}{\Delta t}}\vec{U}_\parallel + \alpha_e \nabla_{\parallel B}(kT_e) + \beta_i \nabla_{\parallel B}(kT_i) \tag{3.2}$$

$$KE = (1 - \nu_E \Delta t)\frac{1}{2}mv^2 \tag{3.3}$$

Where the $\nu$ variables represent collision process frequencies, $m$ is the impurity particle mass, $\Delta t$ is time step, and $\vec{U}$ is relative velocity. The coefficients $\alpha_e$ and $\beta_i$ are coefficients which depend on impurity ion charge and mass, and background

plasma ion mass and $\nabla_{\|B}$ is the gradient operator along the magnetic field B, $k$ is the Boltzmann constant, and $T_e$ and $T_i$ are electron and ion temperatures respectively. In Equation 3.3, $KE$ is kinetic energy, $m$ is impurity particle mass, and $v$ is particle velocity.

The various frequencies represented by $\nu$ in equations 3.2 and 3.3 come from velocity moments of the Boltzmann transport equation and make use of the Fokker-Plank theory of collisions and the solution of the Rosenbluth potentials [1]. They represent characteristic times of collisional processes and are applied in both deterministic and stochastic ways. The zeroth velocity moment results in a dynamical friction (drag) force on the particle noted as $\nu_s$, which represents loss of momentum in the direction of relative travel of the ion, represented by $\vec{U} = \vec{v} - \vec{v}_{flow}$, where $\vec{v}$ is the particle velocity in the lab frame and $\vec{v}_{flow}$ is the flow velocity of the background plasma in the lab frame. The first velocity moment results in a deflective force changing the particle velocity in both the forward (parallel $\nu_{\|}$) and perpendicular ($\nu_{\perp}$) directions. The second moment results in an energy kick up or down for the test particle equilibrating with the background plasma temperature affecting the kinetic energy (KE) of the particle in Equation 3.3. The parallel gradient terms are derived as thermal gradient forces that arise because of the $1/T$ dependence in the collisional force terms [33].

The collisional force terms within the range of parameters of the background plasma that are relevant for laboratory studies and fusion energy, the collisional force terms are found to be significantly smaller than the Lorentz force or the streaming momentum of an ion in the absence of electric and magnetic fields. This difference in force magnitude allows the integration of these equations of motion to be separated into two parts. The first is a Verlet ODE integration of the Lorentz force using the Boris algorithm [34]. The Boris algorithm is a stable and fast ODE integration commonly used in particle-in-cell (PIC) codes and electromagnetic particle codes [35]. Second is the application of the collision force which gives a small velocity kick to the particle each time step.

In addition to these equations of motion, GITR contains a set of Monte Carlo operators for atomic physics processes including ionization, recombination, and charge exchange. Coefficients for these operations are connected to the ADAS database [36] which directly give Maxwellian-averaged reaction rates $\langle \sigma(T_e, n_e) v \rangle$. The mean time for a particular reaction to take place then becomes

$$\tau = \frac{1}{\langle \sigma(T_e, n_e) v \rangle n_e} \tag{3.4}$$

where $n_e$ is the electron density. The probability of the reaction occurring in the given time step is calculated as $P = 1 - e^{\frac{-\Delta t}{\tau}}$ which is then compared to a uniform pseudo-random number $\xi$ to determine if the reaction occurs ($P < \xi$).

Finally, GITR has an ad hoc diffusion operator to simulate anomalous cross-field diffusion (perpendicular to the magnetic field). This is simulated by adding displacements to the particle in the form $\Delta\vec{r} = \vec{r} + \sqrt{6D\Delta t}\hat{B}_{\perp}$ where $\vec{r}$ is position vector, $D$ is diffusion coefficient, and $\hat{B}_{\perp}$ is a random unit vector perpendicular to the magnetic field.

**Surface Model**

The GITR surface model determines the events which occur when an impurity particle intersects the material surface/boundary. Impurities in experiments can come from a variety of source types, such as charged particle sputtering, neutral sputtering, evaporation from overheating, and desorption. The predominant source of impurities in MCF and in the application of GITR is charged particle sputtering as a result of an incoming flux of background plasma and the resulting self-sputtering from the eroded impurity species. The surface model for reflection and sputtering used in GITR uses a particle weighting approach to advance the first generation (background eroded particles) of particles. This approach gives importance to impurities impacting a surface with a high probability of sputtering or reflecting. Sputtering and reflection data can come from analytic models, data tables [37], or simulations by binary-collision model or molecular dynamics [38]. Input coefficients for the surface model can be a function of up to three dimensions (impact energy, impact angle, surface roughness) as is the case with outcoming (sputtered/reflected) energy and angle distributions.

Initial conditions for eroded particles are formulated according to a background ion density or flux value ($n_i$ or $\Gamma_i$) at a surface in combination with an ion distribution function f(E,$\theta$), and sputtering data for the background plasma on the surface composition Y(E,$\theta$). For both the ion distribution function f(E,$\theta$) and the sputtering yield Y(E,$\theta$), E represents the impacting atom/ion energy at the surface, and $\theta$ is the impacting atom/ion angle with respect to the surface normal (0 degrees being normal incidence, 90 degrees being parallel to the surface). Ion distribution functions f(E,$\theta$) can be assumed to be a shifted Maxwellian distribution, come from analytic forms [39], or be computed from kinetic simulations [40]. Integrating the distribution function with a sputtering yield which can have dependencies on energy and angle allows for an effective sputtering yield $\bar{Y}$ to be produced.

$$\bar{Y} = \int \int f(E,\theta) Y(E,\theta) dE d\theta \tag{3.5}$$

The outcoming sputtered particle flux $\Gamma_{impurity}$ is then equal to the incoming flux $\Gamma_i$ scaled by the effective sputtering yield as:

$$\Gamma_{impurity} = \Gamma_i \bar{Y} \tag{3.6}$$

The GITR source strength (number of physical particles per simulated particle) is set proportionally to this effective sputtering yield. The source strength and the sputtered impurity distribution in energy and angle are spatially resolved. Sputtered impurity energy and angle distributions are primarily determined by incident ion energy and angle and material surface properties.

### 3.3.2 Computational Model

The fundamental operations of GITR are based on the interaction of particles with background fields and surface/boundary elements. Therefore, four primary data structures have been designed to represent and organize the simulated problem. The interaction of these data structures occurs during the application to simulate the physical processes described in Section 3.2. These data structures are described in more detail below.

**Fundamental Data Structures**

- **Particles**

  GITR operates on Lagrangian particles which stream freely in 6-dimensional phase space ($3\boldsymbol{x}$ and $3\boldsymbol{v}$). This data structure is implemented as a Particles class which contains vectors of properties such as position, velocity, and charge. The Particles data structure is organized in this fashion to take advantage of vectorized operations and coalesced memory reads when operating on the particles in parallel.

- **Background Grids**

  The Monte Carlo particles (atoms) that are transported in GITR undergo operations making use of two techniques, which are background grid interpolation and a custom analytic functional forms based on a particle's position with respect to the geometry (described in section 3.4). The background grids for slowly spatially varying background quantities such as magnetic field, temperature, density are regular structured grids represented in 2D (with projected symmetry) or 3D. The regular structure of the background grids simplifies bi-linear and tri-linear interpolation, but the memory access is still a significant cost in the execution of GITR.

- **Boundary Elements**

  Boundary elements in GITR are represented either by a collection of lines (2 points per element) or a collection of triangular faces (3 points per element). The boundary class contains properties such as positions for the points, as well as physical composition, and coefficients for the equation of the plane which the element makes up. The boundary intersection with a particle trajectory is a critical calculation and is one that is expensive relative to other steps in the code (described in section 3.4)

- **Surface Elements**

  The surface elements collect information about the simulated particle interaction with a particular boundary element. Only selected boundary elements have a corresponding surface element to reduce the memory requirement for data collection. Surface elements track statistics such as the number of particles to strike a surface, energy and angle distribution of incoming and reflected/sputtered particles, and gross erosion and deposition.

GITR is implemented as a time loop which operates on vectors of particle properties done in a functor-iterator approach.

The physics functors are function objects (which are commonly utilized in Standard Template Library (STL) [41] type iterators) that apply an operation to the vector of elements (particle properties). In GITR this is implemented using the Thrust iterators which are designed to mimic the C++ STL functionality while allowing platform portability and parallelism to be inherent. Thrust is a high-level language that enables platform portability between serial CPU execution, GPUs, and multicore CPUs [42]. Thrust interfaces with CUDA and OpenMP backends to

allow easy integration into existing software on computational clusters. Thrust allows for a unified code base to run in serial, using OpenMP, or CUDA by modifying a flag at compile time.

The functors/operators include particle push, geometry check, and Monte Carlo operations for collisions, diffusion, and atomic physics. All physics functors require significant interpolation of background fields or tabulated data - therefore the emphasis of the code structure is to take advantage of low GPU warp divergence and coalesced memory reads.

### 3.3.3 Geometry Algorithms

Surface and boundary geometries of 2 or 3 dimensions can be input to GITR for representation of material surfaces or particle-absorbing boundaries to the simulation. These boundary elements are used for several necessary operations within the GITR simulation, and several custom algorithms have been implemented to accelerate these operations. The two geometry operations required for the simulation of ion trajectories are:

1. Particle track intersection with a boundary. When particles intersect the boundary elements, the location and velocity need to be computed either for deposition/absorption or to determine the conditions for the reflection/sputtering surface model.

2. Geometry query for analytic force application. Based on the relative location of a particle with respect to the surfaces, background profiles and fields can be adjusted to more accurately represent the local physics while bypassing more involved meshing needs.

A variety of meshing tools have been used to create 2D and 3D geometries for GITR ranging from manual formulation to use of complex CAD models. The essentials for the GITR geometry are to formulate a collection of points which represent a geometry (usually some closed geometry, so particles do not leak out). Geometric plane coefficients can then be pre-computed to accelerate the GITR geometry checks.

#### Custom Meshing Solutions

The global impurity transport problem creates a set of computational challenges based on the physical domain and the relevant physics that needs to be captured within the code. Those operations include determination of particle trajectory intersections with boundary elements and surfaces, and determination of background field values (e.g., electric field) very near the surface elements.

- **Geometry Intersection** GITR simulations have millions to hundreds of millions of simulated particles, a GITR geometry representation with thousands to hundreds of thousands of triangular faces, and a simulation of at least one hundred thousand time steps. Checking the particle-boundary intersection at each time advance becomes an insurmountable task without alternative solutions. Two algorithms have been introduced to allow the simulation of this scale. The first is a fast algorithm for finding if a particle has crossed a triangular plane and if so it's exact intersection point. The second is a boundary hash

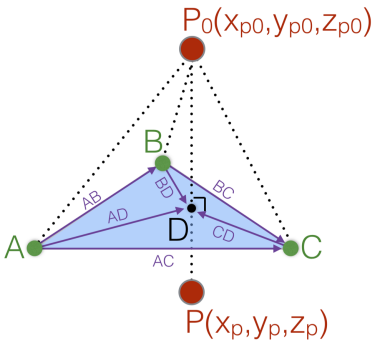


```
|PD| = (ax_p+by_p + cz_p + d)/sqrt(a²+b²+c²)
|P_0D| = (ax_p0+by_p0 + cz_p0 + d)/sqrt(a²+b²+c²)
IF(|PD| • |P_0D| < 0) {
      IF(ABxAC•ABxAD > 0
            && BCxAB•-BCxBD > 0
            && ACxBC•-ACxCD > 0) {
                  This element was crossed
                  Set position to point D
            }
      }
```

Figure 3.1: GITR 3D boundary element particle intersection schematic and algorithm. With an initial position $P_0$ and a current position $P$ the plane equation is used to determine distance to the surface for each position. Then a set of cross-products is used to determine if the intersection is within the triangle.

which is itself an interpolable background field which can be used to determine a subset of boundary elements to check for particle-boundary intersection.

The first algorithm involves a small pre-computation step which casts the geometry intersection problem into a more manageable form. This pre-computation step consists of taking the points and triangles which make up a geometry and computing coefficients which describe an infinite plane of the form, $ax + by + cz + d = 0$, for each boundary element. These coefficients are stored as part of the geometry file and become an object property for each boundary object in GITR. These coefficients can be used to quickly determine if the plane has been crossed by the trajectory of the particle using the following equations:

$$|\bar{P_0D}| = \frac{ax_{p0} + by_{p0} + cz_{p0} + d}{\sqrt{a^2 + b^2 + c^2}} \tag{3.7}$$

$$|\bar{PD}| = \frac{ax_{p} + by_{p} + cz_{p} + d}{\sqrt{a^2 + b^2 + c^2}} \tag{3.8}$$

A change in sign in this distance calculation will determine if the particle has crossed the infinite plane. If the plane has not been intersected, no further computation is required, and the next boundary element is checked. If a particular plane is intersected, then it is necessary to check if that intersection is within the bounds of the triangular element. This check is made by taking a series of cross products. If the crossing of the trajectory is within the triangle boundary element, then the exact line-plane intersection is used as can be seen in Figure 3.1. The edges and vertices are also checked for particle trajectory intersection.

In addition to this fast intersection checking algorithm, a hashing algorithm has been implemented to effectively reduce the number of boundary elements to be checked per particle per time step. The hash reduces the computation from checking the entire geometry to a localized set of boundary elements which can reduce the number of checks from hundreds of thousands down to ten resulting in a speed-up of up to $10^4$ times. Like the previous algorithm, this boundary hashing also requires a precomputing step, but unlike the previous algorithm, this can be an expensive computation. The idea is to create a structured regular mesh on which a fixed number of integers is stored which represents the index of boundary elements of which to check for intersection. Therefore for large 3D geometries, this precomputing step is expensive but only needs to be performed once per geometry. Care needs to be taken in order to ensure all of the necessary boundary elements are checked. Otherwise, it is possible a boundary element will be crossed without an indication from the code. Thus a proper ratio of hash resolution and number of hash elements to the geometry must be kept. I.e., having more boundary elements within a hash grid cell than are stored on each hash node will result in errors.

- **Distance to Surface Geometry Query**

  Another custom meshing solution in GITR is a geometry query that determines the distance to the nearest material surface ($Z > 0$).

  As mentioned previously, GITR uses regular structured grids for background values which performs well for interpolation and gives accurate values for slowly spatially varying values. Plasma potentials, plasma flows, and densities can vary quickly near the material (or PFC) surfaces - on the order of tens of microns. Since regular structured volume meshes at this resolution would require an excessive amount of memory to mesh an entire device, and irregular meshing technologies are not readily available for implementation on accelerated architectures, a workaround solution was needed. This algorithm assumes that if a particle is very close ( tens of microns) to a surface that it is not close to any other surface. The algorithm also uses a hash structure similar to that described for the geometry intersection algorithm. Different from the geometry intersection, this algorithm only uses material surfaces (i.e., not boundary only elements) because only the material surfaces in the simulation will have the properties of being a plasma sink, forming sheath structures, etc. This distance to surface geometry query determines the distance to a material surface which is depicted in Figure 3.2, the direction, surface normal, and local plasma parameters and then uses these values in some analytic form for the given field to determine a more accurate value near the surface. Simple models for sheath fields, plasma flow velocity, and density [43, 44] can be used to adjust and calculate more accurate forces for the impurity particles to undergo near the surface.

Similar to the hash produced for the boundary elements and particle trajectory intersection with the boundary, there is also a hash generated for near-surface field adjustment. This hash is different from the boundary hash in that it only takes into account material surfaces ($Z > 0$ for the input geometry) and that is used to calculate the distance to the nearest surface. The hash once again removes the

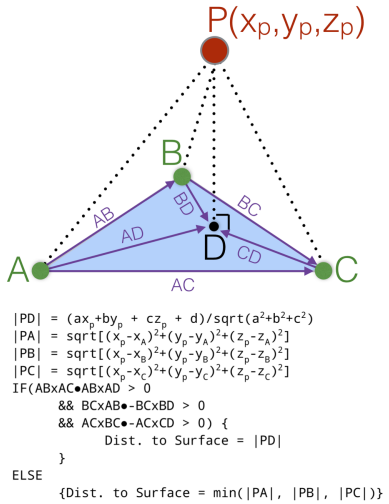


Figure 3.2: GITR particle distance to 3D surface element calculation for force adjustment. The particle position is projected perpendicularly onto the plane. Cross products are used to determine if the projected point is within the triangle.

scaling problem for increased geometry fidelity and allows for a fast calculation of the distance to nearest N surfaces (triangles).

### 3.3.4 Benchmark Problems

A set of simple operator benchmarks is presented in this section to verify that the result of the algorithms is working as expected. These algorithms include the surface model, Monte Carlo ionization and recombination, and collisional effects on particles. In this article, these operators are being shown to work somewhat independently, while a more integrated physics test for impurity transport in scrape-off-layer conditions is the topic of a future publication.

- **Surface Model and Particle Balance**

  The GITR surface model statistics can be elucidated and validated through a simple example. In this example, a finite number of particles, nP, originate in a volume surrounded by a closed geometry. The particles move until coming into contact with a material surface at which point they reflect/sputter/deposit. After striking a surface, the particles then leave that surface to be transported until striking another surface. At each particle-surface impact, the GITR surface model modifies the computational particle weight appropriately during each interaction until all of the particles have been deposited (the computational weights are 0). The mode of transport, forces, and migration patterns are irrelevant for this example as long as the particles continue to be transported to surfaces. Using a constant sputtering yield Y=0.1 and a reflection coefficient R=0.5 it can be seen that for nP=100 particles colliding with a surface, on average, 10 will sputter, and 50 will reflect, leaving 40 particles to net deposit on the surface. GITR uses a statistical weighting approach to simulate this process - weighting each of the particles to 60 percent (Y+R) and giving a gross deposition of 50 and net deposition of 40 to the local surface element. 83 of the 100 particles (R/(Y+R))*nP are then launched with reflected condi-

tions and 17 of the 100 particles (Y/(Y+R))*nP are launched from the surface with sputtered conditions (angle and velocity). The 83 reflected particles each at weight 0.60 represent the 83*0.6=50 reflected particles. The 17 sputtered particles represent the 17*0.6=10 sputtered particles. In the simulated example, this process repeats many times as particles continue to collide with the material surfaces and reflection and sputtering continues. A mathematical model representing this simplified case can be formulated to represent the sum of the net deposition of impurities on all surfaces at the end of the simulation as described by Equation 3.9.

$$netDeposition = nP * (1 - R) \sum_{i=1}^{\infty} (Y + R)^i \\ = nP * \frac{1 - R}{1 - (Y + R)} \quad (3.9)$$

Here $i$ represents each generation of particles colliding with the surfaces. For the present example case, this comes out to be 125 particles net deposited. The example case at the end of section 5 demonstrates this result as calculated by GITR.

- **Ionization Recombination and Monte Carlo Operations**

  GITR can be used for evaluation of charge state distributions in a plasma. With complex plasma profiles and impurity transport patterns, this can be useful for estimating Bremsstrahlung radiation or local surface impact energies. For validation of the recombination and ionization operators, the code can be run and compared to a direct numerical solution of coupled ODEs using the same coefficients for ionization and recombination as used in GITR. For this example, there is no need for input geometry to GITR, and the background plasma parameters are constant with $T_i = T_e = 20eV$ and $n_i = n_e = 1e19m^{-3}$. Constant profiles allow for the ionization and recombination coefficients S and $\alpha$ to have constant values. Applying a collisional ionization equilibrium (CIE) model (sometimes called coronal equilibrium from its application to the hot coronae of stars) [45] requires the solution of a set of equations as follows:

$$\frac{dn(z)}{dt} = n_e \Big\{ - n(z)S(z) + n(z-1)S(z-1) \\ - n(z)\alpha(z) + n(z+1)\alpha(z+1) \Big\} \quad (3.10)$$

  where $n$ is the concentration of a particular charge state $z$ from $z = 0$ to $Z$ where $Z$ is the nuclear charge. In the steady-state, $\frac{dn(z)}{dt} = 0$, the equations reduce to

$$\frac{n(z)}{n(z+1)} = \frac{\alpha(z+1)}{S(z)} \quad (3.11)$$

  where S(z) and $\alpha(z+1)$ are the ionization and recombination coefficients for ions of initial charge z and z+1, respectively.

  The solution of these equations for W impurities in a background plasma $T_i = T_e = 20eV$ and $n_i = n_e = 1e19m^{-3}$ as compared to the GITR result is shown in figure 3.3 and demonstrates good agreement.

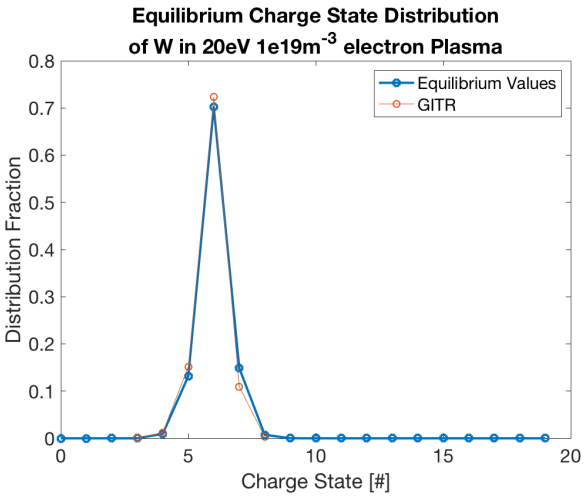


Figure 3.3: Charge state distribution fraction for W ions in a 20eV plasma from the analytic values (blue) and GITR prediction (red).

- **Collision Operations**

  Taking a similar approach as was done for the charge state example, impurities can be launched into an unmagnetized background plasma to view the time evolution of the velocity components due to Coulomb Collisions. This is a test to ensure that particle velocities evolve as expected according to the Fokker-Planck collision operators in GITR. In this example, W with a fixed charge of 1+ (no ionization or recombination) is launched in the z-direction with 10 eV kinetic energy (3300 m/s) into a deuterium plasma with $T_i = T_e = 20eV$ and $n_i = n_e = 1e19m^{-3}$ and a plasma flow in the x-direction of 2,000 m/s. The characteristic times for each of the collisional processes, namely drag, velocity diffusion parallel and perpendicular, and heating are shown in Figure 3.4 as a function of W impurity ion energy. For these operators, three tests are presented: drag, heating, and velocity diffusion. Each of these will compare the GITR average result to an analytic function for velocity evolution.

  Considering the drag force independently, a particle with initial velocity $v_0$ will slow according to frictional drag as given by Equation 3.12.

$$\bar{v_{\|}} = v_0(1 - \nu_S t) \tag{3.12}$$

  Because $\nu_S$ is a function of the relative speed of the particle to the background plasma flow as well as temperature, density, and charge that dependence must be taken into account for the analytic solution which can be given by Equation 3.13.

$$\bar{v_{\|}} = v_0 - \int \nu_S(\bar{v_{\|}})dt \tag{3.13}$$

  Comparison of the analytic solution and average x-directed velocity from GITR gives agreement, as shown in Figure 3.5. The GITR result shows some statistical noise, but almost exactly matches the analytic solution converging to the 2,000 m/s flow velocity in the x-direction.

  The next test of GITR involves the Coulomb collision model and examines heating of the W ions in the D background plasma. The temperature of

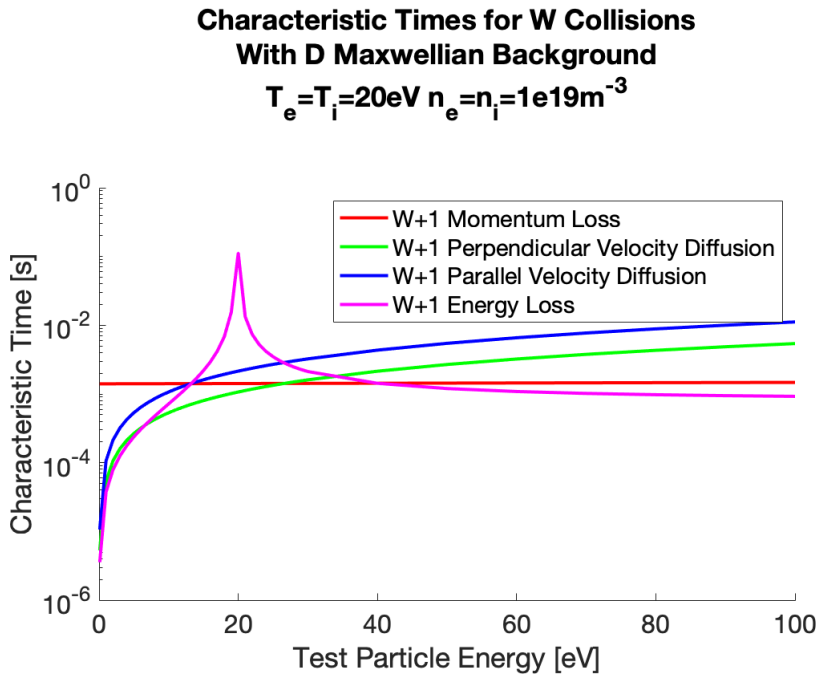


Figure 3.4: Characteristic times (inverses of the frequencies previously described in equation 3.2) for W1+ ion evolution due to Coulomb collisions with a Deuterium and electron background plasma as a function of particle kinetic energy.

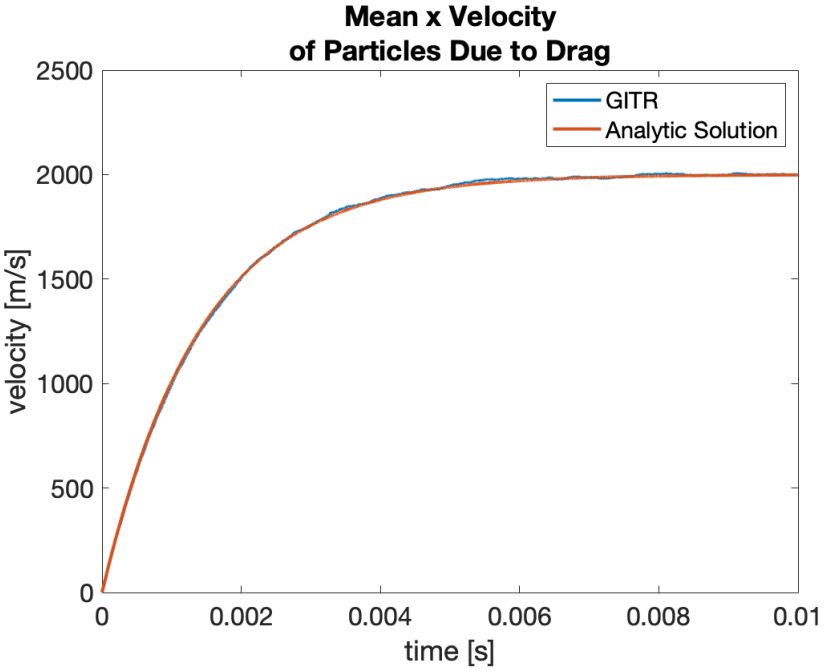


Figure 3.5: Average W ion x-direction velocity over time. W impurity population gets dragged with the background D plasma on the order of milliseconds.

the particle distribution with initial velocity $v_0$ will be heated according to Equation 3.14. This should result in W ion temperature equilibration with the background D plasma on the time scale of $\tau_E = \frac{1}{\nu_E}$.

$$\bar{v} \approx v_0(1 - \nu_E t/2) \tag{3.14}$$

In Equation 3.14 $\nu_E$ is a function of particle velocity, temperature, ion mass, and charge and $\nu_E$ is negative for values below the background plasma temperature and positive above the background plasma temperature giving heating and cooling of the test particle respectively. The analytic form given in Equation 3.14 gives a mean velocity evolution, where here the temperature is being evaluated to converge to the proper value. Therefore there is no exact analytic solution of the time evolution of temperature. Temperature of the W ions simulated in GITR is shown in Figure 3.6 and shows an initial temperature of zero before rising to 20 eV. The initial temperature is zero because of the delta function used for velocity resulting in no random velocity or width in particle velocity distribution. Temperature of the W ions is shown to converge and remain at 20 eV with some statistical noise. The diffusion processes of the angular (perpendicular) velocity and speed (parallel) are treated differently than the drag and heating forces since they are random and diffusive. Therefore an exponential model can be used to approximate the sharing of z-directed velocity in the y-direction. By considering only the collisions which cause deflection of velocity, the time evolution of the ratio of mean y-directed speed to mean z-directed speed can be approximated:

$$\frac{|v_y|}{|v_z|} \approx 1 - e^{-0.5 * \int \nu_\perp dt} \tag{3.15}$$

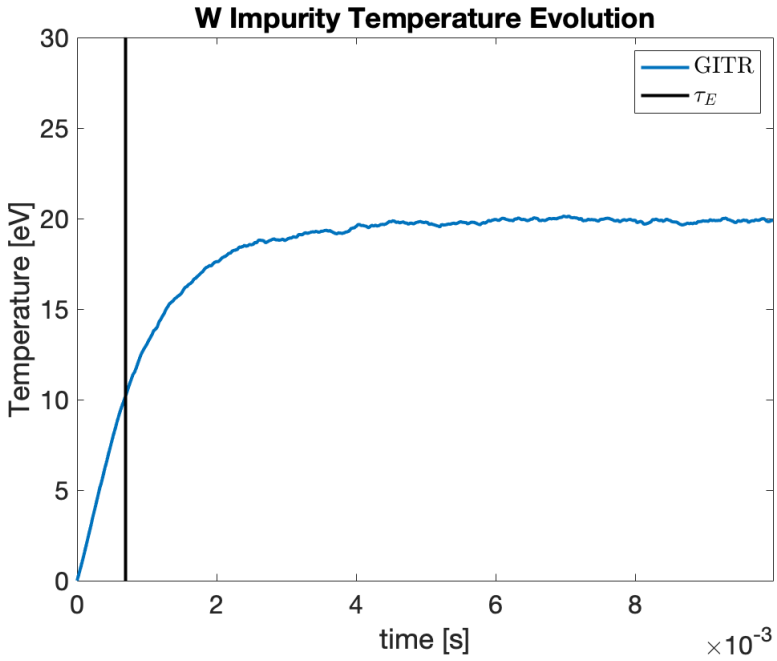


Figure 3.6: Average GITR simulated temperature evolution for 10eV W1+ launched into a flowing (2,000 m/s) D plasma background. Mean time for velocity equilibration $\tau_E$ is shown as a vertical black line.

However, because of the contributions from heating and parallel velocity diffusion, a more additional approximation of this velocity diffusion can be given by using the parallel velocity diffusion frequency:

$$\frac{|v_y|}{|v_z|} \approx 1 - e^{-0.5*\int \nu_\perp dt - \int \nu_{||} dt} \tag{3.16}$$

Comparison of these analytic forms as well as the GITR result is shown in Figure 3.7. Figure 3.7 shows that the two analytic approximations give an approximately bounding range of the GITR result. The reason for the deviation in the GITR result from the exact analytic expression comes from contributions from the parallel velocity diffusion and energy gain. In the simulated problem all particles begin with a z-directed velocity at a velocity less than the mean equilibrated velocity in the background plasma. As particles begin to diffuse perpendicularly to their initial velocity (from z to x and y), the are also diffusing in the parallel direction and being heated. This effectively accelerates the sharing of the initial z-directed velocity to the x and y directions. Therefore, in Figure 3.7 it can be seen that velocity diffusion occurs faster than what would be expected solely due to deflection of particles.

- **Example Case**

  A complete example case to demonstrate GITR and the code outputs are now presented. This example case has some features that are relevant to fusion erosion scenarios but is also simplified for demonstration purposes and satisfies the description given previously in Section 3.5: Surface Model and Particle Balance. In this case a D plasma (mass=2 AMU charge=1) with

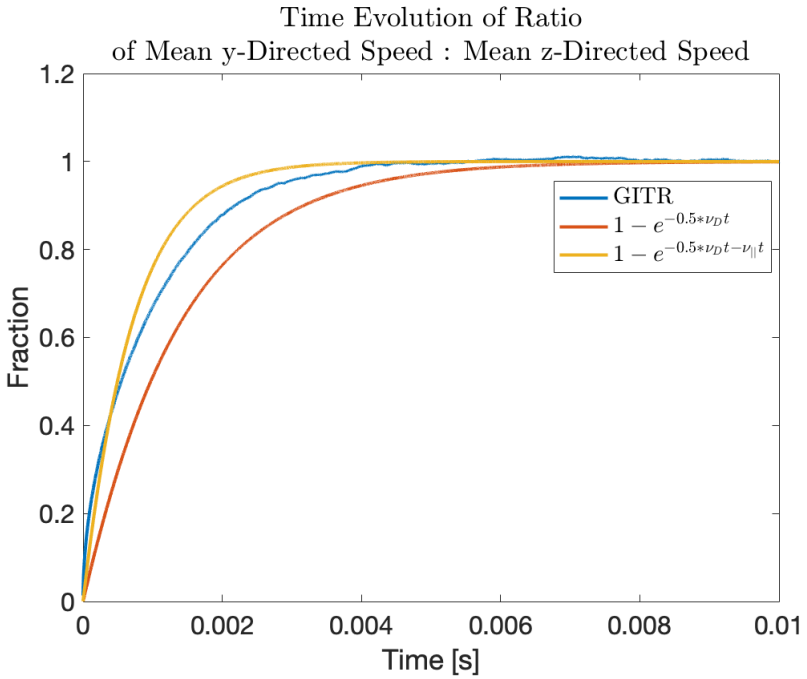


Figure 3.7: Average GITR simulated perpendicular velocity evolution for W1+ in a D background compared to approximate velocity diffusion from Equation 3.15 and 3.16.

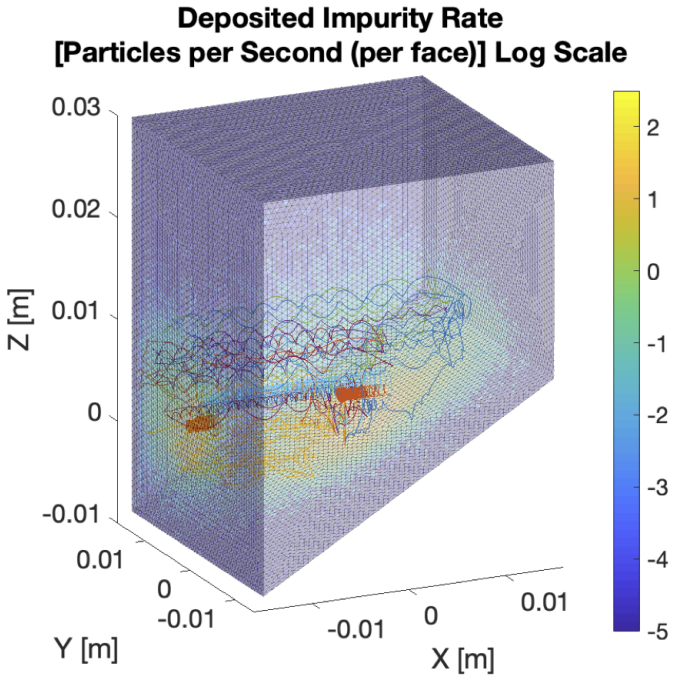


Figure 3.8: GITR example case simulated geometry with side cut away. Deposited particle rate (colored surfaces) and example particle tracks (different colored lines) are shown.

$T_i = T_e = 20eV$ and $n_i = n_e = 1e19m^{-3}$ fills the geometry made up of a plane angled at 30 degrees with respect to a y-z plane and passing through the origin. Connecting walls at x=+-1.5 cm, y=+-1.5 cm and z=3cm complete the closed geometry. The mesh resolution is set to $600\mu m$ and the surface geometry is comprised of 35,347 boundary and surface (triangle) elements in which all boundaries are W material surfaces. This 3D surface geometry is depicted in figure 3.8. The magnetic field is fixed to 2 Tesla in the x-direction. Ionization by electron impact is switched on using coefficients from the ADAS database [36]. Sheath electric field is applied according to the model specified in reference [43]. A simple surface model for reflection (R=0.5) and sputtering yield (Y=0.1) are used where any sputtered/reflected particle leaves the surface with 8eV of energy, an azimuthal angle of $\phi = 45\,\text{deg}$ and $\theta = \xi * 360\,\text{deg}$ where $\xi$ is a random number between 0 and 1. The initial source of eroded particles is a point source at the origin with energy in the z-direction of 10eV with a magnitude set to 1 particle per second and with nP=1e4 particles. Therefore each computational particle represents 1e-4 physical particles. The problem has particles that are launched vertically (in the z-direction), being ionized and then going through gyromotion and being accelerated back to the surface where the particles sputter and reflect to be launched from the surface again. The particles are weighted according to each process and the weights are accounted for in binning for densities of impurities as well as impacts on the material surface.

Typical results of such a simulation can yield particle tracks, charge-resolved volumetric density histograms, surface erosion, deposition, sputtering, and reflection maps and energy-angle distributions at the surface. Returning to the

analytical example of Surface Model and Particle balance where $netDeposition = nP * \frac{1-R}{1-(Y+R)} = 1.25e4$ the GITR result predicts a value of 1.247e4. This value is in reasonable agreement, in which the difference can be attributed to the accumulation of round off error. Additional sample output from the GITR simulation is shown in Figures 3.9 and 3.10.

Since all surface elements in the simulation are W material surfaces which are in contact with plasma there exists a sheath electric field structure according to [43] which serves to accelerate simulated impurity ions toward the local surface. The total potential of the surface set to be $\phi = 3kT_e/e$ where k is the Boltzmann constant, $T_e$ is electron temperature and $e$ is the electron charge. Therefore ions entering the sheath can experience accelerations adding kinetic energy to the particle of up to $Qe(3kT_e)$ where $Q$ is the impurity ion charge number. Since some particles are ionized within the sheath region, in many cases only a fraction of this potential energy is given to the impurity ion traveling back to the surface. The summed ion energy-angle distribution (IEAD) for all of the surfaces in the example problem is shown in Figure 3.9. This result demonstrates that impurity ion charges of approximately 1 to 9 are impacting the material surfaces with a peak between 50eV and 150eV. The surface IEAD also demonstrates the intuitive result that acceleration of higher charges results in more normal incidence impacts.

A second example of GITR simulation output is the W impurity ion density profile shown in Figure 3.10. This profile demonstrates the impurity density of all charge states averaged in the y-direction. The particle source location of z=0 and x=0 can be seen with respect to the surface plane plotted as a white line. It shows that the launch trajectory of the impurity atoms in the z-direction dominates the density profile with a peak around z=6mm. There

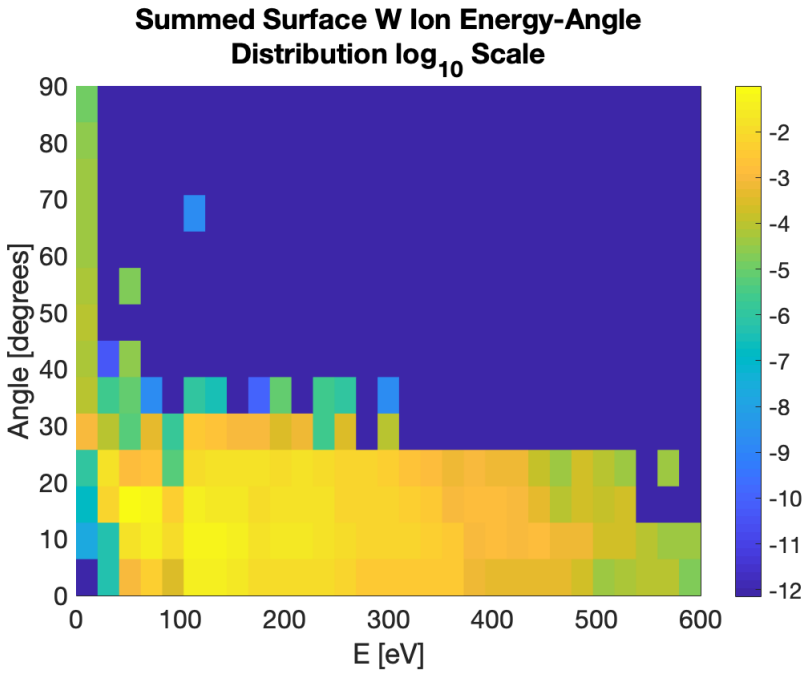


Figure 3.9: GITR example case ion-surface impact energy-angle distribution summed over all surfaces.

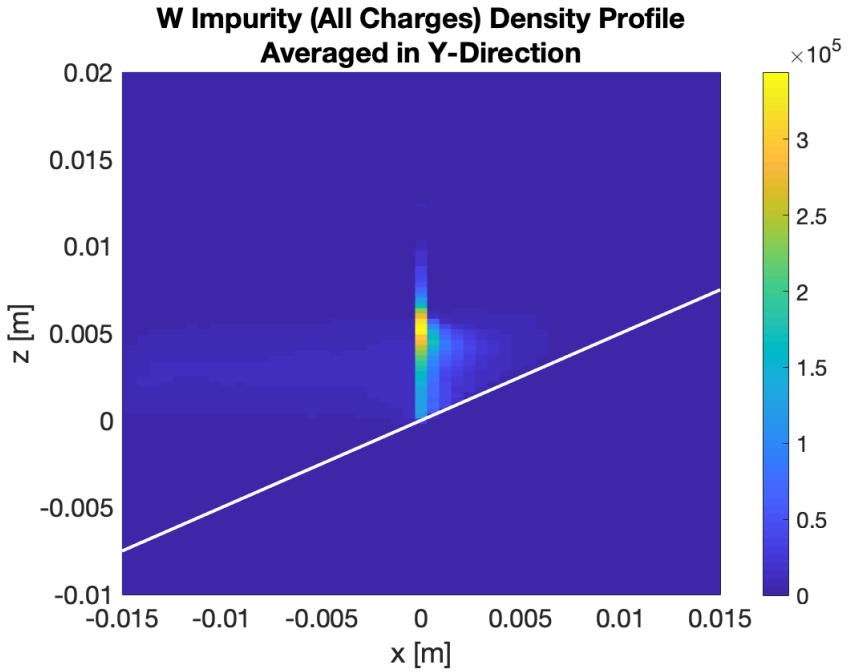


Figure 3.10: GITR example case W density profile (summed over all charge states) integrated over y-domain.

is a tail of density in the positive x-direction showing the acceleration of the launched ions towards the surface. As many of these ions impact the surface, they sputter/reflect with a velocity component in the negative x-direction and are transported to the boundary at x=-1.5cm showing a density tail in the negative x-direction.

### 3.3.5 Performance

A variety of plots have been assembled to demonstrate the scaling of GITR with problem size, as well as the utility of the performance portability solution implemented with the Thrust library. The following simulations are performed using cases similar to the example case previously described (associated with figures 8-10) and are run on a machine made up of 2 nodes in which each node consists of 12 CPU processors and 4 Tesla K80 GPUs. For each of the scaling plots shown, the OpenMP and CUDA labels indicate the compile-time setting for the Thrust library, which indicates the node parallelism utilized. MPI is used for cross-node parallelism where 2 MPI threads are used for the OpenMP implementation and 8 MPI threads for the CUDA implementation (one MPI process per GPU).

The three parameters of the problem size which are shown to scale are the number of simulated particles, the number of time steps, and the geometry size. The GITR scaling of run time with simulated particle number are shown in Figure 3.11 and display the run time for the entire GITR application. Plots for both the OpenMP and CUDA implementations show a flat region before increasing to an approximately linear scale or possibly a super-linear or power law scaling. This flat region is a result of two factors; namely the initialization, MPI reductions, and file writing operations are large compared to the run time of the main loop, and low particle numbers not saturating the available threads. Once the parallel threads

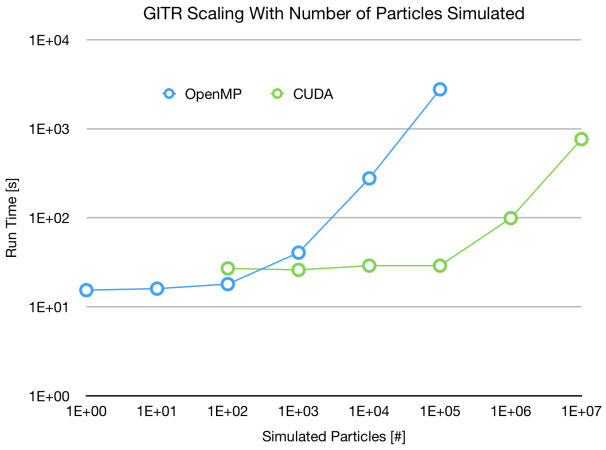


Figure 3.11: GITR run time with increasing particle number shows flat scalings for both OpenMP and CUDA until parallel threads are filled with work at which the run time becomes approximately linearly proportional to number of particles simulated (possibly super-linear or following a power law).

are saturated and the work in the main loop begins to exceed time taken for other operations, GITR scales proportional to the number of particles and demonstrates a marked increase in performance on the GPUs. GITR scaling with the number of time steps is shown in Figure 3.12 and once again shows the total run time of the GITR application. The scaling with the number of time steps demonstrates similar features to scaling with the number of particles; namely a flat region at a low number of time steps before an increase to a linear relationship. Once again this is because at a low number of time steps the initialization processes, as well as MPI reductions, are constant and take more time than the main loop execution time.

Finally, the scaling of GITR with input geometry size (larger number of smaller triangle boundaries) is shown in Figure 3.13. For both the OpenMP and CUDA implementations, the use of the hashing algorithm is shown to return flat performance regardless of geometry input size while once again the CUDA implementation has much-improved performance. In the cases where the geometry hashing algorithm is not utilized, run time is shown to grow proportionally with the size (number of boundary elements) of the geometry. Here the OpenMP and CUDA implementation run times converge as the geometry increases to larger than 200 elements. While the execution time of the main loop can be optimized using the hashing algorithm, this comes at the cost of an increasing pre-computing step. As the geometry fidelity increases, the hashing mesh must become finer which results in a scaling O($N^4$) for the 3-D case where N is the number of boundary elements. These times are shown in Figure 3.14. Once again these algorithms show favorable scaling for the CUDA implementation, and a high fidelity geometry (141,436 elements with a hash resolution of 75x75x100 at 10 closest elements) takes 30 seconds to compute. Additionally, this is a one-time computation per geometry.

### 3.3.6 Discussion and Future Work

Based on the scaling plots, the GITR performance is improved executing on GPU accelerated architectures. It is also a convenient feature that the execution time of

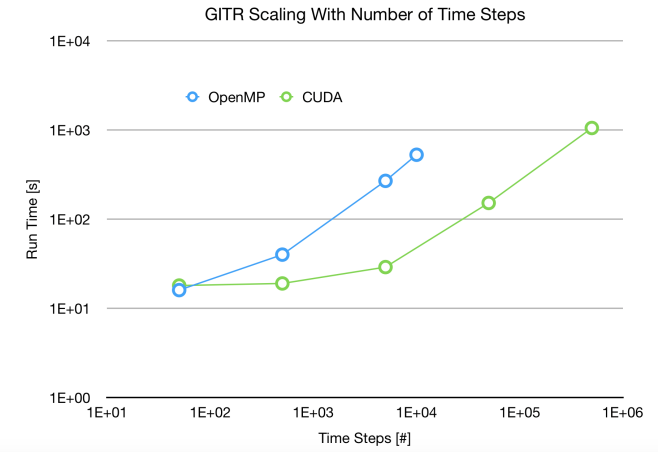


Figure 3.12: GITR full code execution time as a function of increasing number of time steps shows a flat region before reaching a linear relationship with number of time steps. Once the main loop execution time overcomes that of initialization, MPI reductions, and file writing the execution time is proportional to the time spent in the main loop.

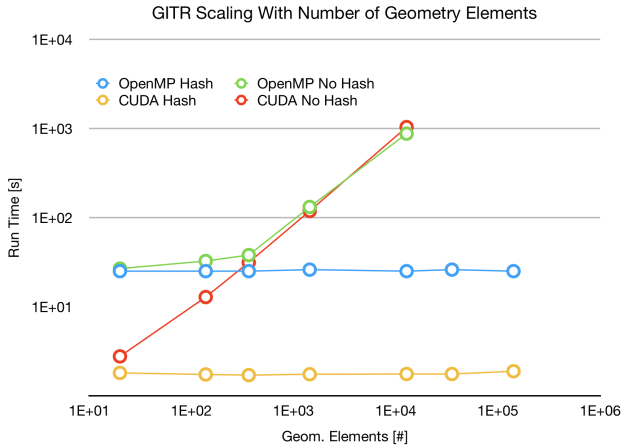


Figure 3.13: GITR main loop run time with number of geometry elements shows vastly different behavior when using the hash. Without the hash, run time is linearly proportional to number of geometry boundary elements. Performance with CUDA is especially bad because of the scattered memory accessing without using a hash. Hashing flattens scaling and results in greater performance with CUDA.

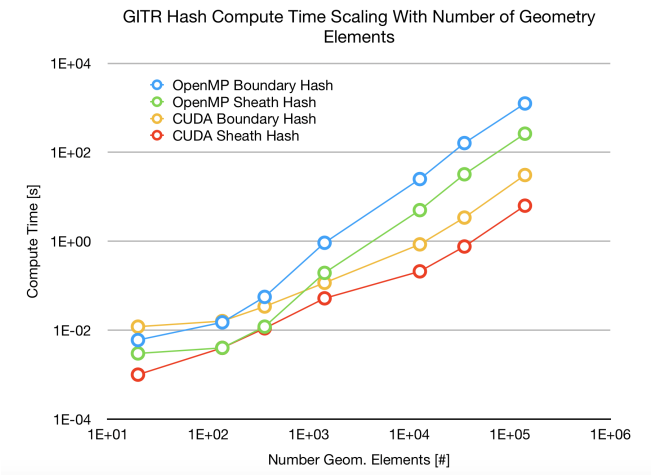


Figure 3.14: GITR hash creation time as a function of number of boundary elements. Despite poor scaling with number of boundary elements (and fidelity required for the hash) compute times for hundreds of thousands of geometry elements are at most thousands of seconds.

the code increases linearly with both particle number and number of time steps. It is possible to improve the scaling with particle number by using particle sorting operations that would remove particles below a threshold computational weight from the simulation. This reduction in particles simulated will come as a trade-off to the sorting process and depending on the physical problem the payoff will vary. Adaptive time stepping is also being investigated since the limiting time step is set by the acceleration of particles through the sheath electric field which is a high force region.

The MPI implementation divides the number of particles evenly across all MPI threads. Copies of geometry, fields, and surface models are present on the machine multiple times for a node when setting multiple GPUs per node. MPI reductions can become a significant although not dominant cost when using a very large surface geometry and many computational nodes.

## 3.4 PSI Integrated Simulation

In addition to the GITR code development, the development of the integrated model of the boundary plasma and surface evolution models capable of predicting the performance of Tungsten PFCs is also an original contribution. This research thrust as part of the PSI2 SciDAC specifically calls for the development of a high-performance code to simulate eroded impurities, their migration, and re-deposition. Additional simulation modules for SOL/edge plasma, plasma sheath, and surface response and their communication and data passing within a framework is required. Parts of this integrated modeling effort were also chosen to be a deliverable DOE fusion theory milestone for fiscal year 2018. Thus simulations targeting the coupled region of the boundary plasma and surface evolution models to predict the net erosion, fuel recycling and tritium retention for the W ITER divertor for D-T operation, and response of the edge and core plasma to impurities and recycled neutrals are needed. These simulations are to take into account impurity erosion, transport, and depo-

sition along with the evaluation of the influence of material deposition and surface evolution on the recycling and retention. The integrated simulation combines physical processes that occur at multiple length and time scales to capture the relevant physics processes. In the PSI workflow, each component code is a high-performance piece of scientific software that treats a specific domain of physics. The trade-off compared to existing integrated simulation is increasing computational time and complexity for a higher fidelity solution. The codes included in this integrated simulation includes SOLPS, Fractal-TRIDYN, hPIC, GITR, and Xolotl. This workflow gives a predictive capability - not relying on interpretive codes or experimental measurements as input. The components of the integrated simulation are briefly described:

- **The Integrated Plasma Simulator** is a python framework designed for file-based code coupling, computing allocation management, and post-processing for integrated workflows. The framework, along with component wrappers, developed for each of the individual codes used, allows for plug-and-play interfacing and sharing of data for integrated workflow setups.

- **SOL-PS** is a fluid approximation for the edge plasma made up of B2 and EIRENE. It will solve for the edge plasma conditions based on the applied magnetic field, heating sources, and boundary conditions. The role of this code in the integrated simulation is to provide background plasma profiles and fluxes to material surfaces. Short description of what the code is and how it works for the larger integrated simulation (big picture here). Details of how the codes interact specifically with GITR is detailed in the research to this point section.

- **hPIC** is a particle-in-cell code which is capable of simulating multiple ion species and electrons in a self-consistent way to simulate particle motion near the plasma-surface interface and ion energy-angle distributions at the surface. The hPIC code can be run with a Boltzmann electron approximation and in limited dimensionality for efficiency (e.g., 1d-3v). Capturing sheath accelerated ion velocities, and ExB drift motions near the surface is important in capturing erosion and ion implantation characteristics.

- **Fractal-TRIDYN** is a binary collision approximation code (BCA) which simulates energetic particles and their interaction with the surface. Parameterized results for different ions and surfaces can be compiled for reflection and sputtering yields (and their respective energy and angular distributions), implantation profiles, and damage due to energetic displacement cascades (DPA, Frenkle pair production).

- **GITR** is the high performance code responsible for impurity generation through erosion, transport through the plasma, and re-interaction with the material surface. GITR is responsible for producing net and gross erosion data for surface elements, volumetric profiles of impurity densities, and kinetic impurity fluxes.

- **Xolotl** is a continuum advection, diffusion, reaction code which calculates the behavior of sub-surface gas species, metal interstitials, and vacancies. Informed by a database of MD data, Xolotl extends cluster dynamics to a larger

scale simulation that can model experimental time scales. Xolotl provides surface composition profiles and changes to the surface morphology.

### 3.4.1 Wrappers and data passing for the integrated simulation

As GITR has been developed as a modular component within a larger integrated simulation, it depends on data from other components to be passed to it. Two of these components include the surface model that contains parameters for physical sputtering, reflection, energy, and angular distributions of such. Thus for the integrated simulation, it is essential to develop proper wrapper routines for data passing within the IPS framework. This is done to represent each component code as a building block of an integrated simulation with the interfaces to built into a larger system. Therefore it is essential for these modular components to work together and communicate to perform the tasks.

- **Background Plasma**

  A wrapper for the background plasma component has requirements of input and output. Input to this component can include updates of released and reflected neutral atoms at the divertor target, and full sputtered impurity density profiles. However, the existing 2D fluid codes contain simple models for reflection, outgassing, sputtering. Therefore to first order, it can be assumed that the background plasma is a self-consistent solution. As the integrated simulation becomes more developed, more advanced iterations, and updates to the background plasma can be calculated using updates from the surface model and impurity transport component.

  The output from this component has two parts - bulk plasma profiles and target profiles. Target profiles are used as boundary conditions in the plasma sheath calculation as well as the surface composition component, and preprocessing for the impurity transport simulations (to formulate initial conditions). These target profiles include ion and electron temperatures, electron density, ion density, ion flux, and magnetic field magnitude and angle. Bulk plasma profiles from the background plasma component include electron temperature and density, ion temperature and density (including neutral density), plasma flow velocity, plasma temperature gradients, and electric field values. These bulk or background plasma values are used solely in the impurity transport module as a fixed background on which impurities traverse. Additional outputs that correlate to the background plasma profiles include magnetic equilibrium and geometry, which correspond to the 2D fluid simulation of background plasma.

- **Plasma Sheath**

  Inputs to the plasma sheath component include the target profiles from the background plasma component, including densities for each ion species. The ion density along with electron temperature, magnetic field magnitude, and angle with respect to the target are the most influential variables which affect the sheath potential and ion energy-angle distributions produced in the sheath simulation. Outputs from the sheath component include ion energy-angle

distributions (IEADs) for each ion species (can be for multiple surface/target locations). For a given species $s$ this distribution is represented by $f_s(E, \theta)$. The impact energy and angle of an ion at a target have a strong influence on the sputtering and reflection yield. Therefore, the fluxes of neutrals, both impurity and gas species, re-entering the plasma from the surface are dependent on this output.

- **Surface Kinetics**

  The surface kinetics component is used in combination with both the impurity transport component as well as the surface composition/morphology evolution component. Therefore, there are multiple types of input/output from this component. Inputs to this component include ion species, target material (and composition profile), and ion energy and angle (or distributions). Outputs that are routed to the impurity transport component include sputtering yields ($Y_s(E, \theta)$ and reflection coefficients as a function of energy and angle for each plasma species on the material target as well as the target-self model. Sputtered particle energy and angle distributions (as a function of incoming energy and angle) are also output. The output which is routed to the surface composition/morphology evolution component includes ion implantation profiles of the background plasma species (using IEADs from the plasma sheath component), and impurity species (using IEADs from the impurity transport component). Frenkel pair (interstitial and vacancy) creation profiles are also output from the surface kinetics.

- **Impurity Transport**

  The impurity transport component accepts the target and bulk plasma profiles from the background plasma component, IEADs from the plasma sheath component, and sputtering and reflection dynamics from the surface kinetics component. This information can be combined to formulate a background plasma erosion source.

$$\bar{Y_s} = \frac{\int \int f_s(E, \theta) Y_s(E, \theta) dE d\theta}{\sum_s \int f_s(E, \theta) dE d\theta} \tag{3.17}$$

  Outputs from the impurity transport simulation include impurity density profiles, which can be used by the background plasma component. Tungsten flux (and net erosion) to the target surface are also provided to the surface composition/morphology evolution component (in combination with the surface kinetics component).

- **Surface composition/morphology evolution**

  The surface composition component makes use of the target ion flux information in combination with the implantation profiles, Frenkel pair profiles, and surface erosion. Outputs from this component include changes in surface height/roughness, released gas fluxes, and evolution of the surface composition. Independent results of this code include gas inventory, diffused gas fluxes, net accumulated material damage.

## 3.5 Summary

In summary, the original contribution of this this dissertation focuses on the integrated development of high fidelity models to simulate the plasma-surface interface. This integrated simulation capability compliments existing approaches and extends physics capability to include predictive modeling of the scrape-off layer plasma, magnetic sheath region near the surface, erosion and impurity migration, and surface evolution and feedback including changes in surface composition, morphology, and outgassing. While many of the codes used in this integration are established and continue to be developed and maintained, the GITR model for impurity transport and the interconnections of the integrated model are explicitly the work of this dissertation. The original contribution begins with the code implementation and moves into integrated benchmarks of GITR and code comparison with DIVIMP. From there GITR is benchmarked experimentally with PISCES-A He exposed W erosion measurements. From that point, addition of components to the integrated model was performed, such as background plasma profiles, erosion and sputtering models for the impurity transport, and the surface model. Formal uncertainty quantification of the PISCES-A experiments was performed in order to evaluate the influence of uncertain background plasma profiles on the impurity transport. Finally, GITR and the integrated model have been applied to ITER helium and D-T burning plasma operation in order to evaluate net erosion of W at the outer divertor target.

# Chapter 4

# Integrated Benchmarks of GITR

## 4.1 GITR Benchmarks with Simple Models and Code Comparison to DIVIMP

Model verification is an essential aspect of code development, although it is challenging to find appropriate integrated physics scenarios that have analytic solutions. For the kinetic 3D simulation domain of GITR, exact analytic solutions are not available. However, in the collisional regime (mean free path of collisions, $\lambda_{mfp}$, is small compared to the size of the domain $L$) where the plasma temperature is low and the density is high, the kinetic simulation should converge to agree with a fluid solution. In order to verify the GITR computational model for parallel transport, a comparison of GITR results to the simple fluid theory (SFT) and the DIVIMP code has been performed. This simple fluid theory is a 1D model of impurity retention in a divertor scenario described in detail in Reference [46].

For these benchmark tests, there are some common features. Carbon with a charge of +4 (A=12, C4+) is simulated with a fixed charge state in a D plasma. Cross-field diffusion is turned off, although the results from GITR are summed to give 1-dimensional results. Friction force, ion temperature gradient force, parallel velocity diffusion, perpendicular velocity diffusion, electric field forces are included in the benchmark problems, although they may vary from case to case. Plasma temperature (and temp. gradient) varies for some cases, D plasma density constant along $s$ ($10^{18}, 10^{19}, 10^{20} m^{-3}$) D plasma flow velocity held constant or may vary from 0 to $s_v$ depending on the case. Plasma flow is zero at $s > s_v$. The coordinate for distance along the magnetic field line is $s$, which is the one spatial coordinate used in this analysis. The domain is decomposed into three regions, A - the plateau or prompt loss region, B - the impurity density decay region, and C - the impurity density buildup or trap region. Physical results of tokamaks have often demonstrated the characteristics which enable the decomposition within this domain. Those characteristics include the fact that the region of plasma flow $s < s_v$ is greater than the impurity ionization distance $s_{inj}$, which is the location of our impurity source. This results in three regions which we can investigate, an impurity density peak near the target and injection point, a decreasing impurity density away from the target $s > s_{inj}$ and $s < s_v$, and an impurity build-up region $s > s_v$. The benchmark cases are summarized in Table 4.1. Used in these benchmark cases, a plasma temperature (and temperature gradient) model is also used to describe the increasing ion temperature away from the target.

Table 4.1: Overview of benchmark cases of GITR with SFT and DIVIMP.

| Case | $T_{D0}[eV]$ | $\frac{dT_D}{ds}[eV/m]$ | $n_e[m^{-3}]$ | $\bar{s}_{inj}[m]$ | $\bar{s}_v[m]$ | $v_D[m/s]$ | $E[V/m]$ |
|---|---|---|---|---|---|---|---|
| A | 10 | 1.38 | $10^{19}$ | 0.15 | 1.2 | Varied - 875 to - 1500 | 0 |
| B | Varied 10 to 130 eV | From Eq. with $f_{cond} = 0.1, M_D = 0.1$ | $10^{20}$ | 0.15 | 1.2 | $-0.1c_{s0}$ | 0 |
| C | 50 | 0 | $10^{18}$, $10^{19}$, $10^{20}$ | 0.15 | 1.2 | 0 | -25 |
| D | 10 | 0 | $10^{19}$ | 0.15 | 1.2 | -112.2 | 0 |
| E | Varied 10 to 130 eV | From Eq. with $f_{cond} = 1, M_D = 1$ | $10^{19}$ | 0.15 | 1.2 | $-1c_{s0}$ | 0 |
| F | Varied 20 to 50 eV | From Eq. with $f_{cond} = 1, M_D = 0.1$ | $10^{19}$ | 5 | 10.85 | $-0.1c_{s0}$ | 0 |

$$T(s)/T_0 = (1 + \frac{7f_{cond}|q_{||}|s}{\kappa_0 T_0^{7/2}})^{2/7} \tag{4.1}$$

Where $T_0$ is temperature at the target, $f_cond$ is the fraction of power carried by electrons along the SOL and $q_{||}$ is the parallel power flux density at the target.

Also, the ion acoustic speed is used as given by Equation 4.2 which is frequently scaled by $M_D$, the fraction of the ion acoustic speed.

$$c_s = [k(T_e + T_i)/m_i]^{1/2} \tag{4.2}$$

### 4.1.1 Region A - the plateau region

Cases A and B aim to investigate region A - the plateau or prompt loss region, through the competition of the friction force, the ion temperature gradient force, and velocity diffusion. With the charged particle source (C4+) placed at $s_{inj} < s_v$, the expected output is a peak in impurity density near $s_{inj}$ that decreases in both +/- $s$ directions. Case A sets the D plasma temperature at the divertor target to 10 eV with a constant temperature gradient of 1.38 eV/m and a plasma density of $10^{19}m^{-3}$. With $s_{inj}$ set to 0.15 m and $s_v$ set to 1.2 m, the D flow velocity is varied from 875 m/s to 1500 m/s toward the target (negative in $s$). With increasing flow velocity, the competition of forces between friction and temperature gradient favors friction, carrying ions toward the divertor target and reducing the peak impurity density $n_p$ near the target. A comparison of GITR results, DIVIMP results, and

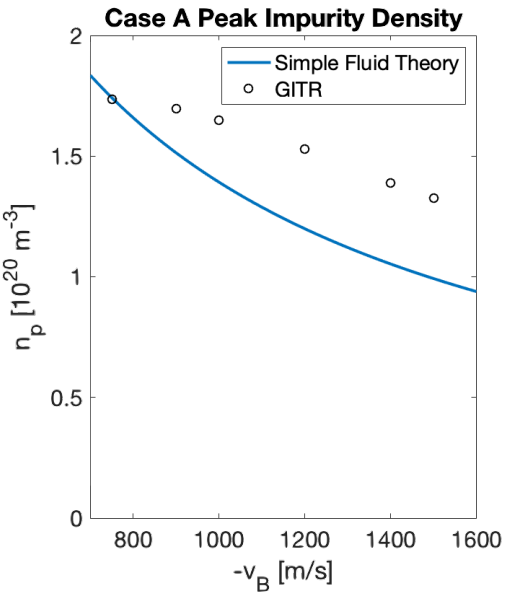


Figure 4.1: Peak impurity density near the target as a function of flow velocity (towards the target). GITR and SFT solution are shown.

the SFT model are shown in Figure 4.1. Although neither GITR nor DIVIMP identically follows the analytic solution to the SFT, the decreasing trend in peak impurity density is successfully predicted.

Case B varies the D plasma temperature at the divertor target from 10 eV to 130 eV and uses the temperature gradient equation. Plasma density is held constant at $10^{20}m^{-3}$ and plasma flow velocity ($s < s_v$) is set to $-0.1 * c_{s0}$. Once again, the competition of the friction force and the thermal gradient forces will result in a peak impurity density near $s_{inj}$. As target temperature is varied, the collisionality varies moving from a $\frac{\lambda_{mfp}}{s_{inj}}$ of approximately 0.01 at $T_{i0} = 10eV$ up to 1.32 at $T_{i0} = 130eV$. In addition to this decrease in collisionality, there is an increase in plasma flow velocity. Because of this increase in plasma flow velocity, the peak impurity density predicted by the SFT continues to fall with increasing $T_{i0}$. In a thermal approximation (transport of the injected impurity flux happens at the rate of the thermal velocity of the particles), the peak impurity density flattens and crosses the trend of peak impurity density for the SFT at approximately 88 eV. The results of the GITR and DIVIMP simulations are compared to the peak impurity density produced by the SFT (blue) and the thermal transport approximation (red) in Figure 4.2. GITR and DIVIMP show under-prediction of peak impurity density at $T_{i0}$ of less than 40 eV. The results of the GITR simulation then converge to the thermal transport approximation in the collisionless regime ($T_{D0} > 75eV$). This demonstrates that the competition of forces (friction and thermal gradient) in GITR is accurate compared to the SFT and transitions nicely to capture kinetic effects with the 1/T collision frequency dependence where the SFT fails to capture this effect.

### 4.1.2 Region B - the impurity density decay region

Moving to region B - the impurity density decay region, cases C and D demonstrate the competition of the Lorentz force (case C) and the drag force (case D) with

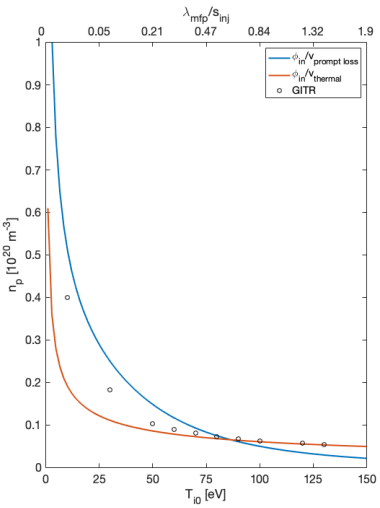


Figure 4.2: Peak impurity density near the target as a function of target ion temperature (and flow varying with $c_s$). GITR and SFT solution are shown.

parallel velocity diffusion. With the Lorentz force and the drag (friction) force directed toward the divertor target, and impurity particle velocity being dispersed by Coulomb collisions, a characteristic (exponential) decay of impurity density toward $s_v$ should be shown. Case C uses $T_{i0}$ set to 50 eV, temperature gradient set to zero, no flow velocity, and an electric field of -25 V/m. Plasma density is varied from case to case, using $10^{18}, 10^{19}$, and $10^{20} m^{-3}$. These simulations result in an exponential fall-off in the s direction all of equal rate, as shown in Figure 4.3. The GITR simulated decay density follows the slope as predicted by the SFT over many orders of magnitude. The difference in peak impurity density is expected, which is responsible for the shift in densities. The peak impurity density varies for each case because of the level of collisionality - the drag force increasing for the cases with higher density. This results in a confining effect near $s_{inj}$, which results in a larger accumulated density. By the same factor of density, the collisional frequency for parallel velocity diffusion also increases, so the balance of diffusion with friction and the Lorentz force is identical for each background plasma density.

Case D uses a set of 3 contrived values of $T_{i0}$ and n plasma density to give identical exponential fall-off of impurity density along s. With $T_0$ of 10 eV, 100 eV, 100 eV, density of $10^{19}, 10^{19}$, and $10^{18} m^{-3}$ and flow velocity of -112 m/s, -3.55e4 m/s, and -3.55e5 m/s, and zero thermal gradient. Using these values result in a common factor of $v_{th}^{-2} * v_B/\tau_s$ of unity and these values are summarized in Table 4.2. The impurity density for GITR compared to the analytic solution slope is shown in

Table 4.2: Contrived values used in case D to give a common decay factor in the impurity decay region.

| $v_{th}[m/s]$ | $v_B[m/s]$ | $\tau_s$ [s] | $\frac{v_{th}^{-2} v_B}{\tau_s}$ |
|---|---|---|---|
| 8.97E3 | -112.2 | 1.41E-6 | 1 |
| 2.84E4 | -3.55E4 | 4.46E-5 | 1 |
| 2.84E4 | -3.55E5 | 4.46E-5 | 1 |

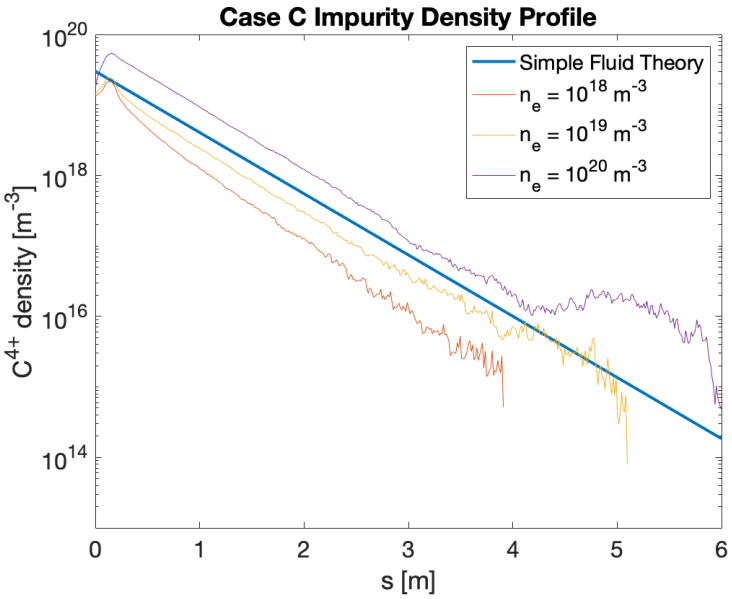


Figure 4.3: Decay of impurity density in the SOL with competition of electric field and parallel velocity diffusion for several cases.

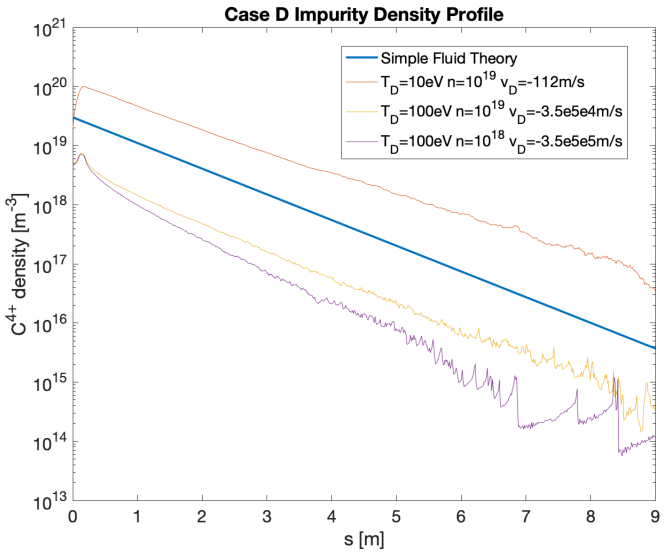


Figure 4.4: Decay of impurity density in the SOL with competition of drag force and parallel velocity diffusion.

Figure 4.4 and agrees with the SFT impurity decay for many orders of magnitude. Each of the simulated cases results in a varying peak impurity density near the target. This decreased peak impurity density will result in fewer computational particles diffusing in the positive s direction and therefore worse statistics for the decay region. As can be seen in Figure Figure 4.4, the orange line corresponding to $T_D = 10eV$, $n = 1 \times 10^{19}$, and $v_D = -112m/s$ has very little Monte Carlo noise, but begins to have some variation in decay rate near $s = 6m$. Moving to the yellow line with $T_D = 100eV$, $n = 1 \times 10^{19}$, and $v_D = -3.5 \times 10^4 m/s$ an increase in Monte Carlo noise can be seen with increased spikes at the lower decades. Finally, the Monte Carlo noise is greatest for the purple line corresponding to $T_D = 100eV$, $n = 1 \times 10^{10}$, and $v_D = -3.5 \times 10^5 m/s$.

### 4.1.3 Region C - the impurity build-up region

Finally, we examine region C - the divertor exit and impurity build-up region. Additional results from case B as well as cases E and F are shown for divertor leakage. The steady-state divertor leakage flux predicted by the SFT is represented by the impurity density at $s_v$ (reduced from $n_p$ at $s_{inj}$ in the decay region by competition of drag and thermal gradient forces) multiplied by the transport velocity caused by the ion thermal gradient force. This is because at $s > s_v$, the thermal gradient is the only remaining net force in the build-up region. In GITR simulations, this flux is found by taking the net number of particles that pass the $s_v$ in a simulation where all particles either strike the target or are trapped in the build-up region. Therefore, upon injection, particles diffuse in velocity, are dragged towards the target and forced toward $s_v$. For the fraction of particles that pass $s_v$, some diffuse in the negative s direction back towards the divertor target. Simulation of the highly collisional (mean free path of collisions $\approx 10cm$) case B for divertor leakage shows agreement with the inverse of square temperature decay as the impurity density fall-off terms for the friction force and ion temperature gradient share this dependence. Therefore higher temperatures result in greater divertor leakage as is shown accurately by both GITR and DIVIMP in Figure 4.5.

Case E uses a decrease in plasma density from case B to alter the collisional mean free path to $\lambda_{mfp} \approx 1m$. This results in a departure from the agreement with the SFT solution in which the leaked fraction of the impurity flux falls below the magnitude predicted by the SFT as shown in Figure 4.6. In this situation, the SFT over-predicts the leaked impurity flux because it is not accounting for kinetic effects. In this scenario, with the long mean free path of collisions, parallel and perpendicular velocities are not quickly altered compared to the time for particles to be transported. This results in a shifted velocity distribution of particles that leak from the divertor ($s > s_v$). This shift in the velocity distribution that results from the friction force manifests in a suppressed positive velocity of particles migrating into the impurity buildup region. Therefore, leaked particles are less likely to migrate/diffuse far into the impurity buildup region and more likely to diffuse back into the divertor region.

Case F represents a deep injection case ($s_{inj} = 5m, s_v = 10.85m$) which is more representative of a seeded impurity case. The plasma density is set to $10^{19} m^{-3}$ with constant flow velocity toward the target at $0.1c_s$. The temperature gradient is used according to the analytic form, and the target temperature is varied from 20 eV

to 50 eV. In this case, the SFT can be computed accounting for the temperature variation and approximated without using this variation. Temperature variation does, in fact, play a large role in the impurity migration because of the scale of $s_{inj}$ and $s_v$ in the problem. GITR results compared to the SFT solution are shown in Figure 4.7.

In addition to these benchmarks of impurity transport parallel to the magnetic field, a test of impurity velocity distribution can be performed. For a C4+ atom in a D+ plasma, an initial velocity distribution of a delta function (50 eV kinetic energy in the x-direction) is given to GITR perpendicular to the z-directed magnetic field. For this case, it is the forces of drag, heating, parallel, and perpendicular velocity distribution working together to form the correct velocity distribution. With a magnetic field magnitude of 0.1 T, plasma temperature of 50 eV, and a density of $10^{19}m^{-3}$, the $\tau_{90}$ time is 20 microseconds. This $\tau_{90}$ is the mean time for an ion with a directed momentum to lose that momentum due to perpendicular deflections. Results for the GITR parallel (z-directed) velocity distribution are shown in Figure 4.8, and agree with an analytic Maxwellian distribution.

## 4.2 Additional GITR Benchmarks

When simulating particles traversing curved field lines and in curvilinear coordinate systems it is necessary to check for artificial particle motions. Two such examples include particle drift due to curved field lines (e.g., what occurs in a forward Euler integration of circular motion), and an artificial pinch of density when particles are diffusing across magnetic field lines. These two benchmark tests are evaluated in the following sections.

In order to make evaluation of these two phenomena easier, and to simplify post-processing of GITR output, a magnetic field with circular features is useful.

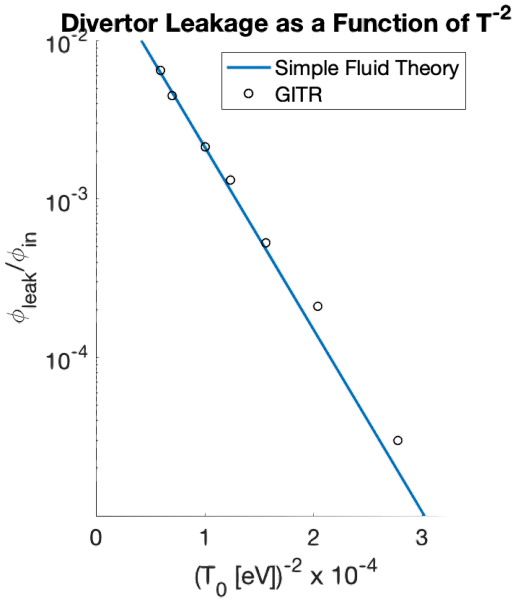


Figure 4.5: Divertor leakage fraction as computed by GITR agrees with the SFT solution for the case B collisional case. Higher temperatures are shown to lead to greater divertor leakage with a $T^{-2}$ dependence.

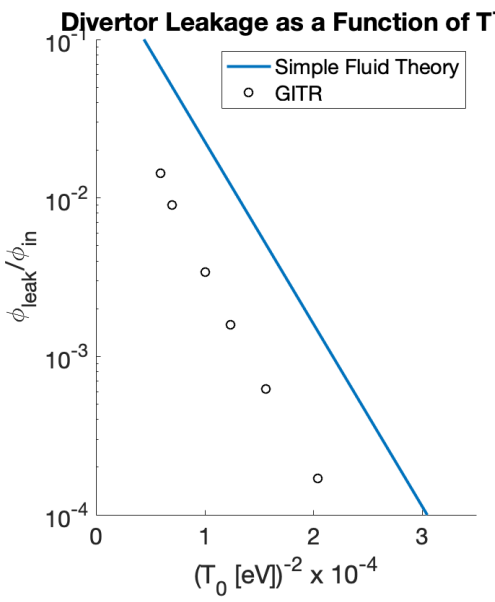


Figure 4.6: SFT divertor leakge in a collisionless case is shown to be over-predicted compared to the results of GITR.

Therefore, a divergence-free magnetic field of the form $\vec{B} = (C_1 B_x, C_2 B_y, C_3)$ is used with cartesian coordinates $B_x = y$, and $B_y = -x$. For cylindrical coordinates, $\vec{B} = (C_1 B_r, C_2, C_3 B_z)$ which takes the form $B_r = z$, and $B_z = -r$. For this case of poloidal curvature, a field of $\vec{B} = (z, 0.1, 1.6 - r)$ T is used such that the null is at (r,z) = (0,1.6) with field lines curving circularly around this point. For toroidal tests of curvature, a field of $\vec{B} = (0, 1, 0)$ T is used where the field is directed completely in the toroidal direction.

### 4.2.1 Cross-Field Diffusion With Curved field lines

In straight field lines, the cross-field diffusion of particles can be handled in a simple way - allowing particles to diffuse uniformly in the perpendicular direction. This leads to the uniform distribution of particles in space and equivalent particle densities across field lines. In curvilinear coordinates, this uniform diffusion perpendicular to the magnetic field leads to an artificially high density on the concave side of the magnetic field curve. This is because the same number of particles are diffusing into an area/volume which is smaller due to the curvature of space - leading to an artificially high density. An example of this uncorrected density profile is shown in Figure 4.9, and clearly shows the artificial pinch of density on the concave side of the magnetic field lines. In this case, 10,000 W10+ impurity particles are injected at r=1.25 m with a kinetic energy of 10 eV and with an azimuthal angle of 45 degrees. The particles then migrate and diffuse (only Lorentz force and cross-field diffusion) for 10,000 time steps with a timestep of 1E-6 s and a diffusion coefficient of 10 $m^2/s$. This is a high diffusion coefficient and a large time step to allow global diffusion in a short period of time. A high density peak is observed at the magnetic null of the solenoidal field, thus demonstrating the artificial density pinch.

4.10. A correction for this artificial pinch begins with a simple schematic of a representative shape - the conical frustum shown in Figure The radius $R_1$ represents

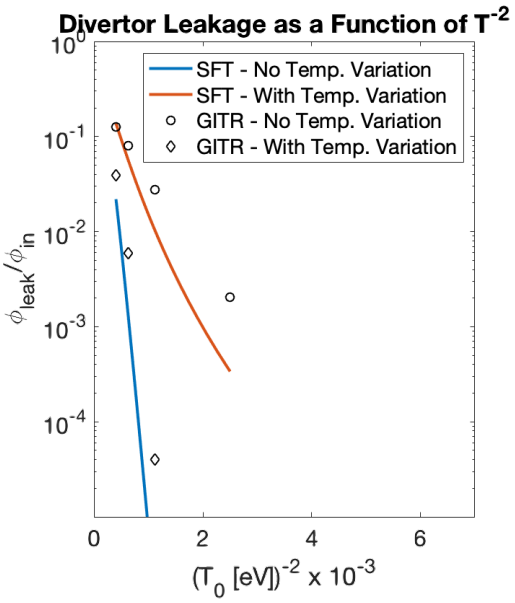


Figure 4.7: Deep injection divertor leakage with and without temperature variation (temperature gradient exists in both cases), which shows good agreement between GITR and SFT.

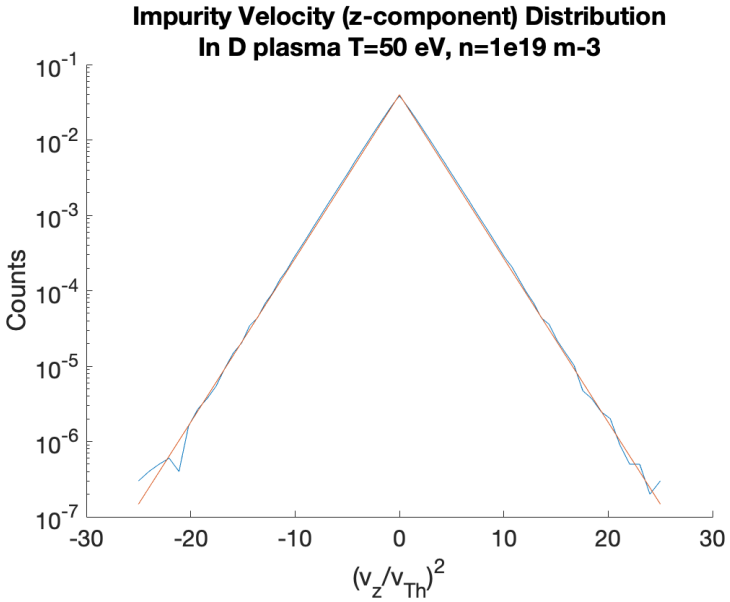


Figure 4.8: Parallel (z-directed) C4+ impurity velocity distribution compared to the analytic solution for T=50 eV.

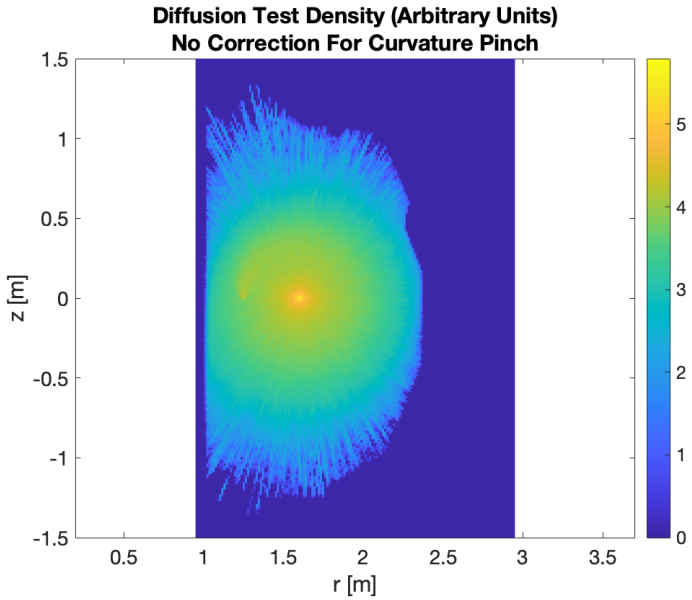


Figure 4.9: Density profile using the solenoidal field and an injected impurity source at r=1.25 m, with D=10 $m^2/s$, and allowed to diffuse for 0.01 s

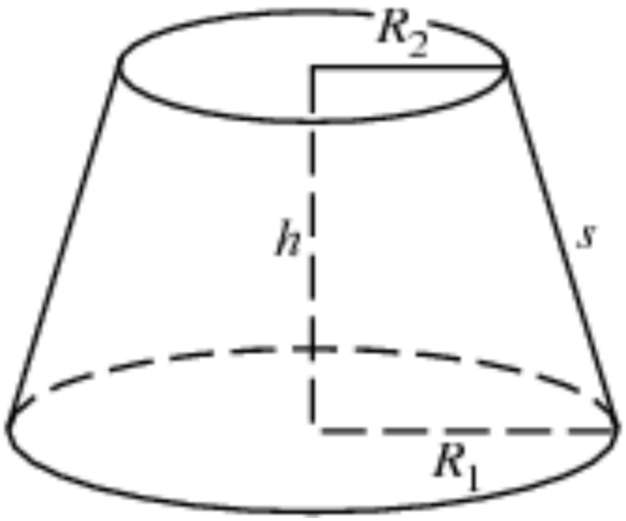


Figure 4.10: Conical frustum, as obtained from mathworld.wolfram.com, showing R1 as the beginning radius and s as the diffusion step length.

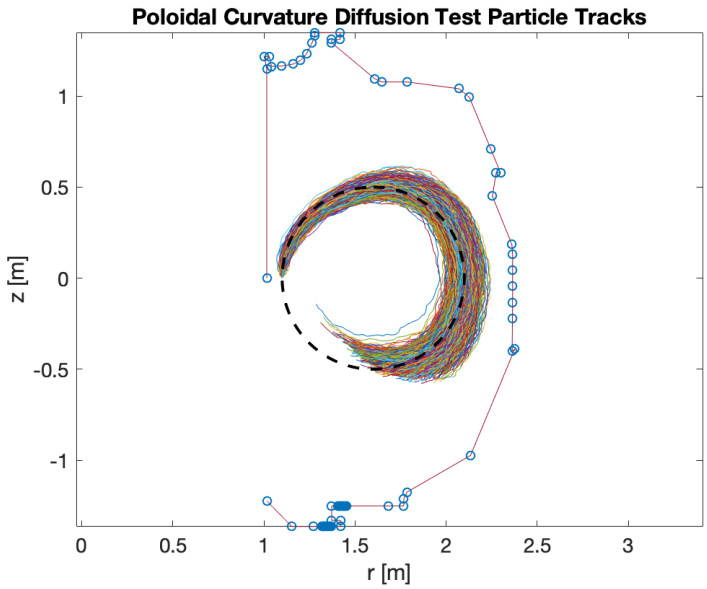


Figure 4.11: W10+ particles injected at r=1.5 m (shown by black dashed line) and diffusing perpendicular to the solenoidal field.

the radius of curvature of the local magnetic field on which the particle sits, and s is the diffusion step length. The angle between $R_1$ and $s$ will be referred to as $\theta$. For a particle sitting at $R_1$ with respect to some curvature of a magnetic field, the diffusion step s will be taken perpendicular to the field line. The probability of a particle diffusing in a particular direction should be proportional to the area of the ribbon swept out in the azimuthal direction spanned by the step length s. This area is equal to:

$$A = \pi(R_1 + R_2)s \tag{4.3}$$

$$R_2 = R_1 - s * cos(\theta) \tag{4.4}$$

$$A = \pi(2R_1 s - s^2 * cos(\theta)) \tag{4.5}$$

Therefore a cumulative distribution function for the proper angle for $\theta$ can be formulated:

$$CDF(\theta') = \frac{\int_{\theta=0}^{\theta=\theta'} A(\theta)d\theta}{\int_{\theta=0}^{\theta=\pi} A(\theta)d\theta} \tag{4.6}$$

where

$$\int_{\theta=0}^{\theta=\theta'} A(\theta)d\theta = \pi(2R_1 s\theta - s^2 * sin(\theta')) \tag{4.7}$$

Therefore

$$CDF(\theta') = \frac{(2R_1\theta' - s * sin(\theta'))}{2\pi R_1} \tag{4.8}$$

Using a random number generator and the analytic forms of this equation and its derivative, a Newton method root finder can be used to efficiently solve for the angle $\theta$. This has been implemented in GITR and has been tested on problems to examine the relative shift of the distribution function. This should effectively result in an drift in the direction of the convex shape of the magnetic field.

For a test in the poloidal direction, the solenoidal field centered at r=1.6 m and z=0 m described previously has been used, and the injection point for impurities is

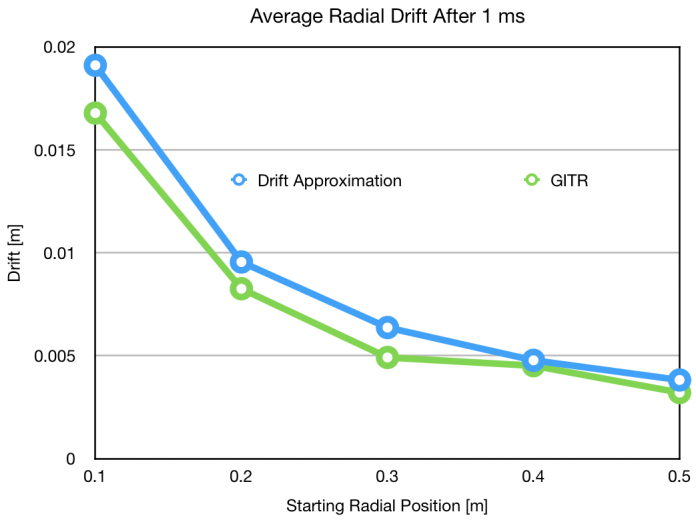


Figure 4.12: Comparison of the GITR radial position drift for the poloidal curvature (green) compared to the analytic drift approximation (blue).

varied from r=1.1 m to 1.5 m. Example particle tracks for W10+ impurities injected at r=1.5 are shown in Figure 4.11.

As a test of the algorithm, the mean radial (in this case minor radius) position can be tested against a drift approximation using the analytic form of the radial diffusion angle described previously. Effectively reducing the diffusion approximation to 1 dimension, the number of time steps needed for the distribution to drift 1 diffusion step length is

$$nSteps = \frac{0.5}{(\frac{CDF(\pi)-CDF(\pi/2)}{CDF(\pi)}) - 0.5} \tag{4.9}$$

Similarly a test in the toroidal direction using the purely toroidal field and varying major radius of injected particles from 0.25 m to 3 m has been simulated. The results for the poloidal and toroidal tests are shown in Figures 4.12 and 4.13. The reduction in drift value with increasing radius indicates that the field lines are more straight or less curved at larger radii. Good agreement is shown between the drift approximation and the GITR implementation.

A final test to evaluate the global density of impurities is performed to ensure that the artifacts introduced by the diffusion pinch has been alleviated. The case described with the density profile as Figure 4.9 has been repeated and Figure 4.14 plots the poloidal density profile. Direct comparison of radial profiles the corrected and uncorrected diffusion density profiles is shown in Figure 4.15. In this figure it can be seen that the sharply peaked density profile of the uncorrected diffusion is effectively flattened with the new algorithm.

### 4.2.2 Lorentz Force Integration in Curved field lines

Evaluation of the Boris integration scheme compared to a Runge Kutta 4 scheme has been evaluated in order to evaluate any artificial particle drifts. Once again using the solenoidal form described earlier with a constant magnetic field component in the toroidal direction, particle tracks in this cylindrically symmetric domain are performed. With varying time step (1E-6 s, 1E-7 s, and 1E-8 s) the Boris and

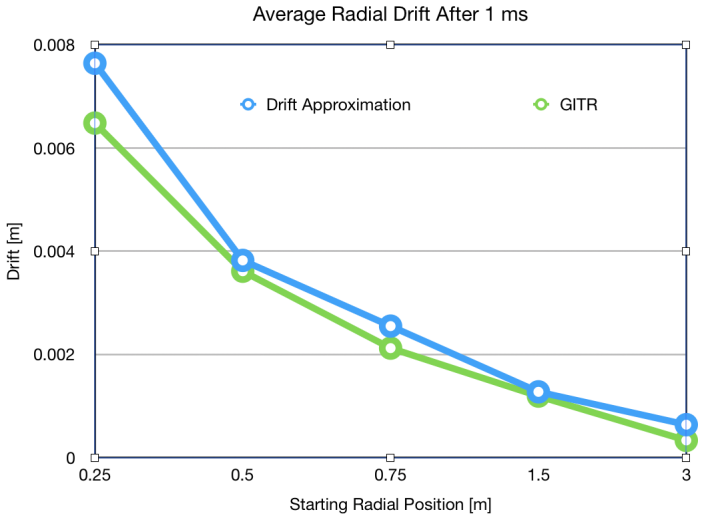


Figure 4.13: Comparison of the GITR radial position drift (green) for the toroidal curvature compared to the analytic drift approximation (blue).

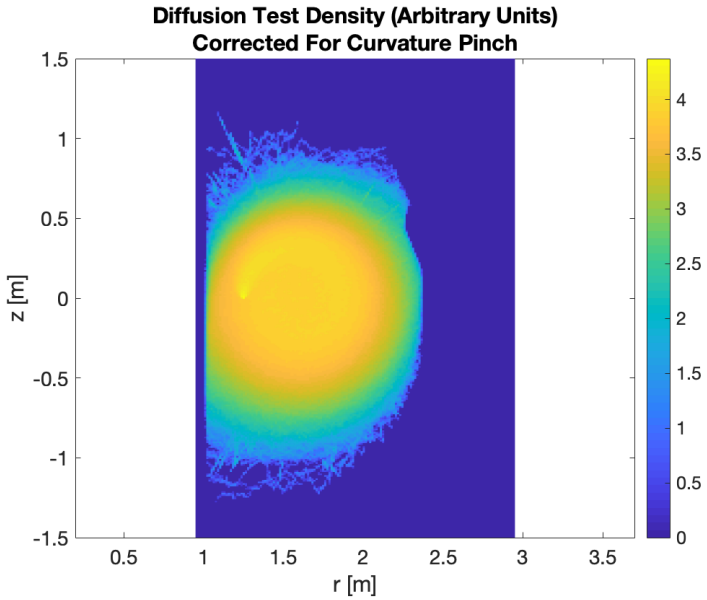


Figure 4.14: Impurity density using the updated diffusion algorithm and running an identical case to Figure 4.9

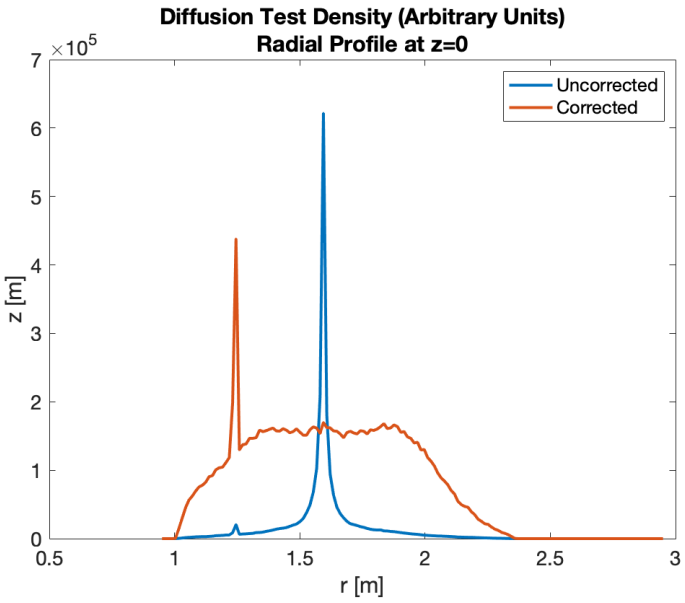


Figure 4.15: Density profile for the corrected and uncorrected diffusion. The corrected algorithm shows a flat density profile across the core decreasing towards the absorbing boundaries.

RK4 integrators simulate a single W10+ impurity particle with 10 eV launched at a azimuthal angle of 45 and a polar angle of 45 degrees and simulated for 0.1 s. One notable feature of this comparison is the inward drift of the particle tracks integrated with the RK4 as shown in Figure 4.16. Runge-Kutta methods are designed to be consistent with the system of differential equations to higher orders such as 4. Yet they are not designed to preserve the underlying Hamiltonian structure, in particular they will cause the orbits of particles to experience energy drift and therefore slowly spiral inward or outward over time. For simulations over longer time scales, this should be avoided. The Boris integration scheme visually shows a much more accurate (non-drifting) integration as is shown in Figure 4.17. The Boris integrator shows some small variation in centered gyro-orbit with varying time-step, but shows no net outward drift or energy drift. As a more direct measure of accuracy, the particle minor radius over time is directly plotted in Figure 4.18 showing a flat line for each of the Boris integrated tracks, and an inward drift for each of the RK4 track integrations, though it tends towards being flat with smaller time step. The reason for the Runge Kutta inward drift is a result of a numerical drift in total velocity. Particle velocity over time is shown in Figure 4.19 showing the change in total velocity for the RK4 integrator, especially for large time steps. With decreasing time step, the RK4 solution converges to match the Boris values which conserve particle velocity.

## 4.3 Summary

In summary, the GITR code has been rigorously tested in simple operator tests as well as integrated tests against analytic solutions and DIVIMP. The fundamental characteristics of Monte Carlo ionization and recombination have been shown to be carried out accurately. The statistics of conserving impurity eroded and deposited

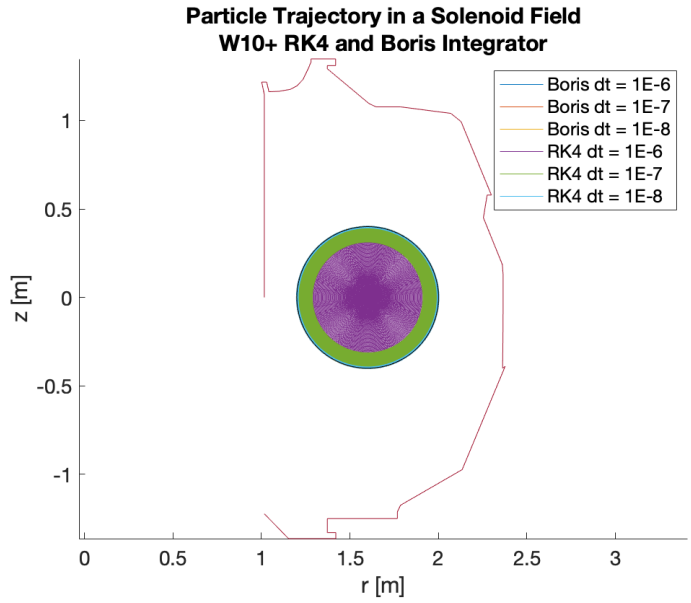


Figure 4.16: Particle tracks simulated by the Boris and RK4 integrators using the solenoidal magnetic field.

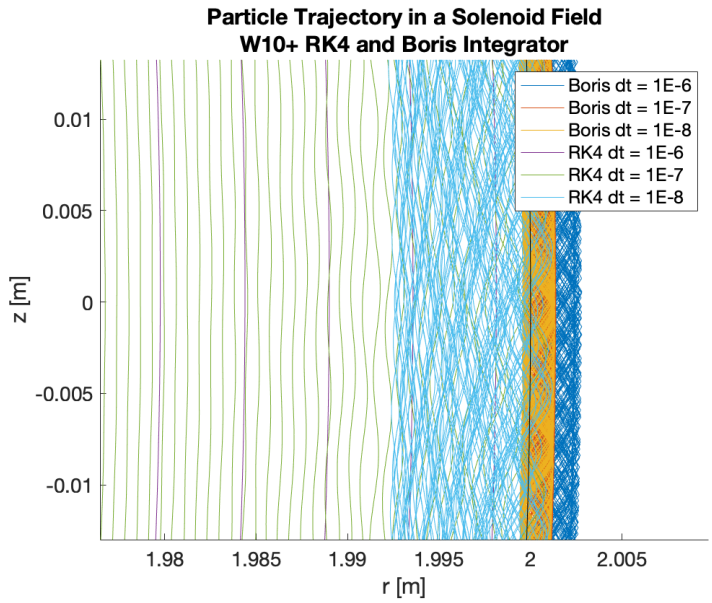


Figure 4.17: Paticle tracks for various integrators and time steps at the outer mid-plane.

mass through example has been shown. The Boris integrator has been demonstrated to be reliable integrator in curved field geometries and conserving velocity of particles. Additionally, artificial pinch of density in curved magnetic fields has been shown to be accounted for to give uniform density profiles.

Perhaps most importantly, the validity of the Coulomb collision operators have been demonstrated to produce proper velocity distributions. This is essential in representing populations of particles which will produce the verified behavior of parallel transport of impurities in the scrape-off layer.

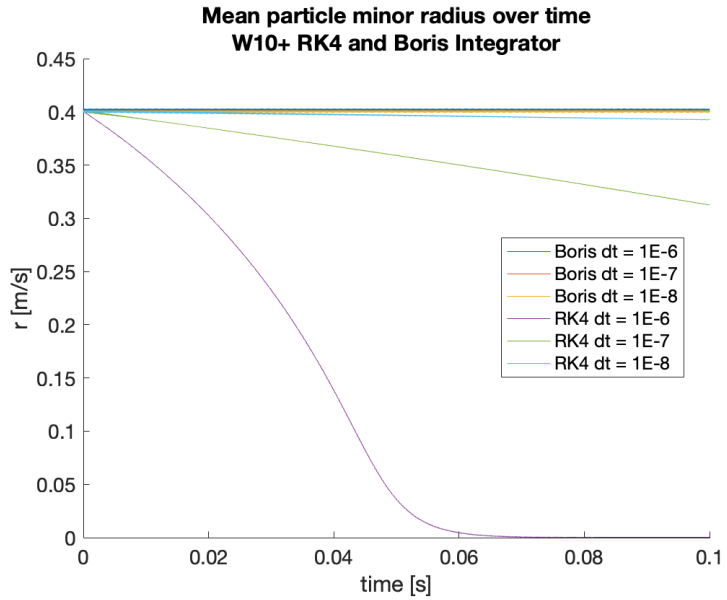


Figure 4.18: Minor radius as a function of time for the various integration schemes and time steps. Boris shows no outward or velocity drift compared to that of the RK4.

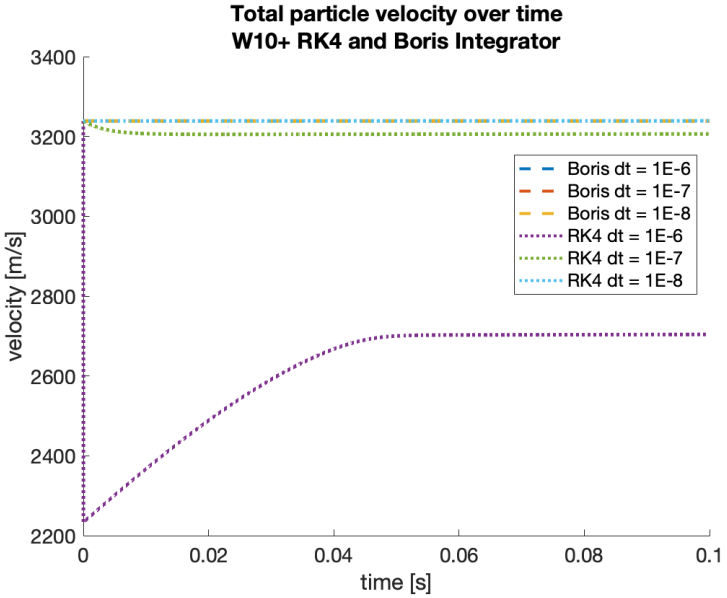


Figure 4.19: Particle velocity over time is conserved by the Boris integration scheme. For large time step of the RK4, velocity is badly distorted.

# Chapter 5

# Benchmarking GITR to Linear Plasma Device with UQ

## 5.1 PISCES-A Experiments

With the collaboration of the University of California, San Diego and the PISCES team, dedicated experiments to expose W to varying plasma conditions have been performed. These experiments are used in order to benchmark and evaluate the validity of the models used for impurity transport. After benchmarking of this model, the results of GITR used for impurity fluxes can be extrapolated to further help benchmark models for gas retention, recycling, and nucleation beneath the surface.

## 5.2 Method

### 5.2.1 Experimental set-up

#### General description of PISCES experiments

Dedicated linear machine experiments have been performed in PISCES-A [47] to benchmark the integrated plasma surface interaction model. In this series of PISCES experiments, there is an array of experimental observables which vary from experiment to experiment. In all of the exposures, experimental observables aim to characterize the W surface erosion, eroded impurity transport and re-deposition, and evolution of the sub-surface composition caused by the exposure to pure He, mixed He-D, and pure D plasmas.

Common to all of the plasma-exposed W experiments are the perpendicular and centered orientation of the plasma column with respect to a circular W base plate/target which is biased to -250 V and held between 400 and 850 degrees C to avoid the tungsten fuzz formation regime. The linear magnetic field strength in the target region is 800 G, perpendicular to the target to minimize any sheath effects that are hypothesized at more oblique angles [43]. The background neutral gas pressure is held to 2.5 mTorr.

The variations between the experiments include changing the W target radius and thickness, plasma species mixtures, background plasma temperature, density, and flux to the target, exposure times, and experimental observations available for

comparison to modeling. An overview of the plasma conditions and experimental setup is provided in Table 5.1 and described in greater detail in the following sections. The 2017 experiments (20170313 and 20170314) are designed for experimental benchmarking with the trace impurity model GITR. The 2018 experiments (20180205, 20180213, and 20180214) are designed to implant plasma ions into the W surface. After the exposures the W target samples probed for gas composition as a function of depth and compared to the surface evolution model.

Table 5.1: Overview of various W exposed plasma experiments in PISCES-A.

| Experiment name/date | 20170313 | 20170314 | 20180205 | 20180213 | 20180214 |
|---|---|---|---|---|---|
| W target radius [cm] | 4.875 | 4.875 | 1.27 | 1.27 | 1.27 |
| Plasma species | He | He | He | 10%He 90%$D$ | D |
| Exposure time [s] | 10,000 | 5,000 | 100 | 1,000 | 3,600 |
| Peak electron temperature [eV] | 6 | 9 | 7 | 10 | 7 |
| Peak electron density [$m^{-3}$] | $0.8 \times 10^{18}$ | $5 \times 10^{18}$ | $6.4 \times 10^{18}$ | $1.1 \times 10^{18}$ | $0.9 \times 10^{18}$ |
| Peak ion flux [$m^{-2}s^{-1}$] | $0.5 \times 10^{22}$ | $4 \times 10^{22}$ | $5.4 \times 10^{22}$ | $1.5 \times 10^{22}$ | $1.2 \times 10^{22}$ |
| Surface temperature [C] | 900 | 900 | 820 | 808 | 500 |
| Experimental observables | Target mass loss, titania tower mass gain, axial profile of W I spectroscopy | | Surface analysis with LIBS and LAMS | | |

### Experiments to study impurity migration

The first pair of experiments were performed with a target orientation and experimental diagnostics set-up to measure net erosion, impurity ionization, and eroded impurity migration. These experiments, labeled 20170313 and 20170314 in Table 5.1, aim at comparison with the GITR impurity (eroded tungsten) transport model [48]. The plasmas for 20170313 and 20170314 are composed purely of He and strike a W base plate which has a radius of 48.75mm, as shown in Figure 5.1. These experiments exposed the W plate to He plasma for 10,000 s and 5,000 s, respectively under steady-state, using different input power to produce different plasma conditions. The 10,000 s exposure (20170313) used a lower peak electron temperature and density producing a lower relative ion flux to the target ($\Gamma = 0.5 \times 10^{18} cm^{-2}s^{-1}$), while the 5,000 s exposure (20170314) reached higher peak electron temperature and densities producing a higher relative He flux ($\Gamma = 4 \times 10^{18} cm^{-2}s^{-1}$). A reciprocat-

Figure 5.1: PISCES Ti-Tower target and collector tower setup for experiments 20170313 and 20170314.

ing Langmuir probe was inserted 30 cm axially from the target plate to obtain the plasma profile measurements plotted in Figure 5.2 (20170313) and 5.3 (20170314), wher $T_e$ is electron temperature, $n_e$ is electron density, and $\Gamma_i$ is ion flux. Probe measurements were made at this distance to avoid plasma perturbations and sputtering of other materials near the W target.

A titania ($TiO_2$) bead tower secured in one of the target mounting holes sits at a radius of 44.6 mm, outside the plasma column to avoid W re-erosion by the background plasma, and is used as a collection probe for W sputtered from the base plate and subsequently transported to the tower. The first bead on the tower is a 12.75 mm long ceramic break, acting to isolate the tower beads from the target bias voltage. Thirteen titania beads sit on top of this ceramic bead, and each $TiO_2$ bead is 10 mm tall and has an outer radius of 5 mm. Thus, the experiments labeled as 20170313 and 20170314 are referred to as "Ti-tower experiments".

During the plasma exposure, axial profiles of W I (429.4 nm) line emission near the W base plate (0 to 5 cm axially) were measured. The axial array of W I emission spectroscopy sight lines is an indication of the neutral W concentrations in the plasma and the rate of ionization near the target plate. After the plasma exposure, the mass loss from the W base plate and mass gain of each of the 13 Ti beads were measured. The mass difference of the target plate is an indication of the erosion source strength as well as re-deposition fraction, thus the net erosion. The mass difference of the titania tower collector beads provides an axial measurement of longer range material migration and deposition.

### Experiments to study surface evolution

The second set of PISCES exposures was performed to examine the evolution of the W sub-surface during exposure to pure He, mixed D-He, and pure D plasmas.

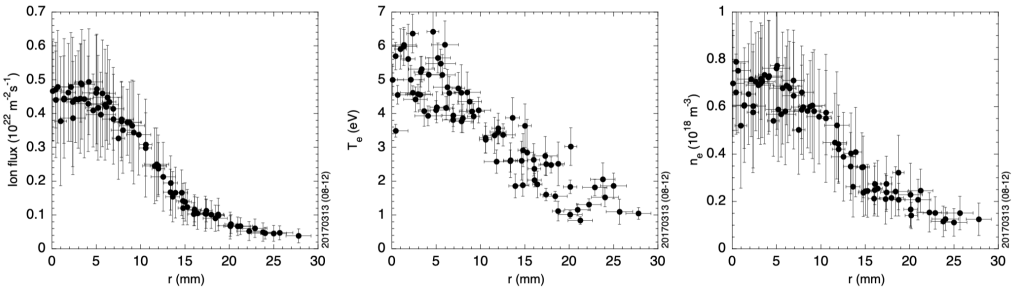


Figure 5.2: Langmuir probe measurements for ion flux, electron temperature, and electron density for 20170313.

These exposures share similarities to the experiments 20170313 and 20170314 in perpendicular orientation to magnetic field, -250 Volt bias voltage, and approximate plasma parameters ($T_e$, $n_e$, and $\Gamma_i$). The target radius was smaller (1 inch diameter) and the goal of experimental observables was changed to examine the surface (i.e. no Ti collector tower or mass difference measurements). Thus, the individual plasma exposures labeled 20180205, 20180213, and 20180214 make up this set of experiments and are referred to as "1 in W disc" exposures. In Table 5.1 the three exposures, 20180205 (He only), 20180213 (He and D mixed plasma), and 20180214 (pure D plasma) are compared to the Ti-tower experimental set-ups. Measurements taken during the 1 inch W disc experiments, such as surface temperature and plasma gas composition, focus on ensuring accurate input parameters for the modeling of the sub-surface evolution for comparison to ex-situ experimental investigation of the W targets. Since the W sample radius is small compared to the width of the plasma column, plasma characteristics (density, temperature, etc.) are only measured by Langmuir probe in the center on the plasma beam. The plasma content (D and He fraction) is determined by D-$\gamma$ (434 nm) and He I 447 nm emission lines. Due to the more efficient energy transfer from He ions to the W substrate (compared to that from D ions), the surface temperature cannot be easily controlled, nor does it equilibrate in the shorter exposures of W discs to pure He plasma. The temperature at the end of the He-only 1-inch W disc exposure (20180205) experiment is 820C. In contrast, the surface temperature of the W 1-inch disc exposed to mixed D-He plasma (20180213) is controlled and fluctuates around 500C during the 1000s exposure.

### 5.2.2 Modeling method

In order to gain physics insight and predictive capability for the plasma-material interaction in fusion-relevant scenarios, an integrated model for PMI has been created. The goal of this integrated simulation capability is to capture relevant physics phenomena from the edge plasma to the material sub-surface using high fidelity component models connected in a loosely coupled fashion (via file transfer). In a realistic fusion PMI scenario, material erosion and resulting migration and deposition occurs as a result of being exposed to plasma flux. Ion implantation and reflection occur at the surface which results in retention, gas bubble formation and creation of interstitials. Diffusion of retained gas, migration of clusters, loop punching, and

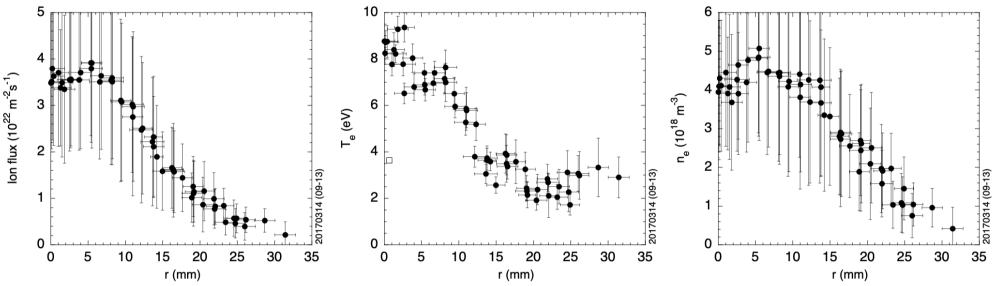


Figure 5.3: Langmuir probe measurements for ion flux, electron temperature, and electron density for 20170314.

bubble rupture results in modification to the material surface and outgassing of neutrals into the plasma. An example of an integrated model for simulation of PMI is shown in Figure 5.4.

The integrated model for PMI used in this research is a point on the development path towards the complete PMI model. As can be seen in Figure 5.4, the flow chart for the present integrated model for PISCES plasma exposed tungsten (right) is simplified in some physics models as well as the directional flow and feedback of physics compared to that of the full integration of the edge plasma-divertor PMI. Beginning from the most outer loop and working our way in, a simulation of the edge plasma (performed with SOLPS [13]) passing plasma profiles and target values is replaced by Langmuir probe measurements ($T_e$, $n_e$, $\Gamma_i$) and simple models for plasma flow velocity and plasma temperature gradient [9]. For the present case, the plasma profiles are assumed to be time independent (steady state) and remain constant throughout the entire simulated time of impurity migration and surface evolution. A simulation of the characteristics of the magnetic pre-sheath and Debye sheath (performed with hPIC [40]) provides electric fields near the material surface and ion energy-angle distributions which affect sputtering and reflection rates and ion implantation profiles. For the present case of the PISCES simulation, the sheath characteristics are assumed to be that of a Langmuir sheath [44] because the magnitude of the voltage applied to the W target (-250 Volts) is significantly greater than the plasma temperature. Therefore, it is assumed that impacting plasma species (D,He) are mono-energetic and at normal incidence. The impurity transport simulations (GITR [48]) for the first iteration of a fully integrated tokamak simulation and the present PISCES simulations are run in identical fashion. Subsequent iterations of the GITR simulation in the fully integrated model would use updated background plasma profiles accounting for outgassing and changes in sputtering yield due to changes in surface morphology. GITR provides net erosion values along with energy-angle distributions of impurities to the surface which can contribute to Frenkel pair formation. Finally, modeling the surface evolution (coupled F-TRIDYN [38] and Xolotl [49]), while the particle fluxes will be continually updated for the fully integrated model, it is assumed they are steady state for the PISCES simulations. F-TRIDYN provides sputtering, reflection, and implantation profiles of ions to the surface. Xolotl then evolves the sub-surface concentrations of gas and metal interstitials to evolve the surface and bulk materials.

For a time dependent coupled simulation, variable dependence must be prop-

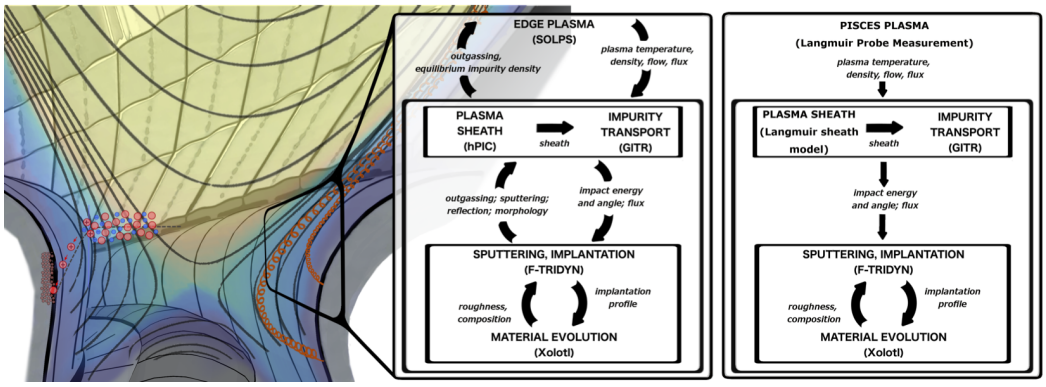


Figure 5.4: Flow chart demonstrating the connection of various physics processes (and models) for a proposed tokamak integrated model (left) and the present PISCES integrated model (right).

erly handled by mathematical algorithms to avoid numerical error in the integration scheme. For the present case, approximations of constant variable values and arguments of time scale separation are used to justify the integration scheme. Given that the surface evolves via ion implantation on longer time scales (O(s)) than impurity migration (O(ms)) and plasma fluctuations (O($\mu$s)), steady-state plasma parameters are used as input to the impurity transport simulation as well as the surface evolution simulation. Additionally, impurity transport simulation results are assumed constant in time as input to the surface evolution. Changes in surface characteristics (roughness, morphology) may reach characteristic length scales of impurity migration (O(mm)) depending on the exposure time, thus requiring an update of the transport calculation, however, in the present experimental comparison and integrated modeling demonstration those variations are assumed to be negligible. Therefore, the only sub-system of our model with time-dependent input is the description of a substrate exposed to continuous ion irradiation. The continuum cluster dynamics code (Xolotl) simulates the time-evolution of implanted species, the damaged substrate, and surface evolution using a BCA model (F-TRIDYN) with a functional dependence on implantation profiles in a Picard iteration. Atomistic methods, such as the binary collision approximation provide the profiles of ion implantation and damage to the substrate (sputtering yields, primary knock-on atom rates, etc.) based on a substrate composition. The BCA model (F-TRIDYN) includes changes in substrate composition and surface morphology, which impact the interaction of energetic ions with the substrate. Thus, ion implantation and substrate damage data input to the cluster dynamics code is updated to ensure a complete and correct description of the (plasma exposed substrate) system. In summary, taking advantage of time-scale separation (in steady-state conditions), plasma and material simulations are executed in a simplified physics simulation to capture W surface evolution in the PISCES experimental setup. Information is exchanged through a loosely coupled file-based system using services provided by the integrated plasma simulator (IPS [50]).

## 5.3 The integrated model of PISCES experiments

The described PISCES experiments are modeled by the integrated combination of the impurity transport code GITR, the binary collision approximation code F-TRIDYN and the continuum based cluster dynamics code Xolotl. The complete model contains two stand-alone components: an integrated model of F-TRIDYN and GITR, which focuses on simulating the erosion and migration of impurities sputtered from the surface; and the coupled system of F-TRIDYN and Xolotl, which follows the dynamics of surface and sub-surface evolution.

First, F-TRIDYN is used to generate a reduced model (in the phase-space of impact energy, angle and surface roughness) for W sputtering yields by D, He, and W, which are used in pre-processing and execution of GITR. A smooth surface (no roughness) is simulated and $10^5$ computational ion impacts are used for each combination of projectile species, energy and angle. Projectile impact angles vary from 0 to 89.9, linearly spaced into 10 intervals. The impact energies range from 1 to $10^3$ eV, with 50 values logarithmically spaced ($10^{i*dLogE}$) where $i$ is an integer from 0 to 49 and $dLogE = 3/(50-1)$. This allows for small spacing at low energies (100s of eV) where the yields change significantly, and larger spacing at higher energies, where the yields vary less. This also allows GITR to have a fast way of interpolation using the even spacing (log-linear) of the logarithmic values. Confidence in F-TRIDYN results can be increased by increasing the number of computational ions impacting on the fractal surface. Calculation of near-threshold sputtering yields require more computational ions because the total yield is orders of magnitude lower than at incident energies well above the sputtering threshold. O($10^5$) computational ions will provide high confidence and smooth sputtering yield curves for ion-target systems. Material parameters for F-TRIDYN are taken from literature references [51, 52]. Binary collision models are particularly sensitive to values for the surface binding energy (BE) and displacement energy, so choices for these values must be as accurate as possible. For instance, setting BE to zero, as done in the present simulations, will result in the upper boundary for sputtering yields, and thus, in the most conservative (or "worst case scenario") estimates.

Next, using the reduced model calculated by F-TRIDYN, GITR simulates the W impurity transport. The GITR simulations consist of $10^5$ computational particles, which are followed for $10^5$ time steps, where each time step is of $10^{-8}$ seconds.

In the second sub-model F-TRIDYN is again used to calculate sputtering yields and implantation profiles for D, He and W flux to the surface. In these simulations, it is assumed the impact energies are 250 eV and normal incidence (0 degrees) for all plasma gas species (He and D). The description of the W ion flux is provided by GITR for the position at the center of the 1 inch target. This description includes a 2-D histogram describing the W ion energy-angle impact distribution where the weight of each angle (0 to 90 degrees, spacing of 1 degree) and energy (0 to 1,000 eV, spacing of 10 eV) is given. Again, the surface is assumed smooth (no roughness) and a sampling of $10^5$ computational ion impacts is used for each combination of projectile species, energy and angle in F-TRIDYN.

Finally, Xolotl is used to calculate the evolution of implanted species and surface morphology. The ion fluxes (D, He, W) at the center of the 1 inch W target is used for scaling implantation profiles and sputtering yields (calculated by F-TRIDYN in the second sub-component) to the correct source magnitude. A wide range of reac-

tions that may take place between the network species (clusters, vacancies, etc), such as reaction, advection, modified trap-mutation, diffusion, moving surface, attenuation and bursting are included. The surface temperature is set to that measured in experiments: 820 degrees C for He-only (20180205), 808 degrees C for the mixed 90%D-10%He plasma (20180213), and 500 degrees C for D-only (20180214). The substrate modeled in Xolotl is 5 $\mu m$ 1-D parallel to the surface normal with a finer mesh near the surface. For the 10 nm closest to the surface, He bubble bursting occurs and the probability is proportional to (1-L/d), where d is the distance between the center of the bubble and the surface and L is the ligament thickness (distance from the outside of the bubble to the surface) dampened exponentially with a characteristic length of 20nm. The top and bottom boundaries of the simulation are free surfaces (i.e., it's a surface He and D can escape from). An initial vacancy concentration is set to $10^{18}$ vacancies/$nm^3$.

This dissertation focuses on impurity transport, and thus, results for the execution of F-TRIDYN in generating input for Xolotl, and Xolotl results will not be shown here.

## 5.4 Results

### 5.4.1 Impurity transport

#### Modeling of Ti-tower experiments

In order to account for W impurities eroded by the background plasma (He, D) as well as W self-sputtering, GITR requires the formulation of 2 separate surface models. In this loosely coupled framework, GITR utilizes output from F-TRIDYN simulations of background plasma species (D,He) during a pre-processing step, and W self-interaction during GITR execution. For the background plasma eroded W it is assumed that all He is singly charged and reaching the tungsten target at 250 eV kinetic energy at normal incidence. F-TRIDYN simulations predict an erosion yield of $4.00 \times 10^{-3}$ with a sputtered atom energy distribution similar to a Thomson distribution with a peak at 3 eV and a max of 10 eV. The sputtered atom angular distribution resembles that of a cosine ($cos(2\phi - \frac{\pi}{2})$ on $\phi = [0, \frac{\pi}{2}]$, peaking near 45 degrees in the azimuthal direction (with respect to the surface normal) and uniform in the polar direction. A fit to the radial ion flux profile (assumed axisymmetric) from Figures 5.2 and 5.3 is used for the spatial erosion profile. These values yield a total He eroded rate of $3.10 \times 10^{18}$ W/s for the lower flux case 20170313 and $3.54 \times 10^{19}$ W/s for the higher flux case 20170314. The ion flux profile along with the sputtered energy and angle distributions are used in a pre-processing step to formulate the initial conditions for eroded tungsten in the GITR simulation. The second surface model from F-TRIDYN describes the characteristics of W ions impacting a W surface and is used during the GITR simulation. Many instances of F-TRIDYN are executed to create a 2D array of sputtering yields and reflection coefficients (and corresponding energy-angle distributions). This gives the probability as a function of incoming W ion energy and angle that reflection or sputtering of additional material will occur. For the present simulations a grid of 10 angles (0 to 90 degrees, 0 being normal incidence) and 50 energies (logarithmically spaced 0 to 1000 eV) were used as a look-up table for interpolation as GITR's surface model.

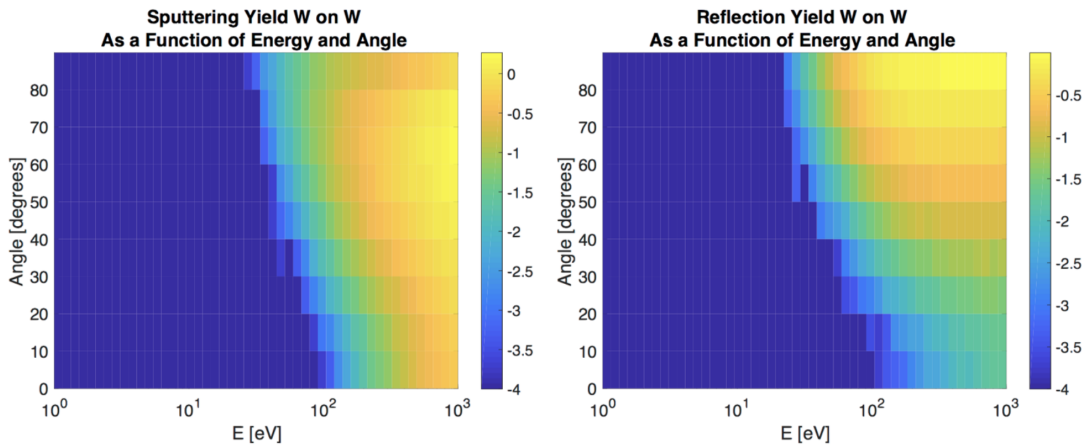


Figure 5.5: Sputtering yield (left) and reflection coefficient (right) for W as projectile and target.

The data produced by F-TRIDYN is displayed in Figures 5.5 and shows increasing sputtering yield and reflection coefficients with both incoming energy and angle.

Additional data from F-TRIDYN simulations used in GITR includes the outcoming (reflected or sputtered) energy and angle distribution of a W atom as a function of incoming energy and angle. Therefore the surface model in GITR makes a correlation of the incoming ion kinetics to the outcoming sputtered or reflected energy-angle distribution. As an example, the sputtered energy and angle distributions as sputtered by a 244 eV W ion are shown in Figure 5.6.

The energy distribution plot in Figure 5.6 (left) shows an increase in average sputtered particle energy with increased impact angle (further from normal incidence) with the peak in sputtered energy shifting from 4eV at 0 degrees to 10eV at 89.9 degrees. Thus more glancing particle impacts will sputter additional material that will have a longer mean free path of ionization (by greater kinetic energy and therefore velocity). The angular distribution of sputtered W atoms sputtered by a 244eV W atom (Figure 5.6, right) shows increased average sputtered atom angle with increasing impact angle, however all of the peak angles for this impact energy are between 55 and 65 degrees. Such angular distributions exist for all of the energies and angles which the sputtering yield and reflection coefficients are calculated by F-TRIDYN, and GITR uses a linear interpolation scheme in several dimensions along with Monte Carlo methods to determine the reflected/sputtered particle energy and angle.

Additional input to the GITR simulations includes a constant magnetic field of 0.08 Tesla parallel to the PISCES machine axis pointing towards the W target. The GITR 3D surface geometry for the Ti-tower experiments is made up of 37,497 boundary elements (triangles) with 1,762 W surfaces. The 3D surface mesh for the 1-inch W disc experiments is made up of 35,000 boundary elements of which 40 are W surfaces. For the Ti-tower experiments, input plasma profiles for $T_e$ and $n_e$ are taken from degree 4 polynomial fits constrained to go to zero outside the plasma column. Ion densities and temperatures are assumed to be equal to electron profiles. For the 1-inch W disc experiments, peak values for $T_e$ and $n_e$ are measured and similar functional forms to the Ti-tower experiments are used to extrapolate profiles.

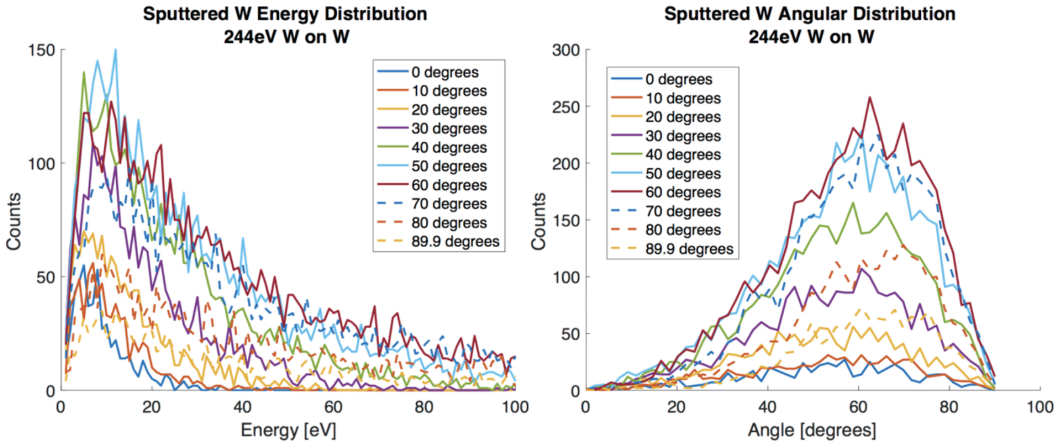


Figure 5.6: Sputtered W atom (via 244 eV W) energy and angle distributions for various impact angles.

Experimental observables related to W impurity transport (mass loss from the W base plate, mass gain of each of the 13 $TiO_2$ beads and axial profiles of W I (429.4 nm) are compared to GITR calculations. As a preliminary uncertainty analysis, a set of 20 simulations were run to account for uncertainties in the model input. An overview of the various combinations of input parameters is shown in Figure 5.7. The plasma temperature and density are varied by +/-20 %, and 4 angular distributions of sputtered particles are tested: an over-cosine ($cos^2$), a cosine ("cos"), and two under-cosines, a "butterfly"-like shape and an exaggerated butterfly ("butter 2").

GITR-simulated results of the Ti-tower experiments for net erosion of the W target, mass gain of the $TiO_2$ beads, and sythetic diagnostic for W I emission are presented here. For the low flux He exposure (20130313), Figures 5.8 and 5.9 show an example result of a single simulation case (blue), the experimentally measured value (black), and a green shaded region which spans the domain of all simulated cases summarized in Figure 5.7. The experimentally measured mass loss of the W base plate for experiment 20170313 is 18.83 mg whereas GITR simulations estimated this value to be between 14.5 mg and 29.5 mg for these input parameter combinations. The simulated fraction of eroded material to return to the W target plate ranged from 32% to 67%. For the experiment 20170313 the simulated mass loss compares well to the experimental measurement of mass loss, falling within the uncertainty caused by input parameters. The mass gain of the titania tower beads also shows qualitative and quantitative agreement between experiments and the model shown in Figure 5.8. There is a slight over-prediction of the mass gain of the beads far from the erosion source (beads 10-13). The variance in the "bead 1" mass gain comes predominantly from the variation in sputtered W angular distribution because the mean free path of ionization is long ($\approx cm$). The synthetic diagnostic of W I 429.4nm line emission decreases for each chord moving away from the target plate at a similar fall-off rate both in experiments and in GITR shown in Figure 5.9. Although the trend has a slightly different shape, dipping down in the model but rolling over in experimental measurements, the variations in the simulations from this initial sensitivity analysis are on the order of the experimental error bars.

The high flux exposure (20170314) shows similar qualitative trends to the low flux case, with the magnitude of the observable features in experiment and simulation

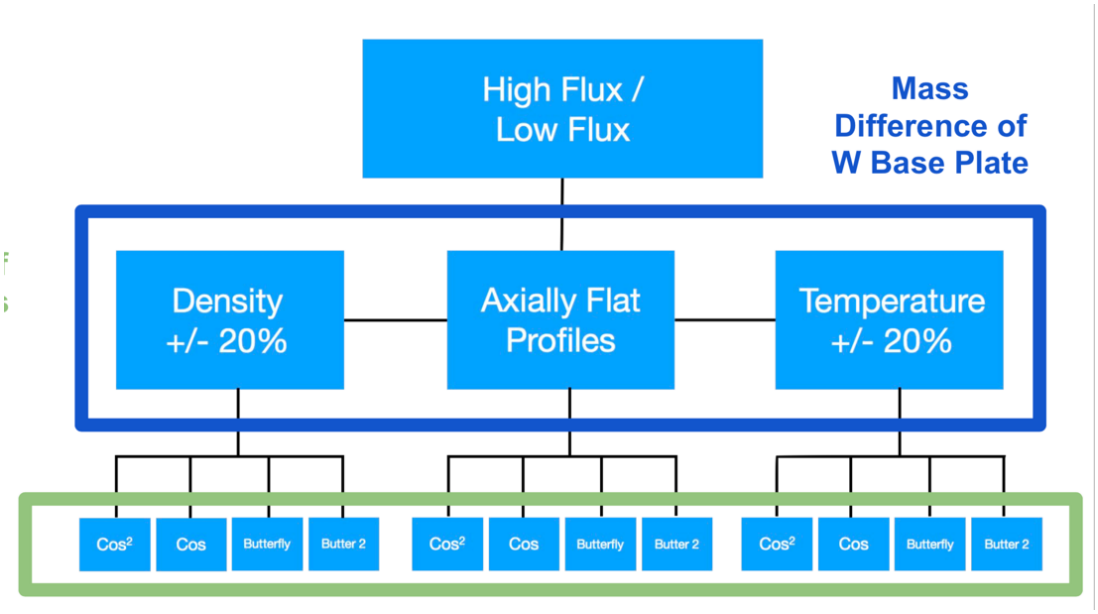


Figure 5.7: Schematic demonstration of the uncertainty/sensitivity scan performed with GITR. For both the lower (20170313) and higher flux (20170314) cases the original fit profiles as well as the $\pm 20\%$ values on $T_e$ and $n_e$ were simulated. Four varying sputtered particle angular distributions were used.

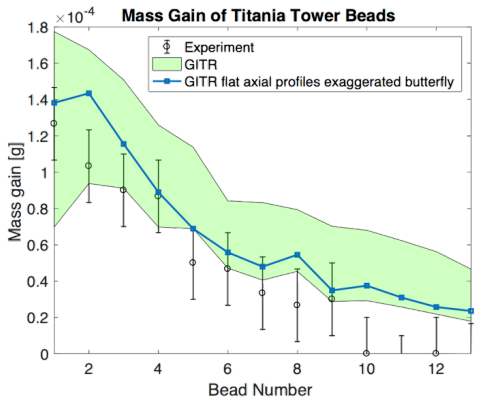


Figure 5.8: Titania tower bead mass gain during exposure 20170313 measured experimentally (black), and simulated by GITR (green band).

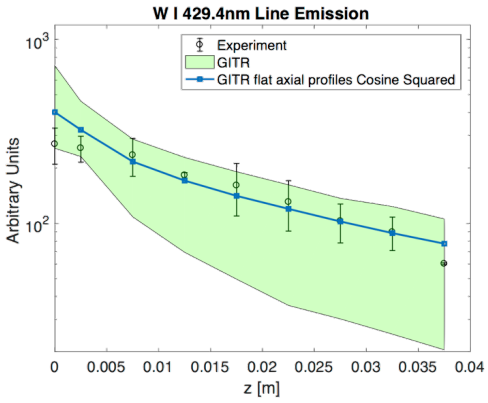


Figure 5.9: W I emission diagnostic during exposure 20170313 measured experimentally (black), and simulated by GITR (green band).

scaled up. The experimentally measured mass loss of 79.5 mg is well reproduced utilizing the original fits to the background plasma profiles. This high flux case shows an increased percent of eroded material returning to the target (65-81 %) which is expected compared to the low flux case because of increased $T_e$ and $n_e$, shortening the mean free path for ionization. The variability in the mass gain of the titania tower beads at the base is once again present as is the slight over-prediction of mass gain of the beads at the top of the collector tower as shown in Figure 5.10. Good qualitative agreement is shown for the W I spectroscopy although the slight difference in fall-off shape remains as shown in Figure 5.11.

### Prediction of impurity transport in the 1in disc exposures to pure He and mixed D-He plasmas

In addition to the impurity transport focused experiments (20170313 and 20170314) in Table 1, exposures of 1 inch W disc samples to He and 90%D10%He plasmas were performed (20180205 and 20180213 in Table 1, respectively). These 1 inch W disc samples were later analyzed to study the sub-surface composition. Given the agreement between the impurity transport model (GITR) and experiments discussed in section 3.1.1, GITR is applied to predict the W flux as input to the surface model in experiments 20180205 and 20180213.

GITR simulations of the 1 inch sample disc exposure to He plasma (20180205) predict a 2.704 mg gross erosion over the 100 s exposure with 1.201 mg being redeposited on the surface resulting in net erosion with a mass loss of 1.503 mg. Since this is a much shorter exposure (100 s) than the previous He exposed W experiments (5,000-10,000 s), a comparison of the mass loss rate is more appropri-

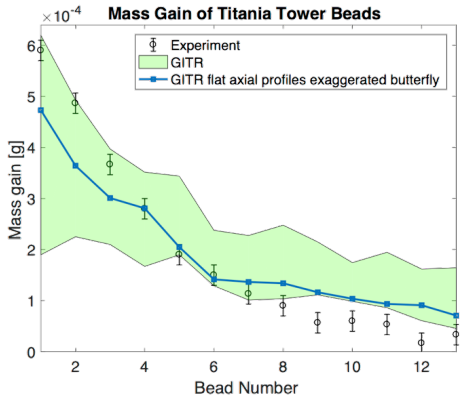


Figure 5.10: Titania tower bead mass gain during exposure 20170314 measured experimentally (black), and simulated by GITR (green band).

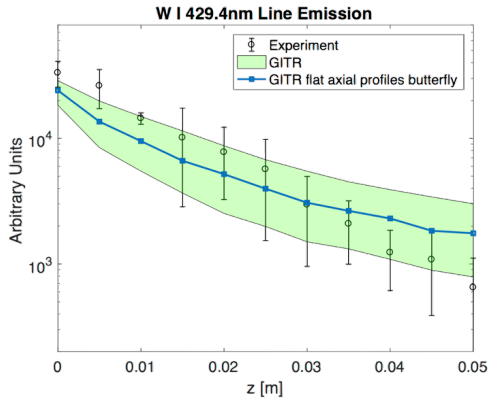


Figure 5.11: W I emission diagnostic during exposure 20170314 measured experimentally (black), and simulated by GITR (green band).

ate than the total mass change. For experiment 20180205, a simulated mass loss rate of of .0150 mg per second shows consistent results with the previously measured experimental results and impurity transport simulations from 20170314. The He exposure 20170314 has comparable background plasma conditions to 20180205, including electron temperatures, densities, and ion fluxes. In 20170314, the experimentally measured mass loss value of the W target was 79.533 mg, which occurred over a 5,000s exposure resulting in an average mass loss rate of approximately 0.0159 mg per second. Comparing the percentage of re-deposited impurities, simulation of the impurity transport focused experiments showed $65\% - 81\%$ of the eroded impurities being deposited back on the target. The simulations of the 1 inch W disc samples exposed to He only plasma (20180205) shows a significantly lower percentage of 44%, which can be attributed to the use of a smaller exposed target geometry. The much smaller target surface (1.27cm radius instead of 4.875cm, resulting in a loss of $> 93\%$ W target surface area) with respect to the plasma column results in less collection of sputtered and ionized impurities for which both the mean free path of ionization as well as the gyro-radius are on the order of cm. Simulation parameters which can affect the gross erosion and deposition of W include the ion flux to the target as a scaling factor for the erosion from the background plasma, background electron temperatures and densities which affect ionization rates which affect prompt redeposition rates.

The following GITR outputs for W exposure to the plasma are passed to the surface evolution iteration simulation performed by the coupled calculation done by F-TRIDYN and Xolotl. The total W impurity flux for experiment 20180205 at the target surface which from GITR simulations peak at $1.4 \times 10^{20} m^{-2} s^{-1}$ at the center of the target and falling off radially shown in Figure 5.12. Examining the kinetics of the W impurity flux which is returning to the surface shows a peak in 250 eV (singly charged W) near normal incidence as shown in Figure 5.13. A tail of higher energy particles are also shown returning to the surface which indicates ionization of W to higher states (W+2 and +3) because of the relatively high electron temperatures and densities ($T_e = 7eV$ and $n_e = 6.4 \times 10^{18} m^{-3}$) in this experiment. The continuous nature of this energy tail indicates that many of these atoms undergo ionization while still within the sheath electric field region near the target contributed to by the surface bias (-250V) and Langmuir sheath model. Finally, the peak in W impact angle is slightly away from normal incidence which can be attributed mostly to the lower energy (250 eV and below) impacts which are a result of prompt ionization and deposition as shown in Figure 5.14. Low energy ions which are impacting the surface (sputtered neutrals which are quickly ionized) are the main contributor to the impacts further from normal incidence.

Predicted results for net erosion as well as W impurity fluxes passed to the surface model for the mixed 90%D-10%He plasma (20180213) were also calculated by GITR. For this plasma composition (and the same biasing voltage), the He sputtering yield of W at 250 eV is $4 \times 10^{-3}$ while the D sputtering yield of W at 250 eV is $\approx 1 \times 10^{-5}$. Therefore, D erosion of W is neglected in these simulations. The reduced He flux (10% of that from the 20180205 experiment) has an effect that predominantly scales the magnitude in the erosion source. Additionally the total ion flux and electron densities are lower than 20170314 and 20180205 and more comparable to the low flux experiment Ti-tower experiment (20170313). The GITR simulations of the He/D mixed plasma show a gross erosion of 0.757 mg of W and a gross deposition of

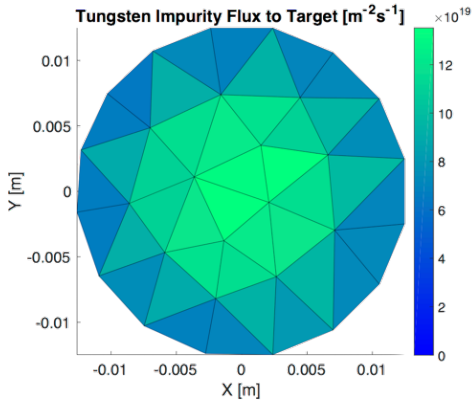


Figure 5.12: W impurity flux impinging on the 1 inch W disc in experiment 20180205.

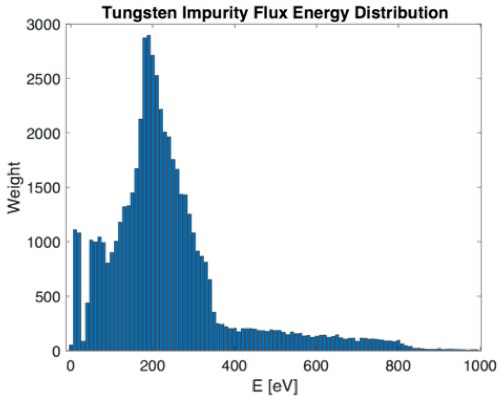


Figure 5.13: Energy distribution of W ions impacting the W target.

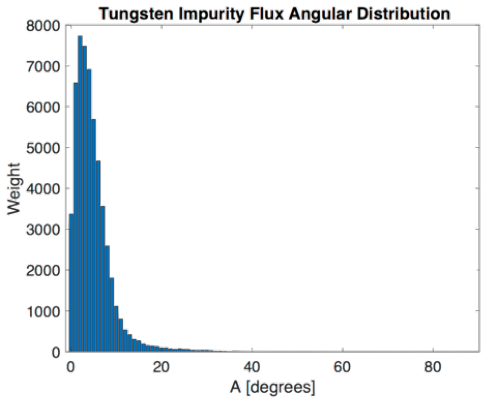


Figure 5.14: Angle distribution of W ions impacting the W target.

0.237mg over 1,000s resulting in a net mass loss of 0.520 mg and a mass loss rate of 0.520 micro-grams per second. The low flux exposure of 10,000 seconds (20170313) resulted in an experimentally measured mass loss of 18.83 mg giving a mass loss rate of 1.883 micro-grams per second. The ratio of the He/D exposure target mass loss rate (0.520 micro-grams per second) to the low flux He exposure 20170313 (1.883 micro-grams per second) is 0.276 which is approximately the same as the ratio of He flux to the target in each experiment ($1.5 \times 10^{21} m^{-2} s^{-1}$ and $5 \times 10^{21} m^{-2} s^{-1}$, respectively). The fraction of eroded impurities that are re-deposited on the target surface for the He/D mixed plasma from GITR simulations is 31.3% which is smaller than the He only exposure of 32%-67% because of large difference in target surface area mentioned previously. The GITR outputs to the coupled F-TRIDYN Xolotl simulation show a peak impurity flux of $2.6 \times 10^{18} m^{-2} s^{-1}$ as shown in Figure 5.15. As expected there is once again a peak in the impact energy at 250 eV as well as a small peak at 500 eV shown in Figure 5.16 resulting from $W^{2+}$ ions. A gap in deposition energy is shown between 300 and 400eV which is attributed to reduced ionization rates of singly charged W near the surface because of lower electron temperatures and densities. A similar angular distribution as 20180205 is also seen in these simulations and shown in Figure 5.17.

## 5.5 Detailed Results of the Titania Tower Experiments Using F-TRIDYN He Sputtering of W

This section provides additional simulation details of the PISCES titania tower experiments as well as results using an updated surface model of sputtering from F-

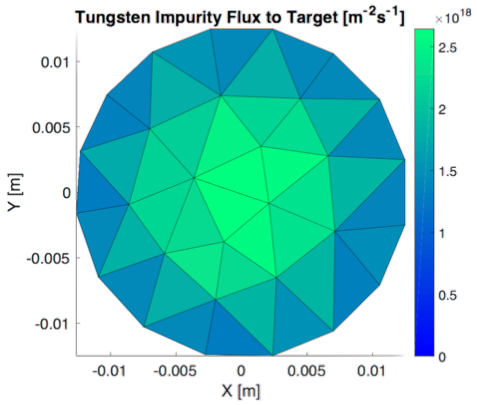


Figure 5.15: W impurity flux impinging on the 1 inch W disc in experiment 20180213.

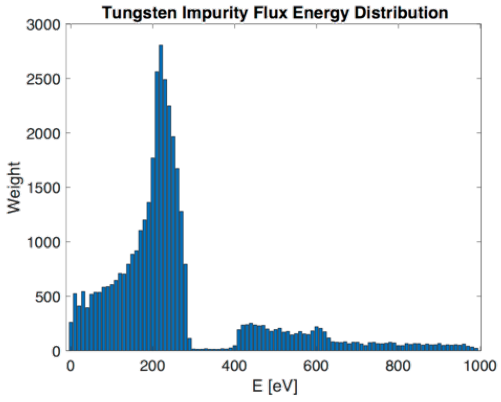


Figure 5.16: Energy distribution of W ions impacting the W target.

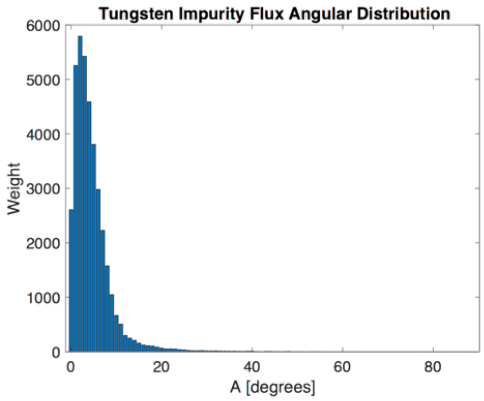


Figure 5.17: Angle distribution of W ions impacting the W target.

TRIDYN. The 20170313 exposure will be referred to as the "low flux" exposure (peak flux of $5 \times 10^{21} m^{-2} s{-}1$ and exposure time of 10,000 s) and the 20170314 exposure will be referred to as the "high flux" exposure (peak flux of $4 \times 10^{22} m^{-2} s{-}1$ and exposure time of 5,000 s).

### 5.5.1 Simulation Details

GITR has been used to model the low and high flux experiments previously described using inputs from various sources including experimentally measured plasma profiles, generated profiles (using simple models), and computed input from other codes. The PISCES-A W target and $TiO_2$ tower geometry are constructed in a CAD program and transformed into a useable input for GITR as shown in Figure 5.18. This geometry consists of 37,497 triangular elements with a maximum element side length of 5 mm, 1,762 surface mesh elements make up the W target surface. The surface elements designated as W surfaces use the GITR surface model for reflection and sputtering, and the remaining elements are treated as purely absorbing boundaries. The purely absorbing boundaries are used as an approximation because peak plasma temperature (9 eV) and peak W sputtered energy by 250 eV He (10 eV) are below the threshold energy for reflection predicted by F-TRIDYN (16 eV). Therefore, only W ions accelerated through the bias voltage to the W target will have sufficient energy to reflect and sputter. Input profiles to the code include a constant magnetic field of 0.8 T directed in the axial direction towards the target. Electron density and temperature profiles measured as a function of radius are fit (using polynomial and exponential polynomial) and assumed symmetric about the axis. Additionally, ion density and temperature are assumed to be equal to electron temperature and density, and all plasma profiles are constant in the axial coordinate. Since the target

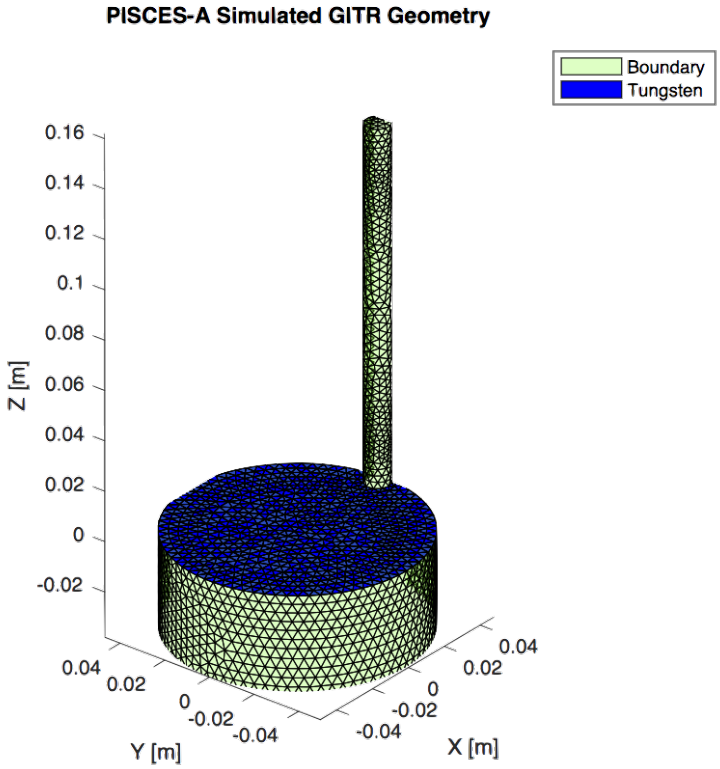


Figure 5.18: GITR simulated geometry showing only the W target plate and titania tower.

bias voltage (-250 V) is significantly greater than the peak electron temperature (6-9 eV) a Langmuir sheath model describing the electric field is used in the region near the target [44].

Additional input to the GITR code is a surface model which is required for formulating initial conditions of He eroded W and W self interaction during GITR execution. The surface model input to GITR comes from F-TRIDYN [38] and describes the beam (He or W) interaction with the target (W) as a function of incoming beam energy and angle. Outputs from F-TRIDYN which are used in this surface model include sputtering yield, reflection coefficient, and sputtering/reflected energy-angle distributions. Since there is a bias voltage applied to the target, it is assumed that He ions from the plasma beam are impacting the W surface at 250 eV kinetic energy with normal incidence. Using F-TRIDYN to simulate this using surface binding energy of 8.79 eV, a sputtering yield of $4.00 \times 10^{-3}$ is found. The sputtered W energy distribution has a peak sputtered W atom kinetic energy of approximately 2.5 eV with sputtered energies ranging from near zero to 10 eV. The sputtered W atom azimuthal angle distribution has a peak near 45 degrees falling off approximately symmetrically toward zero and 90 degrees. Since the He ions are normal incidence, the He sputtered W polar angle distribution is uniform. Additional documentation on these results can be found in [53]. In addition to this surface model for the He-W interaction, the flux profile for the low and high flux profiles set the spatial distribution for eroded W. This is done using a degree 4 constrained polynomial fit

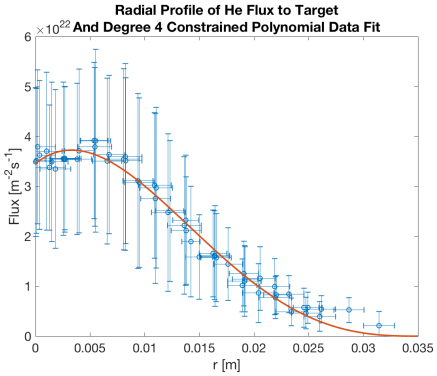


Figure 5.19: High flux (20170314) experimentally measured ion flux profile and data fit used in GITR simulation.

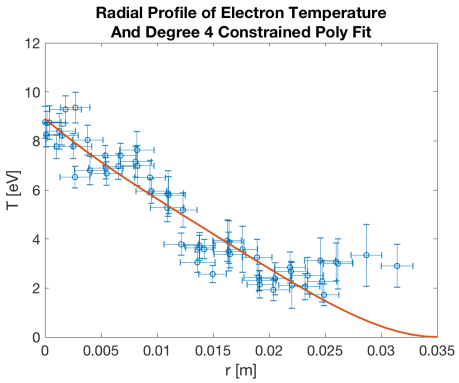


Figure 5.20: High flux (20170314) experimentally measured electron temperature profile and data fit used in GITR simulation.

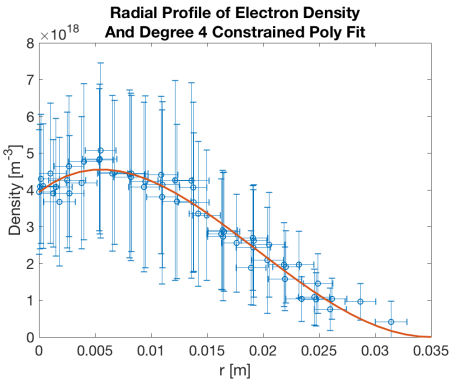


Figure 5.21: High flux (20170314) experimentally measured electron density profile and data fit used in GITR simulation.

as a function of radius and assumed axially symmetric. Flux fits with sputtering yield integrated for low flux results in a total He eroded W rate of $1.14 \times 10^{16}$ atoms per second where for the high flux case is $1.42 \times 10^{17}$ atoms per second. For the purposes of this study, varying input plasma temperature and density profiles, the target flux is kept constant. The W-W self interaction model which is used during GITR execution includes tables of sputtering and reflection yields. Energy and angle distributions for each of those combinations are also included [53].

Execution of GITR includes ionization, recombination, collision forces, sputtering and reflection. For each simulated case $10^5$ particles are simulated for $10^5$ time steps with a time step of $1 \times 10^{-8}$ s for a total simulated time of 1 ms. This time step is larget than a typical time step needed in GITR. This is because the Langmuir sheath region due to the biased target is larger ($10^{-4}m$) than the typical Debye sheath region ($10^{-5}m$) thus allowing a larger integration step size.

### 5.5.2 GITR Simulation Result

GITR output includes spatially resolved W flux, sputtering yield, energy-angle distribution, and ion densities. For brevity, only the results for the simulated observables of the PISCES-A experiments for which the uncertainty quantification is being performed are presented here - target mass loss, tower bead mass gain, and W I emission spectroscopy.

#### Low flux

The GITR simulation of the low flux (20170313) experiment using the baseline inputs described in Section 5.4.1 are presented here. The mass loss of of the W base plate for the 10,000 s exposure is 20.9 mg predicted by GITR compared to the measured 18.8 mg mass loss (+/- $2 \times 10^{-5}g$). Modeling of the synthetic diagnostic for W I emission spectroscopy in GITR is shown in Figure 5.22 and compared to that of the experimentally measured value. For this plot, the GITR simulated light intensity has been normalized to the second point at which z is greater than zero. The emission spectroscopy and sythetic diagnostic show a similar trend, falling off gradually in the 4 cm moving away from the target. However, the synthetic diagnostic produced in GITR for the low flux case shows a sharper decrease in emitted intensity, falling below that of the measured emission. The experimentally measured mass gain of the titania beads is shown in figure 5.23 with GITR simulated mass gain overlaid. The mass gain of the titania tower beads for the low flux case show much better agreement than the emission spectroscopy with GITR results falling within the experimental error bars on every bead except for bead number eleven.

#### High flux

Plots for emitted light intensity and mass gain of the titania tower beads for the high flux case (20170314) are also generated. Synthetic diagnostic emission and experimentally measured W I light is shown in Figure 5.24. In this high flux case, much better agreement is reached than in the low flux case. It should be noted that a much greater decrease in overall magnitude occurs in the high flux case because of the significantly higher ionization rate (due to electron temperature and density). Comparison of the mass gain of the titania tower beads compared to experiment is

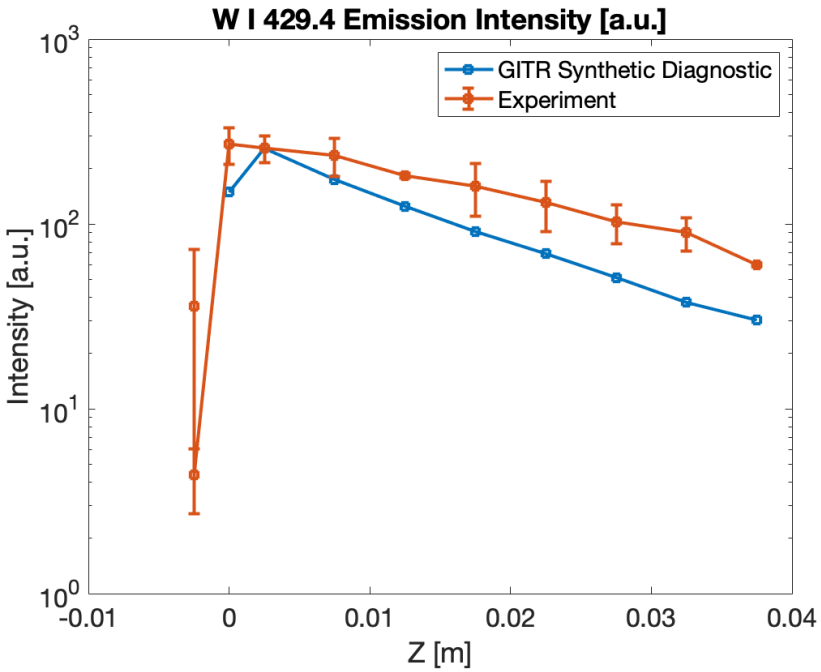


Figure 5.22: Neutral W (WI) emission spectroscopy 429.4 nm experimentally measured and simulated by GITR for the low flux case (20170313).

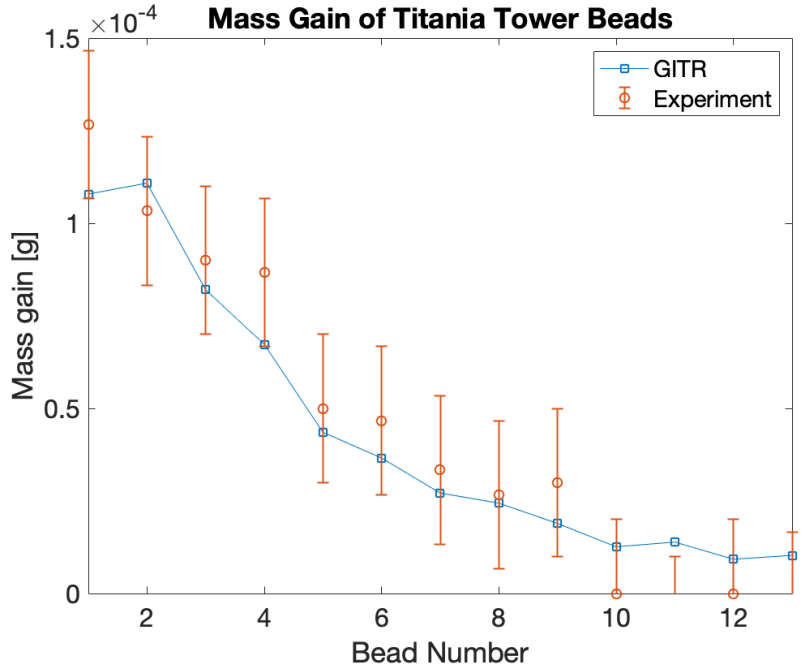


Figure 5.23: Low flux (20170313) results for titania bead mass gain by bead (1 is closest to the target plate, 13 is furthest).

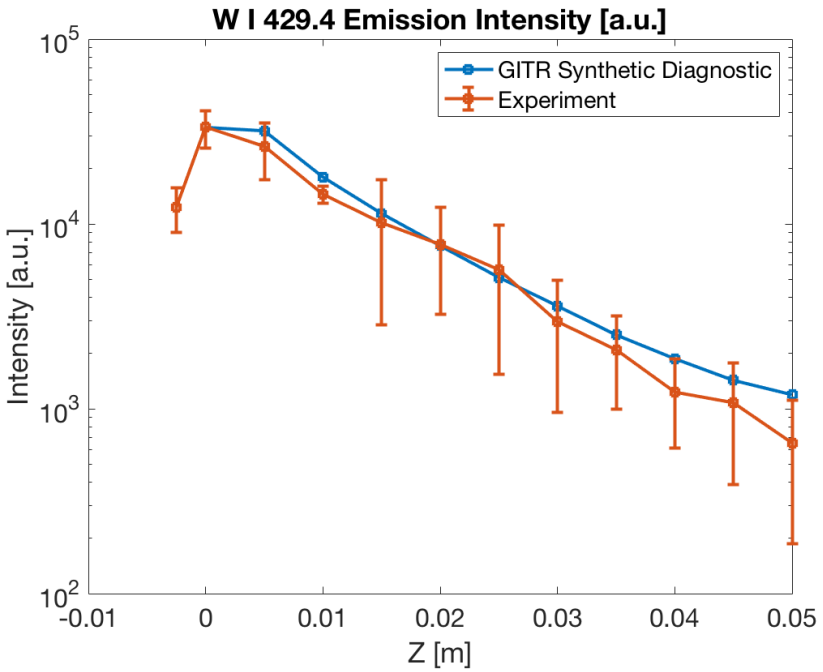


Figure 5.24: Neutral W (WI) emission spectroscopy 429.4 nm experimentally measured and simulated by GITR for the high flux case (20170314).

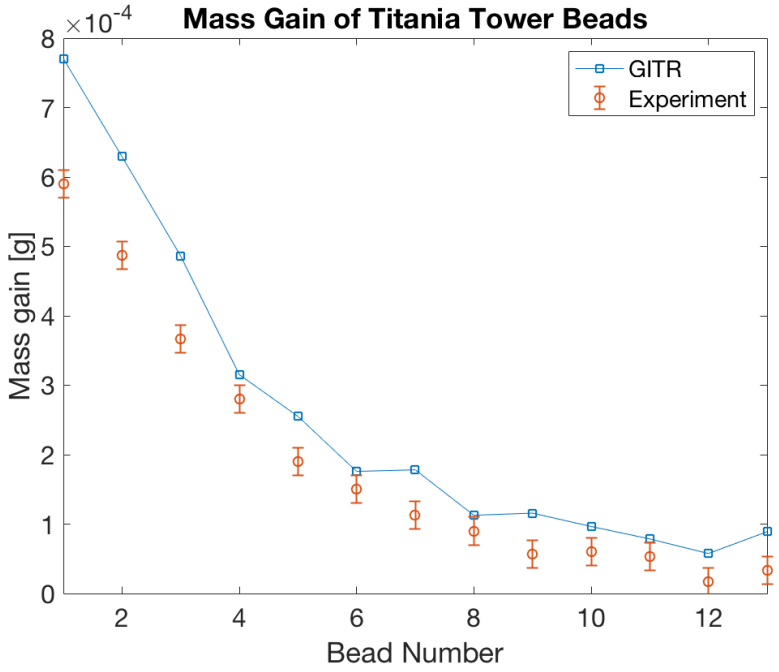


Figure 5.25: High flux (20170314) results for titania bead mass gain by bead (1 is closest to the target plate, 13 is furthest)

shown in Figure 5.25. Once again GITR simulations show a very strong agreement with the experimental measurement. With this high flux exposure, the magnitudes of mass gain are scaled up, resulting in a smaller relative experimental error. However, good agreement in both the magnitudes of the mass gain as well as the relative shape of the trend is present. Mass loss of the W base plate of 87.9 mg is predicted by GITR. An experimental mass loss of 79.5 mg was measured.

## 5.6 Uncertainty Quantification of W Transport

Due to the large uncertainties in measured plasma profile and their strong influence on the transport of impurities, a formal uncertainty quantification study was performed. Electron density and temperature were chosen as variables to study because of their strong influence on W ionization, as well as the line emission radiation coefficients used in the GITR synthetic diagnostic. Although ion flux also has a strong influence on the magnitude of the trace impurity simulation results and the fact that it is correlated to plasma temperature and density, it is not studied as an uncertain parameter here.

A Bayesian inference model has been used to create an uncertain input to the forward model GITR [48] in order to quantify simulated error based on the nature of uncertainty in measured electron density and temperature profiles $(n_e, T_e)$ used as input. This technique has been applied for comparison to dedicated experiments performed in the linear plasma device PISCES-A [47] for high $(4 \times 10^{22} m^{-2} s^{-1})$ and low $(5 \times 10^{21} m^{-2} s^{-1})$ flux 250 eV He exposed tungsten (W) targets designed to assess the net and gross erosion of tungsten and impurity transport. The W target design and orientation, impurity collector, and diagnostics have been designed to eliminate complexities associated with tokamak divertor plasma exposures (inclined target, mixed plasma species, re-erosion etc.) in order to benchmark results against the trace impurity transport model simulated by GITR. The simulated results of the erosion, migration, and re-deposition of W during the experiment from the GITR code coupled to materials response models is presented. Specifically, the modeled and experimental W I emission spectroscopy data for the 429.4 nm wavelength and net erosion through target and collector mass difference measurements are compared. GITR outputs are compiled to give mean and standard error of the experimental observables and correlations and sensitivities to uncertain input variables are drawn. This allows for a bounding in the predictions of the experimental observables based on the uncertainty in the input data and models. The predictions and modeled error bars are in good agreement with experiments.

### 5.6.1 UQ Methods

GITR requires input profiles for temperature $T(r)$ and density $n(r)$. The goal is to create a parametric representation of these profiles accounting for the uncertainty as well. These representations are found via Bayesian inference, given the processed PISCES-A experiment data shown in Figure 5.2. For the sake of notational ease, in this section we will use generic notation $x$ instead of $r$, and $y$ instead of $T$ or $n$.

Given a set of data $\mathcal{D} = \{x_i, y_i, s_i\}_{i=1}^{N}$, the $s_i$'s are interpreted as samples of standard deviation, rather than data noise, hence we strive to fit functions to the mean $y \approx \mu_{\boldsymbol{C}}(x)$ and to the standard deviation $s \approx \sigma_{\boldsymbol{C}}(x)$, where the parameter

vector $\boldsymbol{c} = (\boldsymbol{p}, \boldsymbol{q})$ will be inferred within Bayesian framework, given $\mathcal{D}$. Note that we ignore the errorbars on $x$-data. In fact, we employ polynomial form for both the mean

$$\mu_{\boldsymbol{c}}(x) = \sum_{k=0}^{k_\mu} p_k x^k \tag{5.1}$$

and the standard deviation

$$\sigma_{\boldsymbol{c}}(x) = \sum_{k=0}^{k_\sigma} q_k x^k \tag{5.2}$$

of the logarithm of the model, as will be clarified further below.

Based on the particular dataset, we have selected the best values for the orders $k_\mu$ and $k_\sigma$, simply by visualizing $\mathcal{D}$, without formal methods, e.g. model selection via Bayes factors.

The Bayes' formula reads as

$$p(\boldsymbol{c}|\mathcal{D}) \propto p(\mathcal{D}|\boldsymbol{c})p(\boldsymbol{c}), \tag{5.3}$$

in which prior PDF on coefficients, $p(\boldsymbol{c})$ is updated to find the posterior PDF $p(\boldsymbol{c}|\mathcal{D})$, via the likelihood function $L_{\mathcal{D}}(\boldsymbol{c}) = p(\mathcal{D}|\boldsymbol{c})$. While we use uniform, uninformative priors $p(\boldsymbol{c})$, the key to the posterior estimation is the likelihood function that encapsulates the goodness-of-fit of the parameterized uncertain function with mean $\mu_{\boldsymbol{c}}(x)$ and standard deviation $\sigma_{\boldsymbol{c}}(x)$ to the data $y_i$ and $s_i$, respectively. One can come up with many different 'fit' functions $L_{\mathcal{D}}(\boldsymbol{c})$, in principle, encapsulating various assumptions about the data and model. The posterior is then sampled via adaptive Markov chain Monte Carlo (MCMC), resulting in a sample set of the parameters $\boldsymbol{c}$ drawn from $p(\boldsymbol{c}|\mathcal{D})$.

### 5.6.2 Uncertainty Quantification Results

First, as described in Section 5.5.1 we fit polynomials for the first two moments. We selected second order polynomial for the mean trend, i.e. $k_\mu = 2$, and a linear and constant fits for the standard deviations, $k_\sigma = 0$ and $k_\sigma = 0$, for the low flux and high flux cases, respectively. This selection was based on a few trials and visualizing the data, *both* for $n(r)$ profile and for $T(r)$ profile.

To this end, we have obtained uncertain representations for the profiles of density and temperature as

$$\begin{aligned} n(r) &= n(r; \xi_1, \ldots, \xi_{K_1}, \xi_{K_1+1}) = & (5.4)\\ &= \exp\left(\mu^{(n)}_{\boldsymbol{c}(\xi_1,\ldots,\xi_{K_1})}(r) + \sigma^{(n)}_{\boldsymbol{c}(\xi_1,\ldots,\xi_{K_1})}(r)\xi_{K_1+1}\right) & (5.5)\end{aligned}$$

and

$$\begin{aligned} T(r) &= T(r; \xi_{K_1+2}, \ldots, \xi_{K_1+K_2+1}, \xi_{K_1+K_2+2}) = & (5.6)\\ &= \exp\left(\mu^{(T)}_{\boldsymbol{c}(\xi_1,\ldots,\xi_{K_1+K_2+1})}(r) + \sigma^{(T)}_{\boldsymbol{c}(\xi_1,\ldots,\xi_{K_1+K_2+1})}(r)\xi_{K_1+K_2+2}\right). & (5.7)\end{aligned}$$

The overall stochastic dimension is therefore $K_1 + K_2 + 2$ corresponding to a vector $\boldsymbol{\xi}$ with entries:

- $\xi_1, \ldots, \xi_{K_1}$ : due to posterior PDF of fitting $n(r)$

- $\xi_{K_1+1}$ : due to standard deviation of the fitted profile of $n(r)$
- $\xi_{K_1+2}, \ldots, \xi_{K_1+K_2+1}$ : due to posterior PDF of fitting $T(r)$
- $\xi_{K_1+K_2+2}$ : due to standard deviation of the fitted profile of $T(r)$

GITR takes $n(r)$ and $T(r)$ as inputs, i.e. $g(\boldsymbol{\xi}) = G(n(r, \boldsymbol{\xi}), T(r, \boldsymbol{\xi}))$, where $G$ denotes a scalar or vector quantity of interest. We build an uncertain representation in the polynomial chaos (PC) form , using a training set of samples of $\boldsymbol{\xi}$ and regression. The final PC representation then can be decomposed into variance contributions to arrive at sensitivities.

**Low-flux case**

Figure 5.26 shows shaded plots (top row) of posterior predictive quantiles, as well as samples (bottom row) of posterior profiles obtained from MCMC sampling of coefficients $\boldsymbol{c}$ that describe the mean trend and the standard deviation. By viewing the shaded plots of the posterior predictive quantiles we can gather two trends visually. First is that the electron density data scatter has a rather small variance, with the large uncertainty being the cause of the wide shaded band. Second, the electron temperature data has a significant scatter resulting in a greater variance, with smaller error bars which contribute to the width of the shaded band. So the reason for the uncertainty in electron temperature and density is quite different. The samples of the posterior profiles are used as input to the forward model GITR for simulation. In the case of the low flux, 409 samples for electron temperature and density were simulated.

The polynomial chaos representation provides uncertainty predictions of all 13 outputs that correspond to mass gain at various locations, visualized in Figure 5.27, together with experimental data. The very first output, target mass loss is visualized in the first panel of Figure 5.28, together with the rest of the output PDFs, simply another way of visualizing the results presented in Figure 5.27. This posterior predictive plot shown in Figure 5.27 uses a linear range of red shades (50 in total) to demonstrate the area in which a constant fraction of simulations result.

The posterior predictive of the titania tower bead mass gain as predicted with GITR shows accurate values for the mass gain and very small variance about the mean as shown in Figure 5.27. In Figure 5.28 the experimental data is shown alongside the posterior predictive. The predictive passes within the error of each titania tower bead experimental measurement.

The sensitivity plot shown in Figure 5.29 demonstrates consistent contributions to sensitivity from the posterior of electron temperature and the standard deviation of electron temperature, but also has contributions from the posterior of electron density and very little contribution from the standard deviation of electron temperature. This shows that at the temperatures and densities for the low flux case, both electron temperature and density play a large role in impurity transport. However, with the data collected, this sensitivity shows that the scatter in the electron density data is more largely responsible for changes in impurity transport than the uncertainty in the measurement. Conversely, it is the uncertainty (error bar) in the electron temperature which has the greater effect on sensitivity compared to the standard deviation of electron temperature.

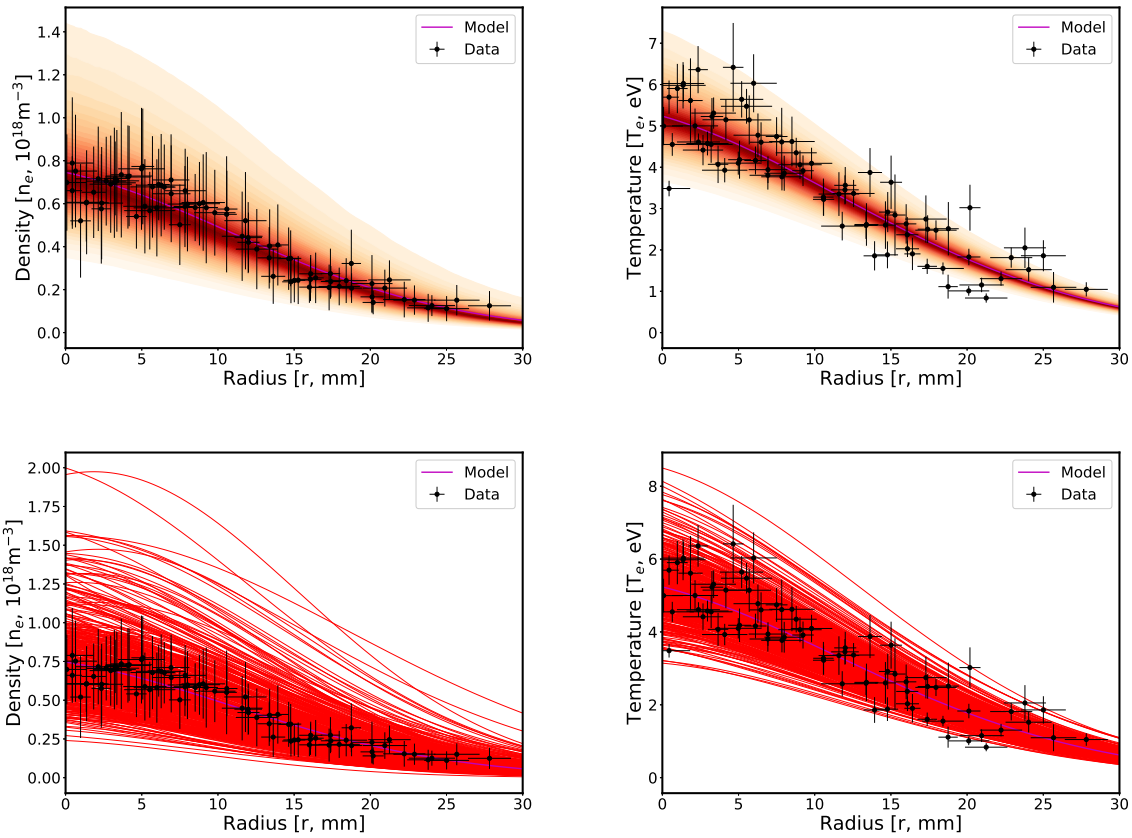


Figure 5.26: Posterior predictive fits as well as posterior samples of the profiles $n(r)$ and $T(r)$.

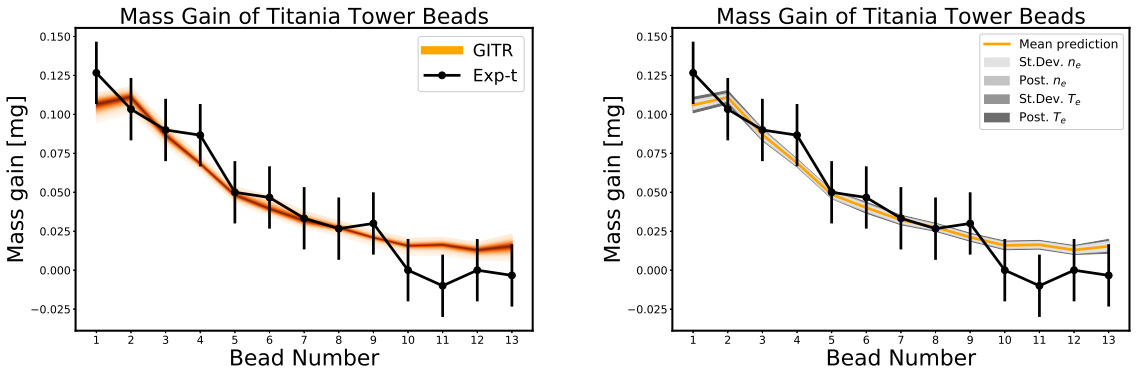


Figure 5.27: Posterior predictive of GITR outputs together with experimental data. The left plot shows quantiles, while the right plot shows the variance contributions.

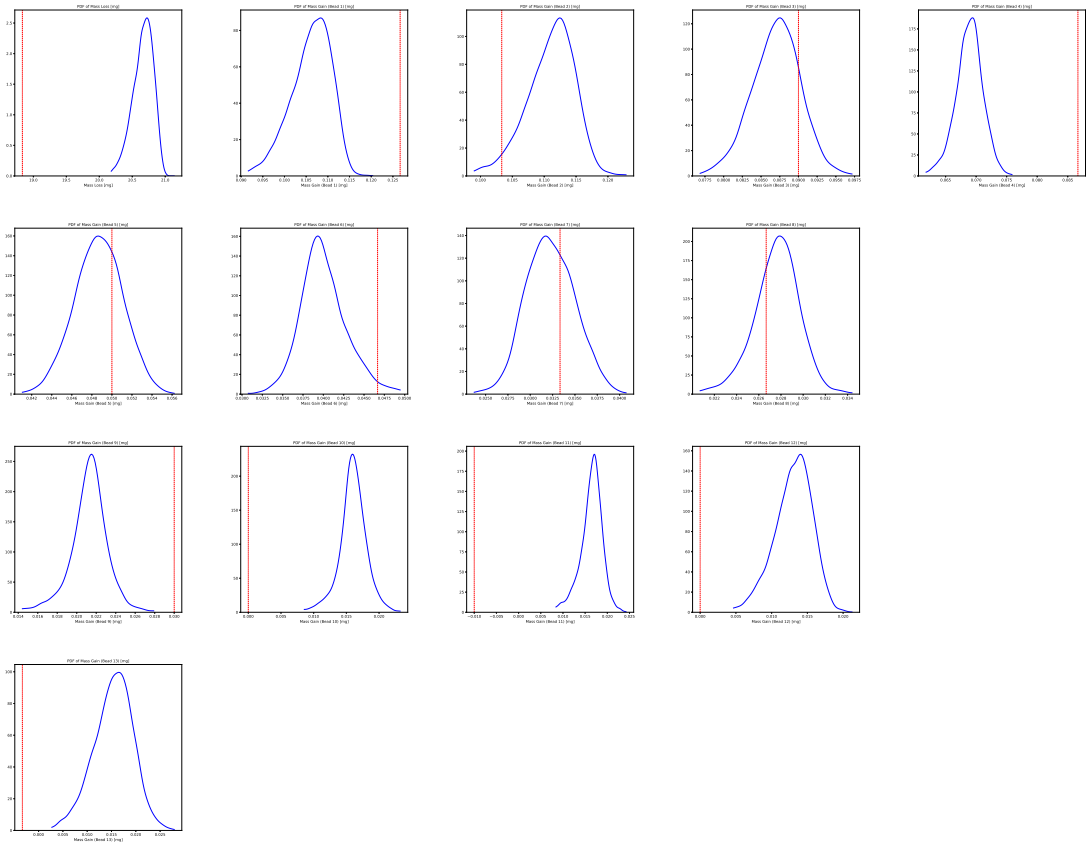

Figure 5.28: One-dimensional marginal output PDFs for all 14 outputs.

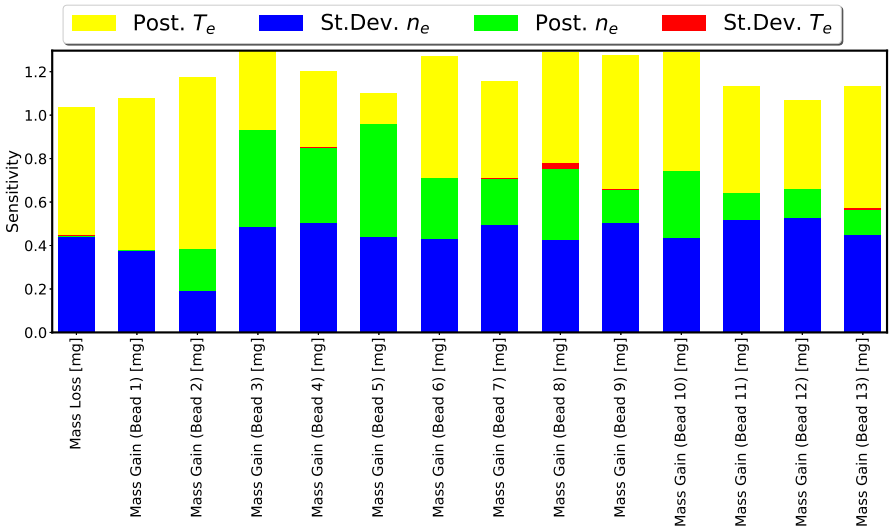


Figure 5.29: Total sensitivities, i.e. variance contributions with respect to the four components, for all 14 outputs of interest.

### Emission intensity

For the W I line radiated emission intensity, we also have the posterior predictive plots as were shown for target mass loss and tower bead mass gain. This is shown in Figure 5.30 and although the synthetic diagnostic accuracy is slightly off, the PC representation gives an error estimate given by the width of the band.

The corresponding sensitivity plot is given in Figure 5.31 showing that once again, the sensitivity is predominately due to the standard deviation of electron density and the posterior of electron temperature.

### High-flux case

Figure 5.32 shows shaded plots (top row) of posterior predictive quantiles, as well as samples (bottom row) of posterior profiles obtained from Markov Chain Monte Carlo (MCMC) sampling of coefficients $\boldsymbol{c}$ that describe the mean trend and the standard deviation for the high flux case.

Here we look at two sets of outputs from GITR, described in the next two subsections.

### Mass Gain/Loss

A total of 14 outputs of target mass gain and titania bead mass loss exist, hence the regression and sensitivity extraction is repeated for all 14 of them.

The PC representation provides an uncertain prediction of all 13 outputs that correspond to bead mass gain at various locations as well as sensitivities. This is visualized in Figure 5.33, together with experimental data. The posterior predictive outputs of bead mass gain show a greater mean mass gain than the original result shown in Section 5.4. However, the posterior predictive still encompasses all of the data points as shown in Figure 5.34. At the base of the titania tower beads, uncertainty due to the background plasma profiles is larger than the experimental error, but decreases away from the target. The very first output, Mass Loss is visualized in the first panel of Figure 5.34, together with the rest of the output PDFs, simply another way of visualizing the results presented in Figure 5.33. The target mass loss is slightly over-predicted by GITR simulations, however the experimental value is well within the bounds of uncertainty.

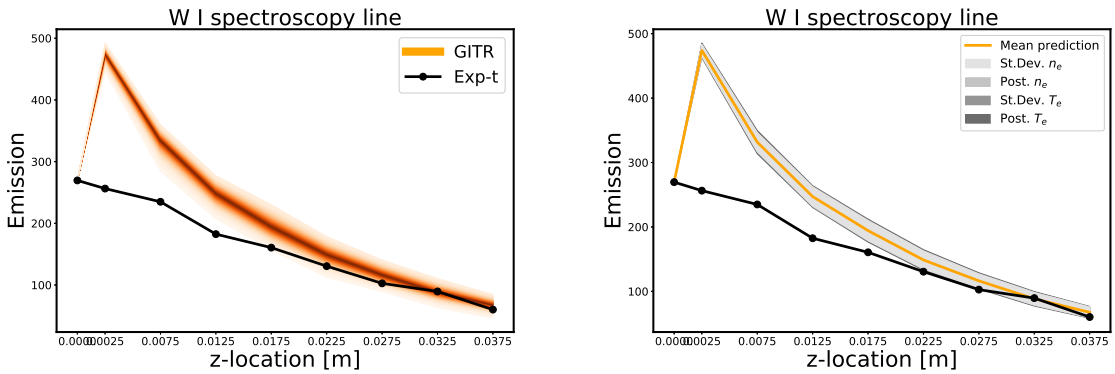


Figure 5.30: Posterior predictive of GITR outputs together with experimental data. The left plot shows quantiles, while the right plot shows the variance contributions.

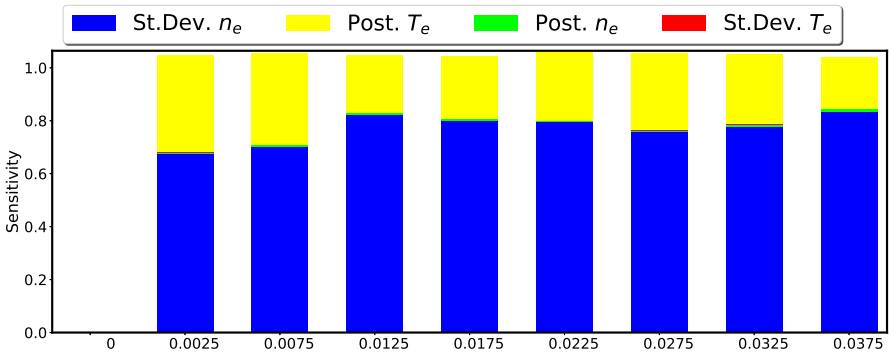


Figure 5.31: Total sensitivities, i.e. variance contributions with respect to the four components, for all 9 outputs of interest.

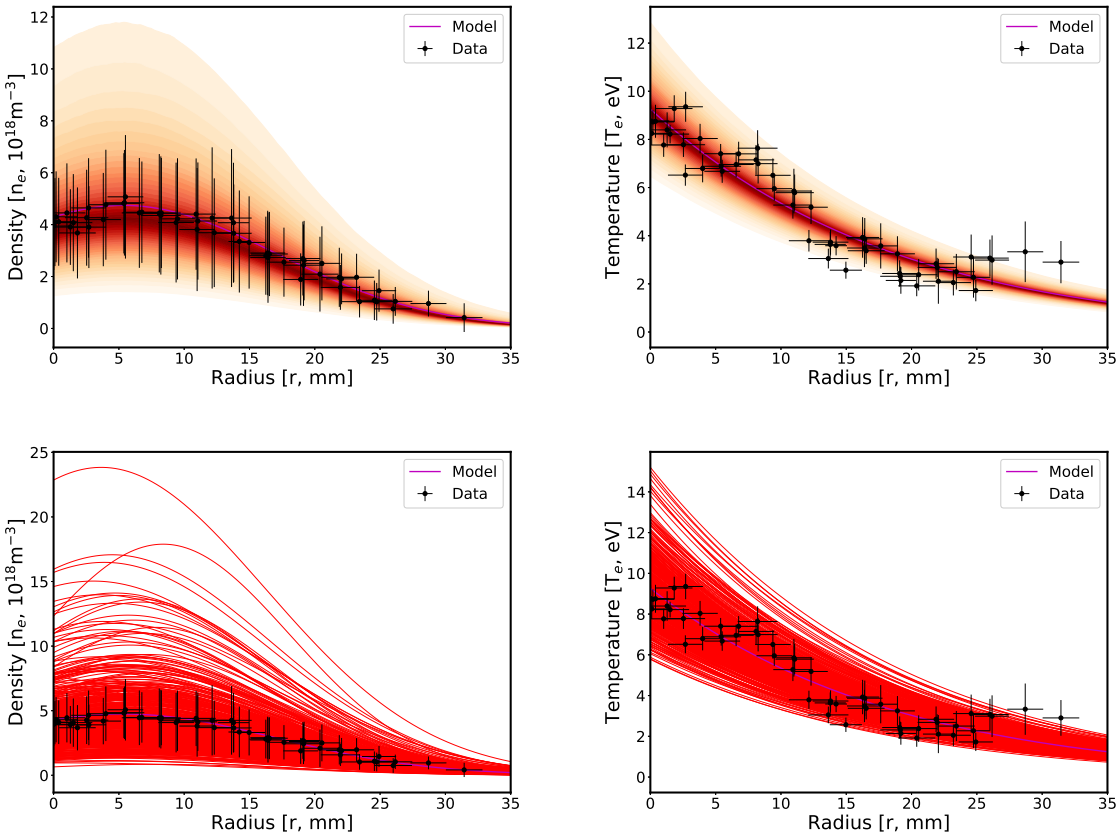


Figure 5.32: Posterior predictive fits as well as posterior samples of the profiles $n(r)$ and $T(r)$.

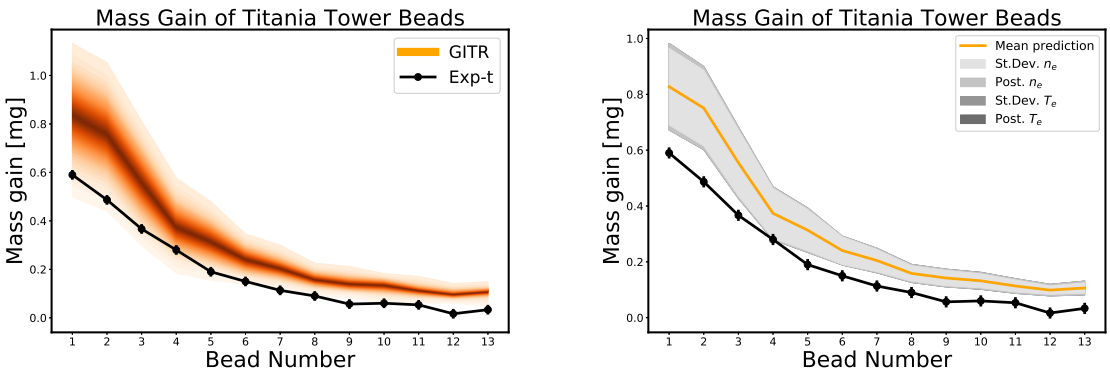


Figure 5.33: Posterior predictive of GITR outputs together with experimental data. The left plot shows quantiles, while the right plot shows the variance contributions.

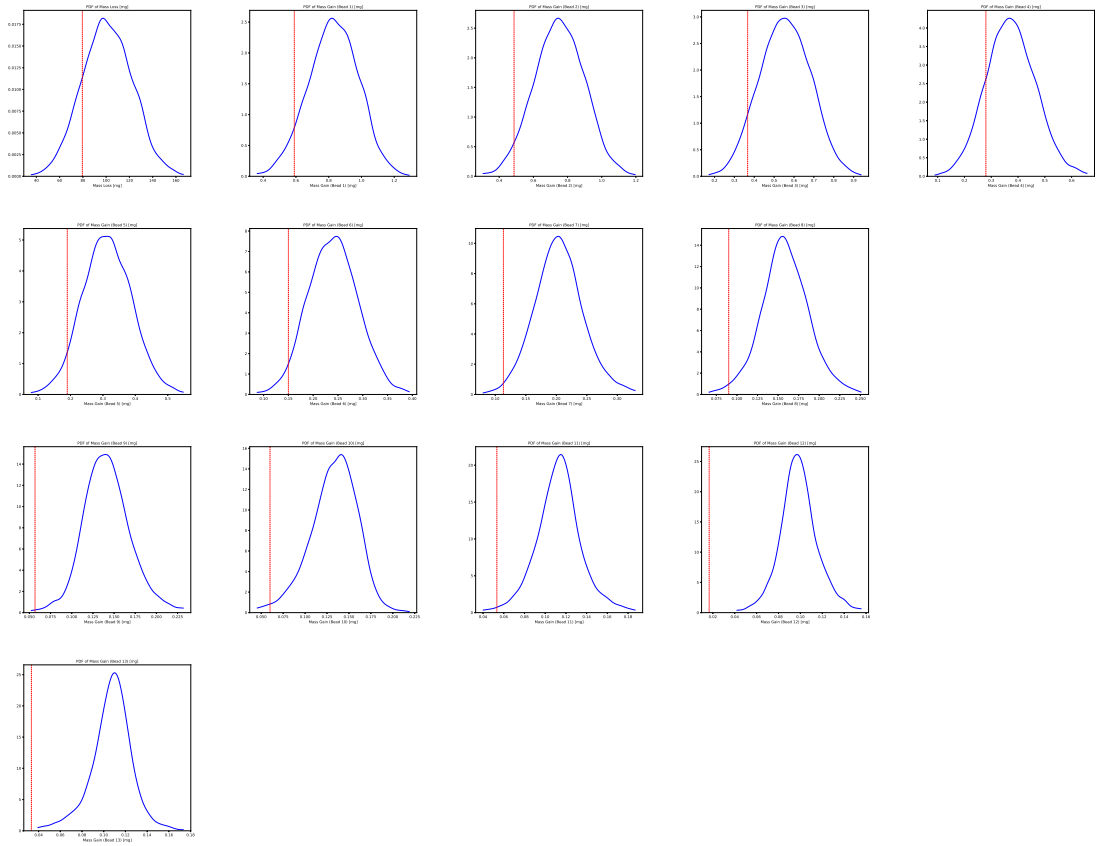

Figure 5.34: One-dimensional marginal output PDFs for all 14 outputs.

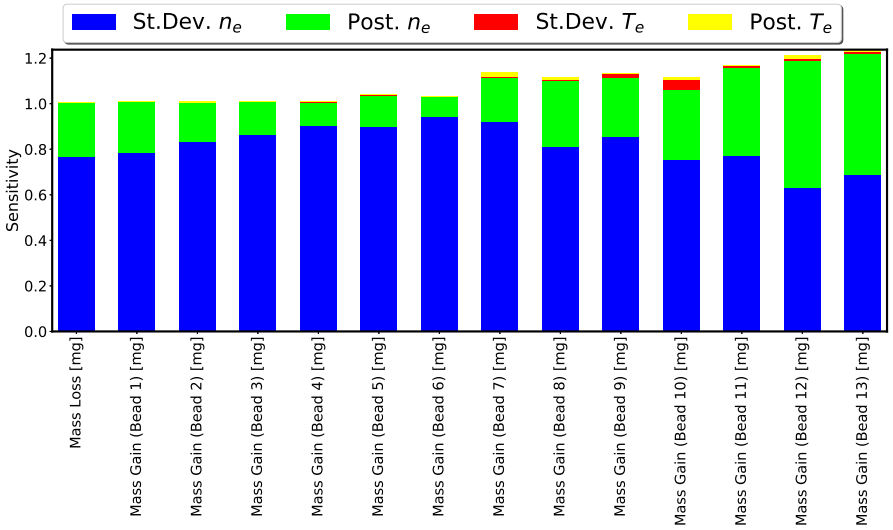


Figure 5.35: Total sensitivities, i.e. variance contributions with respect to the four components, for all 14 outputs of interest.

Sensitivities are shown in Figure 5.35. In the high flux case, the predominate sensitivity of the impurity transport is now to the posterior and standard deviation of electron density. The posterior and the standard deviation of electron temperature give a much smaller contribution.

#### Emission intensity

For the high flux case, there exist 10 measurement locations for the emission intensity. The emission intensity posterior predictive is shown in Figure 5.36. The variance in emission intensity shows a significant increase in magnitude as the position moves further from the target. The corresponding sensitivity plot is given in Figure 5.37 once again showing the strong sensitivity to standard deviation and posterior of electron density.

### 5.6.3 Conclusions

In using the formal uncertainty quantification methods we have presented to study the effect of background plasma profiles on impurity transport, the magnitudes of variance in the modeled results and the sensitivities to the parameters have been shown. By forming quantiles of the electron temperature and density profiles, a finite number of posterior samples were generated using MCMC. These samples are representative of the variance in the background plasma profiles and are used in GITR simulation of both the high flux and low flux exposures.

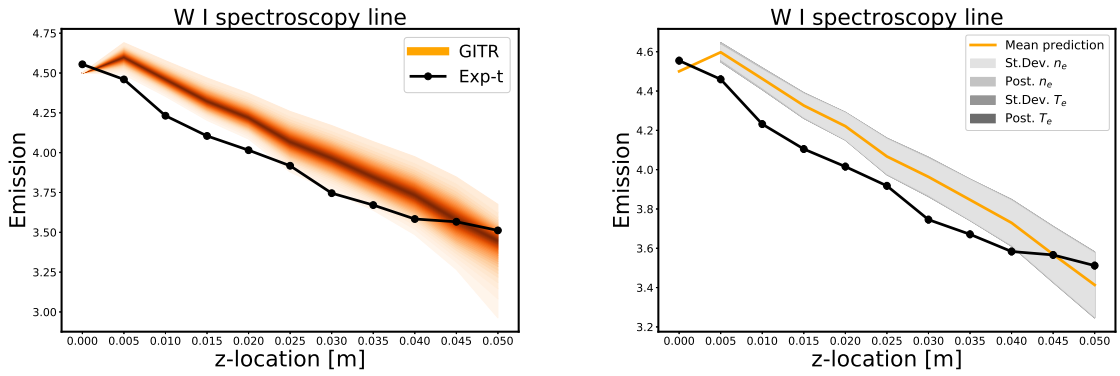


Figure 5.36: Posterior predictive of GITR outputs together with experimental data. The left plot shows quantiles, while the right plot shows the variance contributions.

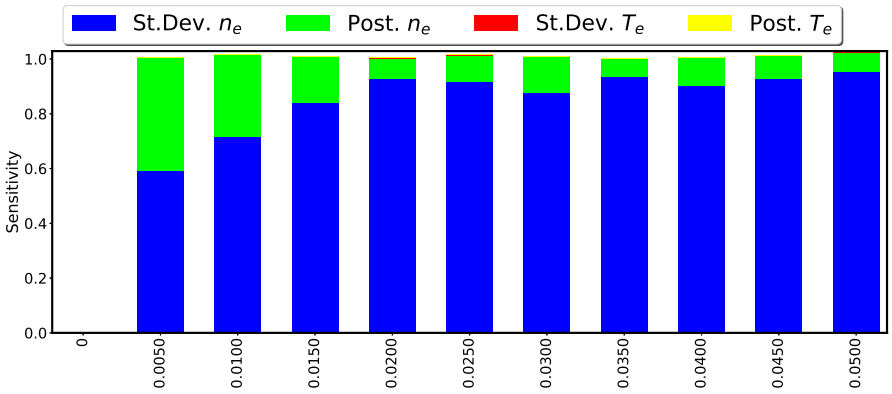


Figure 5.37: Total sensitivities, i.e. variance contributions with respect to the four components, for all 11 outputs of interest.

By using the PC scheme for reconstruction of the results, quantiles of the results as well as sensitivities are acquired. For the low flux case, the overall magnitude of uncertainty in the plasma profiles is small which results in accurate simulation of mass loss of the target plate, mass gain of the titania beads, and the W I emission intensity. For these cases the uncertainty due to the error in the background plasma profiles is less than the experimentally measured value. Sensitivities in mass change are largely due to the uncertainty due to Bayesian fitting of the electron temperature, but also the inherent uncertainty in electron temperature. For the high flux case, the magnitude of temperature and density as well as the posterior uncertainty is larger than the low flux case. The slight over-prediction of mass loss of the target plate as well as mass gain of the titania beads from the previous results persists here. However, now placing a finite error bar on the results due to uncertainty in the background plasma has been performed. The uncertainty and sensitivity of the GITR impurity transport model at these higher temperatures and densities has shifted to lie predominately with the inherent and posterior uncertainty of electron density. Overall this is an extremely useful study, as the plasma parameters in PISCES are divertor-relevant. Therefore the trends and uncertainties, which begin with Langmuir probe measurement, carry through the modeling with GITR, playing a significant role in the ionization rates and resulting impurity transport, and end with additional use in the line emission coefficients for the modeling of the synthetic diagnostic have been demonstrated to have an important effect which has been quantified here.

## 5.7 Summary

In summary, there has been a three-step progression in simulation of the PISCES-A dedicated linear device He plasma exposures. First was the modeling of these experiments making use of analytic models and fits for the sputtered W energy and angle distributions. Second was the updated result integrating the results from the sputtering model from F-TRIDYN for the energy and angle distributions of sputtered atoms. Third was the formal uncertainty quantification on the effect of uncertainty in plasma temperature and density on impurity migration. The first part of the modeling demonstrated that the energy-angle distribution of sputtered particles makes a significant difference in environments with long mean free path of ionization. By updating the source of these distributions, an increased confidence in the results for both He sputtered W and W self sputtering was gained. Finally, the effect of variation in the plasma profiles was quantified. Aside from the sheath model used, and the fundamental forces used in the trace impurity transport model within GITR, these simulations represents a comprehensive study on the impact of various inputs to the model. Therefore it is important to note that the modularity and the execution efficiency of the GITR code has helped to enable the examination of various inputs.

# Chapter 6

# Simulation of ITER PSI

## 6.1 ITER Integrated Model Simulation

As an application of the integrated model for plasma-surface interactions, ITER operation with either a 40 MW He or a 100 MW D-T burning plasma discharge has been simulated. These simulations make use of edge plasma simulations, particle-in-cell calculations for magnetic presheath and particle kinetics, a sputtering / reflection / implantation model, impurity transport, and surface morphology and composition evolution, following the code coupling approach described earlier in Chapter 5.2.2. The effect of the plasma-surface interaction at the outer divertor target is the focus of these studies. Although the direct simulation of the edge plasma and the particle-in-cell calculations for particle distributions were performed by others (J.M. Canik and D. Curelli, respectively), the output results, processed through developed wrappers and functions within the integrated framework is a part of the unique technical contributions described in this dissertation. Additionally, the details of the outputs directly affect the simulations of impurity transport which are also work for this dissertation.

## 6.2 He plasma discharge

### 6.2.1 Integrated Model for PSI

#### SOLPS Modeling of the Edge Plasma

The equilibrium plasma characteristics are calculated using the SOLPS-ITER package, which includes the neutral transport calculated by the kinetic Monte Carlo code EIRENE and plasma transport simulated by the 2-D fluid model B2.5. Given the toroidal symmetry assumed in the fluid description, only a poloidal cross section of the tokamak is modeled in SOLPS. Figure 6.1 shows the geometry modeled in B2.5, which is a grid encompassing most of the edge plasma and aligned with the plasma flux surfaces, with 90 points in the poloidal direction and 36 flux surface in the radial direction. The flux surface shape does not conform to that of the wall, leaving areas near the wall, which are dominated by neutral transport, out of the fluid model geometry. The grid extends 10-20 cm into the core (at the midplane) and several scrape-off layer heat flux widths into the scrape-off layer (SOL). The last grid surface is located as close as 2 cm off the inner wall, and at a distance of 8 cm

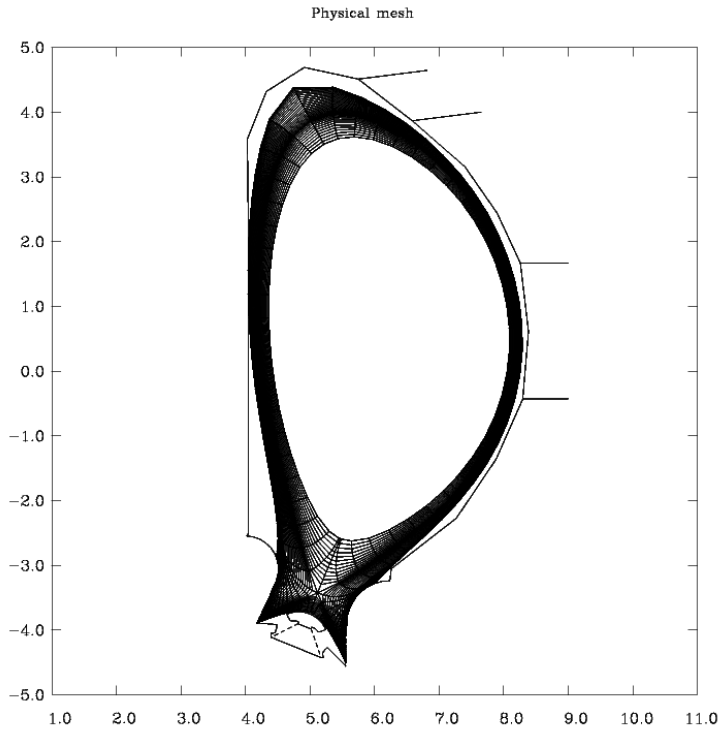


Figure 6.1: SOLPS-ITER grid for B2.5 simulation of fluid quantities in the ITER geometry.

off the inner midplane, 9 cm off the outer midplane and 15-25 cm off the top of the machine. The B2.5 geometry also resolves the divertor in greater detail, extending the grid all the way to the wall in the inner and outer vertical targets, and 2 cm away from the dome. The background scrape-off layer and divertor plasma has been calculated for ITER using the SOLPS-ITER code, which couples a 2D fluid transport model with a Monte Carlo treatment of neutral transport in the plasma edge. The first modeling scenario of ITER for the plasma-surface interaction simulations is a representative scenario during the helium campaign. The helium campaign is planned for early in ITER operations, with helium plasma discharges anticipated to enable H-mode access in the initial reduced magnetic field scenarios. While not presenting the same level of power load challenge as later campaigns, these plasmas are of special interest for the PMI simulations due to the intense interactions anticipated between helium and the tungsten surface. In the SOLPS simulations described here, the input power was set to 40 MW, representative of these anticipated early ITER operations. The transport was fixed as spatially constant, with values for the particle and electron/ion thermal diffusivities of $D = 0.3m^2/s$ and $c_e = c_i = 1.0m^2/s$. These represent the standard values for ITER SOLPS simulations, and produce SOL solutions that have been well-documented. Helium and hydrogen species are included in the simulation; the plasma is predominantly helium, with $\approx 5\%$ hydrogen content included to model residual hydrogen present in the system (potentially due to pellet fueling). Realistic pumping in the divertor is included, and the plasma is fueled by edge gas puffing set to a level that produces a midplane separatrix density of $ne \approx 1.5x10^{19}m^{-3}$ as shown in Figure 6.2. Strong radiation is predicted for the helium scenarios under these conditions. SOLPS finds

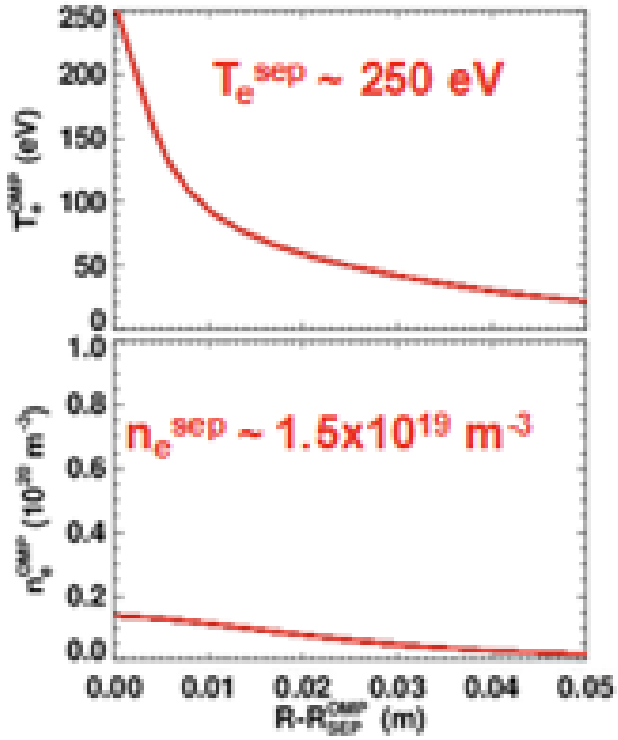


Figure 6.2: SOLPS-ITER outer midplane profiles for electron temperature (top) and density (bottom) for a 40 MW He plasma discharge.

that 25 MW out of the 40 MW input power is radiated, with nearly the entirety being localized in the divertor region (with only modest differences between the inner and outer leg). As a result, the parallel heat flux near the strike point is significantly reduced at the target compared to the midplane. The resulting heat fluxes on the target are quite manageable, with $\approx 2MW/m^2$ or less carried by the plasma onto the target plates. The radial profiles of the divertor electron density and temperature and ion flux are shown in Figure 6.3. The profile shapes shown in Fig. 6.3 are characteristic of the partially detached divertor state, with very low temperature ($\approx eV$) near the strike point, and radially increasing temperatures into the 20 eV range farther into the SOL where the plasma is attached. The electron density is highest near the strike point, but reaches relatively modest values of $\approx 4x10^{20}m^{-3}$ in this low power scenario. Likewise the ion flux is high near the strike point, with a peak value of $\approx 2x10^{23}m^{-2}s^{-1}$. The density and ion flux both decrease significantly farther into the SOL. The presence of the sharp changes in electron temperature and density in this radial region is expected to lead to strong changes in the erosion and re-deposition behavior along the divertor target. It should be noted that the SOLPS grid along the divertor target extends from the radial coordinate $R - R_{sep} = -0.1m$ to $R - R_{sep} = 1.3m$. Additional profiles are extracted from SOLPS for use in the GITR impurity transport simulations. Electron and ion density and temperature profiles, as well as ion flow velocity, electric field and temperature gradients are used. The parallel ion temperature gradient is shown in Figure 6.4. The ion temperature gradient shows large values (greater than 20 eV/m) in the divertor with different signs in the inner and outer divertor regions. With the magnetic field directed predominately in the toroidal direction (into the page), this indicates that

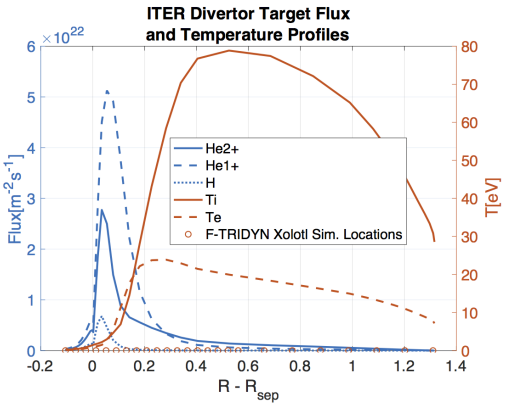


Figure 6.3: Plasma flux and temperature profiles at the outer divertor target, as a function of distance $R$–$R_{sep}$ in meters, including red circles to denote the location of coupled F- TRIDYN and Xolotl simulations.

the ion temperature is increasing strongly away from the target for both the inner and outer divertor regions. Electron density which is an influential factor ion eroded W ionization and re-deposition is shown in Figure 6.4b. Electron density values are shown to be largest ($\approx 4 \times 10^{20} m^{-3}$) along the separatrix and near the x-point. Extending along the field lines of the SOL as well as radially into the SOL there is significant reduction in the electron density ($1 \times 10^{19} m^{-3}$ or less).

In addition to outputs from SOLPS, common inputs to SOLPS must be shared with other models in the integrated simulation. For example, the magnetic field magnitude and angle of incidence at the divertor target is used in SOLPS, hPIC, and GITR. This processing is performed using Python scripts as part of the integrated simulation performed using the integrated plasma simulator framework. GITR makes use of the entire magnetic equilibrium, not just values at the target. The magnetic field values at the target are shown in Figure 6.5, and are between 5.5 and 6 T with highly oblique angles (87 to 90 degrees). The relative poloidal curvature as well as the shaping of the divertor target is responsible for forming the angle of incidence. Angle of incidence of the magnetic field plays a large role in the magnetic pre-sheath form, as well as prompt re-deposition rates of eroded impurities. The $1/R_{major}$ dependence of the magnetic field is shown, where $R_{major}$ is major radius. The approximately flat region of magnetic field magnitude from $R - R_{sep} = -0.1m$ to $R - R_{sep} = 0.5m$ represents the region where the divertor target is essentially vertical. The region of decreasing magnetic field magnitude represents the curved portion of the divertor target which is moving outward in major radius, thus decreasing at a faster rate.

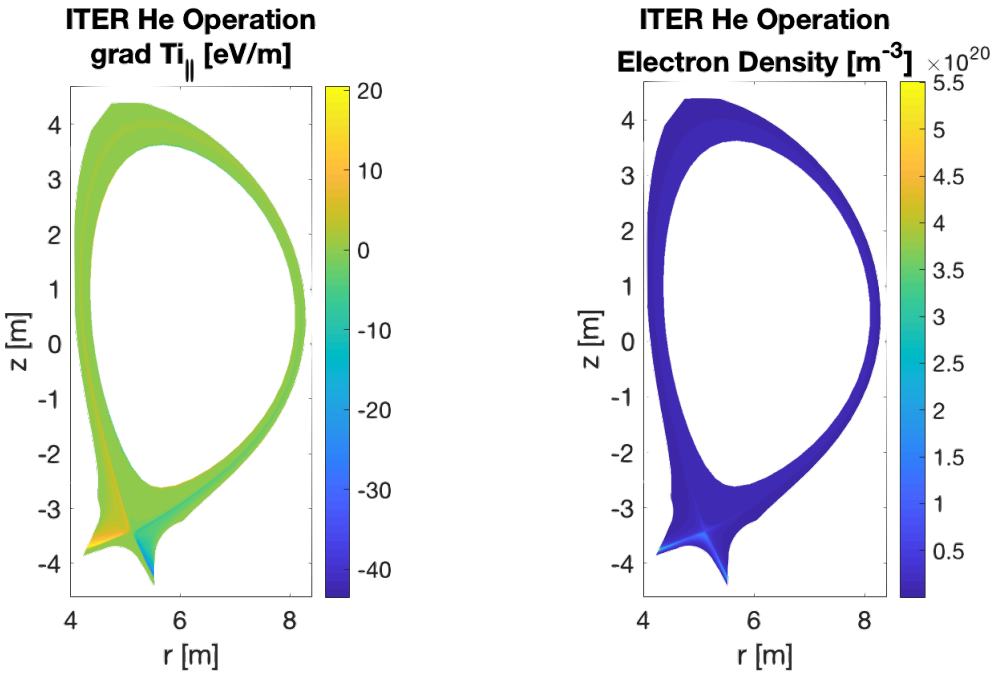


(a) Parallel ion temperature gradient.

(b) Electron density.

Figure 6.4: Ion temperature gradient parallel to the magnetic field line (a), as processed output and electron density profile interpolated (b) for He operation.

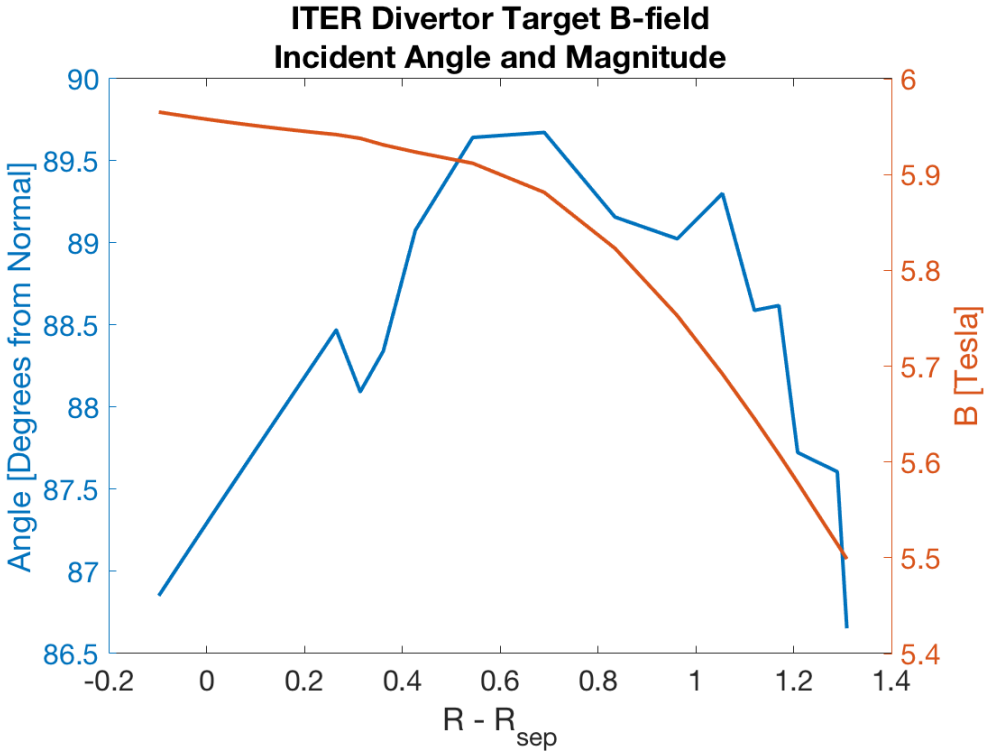


Figure 6.5: Magnetic field at the outer divertor target as shown along $R-R_{sep}$ in meters. Magnetic field vector is largely in the toroidal direction with some components in r and z.

**hPIC simulation of Ion Energy Angle Distributions at the Target**

The SOLPS output along the target coordinate $R - R_{sep}$ have been sampled at 38 locations spanning a region including the strike point. The plasma conditions provided by SOLPS are passed as input to the hPIC Particle-in-Cell (PIC) code. The code is a full-f, full-orbit PIC that models the plasma sheath physics. In the present work, hPIC provides output about the ion energy-angle distribution (IEAD) of the particles striking the wall. The code has been modified to accept as input the local plasma properties from SOLPS at the point of interest on the target plate, plus information on the local magnetic field (magnitude of the field and angle with respect to the wall). The code also requires a number of discretization parameters necessary to setup the PIC simulation in ITER-relevant conditions (number of grid points per Debye length, number of time steps per gyro-period, number of ion transit times, numbers of particle per cell), as described in further detail in Ref. [40]. hPIC provides the energy-angle distribution of the ions impacting the surface, to the material codes handling surface erosion and implantation (F-TRIDYN and GITR). A single hPIC simulation was performed by UIUC (Curreli group) per SOLPS target point was performed in 1D3V electrostatic mode (one spatial dimension and 3 velocity dimensions). Each simulation resolves a region of approximately 500 Debye lengths along the normal to the surface, using an average of 1000 particles per cell, 5 grid points per Debye length and 50 time steps per ion gyro-period. Each hPIC simulation was performed for both $He^{1+}$ and $He^{2+}$ plasmas to reach steady state conditions, after which the ions hitting the wall were recorded. Figure 6.6 shows an example of an IEAD produced by hPIC at a point along the $R - R_{sep}$ coordinate, which reports the distribution of $He^{2+}$ ions at the wall on a two-dimensional energy-angle plane, where the angle is measured with respect to the normal to the surface (0° indicates that the ions arrive at normal incidence on the surface, 90° indicates parallel to the surface).

reports the distribution of $He^{2+}$ ions at the wall on a two-dimensional energy-angle plane, where the angle is measured with respect to the normal to the surface (0° indicates that the ions arrive at normal incidence on the surface, 90° indicates parallel to the surface). The top red line on each plot marks the most probable energy (eV) as expected from the classical sheath theory; in all cases it corresponds to the peak of the distribution as calculated by hPIC. The energy-angle plot also shows the effect of the magnetic angle; for the large magnetic inclinations expected in ITER (magnetic angles comprised between 86.8 and 89.6 degrees along $R-R_{sep}$), the most probable impact angle of the ions at the surface is within the interval of 70-80 degrees. Figures 6.7 and 6.8 summarize the energy distribution (i.e., integral of the IEAD over the angles) calculated by hPIC as a function of the geometrical coordinate $R - R_{sep}$ along the outer divertor target of ITER. The two figures are for $He^{1+}$ and $He^{2+}$, respectively. A black horizontal line marks the sputtering threshold of helium on tungsten (119.95 eV). In the $He^{1+}$ case, while the peak of the distribution is always below the sputtering threshold, a portion of the high-energy tail is above threshold. Such portion of the distributions contributes to sputtering and erosion, as analyzed in detail in the next section. In the $He^{2+}$ case, the peak of the distribution results above the sputtering threshold on a region of approximately 0.5 meters above the strike point. Furthermore, a significant portion of the $He^{2+}$ distribution is above the sputtering threshold, contributing to wall erosion. A quantitative analysis of gross and net erosion has been performed by

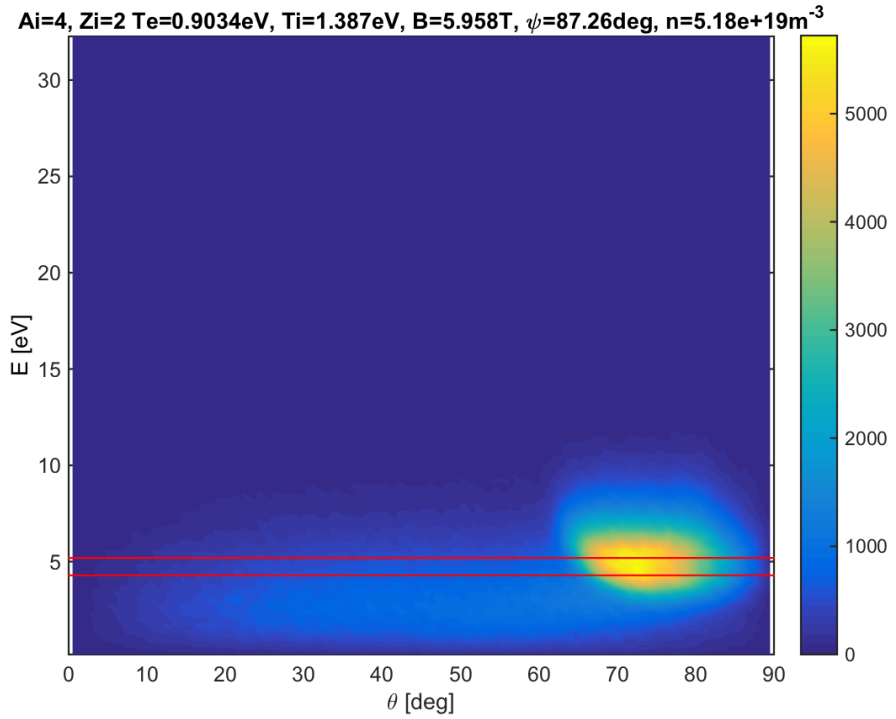


Figure 6.6: Helium 2+ ion energy angle distribution along the divertor target.

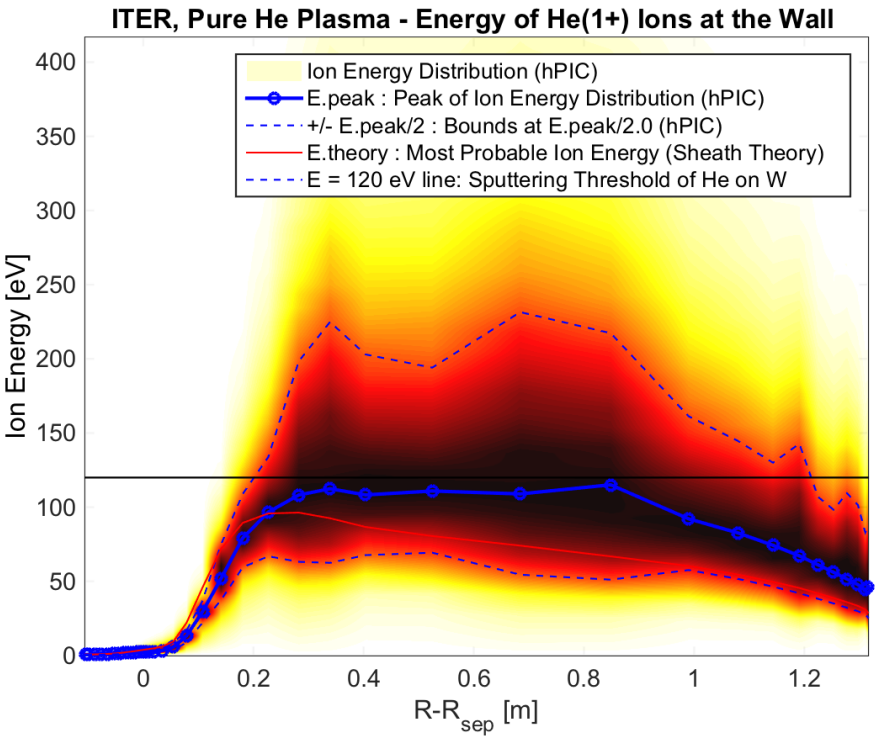


Figure 6.7: Ion energy angle distributions from hPIC summed over the angular component to predict the $He^{1+}$ energy distributions along the divertor target.

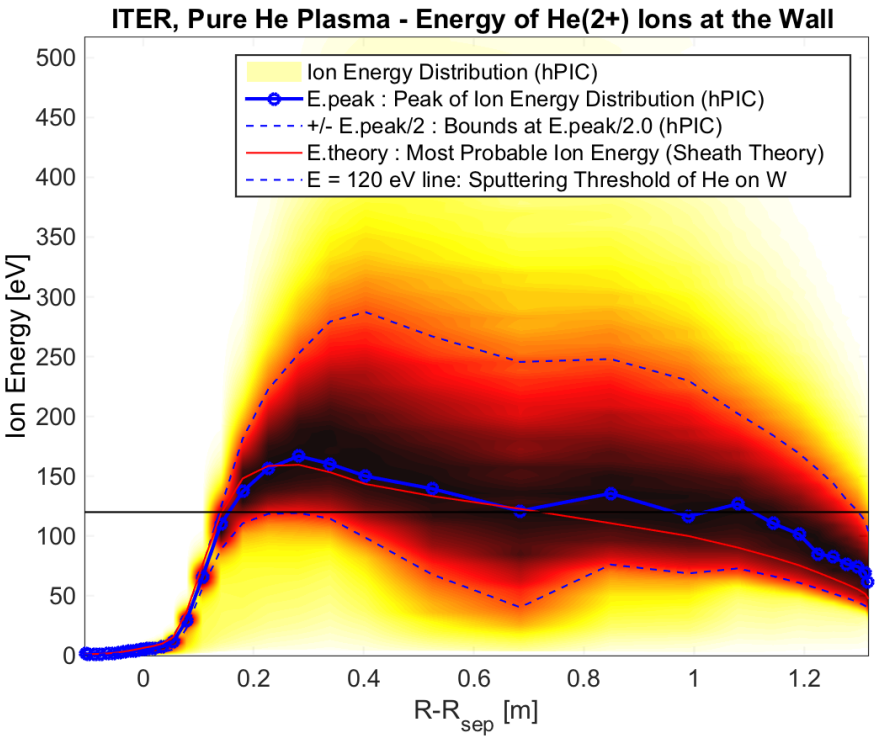


Figure 6.8: Ion energy angle distributions from hPIC summed over the angular component to predict the $He^{2+}$ energy distributions along the divertor target.

passing the IEADs calculated by hPIC to the F-TRIDYN and GITR codes, as described in the next section.

### Fractal TRIDYN Simulation of Surface Kinetics

Based on the background plasma data (SOLPS background plasma profiles and ion energy-angle distributions of He plasma species at the outer divertor target shown in Figures 6.2 through 6.8), initial conditions for the He sputtered W source in GITR can be produced by F-TRIDYN. The overall energy-angle dependence of He sputtered W is shown in Figure 6.9. These sputtering yields are highly dependent on incident ion energy and angle, can be integrated with the incoming ion energy-angle distribution to produce a sputtering yield and effective sputtering yield. Additional data provided from F-TRIDYN includes energy-angle distributions of sputtered atoms for each energy-angle pair as shown in Figure 6.9. These quantities, together with the yields and target fluxes, are used in the formulation of initial conditions for sputtered impurities simulated by GITR.

With the sputtering yield for a given species from F-TRIDYN as $Y_s(E,\theta)$ (the s subscript indicating different elemental species) and $f_s(E,\theta)$ as the IEADs given by hPIC for each charge state species, the sputtering yield by a given ion species is given by:

$$Y_s = \int\int f_s(E,\theta) Y_s(E,\theta) dE d\theta \tag{6.1}$$

Figure 6.10 plots the sputtering yields and sputtered flux of tungsten resulting from this integration, and shows that both $He^{1+}$ and $He^{2+}$ reach sputtering yields of greater than $3 \times 10^{-3}$ at locations along the divertor target. The sputtering yield

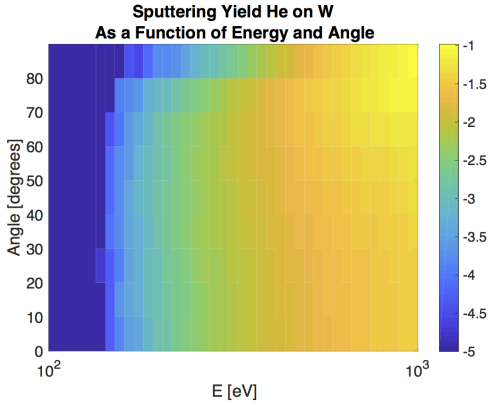


Figure 6.9: 2D histogram of sputtering yields for He impacting W at various energies and angles. The scale is log10 and shows a sputtering threshold energy between 100 and 200 eV.

for each species somewhat follows the electron temperature profile at the target. At the strike point ($R - R_{sep} = 0$) the temperature is too low to generate sputtering. However, ion populations with kinetic energies both above and below the sputtering threshold exist along the divertor target, and the relative balance of these populations also affects the sputtering yield. When the relative flux magnitudes of each ion species at the target are taken into account we can produce an effective yield. This operation is performed by dividing each sputtering yield $Y_s$ by the summed integral of each species distribution function and is defined by:

$$\bar{Y_s} = \frac{\int\int f_s(E,\theta) Y_s(E,\theta) dE d\theta}{\sum_s \int\int f_s(E,\theta) dE d\theta} \tag{6.2}$$

By multiplying the effective sputtering yield by the total ion flux, the W erosion flux is computed. The sputtered flux of W caused by both $He^{1+}$ and $He^{2+}$ is shown in Figure 6.10. Since the fluxes of helium species are on the same order of magnitude at the target (peak $He^{1+}$ flux being approximately a factor of 2 greater than the $He^{2+}$ flux), and the sputtering yields are also on the same order, the resulting sputtered W fluxes are also comparable. However, the W erosion due to $He^{2+}$ is approximately a factor of two larger than that of $He^{1+}$. The He eroded W source on the outer ITER divertor target, which projected on the GITR simulated geometry (shown in Figure 6.11 and described in the next section) results in the W flux shown in Figure 6.12.

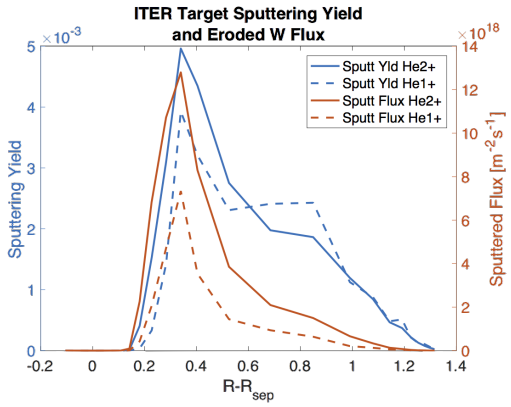


Figure 6.10: Helium sputtering yield and eroded W flux of helium as a function of the charge state of the helium ions responsible for the sputtering, as a function of distance along the outboard divertor target.

## GITR

The ITER divertor is divided into 54 essentially identical cassettes. Therefore, any given toroidal slice, which encompasses the entire width of a cassette should be representative of the physics throughout the entire toroidal symmetry. Thus, the impurity migration and re-deposition in a single divertor cassette has been modeled, assuming periodic boundary conditions, in anticipation that this approach will provide the most efficient, yet complete representation of the entire ITER divertor geometry.

The divertor cassette is represented in GITR by a 1/54 scale representation of a fully cylindrically symmetric model of ITER. The divertor tiles within a cassette incorporate 2816 units, with tile gap widths and depths specified as 0.5 mm and 2 mm, respectively, as shown in Figure 6.11. The mono block tile faces range in size from 24 to 44 mm in either of the "face" directions. These sizes were chosen to "fit" with the given gap width and toroidal extrusion. At a minimum, each tile is resolved in the geometry grid, resulting in 66,000 triangle faces for the geometry, which is an easily manageable geometry for GITR. The fidelity can be increased to isolate areas of special interest within our modeling. For instance, the area around the outer strike point, where the highest plasma ion fluxes, erosion and W prompt re-deposition are expected, can be modeled with higher spatial resolution to better capture variations in surface conditions, necessary to accurately model the evolution of the divertor tile target.

The geometry, magnetic field, background plasma profiles, and sputtering / reflection surface model used as input to GITR for the impurity transport simulation

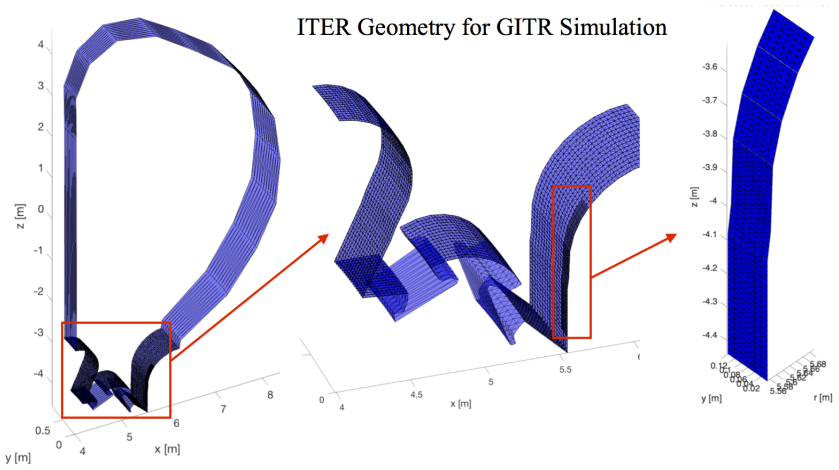


Figure 6.11: 3D surface geometry modeled in GITR, comprised of 1/54th toroidal symmetry (e.g., 1 divertor cassette). The divertor tiles and refined GITR mesh along the tile faces of the target are also shown.

has previously been described in Section 6.2.1. The GITR model used a simulated $10^6$ particles to represent the erosion and migration of the impurities for a duration of 2 ms. This provides sufficient statistics and time duration to capture the prompt re-deposition behavior as well as significant transport of impurities in the scrape-off layer plasma.

The results of the impurity transport simulation show net erosion along the ITER outer divertor target over a distance of approximately 90 cm in the positive $R - R_{sep}$ coordinate, as shown in Figure 6.13. The shape of this erosion profile mimics the erosion profile from the background $He^{1+}$ and $He^{2+}$ plasma flux. The gross deposition flux is slightly less than the gross erosion flux resulting in the net erosion. In these simulations approximately 80% of the eroded tungsten is re-deposited while 20% of the eroded impurities are lost to the private flux region, scrape-off layer, or other surface locations away from the outer divertor target. The gross erosion flux can be broken down into its contributing species to show that $He^{2+}$ is the dominant erosion source followed by $He^{1+}$ and then the W self erosion, as shown in Figure 6.13.

### Summarized results from Integrated PMI/PSI modeling of 40 MW He plasma discharge in ITER

This use of the integrated model to simulate the 40 MW ITER helium discharge demonstrates the establishment of many building blocks of component codes assembled together. The coordination of the wrappers of each component code shows an understanding and familiarity with the physics and file outputs of the individual codes. The assembly of these models provides the computational capability of such an integrated model to share data across components to simulate the edge plasma

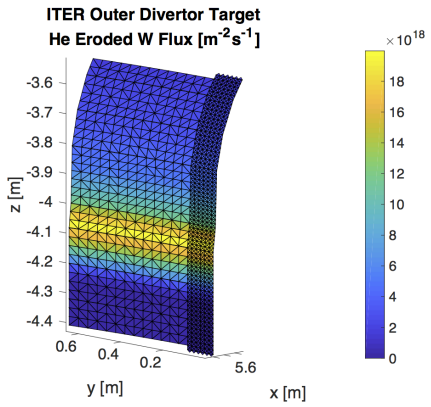


Figure 6.12: W erosion flux by the background plasma as displayed on the 3D GITR geometry. This is the vertical part of the outer divertor with the erosion source above the strikepoint.

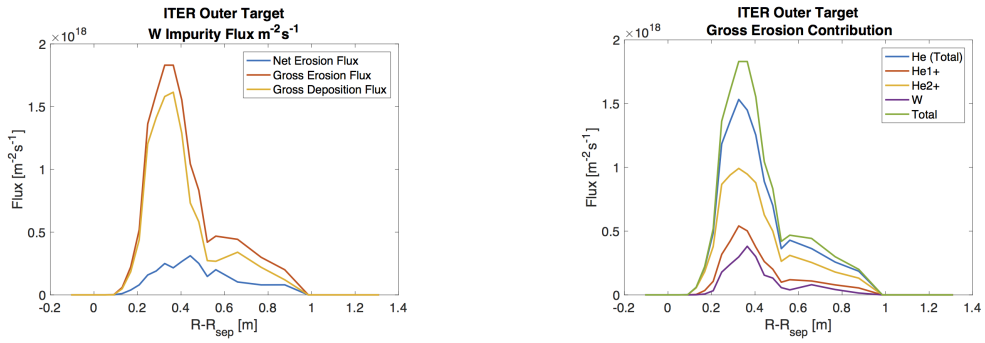


(a) (b)

Figure 6.13: Gross erosion and deposition, and net erosion W at the outer divertor target. Also the break-down of gross erosion of W is shown by species.

quantities, ion distributions at the target, erosion and impurity transport (as well as ion implantation and surface morphology not shown). The results of this integrated simulation show evidence of W erosion by He species along the outer divertor, as well as gross erosion due to the eroded W transport and self-sputtering. Therefore, even during the He operating campaign of ITER, divertor temperatures, densities, and fluxes should be considered in evaluating the net erosion and projected material lifetimes of divertor components. The next section presents a discussion of a more detailed local analysis of the GITR predictions for W erosion and re-deposition in the ITER 40 MW helium discharge.

### 6.2.2 GITR 2D Impurity Transport Study

In order to provide further analysis of model inputs and systematically evaluated forces, simulations using a 2D geometry have been performed. This allows for increased efficiency in checking for particles crossing material boundaries and correspondingly the ability to simulate more particles for more time steps. Identical initial conditions of eroded W impurities are used in this simulation to that from Section 6.2.1. Updates to the background plasma fields obtained from SOLPS (electric field and parallel temperature gradients) have been made for accuracy. Since both electric field and temperature gradient come from taking derivatives (electric field coming from the derivative of potential), these derivatives are updated to be taken on the SOLPS grid using local parallel values.

#### Force Evaluation

To evaluate the patterns of impurity migration in ITER it is useful to produce mappings of relative forces and atomic reactions. For a given input (ion species, charge, velocity, and time interval), GITR will produce mappings using the physics operators within. For the maps to be presented, all of the force/operator evaluation plots are for a $W^{1+}$ ion with 4 eV of kinetic energy (a representative energy of a W atom sputtered by He). These mappings can be used to uncover the physical mechanisms controlling the observed trends in the impurity transport simulation. The first effect to be examined is ionization and recombination. Clearly ionization has a strong effect on prompt re-deposition, allowing particles ionized within one gyroradius of the surface to be deposited on the surface. As well, Coulomb collisions play a large role in the impurity migration of charged ion species which is affected by ion charge. Ionization times are a function of electron temperature and density, and mean free path of ionization must also account for the velocity of the particle. Figure 6.14 shows mean ionization and recombination times (on a base 10 log scale) for a $W^{1+}$ ion in the various regions of the ITER He plasma. Figure 6.14 show that W will be quickly ionized ($10^{-8}s$ or even faster) to higher charge states except for in the periphery of the scrape-off layer and in the private flux region. Recombination on the other hand occurs much more slowly for $W^{1+}$.

The next group of forces to evaluate are those that result from Coulombic interactions. Namely the heating (temperature equilibration), velocity scattering/diffusion and drag forces, and the temperature gradient forces. Figure 6.15 plots the change in velocity in one time step as produced by GITR for a 4 eV $W^{1+}$ ion in $1 \times 10^{-8}s$. The most notable feature of these plots is the strong forces due to the ion temperature gradient force which is observed in the divertor (Figure 6.15b). This force causes a

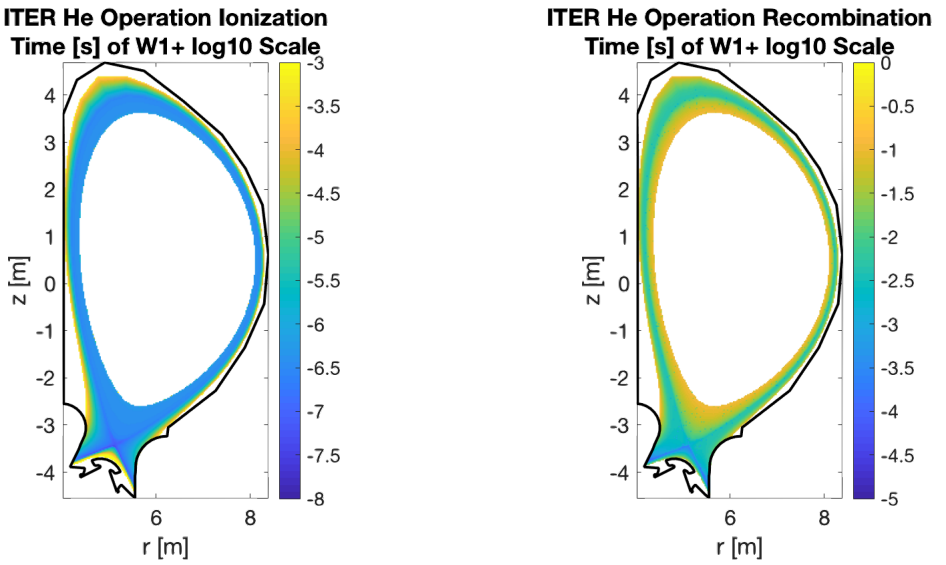


(a) Mean ionization time for 4 eV $W^{1+}$. (b) Mean recombination time for 4 eV $W^{1+}$.

Figure 6.14: Mean times for atomic physics operations ionization (6.14a) and recombination (6.14b) in the ITER He plasma.

change in velocity $\delta v \approx 0.1 m/s$ per time step ($1 \times 10^{-8} s$). This is a very large force in the direction parallel to the magnetic field lines as can be seen in comparison to the change in velocity due to the Fokker Planck collisions in Figure 6.15a. As is typical in tokamaks, the temperature gradient force on ions is directed away from the target going into the page at the inner divertor and out of the page at the outer divertor. These velocity change maps can help in interpretation of results.

### Impurity Density Profiles

Making use of the erosion pattern by the background plasma (He) and magnitude at the outer target described in Section 6.1, the impurity transport simulation has been performed using GITR and the representative 2D geometry which matches the SOLPS geometry. Output from this simulation provides impurity density profiles, as shown in Figure 6.16. This total (summed over all charge states) W impurity density shows that high densities of impurities are near the divertor, outside the separatrix and at the top of the torus. In these regions impurity density levels reach values of greater than $10^{18} m^{-3}$. Other notable features of the impurity density profile are the lack of impurity density in the private flux region. The stark difference in the impurity density in the divertor ($10^{18} m^{-3}$ outside the separatrix, and less than $10^{12} m^{-3}$ in the private flux region result from the very strong ion temperature gradient force, which is shown in Figure 6.15b. At the outer divertor, impurities are forced upstream and away from the divertor target. Once these particles reach the area near the inner divertor target, this force is once again very strong and is responsible for 'pushing' the particles away from the inner divertor. For this reason there is very little impurity density near the inner divertor target.

Impurity density profiles along with background plasma temperature and density can be used to construct radiation profiles in order to predict the amount of energy radiated by the eroded impurities. The three sources of radiation considered here are recombination, Bremsstrahlung, and excitation. Coefficients from the

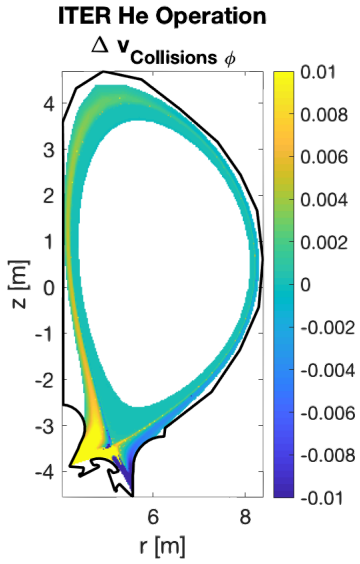


(a) Velocity change in one time step due to $W^{1+}$ ion collisions with the background plasma.

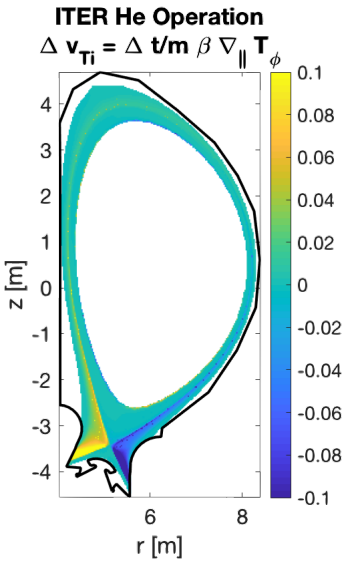


(b) Velocity change in one time step due to the ion temperature gradient force.

Figure 6.15: Velocity change in one time-step due to Coulomb collision forces.

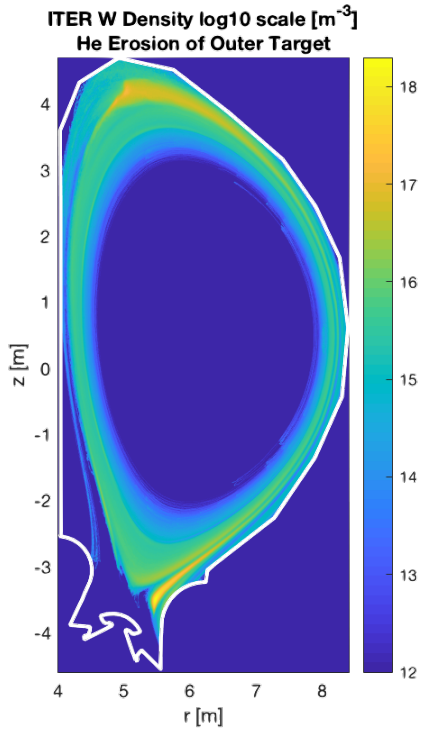


Figure 6.16: Total (all W charge state) impurity density on a log 10 scale for ITER He operation.

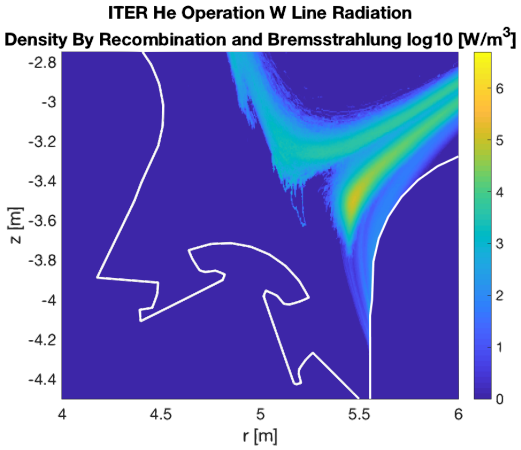


(a) Radiation by recombination and Bremsstrahlung processes for the ITER divertor in He operation.

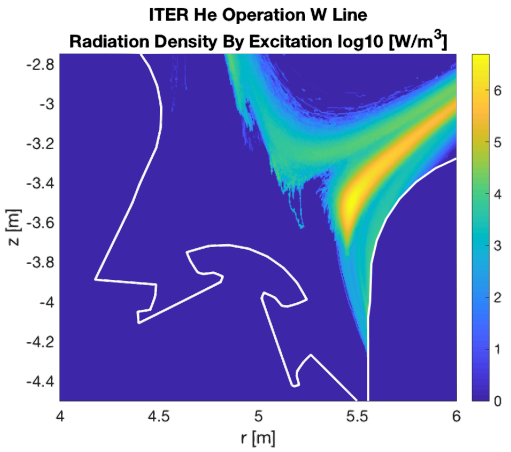


(b) Radiation by excitation for the ITER divertor in He operation.

Figure 6.17: Contributions to radiation by W impurities in the divertor during He operation. Figure 6.17a shows a smaller contribution coming from recombination and Bremsstrahlung than excitation in Figure 6.17b.

ADAS database have been used [36]. Figure 6.17 shows radiation in the divertor on a log 10 scale in units of Watts per meter cubed. Each of the subplots show a strong resemblance to the impurity density profile, with the peak value outside the separatrix in the outer divertor. The two subplots Figure 6.17a, and Figure 6.17b are plotted on the same scale to demonstrate that although these contributions are both significant, the radiation from excitation exceeds the sum of the radiation from Bremsstrahlung and recombination.

### Erosion at the Divertor Target

In addition to the impurities in the plasma, the gross erosion, gross, deposition, and net erosion of the surface can be examined. Figure 6.18 shows the W ion energy-angle distribution along the outer divertor target (Figure 6.18a), as well as the total energy distribution along the divertor target (Figure 6.18b). The energy-angle distribution shows a grouping of relatively low energy (less than 100 eV) particles impacting the surface. Many of these particles are likely to deposit, as the W self-sputtering threshold is $\approx 55eV$ (therefore particles with less than 100 eV will either deposit or sputter a small amount of additional W). There is a separate population of higher energy W ions returning to the surface at several hundred eV. These particles are highly likely to sputter additional W and/or reflect. While Figure 6.18a shows the sum of all divertor surfaces to acquire the IEAD, Figure 6.18b shows the sum over angles and thus plots the energy distribution along the divertor target. The mean impact energy shows an area of lower impact energy (less than 150 eV) at $R - R_{sep} < 0.7m$. A higher mean impact energy is predicted further away from the strike point ($R - R_{sep} > 0.7m$). This trend is not indicative of effects from the sheath potential, as the electron temperature peaks at $R - R_{sep} = 0.2m$ and continues to decay as $R - R_{sep}$ increases. The reason for this effect (the dichotomy of mean energy impact angle along the outer divertor target) lies in the combination of both electron density and temperature and how it effects ionization rate of W. Eroded

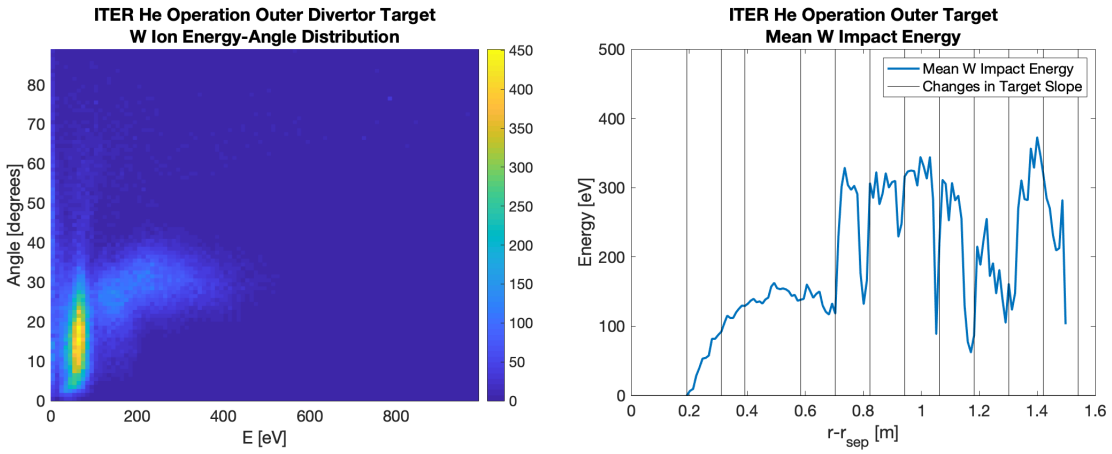


(a) (b)

Figure 6.18: Characterization of the energy and angle of eroded W returning to the outer divertor target. Figure 6.18a shows the full W ion energy-angle distribution, while 6.18b shows the mean impacting energy of W ions.

W atoms near the strikepoint are ionized quickly and return to the surface without heating or reaching higher charge states. Their energy is lower than ions returning further from the strikepoint despite the sheath electric field being larger. Eroded W ions far from the strikepoint do not ionize quickly and therefore travel further from the divertor target (resulting in greater net erosion). The W ions which do return to the surface in this region have greater energy, thus sputtering more W material and producing increasing levels of W erosion. This trend is directly shown in Figure 6.19 which plots the gross erosion, gross deposition, and net deposition of tungsten at the outer divertor target. Figure 6.19a shows the He eroded W flux (blue) and the gross erosion flux (orange) which is slightly greater than the He eroded W. The difference between these two curves is the contribution of W self sputtering, and is small compared to that of He. Upon subtraction of gross erosion and gross deposition, the net deposition is obtained. Figure 6.19b shows that the net deposition flux is largely negative indicating net erosion. The net erosion is significantly smaller on average in the area near the strikepoint ($R - R_{sep} < 0.6m$) than in the region away from the strikepoint ($0.6m < R - R_{sep} < 1.25m$), and there is an impurity buildup near $R - R_{sep} = 1.4$ m. The spikes in the gross and net erosion profile are due to changes in the divertor geometry slope. Sharp features in the geometry can result in significantly different prompt re-deposition characteristics. The changes in divertor geometry slope are shown as black vertical lines in Figure 6.19a corresponding to the sharp changes in erosion patterns.

The spikes in the gross and net erosion profile are due to changes in the divertor geometry slope. Sharp features in the geometry can result in significantly different prompt re-deposition characteristics. A simple example of how this can happen is shown in Figure 6.20. This figure shows an impurity particle track near the surface. The eroded atom is quickly ionized and begins to gyrate near the surface. If the surface was flat (indicated by the dashed line) the impurity atom would deposit. But with the change in the slope the particle does not re-deposit. Assuming equal conditions otherwise, this will result in a greater prompt re-deposition rate for the positively sloped segment of the surface than the flat segment of the surface.

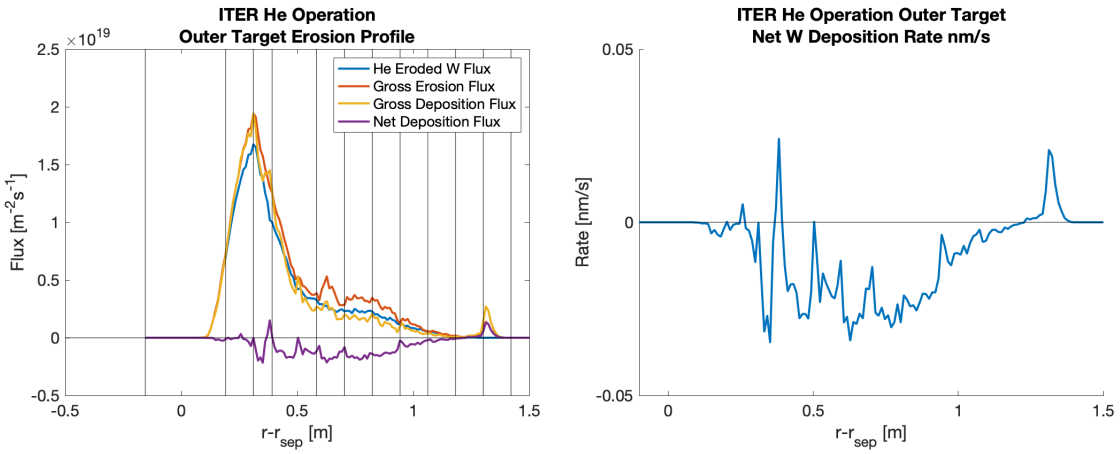


(a) (b)

Figure 6.19: Gross erosion (He and total), gross deposition, and net deposition as simulated for the ITER He operation.

Therefore, what is expected moving in the positive direction of $R - R_{sep}$ is a peak in net deposition flux followed by a trough. This is in fact what is seen in Figure 6.20 where the changes in divertor geometry slope are shown as black vertical lines. Greater amplitude spikes of the net deposition peaks occur in the region of greater prompt re-deposition $R - R_{sep} < 0.7m$. The details of whether changes in surface geometry increase or decrease prompt re-deposition depend on the direction of the surface change and the magnetic field orientations with respect to the surface. Some subtle spikes in the net erosion flux in Figure 6.13a are also visible. By superimposing the locations of the changes in the divertor slope over the net erosion flux shown in Figure 6.13a this can be more clearly seen. Also, since in this case the net value is plotted as erosion instead of deposition, the opposite spike trend should be observed. I.e. there will now be a decrease in net erosion followed by an increase in net erosion. It is the case that with such a large 3D surface geometry complete with tile gaps, significant sorting and averaging was performed in the post-processing to obtain this result. Therefore, the small scale features of variations in net erosion due to changes in slope or tile gaps have been averaged away.

The peak net erosion flux predicted in Figure 6.19b corresponds to approximately 40,000 seconds of ITER He operation to erode 10 microns of W (dividing peak erosion flux by 62.8 $atoms/nm^3$. Averaging over the divertor target, 86% of the eroded W mass is re-deposited on the divertor target. While large fractions of the eroded mass are re-deposited at the target, the remaining eroded mass is distributed about the machine. Figure 6.21 shows the W deposition and erosion flux around the machine. The coordinate at the bottom of Figure 6.21 is a measure of accumulated distance along the first wall with zero being at the outer strikepoint. The green band highlights the area of the outer divertor which is shown in greater detail in Figure 6.19. Moving up the outer wall, W deposition decreases until it completely vanishes before returning at the top of the machine. There is also W deposition at the inner divertor target, but no deposition on the dome.

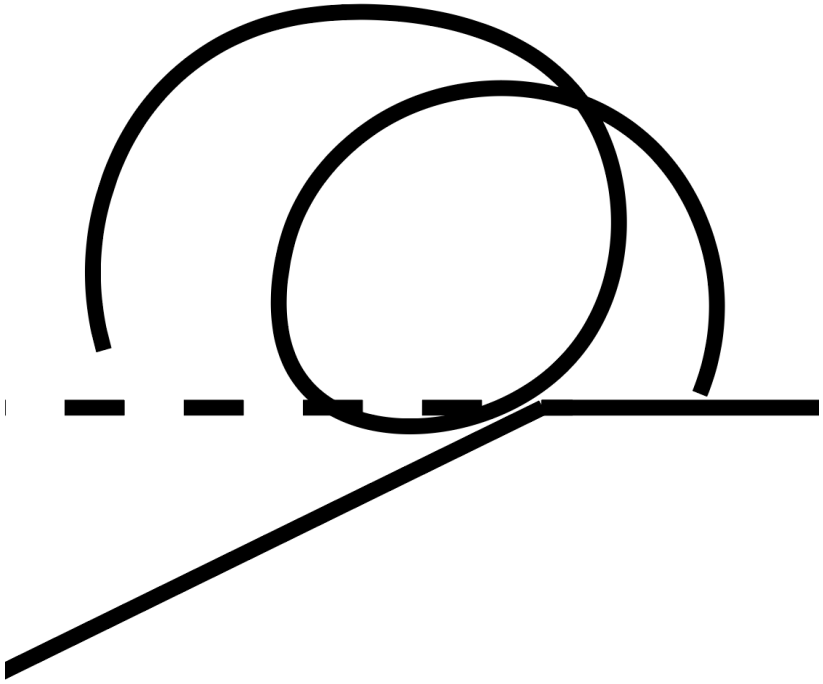

Figure 6.20: Schematic of an eroded impurity being ionized and gyrating near the surface. The curved line is the impurity path, the solid straight line is the surface, and the dashed line is an imaginary surface which would result in prompt re-deposition.

**Summary of results from the GITR 2D impurity transport study of the ITER He discharge**

In summary, by examining the inputs to the GITR impurity transport simulations in greater detail and simplifying the geometry simulated, particular trends and causes for these trends have been uncovered. In particular the ion temperature gradient force is extremely strong in the legs of the divertor, forcing impurities into the scrape-off layer. Additionally, combinations of electron temperature and density can cause large disparities in re-deposited impurity behavior which can also be altered by local geometry. With the framework in place for integrated simulations and investigation of the impurity erosion and migration, additional power and plasma species can be added to simulate ITER D-T operation.

## 6.3 ITER Fusion Power Operation

The second scenario for the integrated plasma-surface interaction simulations is ITER D-T burning fusion plasma operations. The burning plasma case is characterized by high power levels, strong seeded impurity presence as needed to disperse the heat flux, and a mixed plasma species made up predominantly of the main-ion deuterium and tritium ions but with a significant helium component due to helium ash.

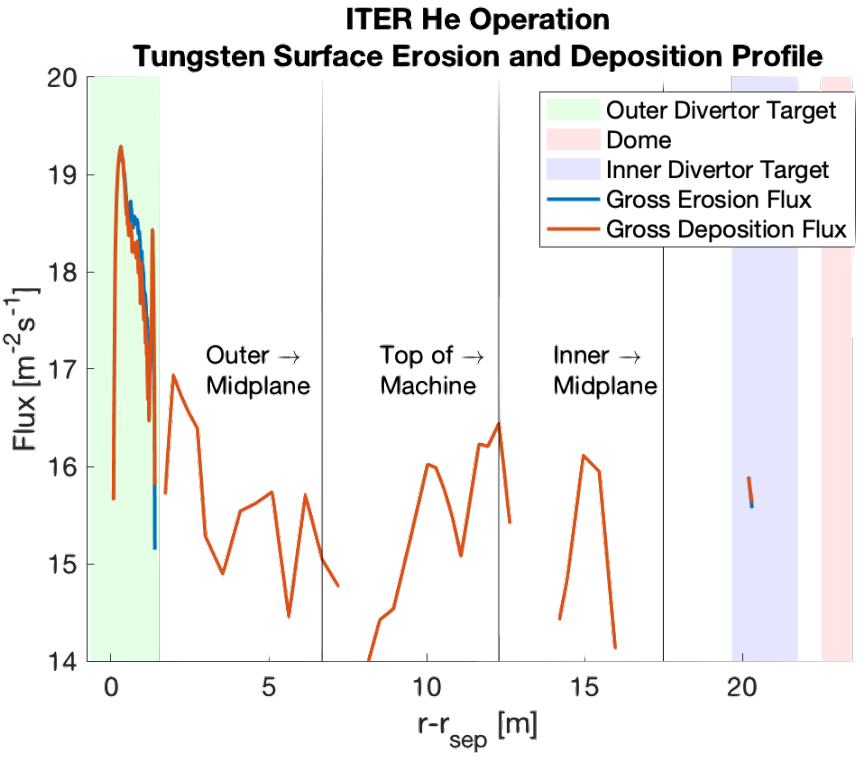


Figure 6.21: Gross deposition flux along the ITER wall. The x-coordinate of this plot is distance along the first wall with zero being at the outer strike point, and working counter-clockwise around the machine.

### 6.3.1 Integrated Modeling Results

#### SOLPS

The scrape-off layer and divertor plasma quatities have been calculated for this ITER scenario once again using the SOLPS-ITER code, and performed by John Canik (ORNL). In the SOLPS simulations described here, the input power was set to 100 MW, representative of full power operations. Deuterium, tritium, helium, beryllium, and neon species are included in the simulation; the plasma is predominantly hydrogenic, with strong radiation being provided by neon seeding. Strong radiation is predicted: 73 MW out of the 100 MW input power is radiated, with nearly the entirety being localized in the divertor region (with only modest differences between the inner and outer leg), and over 80% due to neon. As a result the parallel heat flux near the strike point is significantly reduced at the target compared to the midplane. The resulting heat fluxes on the target are reduced to $\approx 7MW/m^2$ carried by the plasma onto the target plates. The radial profiles of the divertor electron temperature and ion flux are shown in Figure 6.22. The profile shapes are similar to the previously described helium cases, with very low temperature ($\approx eV$) near the strike point and increasing farther into the SOL, but now with much higher densities and ion fluxes. The electron density is very high near the strike point, reaching values of $\approx \ 3 \times 10^{21} m^{-3}$. Likewise the ion flux is high near the strike point, with a peak value of $\approx 1 \times 10^{24} m^{-2} s^{-1}$. The density and ion flux both decrease significantly farther into the SOL. Figure 6.22 shows D, $He^{2+}$, and $Ne^{3+}$ fluxes ($He^{2+}$ is the highest peak He flux and $Ne^{3+}$ is the highest peak

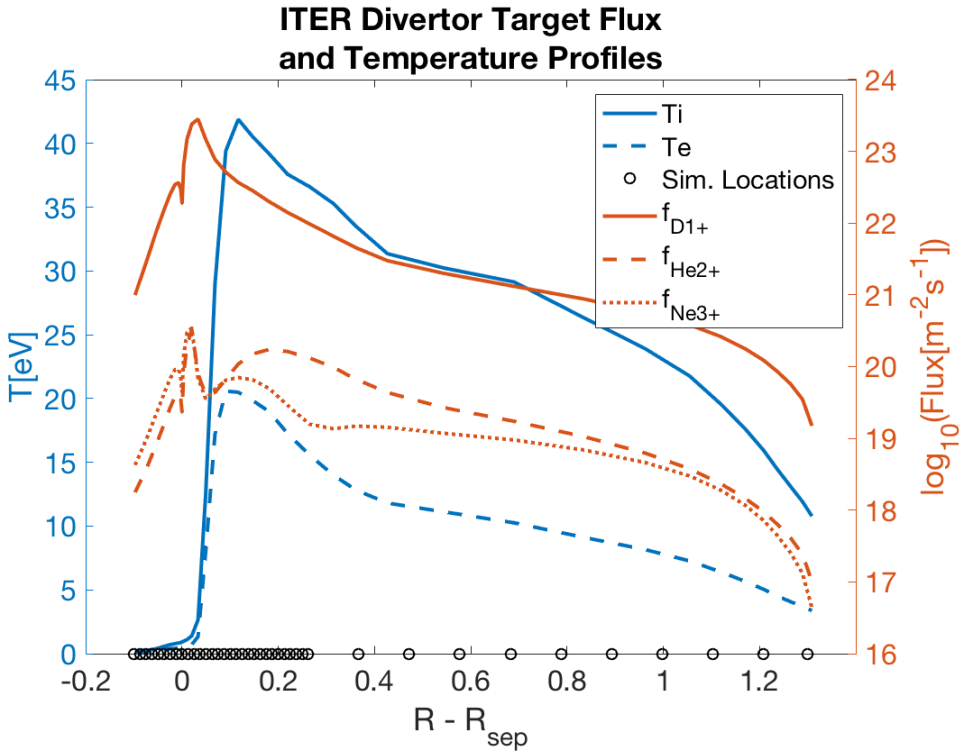


Figure 6.22: Ion and electron temperatures at the outer divertor target in coordinates of $R - R_{sep}$ in meters. Fluxes for D, $He^{2+}$ and $Ne^{3+}$ are also plotted (log 10 scale).

Ne flux) to demonstrate the relative magnitudes of the flux at the outer divertor target, in addition to the electron and ion temperatures. One additional example of SOLPS output is the ion temperature profile which is shown in Figure 6.23. The ion temperature is shown to be significantly reduced in the SOL and divertor legs (100s of eV) compared to that inside the last close flux surface (1,000s of eV). This figure is also a good demonstration of how the B2 simulated grid matches the geometry in the divertor. Along the divertor where field lines from the SOL intersect the target, there is full data available from SOLPS. In the pumping region and in some areas of the first wall, gaps in the data can be observed.

### hPIC

The SOLPS data of the ITER fusion power D-T operation scenario have been sampled at 36 locations along the poloidal coordinate '$R - R_{sep}$' at the outer divertor target. The data provided includes the plasma conditions in at the divertor target, for a total of 18 charged species including D, T, He, Ne (each with multiple charged states). The SOLPS data are passed as input to the hPIC Particle-in-Cell (PIC) code, a full-f, full-orbit PIC resolving the plasma sheath physics. The hPIC code once again receives information on the local magnetic field (magnitude of the field and angle with respect to the wall) at the point of interest on the target plate, and provides as output the energy-angle distribution of the ions impacting on the surface. Figure 6.24 is a reduction of the IEADs produced by hPIC for neon to shown the energy distribution of Ne ions along the outer divertor target. The energy distribution of neon as well as other ion species follows the shape of the electron density

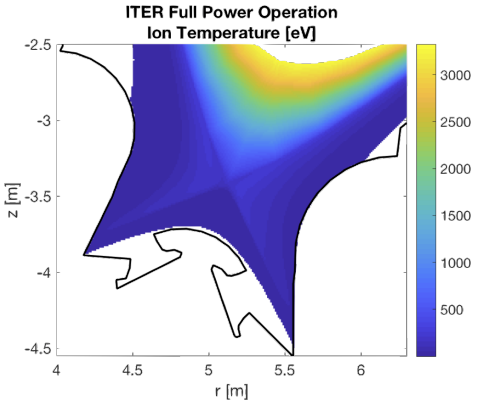


Figure 6.23: A single ion temperature is used in SOLPS plasma simulation to represent all plasma ion species. This temperature [eV] is shown in the divertor for fusion power operation.

profile at the outer divertor target. In addition to the energy distribution shown in Figure 6.24, a sputtering yield for Ne on W is also given using the mean neon energy at normal incidence as the white line overlaid which reaches nearly 0.08. A more accurate representation of sputtering yield is later given.

### F-TRIDYN

Fractal TRIDYN has once again been employed to generate sputtering yields for background plasma species (D, T, He, Ne, Be omitted). In the interest of brevity, this section only shows a limited number of F-TRIDYN preodictions, in this case one direct output of the sputtering yield as a function of energy and angle for Ne on W. Figure 6.25 shows a sputtering threshold of less than 100 eV and a range of more than four orders of magnitude in sputtering yield between 10 eV and 1,000 eV impact energies. The combination of the F-TRIDYN sputtering model along with the hPIC IEADs and the SOLPS surface fluxes for each ion species gives the erosion flux of the W divertor by the background plasma ions. Once again, with the sputtering yield for a given species given from F-TRIDYN as $Y_s(E, \theta)$ (the s subscript indicating different elemental species) and $f_s(E, \theta)$ as the IEADs given by hPIC for each charge state species, the sputtering yield by a given ion species is given by Equation 6.1.

Upon performing this integration, Figure 6.26 shows that the neon species have much larger sputtering yield than the background hydrogen and helium species. The neon sputtering yields reach as high as 0.12, and the sputtering yield is generally higher for the higher charge state neon species. This trend comes about because of

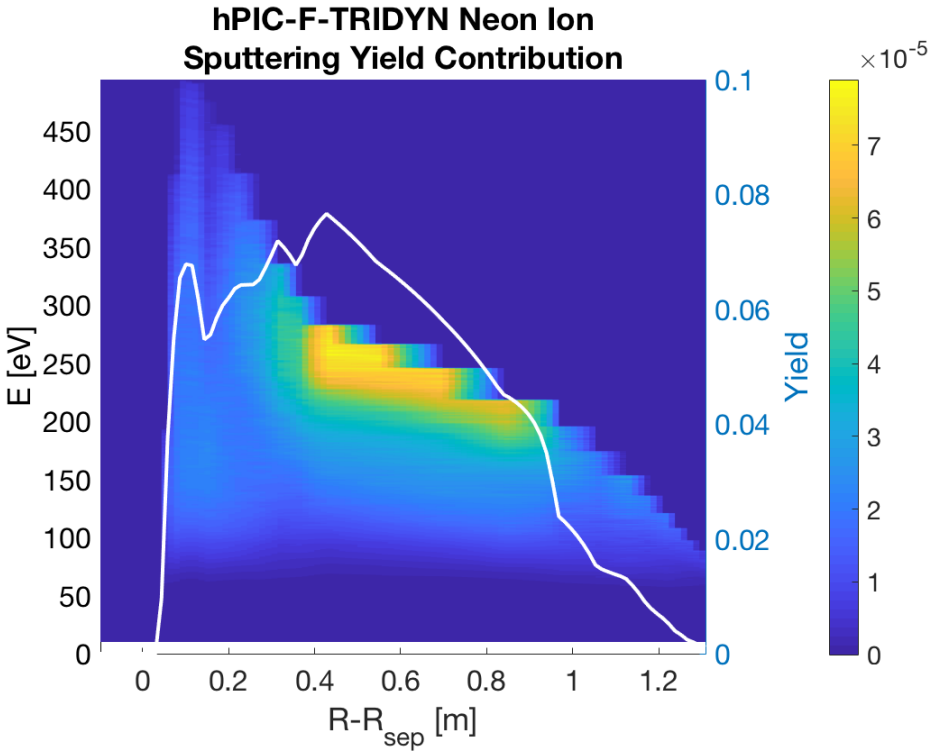


Figure 6.24: Neon energy distribution function and sputtering yield resulting from the energy-angle distribtution.

the increased impact energies of higher charge states accelerated through the sheath electric field. When the relative flux magnitudes of each ion species at the target are taken into account we can produce an effective yield. This operation is performed according to Equation 6.2. Figure 6.27a plots the effective yield summed over each element. By multiplying these yields by total ion flux we can obtain eroded W flux $\Gamma_W = \bar{Y}_s * \Gamma_{ion}$ Figure 6.27b then shows which background plasma ion species are responsible for most of the sputtering of W divertor material and the sputtering trend along the target. Neon is the dominant contributor to erosion, although it can be seen that T is a significant sputtering contributor while D erodes much less W material and that the contribution of He to W sputtering is nearly negligible. One notable feature in the neon effective yield is the double peak with a reduced effective sputtering yield between the peaks at $R - R_{sep} = 0.15m$. This feature can be explained by examining the Ne energy distributions along the ITER outer divertor target as well as the relative flux fractions of Ne in Figure 6.24. We can see that in general, the impact energies are proportional to electron temperature and fall between $3 \times T_e$ and $24 \times T_e$. Between these two bounds, we can see that the relative populations of the energy distribution shift with respect to the upper and lower bounds as well as the average energy. In particular between $R - R_{sep}$ of 0.3 m to 1 m there is an increase in the energy distribution that arises because of an increase in the higher charge ($Ne^{8+}$ and $Ne^{3+}$) fluxes to the target. This becomes more apparent when multiplying the energy distributions by the sputtering yield as shown in Figure 6.24, which shows the relative contribution of each energy to the sputtering of the tungsten target by neon. This highlights the contribution of the high energy IEADs of neon and their impact on erosion of the W target. By

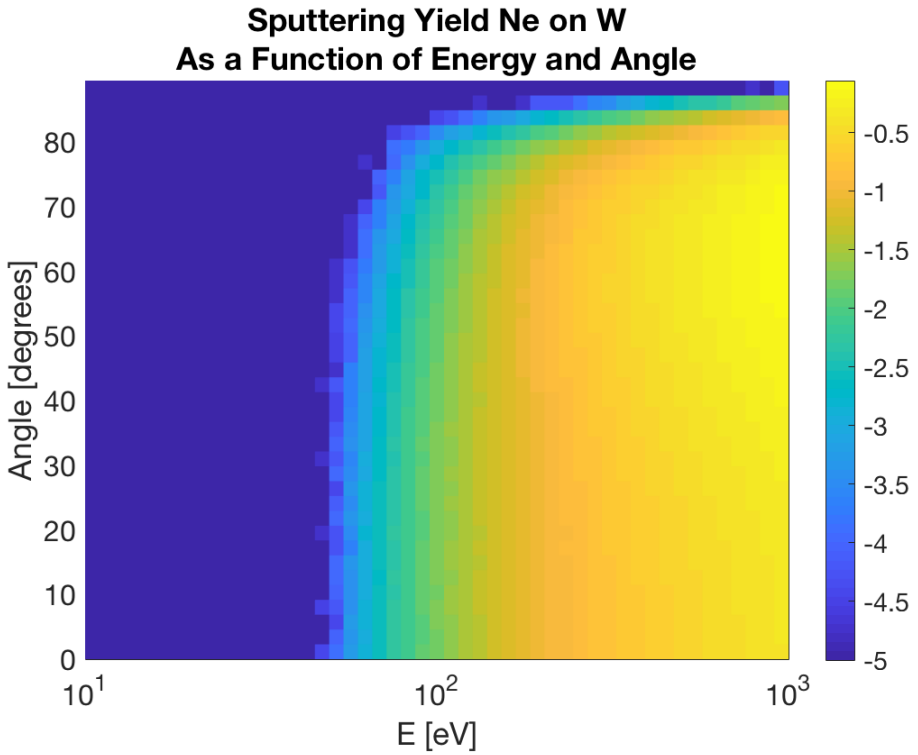


Figure 6.25: Neon sputtering yield on W as a function of energy and angle as produced by F-TRIDYN

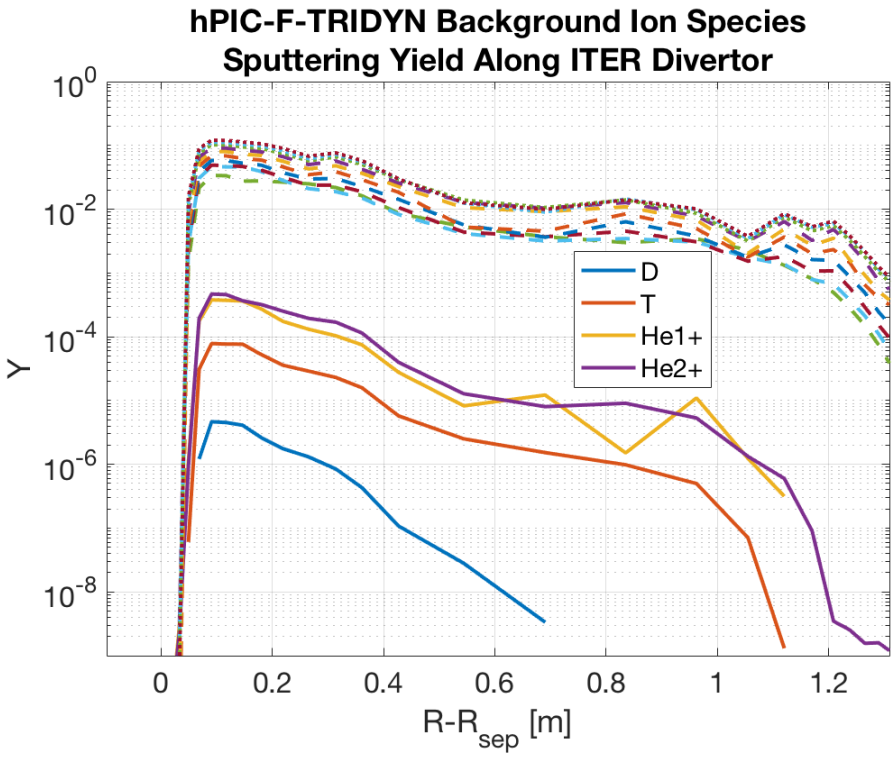


Figure 6.26: Sputtering yield for species included in the fusion power operation for ITER. The unlabeled (dashed) lines are the 10 charge states of neon.

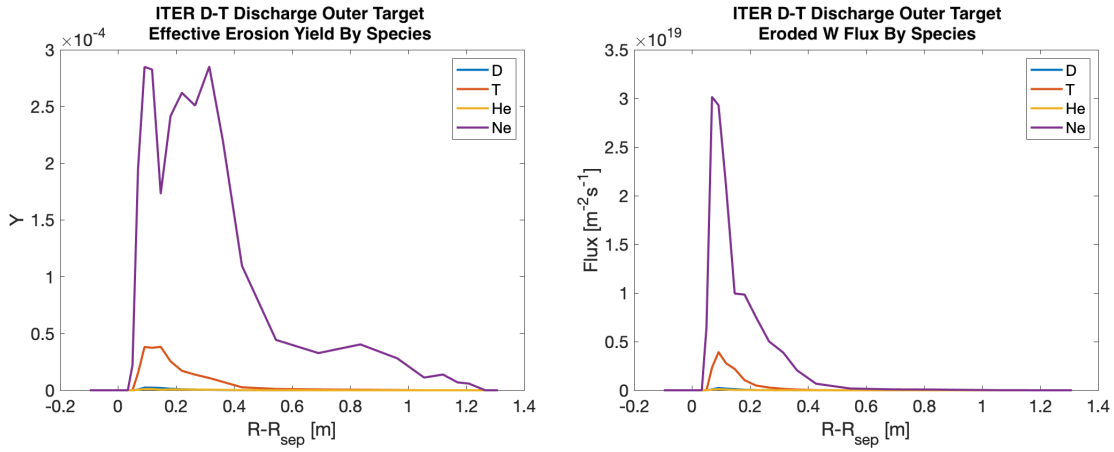


(a) (b)

Figure 6.27: Effectve erosion yield and flux by background ion species along the outer divertor target for fusion power operation.

summing over these relative contributions a total effective yield for neon is acquired (white line using the right axis), and the double peaked behavior of the effective sputtering yield of the background plasma (dominated by neon) is reproduced.

The general flux trend in the area with temperatures high enough to create erosion by background plasma species is to decrease away from the strike point. This results in a significant change in the shape from the effective sputtering yield to the eroded W flux. Figure 6.27b plots the W sputtering calculated for the 100 MW D-T burning plasma discharge in ITER, as a function of the elemental contribution, clearly showing that neon is the species responsible for the majority of the tungsten erosion.

### GITR predictions of gross and net erosion

Applying the background plasma eroded W profile along the divertor target plotted in Figure 6.28, we acquire our initial conditions for the spatial distribution of the eroded W impurity flux in the 3D ITER geometry. In addition to the spatial distribution of eroded W impurities, the integration of the F-TRIDYN-hPIC simulation data provides the sputtered W energy and angle distributions. The sputtered W energy distribution involves an average energy of 9 eV for the sputtered W along the majority of the eroded area. The median energy, however, is only on the order of 4 eV. For these simulations, we make use of the conservative assumption in F-TRIDYN of zero bulk binding energy for the target and this results in a conservative (over-prediction) of the erosion yields, as well as the sputtered energies. The additional initial conditions include the sputtered angle distributions of W by the background plasma. The average sputtered W azimuthal angle is between 50 and 60 degrees where 0 degrees is normal incidence, with the peak of the distribution between 60 and 70 degrees. This indicates that most W atoms sputtered by the background plasma are sputtered more along the direction of the surface (greater than 45 degrees) than in the direction perpendicular to the surface. With the additional information from the poloidal angle of the sputtered W averaging 90 degrees, this shows that the W atoms are sputtered in the “forward” direction with respect

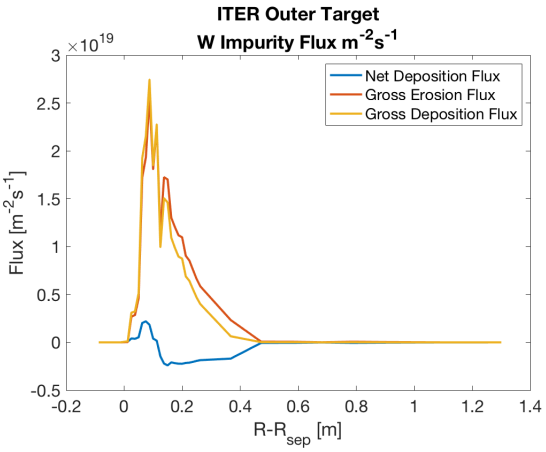


(a) Total gross erosion, gross deposition and net deposition flux.

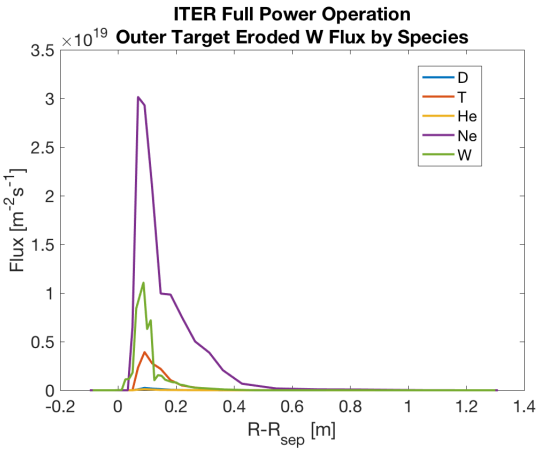


(b) Eroded W flux by species.

Figure 6.28: Gross deposition and erosion, and net deposition of tungsten at the outer divertor for fusion power operation.

to the magnetic field angle and the impact of the background plasma ions.

The results of the W impurity transport simulation performed with GITR predict a gross W erosion profile along the target, shown by the orange line in Figure 6.28a. Much of the eroded W impurity flux is re-deposited, as shown by the yellow line representing gross deposition. However, a fraction of the eroded impurities are transported in the direction of the strike point creating a net deposition region ranging from $R-R_{sep} = 0$ to $R-R_{sep}$= 0.1 m. In total for the impurity transport simulation, 93% of the eroded W is deposited in the divertor region with approximately 7% of the eroded W being transported to the scrape-off-layer or divertor plasma (including the private flux and open magnetic field regions) and re-distributing. Taking the gross erosion flux contribution from W self-erosion in GITR and comparing it to the magnitudes of the erosion due to the background plasma ions, Figure 6.27a shows that Ne is the dominant eroding species, but W becomes a significant contributor, especially at $R - R_{sep} < 0.05m$.

In comparing the erosion and deposition profiles of the D-T operation to that previously described for the ITER He plasma discharge, it is noted that the distance along the divertor target which is affected by significant erosion or deposition is significantly smaller for the D-T plasma discharge. The D-T plasma discharge results in a region of approximately 10 cm of net deposition followed by an area of net erosion which is approximately 40 cm. The zone of notable impurity flux in the He ITER discharge spans approximately 80 cm extending from $R-R_{sep}$= 0.2 m to $R-R_{sep}$= 1.0 m. This results from the difference in area affected by erosion by the background plasma. By comparing the effective sputtering yields of the He species from Figure 6.10 and Figure 6.27a, the peak of the neon sputtering yield is significantly more narrow than that of the helium from the ITER Helium discharge. In both the He and the D-T discharges, multiplying these effective yields by a decaying flux to the target across the SOL continues to narrow the region of erosion. The peak magnitude of sputtering by neon in the D-T discharge is half the magnitude of that for helium in the He discharge. Therefore, the peak magnitude of erosion for both the He and D-T discharges which have been characterized here is approximately equal (erosion flux of

$2 \times 10^{18} m^{-2} s^{-1}$), with a broader erosion zone in the He discharge. Figure 6.28b plots the gross W eroded flux by species including W. After Ne, W is the major species responsible for erosion, which follows the pattern of erosion by Ne very closely. The area of greatest gross erosion by W is also the area of impurity accumulation near the strikepoint. Therefore, eroded impurities that are from further away from the strikepoint are transported to this area ($R - R_{sep}$=0 to $R - R_{sep}$=0.1 m) where significant erosion occurs with a high re-deposition fraction. I.e., tungsten eroded from the net erosion area ($R - R_{sep}$=0.2 to $R - R_{sep}$=0.4 m) is transported to the region of net deposition ($R - R_{sep}$=0 to $R - R_{sep}$=0.1 m) and causes significant sputtering. However, very large fractions (greater than 95%) of the W sputtered W in this region is promptly deposited.

Finally, the impurity density near the divertor target is shown in Figure 6.29. The reduced length of the divertor which is eroded by the background plasma profile in the burning plasma discharge is noticeable compared to the impurity density profile shown for the He discharge. This is evident by the impurity density not extending up the curved part of the divertor target with the same magnitude as it is more near the strikepoint. Similar to the impurity density profile from the He discharge, the impurity density profile for the D-T discharge is once again marked by sharp changes across the separatrix (5 orders of magnitude). Along the separatrix, the largest relative values of density can be observed, indicating a strong pinch inward at this location. As has been performed for the He discharge, force mappings and updated plasma profiles should be used to continue to investigate the reasons for the impurity migration trends observed here.

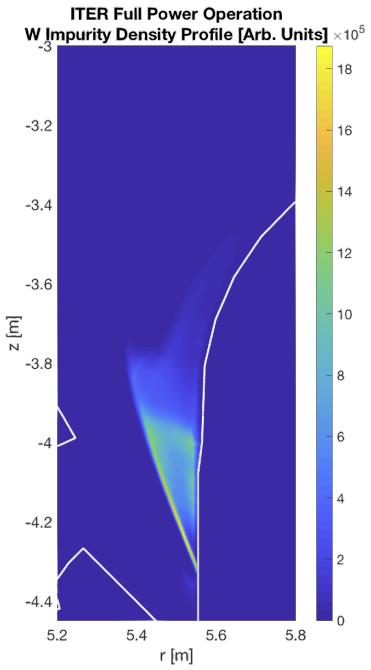


Figure 6.29: W impurity density at the outer divertor target.

## 6.4 Summary

In summary, a suite of high fidelity physics codes have been integrated in order to produce results for the plasma-surface interactions in ITER. Helium and D-T fusion power operations have been simulated with fluid edge plasma codes, and making use of target conditions the boundary conditions of the surface model have been enhanced to include ion energy-angle distributions. The distributions and flux magnitudes in combination with ion sputtering and reflection kinetics show areas of erosion for both He and D-T operation of ITER at the outer divertor target. However, the width of the erosion area (in poloidal distance) is significantly larger in the He discharge at 80 cm compared to that for the D-T discharge (40 cm). With this eroded source as the initial conditions for the GITR impurity transport model, re-deposition rates as well as migration and radiation have been evaluated. Simulation of impurity migration in the He discharge revealed that divertor geometry with respect to the magnetic field can result in variations in deposited impurity flux. Ion temperature gradients can be a driving force in divertor leakage in ITER, leading to impurity densities of greater than $1 \times 10^{18} m^{-3}$ in the scrape-off layer. W impurities may radiate greater than $10^6 W/m^3$ in the divertor, and areas of low plasma density may contribute to more net erosion than areas with greater density. Simulation of the D-T discharge in ITER has revealed that seeded impurities can be the dominant source of erosion of the divertor with effective yields as high as $2.5 \times 10^{-4}$. However, increased input power does not directly translate to greater erosion, as radiation and prompt re-deposition can buffer increased particle fluxes. The D-T discharge resulted in a greater peak erosion by the background plasma ($3 \times 10^{19} m^{-2} s^{-1}$) than the helium discharge ($2 \times 10^{19} m^{-2} s^{-1}$). Although improvements to code performance and verification are still underway, the ground work in implementing the infrastructure for data passing and code execution has been accomplished through this project.

# Chapter 7

# Summary and Direction for Future Research

## 7.1 Motivation for Modeling PSI

In order to create a neutron source via thermonuclear fusion, a hot (10s of keV), dense ($\approx 10^{22} m^{-3}$), plasma of certain species (most favorably D-T) must be confined for a sufficiently long time to fuse. Magnetic confinement devices such as tokamaks use closed field lines to confine the plasma with open field lines connected to a diverted target region to localize the plasma-surface interaction away from the core plasma. This is designed to increase the migration length for impurities required to reach and contaminate the core plasma, as only a tolerable fraction ($10^{-5}$ for W) can exist in the core before radiation and fuel dilution extinguish the fusion reaction and plasma. At the plasma-material interface in the divertor, the edge plasma meets the divertor target with large ion flux ($\approx 10^{22} m^{-2} s^{-1}$ where background plasma ions reflect, implant, and sputter surface atoms. The SOL plasma parameters affect the ionization, migration, and re-deposition of eroded impurities affecting the net gain or loss of material from the surface. Implanted ion species change the surface composition and material characteristics and surface morphology. These resulting changes can affect sputtering behavior, the material's ability to remove heat flux, and fuel recycling and retention behavior. Therefore, an integrated model of the plasma-surface interaction making use of high fidelity physics codes, coupled in a computational and data resource management framework is needed to address the necessary physics and investigate the cumulative effect.

## 7.2 Prior Research

Prior research shows two major approaches in modeling eroded impurities and their migration. The first being fluid models for the scrape-off layer, the second being Monte Carlo codes in 2D or 3D which track the kinetics of eroded impurities. As an example, SOLPS has been updated to simulate all charge states (or a truncated or bundled set of charges) for heavy metal impurities such as W. This comes at a computational cost of adding additional fluid species, but self-consistently models the interactions between species and the effect on the scrape-off layer plasma. Drawbacks to this approach include the use of simple models for erosion which do not

capture the direct re-deposition of heavy ions, as well as field-aligned grids which do not conform to the wall of the machine at all points. Kinetic Monte Carlo codes such as DIVIMP and ERO have demonstrated success in modeling light and heavy impurity ions, although not treated in a self-consistent manner. DIVIMP has the capability of modeling global impurity transport and has shown success in modeling impurities for a variety of tokamaks including JET discharges with the ITER-like wall. ERO has modeled numerous linear device experiments as well as local limiter and divertor experiments with tuning of certain parameters. Drawbacks to DIVIMP include the approximation of prompt local re-deposition because the guiding-center approximation used. It is also limited to 2D toroidally symmetric geometries which omit 3D toroidal asymmetries which may be important. Although ERO makes use of 3D geometries, the computational layout of the code is limiting to non-global areas. Additionally by its use of simple models for the background plasma profiles within the code, it is not easily modified for interfacing/integration with other component physics modules.

Accounting for the strengths and weaknesses of existing computational tools, the opportunity to develop additional models to evaluate the plasma-surface interaction and plasma-facing devices exists. With an advanced computational model, full-wall simulation of eroded mass can be simulated making use of high fidelity 3D geometries. This model includes full gyro-orbit simulation to capture prompt re-deposition, as well as many-hop and long range migration making use of input physics models for background plasma, sheath, and surface models.

## 7.3 Tool Development and Original Contribution

This dissertation performs a wide range of development of computational tools in working towards an integrated simulation of the plasma-surface interaction. In particular the work in developing the global impurity transport code as well as the tools to adapt, execute, and process output from component physics codes for edge plasma simulation, surface models for sputtering and reflection, along with input of additional particle kinetics of the background plasma. Additionally, wrappers for GITR to interface with additional component physics codes have been developed.

The GITR code development effort makes use of a platform-portability solution, the THRUST library, enabling various parallel device options at compile time, including CUDA and openMP. The implementation of a Boris particle push, Fokker-Planck Coulomb collisions for a test particle, thermal gradient forces, as well as ionization and recombination are effectively implemented. Custom 2D and 3D surface geometry algorithms have been formulated for checking particle trajectory intersection with boundaries. Additionally sputtering and reflection models are applied at the material surfaces to simulate the erosion, reflection, and deposition of impurities.

## 7.4 Code Verification and Benchmarking

Various simple metrics have been used to verify the integration of particle paths, including in curved and varying magnetic fields. Checks on average evolution of particle distributions and Maxwellianization has been clearly demonstrated. Additionally, integrated benchmarks with simple fluid theory and code-code comparison

with DIVIMP have been performed to evaluate parallel transport of ions in the scrape-off layer. This evaluation of impurity transport in the scrape-off layer is an essential check that in the collisional regime the kinetic model converges to agreement with a fluid approximation. With such results in hand, kinetic effects with increasing temperature and decreasing density can be investigated with a sub-set of physic so that results can be easily rationalized. This code verification gives confidence that physics algorithms are implemented in the correct way, however, continued physical evaluation of the model remains.

## 7.5 PISCES-A simulations of He exposed W

Simulation of dedicated linear plasma device exposures in the PISCES-A device have been performed at various levels of GITR implementation, investigating the effect of adding additional physics. An exposure set-up making use of mass change measurements as well as emission spectroscopy gives comparable results for GITR as the experiment is used as a benchmark. The three phases of PISCES-A simulation include the use of analytic fits for eroded W energy and angle distributions, updating the surface model to use inputs from F-TRIDYN as part of the integrated simulation, and the formal uncertainty quantification of the effect of uncertainty in background plasma profiles on the W impurity transport. Making use of various energy-angle distributions for eroded W and varying the plasma temperature and density profiles by $+/-20\%$ results in an uncertainty band on the order of the experimental error for the target mass loss, bead mass gain, and emission spectroscopy measurements. It is clear that variation in the angular distribution of sputtered tungsten has a substantial effect on the amount of mass deposited at the base of the bead tower. Implementation work creating parallel programs to call F-TRIDYN to build up data tables for GITR (as well as Xolotl) has resulted in a very useful tool. Adapting this output for GITR, the results of the impurity transport simulations are updated to give better agreement with a more reliable source for W energy-angle distributions. Finally, a formal uncertainty quantification effort was performed with collaborators at Sandia National Labs in order to investigate the impact of uncertainty in background plasma profiles on impurity transport. By addressing the nature of the error coming from Langmuir probe and using Bayesian analysis with Markov Chain Monte Carlo, a finite number of samples of the uncertain input (electron temperature and density) were created and simulated with GITR. Results for the high and low flux exposures demonstrate the type of error (fitting or inherent uncertainty) and the relative sensitivity of the parameters.

## 7.6 ITER Research

Simulating the plasma-surface interaction at the ITER outer divertor target has been performed for a 40 MW He discharge as well as a 100 MW D-T Neon seeded discharge. Making use of plasma profiles simulated with SOLPS-ITER, plasma and target profiles are passed to other physics simulations. hPIC provides additional particle kinetics (ion energy-angle distributions at the target), which along with F-TRIDYN sputtering yields give a sputtered W source. The sputtered W source is then simulated by GITR. The erosion source for the He exposure shows a broad

area of eroded W by He species. Over this broad area the plasma density varies significantly giving distinct areas of prompt re-deposition and net erosion with approximately 80% of material returning to the divertor target. Partially responsible for the relatively low re-deposition rates is the large ion temperature gradient which forces particles away from the divertor. During the D-T discharge, Ne is shown to be a dominant erosion species with a more narrow band of erosion on the outer divertor. The D-T discharge is characterized by higher re-deposition fractions (93%) with a pile-up of material near the strike-point. Evaluating both the He and D-T dishcarges, the peak erosion of each is approximately equal, eroding approximately 0.04 nm/s of steady state operation.

## 7.7 Code adoption

With the need for PSI modeling at various research organizations, the adoption of GITR as well as other parts of the integrated simulation capability is underway. In particular, use of these tools at Oak Ridge National Lab, DIII-D, and WEST has begun. At ORNL, the prototype materials exposure facility is developing exposure hardware to vary the exposure angle of a W plate with respect to the plasma to investigate prompt re-deposition fractions. Modeling of this effort is being performed with GITR. At the DIII-D tokamak, several experimental scenarios are in need of modeling support. DiMES experiments are underway to understand the migration patterns and prompt re-deposition fractions in the divertor. A combination of OEDGE for the background plasma, with GITR for the impurity transport simulation is being used. The SAS (slot angle divertor) which contains W components is being investigated for eroded W leakage. SOLPS is being used for the background plasma profiles with F-TRIDYN and GITR used for sputtering and impurity transport. Additionally, the WEST toakamak is performing probe exposures to investigate the comprehensive effects of PMI including erosion, the effects of particle kinetics at the surface, as well as implantation of ions and evolution of surface composition and morphology, making use of the full integrated simulation capability.

## 7.8 Direction for future research

As a direction for future research, additional fundamental scenarios including flow reversal in the SOL should be investigated to see the fundamental effect on impurity leakage. To this end, fundamental benchmarks should become part of the hardening and verification of the integrated model. Opportunities for linear machine experiments at ORNL should continue to be sought out and capitalized on. In depth analysis of background plasma profiles for ITER simulations should continue to be investigated to show the effects of erosion and the ion temperature gradient force. In summation, the groundwork in development of various computational tools together in a framework or separately will hopefully provide continued opportunities for science discovery, interpretation, and advancement.

# Bibliography

[1] Weston M. Stacey. *Fusion plasma physics*. Weinheim Chichester: Wiley-VCH ; John Wiley distributor, 2005, xiv, 557 p. ISBN: 3527405860.

[2] J. Ongena and G. Van Oost. "Energy for Future Centuries: Prospects for Fusion Power as a Future Energy Source". In: *Fusion Science and Technology* 61.2T (2017), pp. 3–16. ISSN: 1536-1055 1943-7641. DOI: 10.13182/fst12-a13488.

[3] C.S. Pitcher. "Tokamak Plasma Interaction with Limiters". Thesis. 1987.

[4] Jeffrey P. Freidberg. *Plasma physics and fusion energy*. Cambridge: Cambridge University Press, 2007, xvii, 671 p. ISBN: 9780521851077 0521851076.

[5] T. Pütterich et al. "Calculation and experimental test of the cooling factor of tungsten". In: *Nuclear Fusion* 50.2 (Jan. 2010), p. 025012. DOI: 10.1088/0029-5515/50/2/025012. URL: https://doi.org/10.1088%2F0029-5515%2F50%2F2%2F025012.

[6] EuroFusion. *The plasma edge research for tomorrow's energy supply*. 2014. URL: https://www.euro-fusion.org/fusion/spot-on-jet-operations/maintaining-the-plasma/plasma-edge/ (visited on 11/10/2017).

[7] C Corr et al. "Fusion-relevant plasma surface interactions". In: *31st ICPIG, Granada, Spain* (2013).

[8] V Barabash et al. "Armour Materials for the ITER Plasma Facing Components". In: *Phys. Scr.* 74 (1999).

[9] P.C. Stangeby. *The Plasma Boundary of Magnetic Fusion Devices*. IOP Publishing Ltd., 2000.

[10] R.P. Doerner M.J. Baldwin. "Formation of helium induced nanostructure 'fuzz' on various tungsten grades". In: *Journal of Nuclear Materials* 404 (3 2010), pp. 165–173.

[11] G. Kalinin et al. "The ITER Home Teams, Assessment and selection of materials for ITER in-vessel components". In: *Journal of Nuclear Materials* 283–287 (2000), pp. 10–19.

[12] B. D. Wirth et al. "Fusion materials modeling: Challenges and opportunities". In: *MRS Bulletin* 36.03 (2011), pp. 216–222. ISSN: 0883-7694 1938-1425. DOI: 10.1557/mrs.2011.37.

[13] R. Schneider. "B2-EIRENE simulation of ASDEX and ASDEX-Upgrade scrape-off layer plasmas". In: *J. Nucl. Mater.* 196-198 (1992), pp. 810–815.

[14] T.D. Rognlien. "2-D fluid transport simulations of gaseous/radiative divertors". In: *Contributions to Plasma Physics* 34 (1994), pp. 362–367.

[15] R. Zagorski. "Numerical Simulation of the TEXTOR Edge Plasma Including Drifts and Impurities". In: *Contributions to Plasma Physics* 38 (1998), pp. 61–66.

[16] X. Bonnin and D. Coster. "Full-tungsten plasma edge simulations with SOLPS". In: *Journal of Nuclear Materials* 415.1 (2011), S488–S491. ISSN: 00223115. DOI: 10.1016/j.jnucmat.2010.10.041.

[17] A. Fukano et al. "Modeling of multi-dimensional impurity transport in a realistic tokamak geometry". In: *Journal of Nuclear Materials* 363-365 (2007), pp. 211–215. ISSN: 00223115. DOI: 10.1016/j.jnucmat.2007.01.037.

[18] M. Toma et al. “Comparison of kinetic and fluid models for tungsten impurity transport using IMPGYRO and SOLPS”. In: *Journal of Nuclear Materials* 438 (2013), S620–S624. ISSN: 00223115. DOI: 10.1016/j.jnucmat.2013.01.130.

[19] J. N. Brooks. “Near-surface sputtered particle transport for an oblique incidence magnetic field plasma”. In: *Physics of Fluids B: Plasma Physics* 2.8 (1990), pp. 1858–1863. DOI: 10.1063/1.859457. eprint: https://doi.org/10.1063/1.859457. URL: https://doi.org/10.1063/1.859457.

[20] J Hogan et al. “Integrated impurity model for actively cooled plasma facing components”. English. In: *FUSION ENERGY 1996, VOL 2*. PROCEEDING SERIES OF THE INTERNATIONAL ATOMIC ENERGY AGENCY. 16th International Conference on Fusion Energy, MONTREAL, CANADA, OCT 07-11, 1996. Int Atomic Energy Agcy. WAGRAMERSTRASSE 5, PO BOX 100, A-1400 VIENNA, AUSTRIA: INT ATOMIC ENERGY AGENCY, 1997, 625–631. ISBN: 92-0-102997-7.

[21] A. Kirschner et al. “Modelling of Impurity Transport and Plasma-Wall Interaction in Fusion Devices with the ERO Code: Basics of the Code and Examples of Application”. In: *Contributions to Plasma Physics* 56.6-8 (2016), pp. 622–627. ISSN: 08631042. DOI: 10.1002/ctpp.201610014.

[22] P.C. Stangeby and J.D. Elder. “Calculation of observable quantities using a divertor impurity interpretive code, DIVIMP”. In: *J. Nucl. Mater.* 196-198 (1992), pp. 258–263.

[23] A. Eksaeva et al. “ERO modelling of tungsten erosion in the linear plasma device PSI-2”. In: *Nuclear Materials and Energy* 12 (2017), pp. 253–260. ISSN: 23521791. DOI: 10.1016/j.nme.2017.03.014.

[24] R. Ding et al. “Simulation of gross and net erosion of high-Z materials in the DIII-D divertor”. In: *Nuclear Fusion* 56.1 (2016). ISSN: 0029-5515 1741-4326. DOI: 10.1088/0029-5515/56/1/016021.

[25] PC Stangeby. In: *Nucl. Fusion* 52.083012 (2012).

[26] A. Järvinen et al. “DIVIMP simulation of W transport in the SOL of JET H-mode plasmas”. In: *Physica Scripta* T145 (2011). ISSN: 0031-8949 1402-4896. DOI: 10.1088/0031-8949/2011/t145/014013.

[27] K. Schmid, M. Reinelt, and K. Krieger. “An integrated model of impurity migration and wall composition dynamics for tokamaks”. In: *Journal of Nuclear Materials* 415.1 (2011), S284–S288. ISSN: 00223115. DOI: 10.1016/j.jnucmat.2011.01.105.

[28] K. Schmid et al. “WALLDYN simulations of global impurity migration in JET and extrapolations to ITER”. In: *Nuclear Fusion* 55.5 (2015). ISSN: 0029-5515 1741-4326. DOI: 10.1088/0029-5515/55/5/053015.

[29] Shuyu Dai et al. “Modelling of surface roughness effects on impurity erosion and deposition in TEXTOR with a code package SURO/ERO/SDPIC”. In: *Nuclear Fusion* 54.12 (2014). ISSN: 0029-5515 1741-4326. DOI: 10.1088/0029-5515/54/12/123015.

[30] Lyman Spitzer Jr. *Physics of Fully Ionized Gases*. Interscience Publishers Inc., 1962.

[31] D.C. Montgomery and D.A. Tidman. *Plasma Kinetic Theory*. McGraw-Hill, 1964.

[32] J.D. Callen. *Coulomb Collisions Course:Fundamentals of Plasma Physics*. http://homepages.cae.wisc.edu/ callen/chap2.pdf. 2006.

[33] S.I. Braginskii. *Transport Processes in a Plasma*. Consultants Bureau, 1965.

[34] J.P. Boris. "Relativistic plasma simulation-optimization of a hybrid code". In: *Proceeding of Fourth Conference on Numerical Simulations of Plasmas* (1970).

[35] C.K. Birdsall and A.B. Langdon. *Plasma Physics Via Computer Simulations*. Bristol and Philadelphia: Institute of Physics Publishing, 1991.

[36] H. P. Summers. *The ADAS User Manual, version 2.6*. 2004. URL: http://www.adas.ac.uk.

[37] Rainer Behrisch and Wolfgang Eckstein. *Sputtering by Particle Bombardment: Experiments and Computer Calculations from Threshold to Mev Energies*. Berlin: Springer, 2007.

[38] Jon Drobny et al. "F-TRIDYN: A Binary Collision Approximation code for simulating ion interactions with rough surfaces". English. In: *JOURNAL OF NUCLEAR MATERIALS* 494 (OCT 2017), 278–283. ISSN: 0022-3115. DOI: {10.1016/j.jnucmat.2017.07.037}.

[39] V.A. Abramov et al. "First wall and divertor plate sputtering in a tokamak reactor". In: *Journal of Nuclear Materials* 162-164 (1989), pp. 462–466. ISSN: 0022-3115. DOI: https://doi.org/10.1016/0022-3115(89)90313-9. URL: http://www.sciencedirect.com/science/article/pii/0022311589903139.

[40] Rinat Khaziev and Davide Curreli. "Ion energy-angle distribution functions at the plasma-material interface in oblique magnetic fields". In: *Physics of Plasmas* 22 (2015). DOI: https://doi.org/10.1063/1.4916910.

[41] P.J. Plauger et al. *C++ Standard Template Library*. 1st. Upper Saddle River, NJ, USA: Prentice Hall PTR, 2000. ISBN: 0134376331.

[42] Jared Hoberock Nathan Bell. "Thrust: A Productivity-Oriented Library for CUDA". In: *GPU Computing Gems, Jade Edition, Edited by Wen-mei W. Hwu* (2011).

[43] Chodura R. In: *Phys. Fluids* 25.1628 (1982).

[44] M.A. Lieberman and A.J. Lichtenberg. *Principles of Plasma Discharges and Materials Processing*. Wiley, 2005. ISBN: 9780471724247. URL: https://books.google.com/books?id=m0iOga2XE5wC.

[45] Richard D. Gill. *Plasma Physics and Nuclear Fusion Research*. Academic Press, 1981, p. 708. ISBN: 978-0-12-283860-6.

[46] P.C Stangeby and J.D Elder. "Impurity retention by divertors. I. One dimensional models". In: *Nuclear Fusion* 35.11 (Nov. 1995), pp. 1391–1412. DOI: 10.1088/0029-5515/35/11/i06. URL: https://doi.org/10.1088%2F0029-5515%2F35%2F11%2Fi06.

[47] R.P. Doerner. In: *Nuclear Fusion* 52 (2012).

[48] T.R. Younkin et al. “GITR: An Accelerated Global Scale Particle Tracking Code For Wall Material Erosion and Redistribution In Fusion Relevant Plasma-Material Interactions”. In: *Computer Physics Communications* (2019).

[49] S. Blondel et al. “Benchmarks and Tests of a Multidimensional Cluster Dynamics Model of Helium Implantation in Tungsten”. In: *Fusion Sci. Technol.* 71 (2017)).

[50] W. R. Elwasif et al. “The Design and Implementation of the SWIM Integrated Plasma Simulator”. In: *18th Euromicro Conference on Parallel, Distributed and Network-based Processing* (2010), pp. 419–427.

[51] H.H Binder. *Lexikon der chemischen Elemente*. Hirzel Verlag Stuttgart/Leipzig, 1999.

[52] K. Schafer and C. Synowietz. *D'Ans-Lax Taschenbuch fur Chemiker und Physiker*. Springer-Verlag Berlin Heidelberg, 1970.

[53] T.R. Younkin et al. “GITR: An Accelerated Global Scale Particle Tracking Code For Wall Material Erosion and Redistribution In Fusion Relevant Plasma-Material Interactions”. In: *Computer Physics Communications* (2019).

# Vita

Timothy Younkin is originally from Oak Ridge, Tennessee. He graduated from Oak Ridge High School in 2007 and went on to attend the University of Tennessee, Knoxville. In 2012 Tim graduated with his Bachelor of Science in Physics. From there Tim decided to pursue nuclear engineering, accepting a fellowship from the Nuclear Regulatory Commission at the Georgia Institute of Technology. There Tim completed a Masters in Nuclear engineering with research focused on fuel burn-up in boiling water reactors, graduating in 2014. In the Fall of 2014 Tim returned to the University of Tennessee to complete his Doctorate degree studying fusion reactor physics and impurities. Upon Tim's graduation he has accepted the Department of Energy Fusion Energy Sciences Postdoctoral Research Fellowship and will be continuing his research at Oak Ridge National Lab.